

Electronic Theses and Dissertations, 2004-2019

2015

Combustion Kinetics of Advanced Biofuels

Ghazal Barari
University of Central Florida

 Part of the [Mechanical Engineering Commons](#)
Find similar works at: <https://stars.library.ucf.edu/etd>
University of Central Florida Libraries <http://library.ucf.edu>

This Doctoral Dissertation (Open Access) is brought to you for free and open access by STARS. It has been accepted for inclusion in Electronic Theses and Dissertations, 2004-2019 by an authorized administrator of STARS. For more information, please contact STARS@ucf.edu.

STARS Citation

Barari, Ghazal, "Combustion Kinetics of Advanced Biofuels" (2015). *Electronic Theses and Dissertations, 2004-2019*. 1444.
<https://stars.library.ucf.edu/etd/1444>

COMBUSTION KINETICS OF ADVANCED BIOFUELS

by

GHAZAL BARARI

M.S. Iran University of Science and Technology, 2010

B.S. Iran University of Science and Technology, 2006

A dissertation submitted in partial fulfillment of the requirements
for the degree of Doctor of Philosophy
in the Department of Mechanical and Aerospace Engineering
in the College of Engineering and Computer Science
at the University of Central Florida
Orlando, Florida

Fall Term
2015

Major Professor: Subith S. Vasu

© 2015 Ghazal Barari

ABSTRACT

Use of biofuels, especially in automotive applications, is a growing trend due to their potential to lower greenhouse gas emissions from combustion. Ketones are a class of biofuel candidates which are produced from cellulose. However, ketones received rather scarce attention from the combustion community compared to other classes such as, alcohols, esters, and ethers. There is little knowledge on their combustion performance and pollutant generation. Hence their combustion chemistry needs to be investigated in detail. Diisopropyl ketone (DIPK) is a promising biofuel candidate, which is produced using endophytic fungal conversion. A detailed understanding of the combustion kinetics of the oxidation of DIPK in advanced engines such as, the homogeneous charge compression ignition (HCCI) engine is warranted. This dissertation concentrates on the combustion kinetics of DIPK over a wide range of temperature and pressure with a focus on HCCI engine application.

An existing DIPK kinetic mechanism has been reviewed and a single zone HCCI engine model has been modeled and validated against recent experimental data from Sandia National Lab. Therefore different HCCI modeling assumptions were tested and the DIPK reaction mechanism was modified with missing reactions and the required thermochemical data. As a result, the HCCI pressure trace, heat release rate and reactivity have been improved. In order to improve the ignition delay time simulation results, the low temperature oxidation of DIPK was studied as the fuel chemistry effects on the autoignition behavior becomes important in low temperature. Therefore DIPK low temperature oxidation experimental data was obtained from the synchrotron photoionization experiments conducted at the Advanced Light Source (ALS) so that the primary products as well as the dominant oxidation pathways are identified. Furthermore, the aldehydes

oxidation, as a result of partial or incomplete combustion and as the primary stable intermediate products in oxidation and pyrolysis of biofuel were studied at low temperature in ALS.

A high temperature reaction mechanism was created using the reaction class approach. The reaction mechanism for DIPK was improved using the experimental data along with quantum chemical calculation of activation energies and barriers as well as vibrational modes for the important reactions identified in ALS experiment. The rate constants for important reactions were calculated based on modified Arrhenius equation. DIPK oxidation and pyrolysis were studied at high temperature and pressure using UCF shock tube. The ignition delay times as well as the product (methane) time histories were investigated and used as validation targets for the new model.

To my mom and dad

ACKNOWLEDGMENTS

I would like to use this opportunity to express my gratitude to all the people who have helped me in the challenging path of finishing my PhD, without their supports, my accomplishments would not be possible.

I would like to express my deepest gratitude to my advisor *Dr. Subith Vasu* who undoubtedly was the most influential person in shaping up my academic career for his excellent guidance and brilliant management, caring and patience and providing me with encouragement for the past years of my PhD study. I thank him for all the time and supports for teaching me his knowledge and guiding me during the research work, giving such thoughtful feedbacks and always aimed at moving me forward. I could not have imagined having a better advisor and mentor for my PhD study.

I would also like to thank *Dr. Artem Masunov*, who was guiding the computational part of my research for the past year and helping me to develop my background in quantum chemistry and was willing to participate in my final defense committee. Without his precious support for giving me the access to the useful computational programs and his patience for directing me, it would not be possible to conduct this research.

I would like to express my sincere gratitude to *Dr. Kapat* and *Dr. Kassab* as my candidacy and dissertation committee members for their assistance and insightful comments about my project.

My sincere thanks also go to my fellow lab mates as we were working together before deadlines and all their supports during the past years.

I would also like to thank my parents, for all their unconditional love, motivations and supports during my PhD and all my life in general. They were always supporting me and encouraging me with their best wishes. I am grateful to my brothers, *Bamdad* and *Kian* and my baby sister, *Nicky* for supporting me spiritually and making me happy as always with their encouraging words.

Finally I would like to devote my special gratitude to my husband, *Mohammad*, for all his love and support and all the fun we have had in UCF being PhD students, friends and as a couple.

TABLE OF CONTENTS

LIST OF FIGURES	xiii
LIST OF TABLES	xix
LIST OF SCHEMES.....	xx
CHAPTER 1: INTRODUCTION.....	1
1.1 Motivation	1
1.2 Objective.....	7
CHAPTER 2: IMPROVED COMBUSTION KINETIC MODEL AND HCCI ENGINE	
SIMULATION OF DIPK.....	10
2.1 Introduction	10
2.2 Computational Approach.....	13
2.2.1 Single-zone adiabatic engine model with the original mechanism.....	13
2.2.2 Improved chemical kinetic mechanism.....	16
2.2.3 Multi-zone engine modeling	21
2.3 Results and discussions	23
2.4 Ignition delay times	23
2.4.1 Pyrolysis experiments	25
2.4.2 Single-zone model with heat transfer effects using improved reaction mechanism	27

2.4.3	Sensitivity analysis	30
2.4.4	HCCI reactivity by engine speed sweep	31
2.4.5	Intake temperature effects on HCCI autoignition	33
2.4.6	Multi-zone engine	34
2.5	Conclusion	37
CHAPTER 3: QUANTUM CHEMICAL CALCULATIONS OF MAJOR REACTIONS OF		
DIPK		
3.1	Introduction	39
3.2	Theoretical method	41
3.2.1	Potential energy surfaces calculations.....	41
3.3	Rate constant calculations	42
3.4	Computational procedure	43
3.5	Results and discussion	47
3.5.1	α -R + O ₂ reaction	47
3.6	Conclusion	54
CHAPTER 4: OH-INITIATED OXIDATION OF DIPK AT LOW TEMPERATURE.....		
4.1	Introduction	55
4.2	ALS Experimental method	57
4.3	Results and discussion	62

4.3.1	Diisopropyl ketone (DIPK) OH-initiated oxidation.....	62
4.4	Conclusions	72
CHAPTER 5: Cl-INITIATED OXIDATION OF MAJOR ALDEHYDES INTERMEDIATES		
FROM DIPK COMBUSTION		73
5.1	Introduction	73
5.2	Experimental method.....	76
5.3	Results and discussion	77
5.3.1	Products and pathways in acetaldehyde low temperature Cl-initiated oxidation	77
5.3.2	Products and pathways in propanal low temperature Cl-initiated oxidation ..	84
5.3.3	Products and pathways in 2-propanal low temperature Cl-initiated oxidation	90
5.4	Conclusion	93
CHAPTER 6: SHOCK TUBE IGNITION AND PYROLYSIS OF DIPK		
6.1	Introduction	95
6.2	Experimental setup	98
6.2.1	UCF shock tube facility.....	98
6.3	Results and discussion	99
6.3.1	Shock tube experiments	99
6.3.2	Laser-absorption measurement	101

6.3.3	DIPK pyrolysis	102
6.3.4	DIPK oxidation	104
6.4	Conclusion	105
CHAPTER 7: NEW DIPK REACTION KINETICS MECHANISM DEVELOPMENT USING THE REACTION CLASS APPROACH..... 106		
7.1	Introduction	106
7.2	High temperature DIPK kinetic model development using reaction class approach .	107
7.2.1	Unimolecular fuel decomposition reactions.....	107
7.2.2	Fuel H-atom abstraction reactions.....	109
7.2.3	Ketonyl radical decomposition.....	114
7.2.4	Fuel radical isomerization reaction	115
7.2.5	Olefin unimolecular decomposition reactions.....	116
7.2.6	Olefin H-abstraction reaction	117
7.2.7	Olefin radical isomerization reaction	119
7.2.8	Olefin radical decomposition reaction	119
7.2.9	Keto-enol tautomerization.....	120
7.3	Low temperature DIPK kinetic model development.....	120
7.4	Mechanism validation.....	121
7.4.1	122	

7.4.2	Kinetic model analysis	122
7.5	Conclusion	125
CHAPTER 8: SUMMARY.....		126
APPENDIX A.....		128
DIPK HIGH TEMPERATURE MECHANISM.....		128
APPENDIX B		134
QUANTUM CHEMICAL CALCULATIONS OF DIPK RADICALS REACTIONS WITH O ₂		134
LIST OF REFERENCES		188

LIST OF FIGURES

Figure 1-1- Biofuel-engine co-development [4].....	2
Figure 1-2- Ketone production from cellulose by endophytic fungi[4]	3
Figure 1-3- DIPK 3D structure	5
Figure 1-4- Experimental (markers) and modeled (solid line) ignition delay times for DIPK oxidation in a rapid compression machine (Allen et al. 2014 [6])	5
Figure 1-5- Experimental (markers) and modeled (lines) mole fractions for major products of DIPK pyrolysis at 760 Torr (red dashed line, square markers) and 30 Torr (blue solid line, circle markers) (Allen et al 2014 [6])	6
Figure 1-6- DIPK (denoted as DMPN) temperature sensitivity comparing to ethenol (left) and gasoline (right) (Yang and Dec 2013 [16]).....	7
Figure 2-1- Comparison of simulated and measured pressure traces for TBDC sweep, $\Phi=0.4$, 1200 rpm using the original mechanism file for DIPK	16
Figure 2-2- CO and CO ₂ rate of production for 3-pentanone [41] and DIPK [25]	21
Figure 2-3- Modelled and measured [25] DIPK ignition delay times in shock tube and rapid compression machine at 10 bar.....	24
Figure 2-4- Measured (symbols) and predictions by the modified mechanism (lines) for the mole fractions during DIPK pyrolysis at 950-1350K at 30 Torr(blue) and 800-1200K at 760 Torr (black). The original mechanism predictions are also shown (red) at 30 Torr(solid) 760 Torr (dashed).	26
Figure 2-5- Single-zone model improved pressure trace for TBDC=456K.	28
Figure 2-6- Single-zone model improved pressure trace for TBDC=452K	28

Figure 2-7- Ignition delay time sensitivity analysis at 1023 K, 30 bar.....	31
Figure 2-8- Comparison of HCCI reactivity, speed sweep vs. TBDC(model) and T_{in} (experiment[2]) at constant CA 372 deg. CA, P=100kPa, $\Phi=0.38$	33
Figure 2-9- Comparison of experimental [2] BDC temperature with the simulation, the effects of BDC temperature on HCCI autoignition.....	34
Figure 2-10- DIPK HCCI multi-zone model (TBDC,max = 450K); pressure (top left), average temperature (top right) average accumulated heat release (bottom left), and heat release rate (bottom right) vs. degree crank angle compared with the experimental data (TBDC=456K).....	36
Figure 2-11- Pressure effects on ITHR of DIPK, Experimental ITHR (left) [15] and simulated ITHR (right). DMPN in the left graph stands for 2,4-dimethyl-3-pentanone (DIPK)	37
Figure 3-1- Potential energy curve for a two atom molecule; R is the equilibrium bond length; Do-De is the zero vibration energy.....	40
Figure 3-2- A sample job script in Gaussian, with the z-matrix shown in the red box	45
Figure 3-3- CanTherm input file sample	46
Figure 3-4- Stationary points on PES for α -R+O ₂ reaction. Energies are computed at CBS- QB3 level of theory and presented at 0K relative to the reactants. The HO ₂ elimination from α -Q _p OOH (shown as α -Q _{p2} in this figure) is the most favorable pathway, illustrated in red. .	50
Figure 4-1- Schematic of experimental apparatus [69]	59
Figure 4-2- A sample three dimensional dataset measured in [76]	60
Figure 4-3- Experimental setup schematic [76].....	61

Figure 4-4- Integrated difference mass spectra for OH initiated oxidation of DIPK at 300, 450 and 500 K, obtained by integration over the photon energy 8.4-11.0 eV and the kinetic times until 20 ms after the laser photolysis 64

Figure 4-5- Photoionization spectra of $m/z=42$, 44 and 58 at different temperatures simulated by the standard PIE spectra of Propene [78], Acetaldehyde [78] and Acetone+Methyloxirane respectively 65

Figure 4-6- Photoionization spectra of $m/z=112$ corresponding to $C_7H_{12}O$, (left) and $m/z=128$ corresponding to cyclic ether, $C_7H_{12}O_2$ (right) at different temperatures along with a comparison to the PIE spectra from Cl-initiated experiment (Allen et al. [6]) 66

Figure 4-7- Possible cyclic ethers formed in DIPK oxidation..... 67

Figure 4-8- a) Time profiles of $m/z = 42, 44, 58, 112, 128,$ and 71 at 500 K, obtained by integration over photon energies from 8.4 – 11.0 eV. The consumption of DIPK is shown by the profile of its daughter ion at $m/z = 71$, shown multiplied by (-1); b) time profiles of larger view ($m/z=58$ excluded); c) Time profiles at 450 K; d) time profiles of larger view 68

Figure 4-9- Time profiles of $m/z = 42, 44, 58, 112,$ and 128 at 500 K, obtained by integration over photon energies from 8.4 – 11.0 eV, scaled such that all the profiles intensities (in arbitrary unit) are equal to unity at a kinetic time of 40 ms (20 ms after the laser photolysis).
..... 69

Figure 4-10- Time profiles of Propene, Acetaldehyde, $C_7H_{12}O$ and cyclic ether at 300, 450 and 500 K up to 30 ms after laser photolysis..... 71

Figure 5-1- Aldehyde mole fraction in 2% DIPK oxidation in Ar in 1300 K and 0.9 atm 76

Figure 5-2- Integrated difference mass spectra for Cl-initiated oxidation of Acetaldehyde at 550 K and 700 K, obtained by integration over the photon energy 9.5-11.5 eV and the kinetic times until 25 ms after the laser photolysis 78

Figure 5-3- Primary products photoionization spectra of Acetaldehyde Cl-initiated oxidation at 550 and 700 K obtained by integration over kinetic time 25 ms after laser photolysis, compared to the corresponding standard photoionization cross section 79

Figure 5-4- The scaled time profiles of m/z=30 (formaldehyde), 42 (ketene), 47 (methyl peroxy) and 60 compared to the inverted depletion rate of parent fuel, m/z=44 (acetaldehyde) in Cl-initiated oxidation of acetaldehyde at 700 K..... 80

Figure 5-5- The scaled time profiles of m/z=30 (formaldehyde), 42 (ketene), 47 (methyl peroxy) and 60 in Cl-initiated oxidation of acetaldehyde at 550 K..... 80

Figure 5-6- Temperature dependent time profiles of the products in Cl-initiated oxidation of acetaldehyde 84

Figure 5-7- Cl-initiated oxidation of Propanal mass spectra at 550 K and 700 K, obtained by integration over the photon energy 9.5-11.5 eV and the kinetic times until 25 ms after the laser photolysis 88

Figure 5-8- Primary products photoionization spectra of propanal Cl-initiated oxidation at 550 and 700 K compared to the corresponding standard PIE 88

Figure 5-9- Temperature dependent time profiles of the products in Cl-initiated oxidation of propanal 89

Figure 5-10- Cl-initiated oxidation mass spectra of 2-propenal at 550 K obtained by integration over the photon energy 9.5-11.5 eV and the kinetic times until 25 ms after the laser photolysis	91
Figure 5-11- Primary products photoionization spectra of 2-propenal Cl-initiated oxidation at 550 compared to the corresponding standard PIE	92
Figure 5-12- Comparison of the photoionization spectra of the peak at $m/z=44$ with the corresponding standard PIE of ethenol and acetaldehyde, along with the data fit, in 2-propenal Cl-initiated oxidation at 550	92
Figure 6-1- An ideal shock tube with different waves formed after diaphragm ruptures [100]	95
Figure 6-2- Rapid compression machine and shock tube experimental and modeled ignition delays (Allen et. al [6])	98
Figure 6-3- Methane Absorption Cross-section at each wavelength [99]	102
Figure 6-4- Methane Time history for 2% DIPK pyrolysis in Ar at 1300 K.....	103
Figure 6-5- Methane Time history for 2% DIPK pyrolysis in Ar at 1400 K.....	103
Figure 6-6- DIPK experimental ignition delay time data for stoichiometric mixture of 2% DIPK in 20% O ₂ and 78% Ar at 0.9 bar compared to the original model for DIPK (Allen et al)	104
Figure 7-1- The total rate constants estimated for DIPK reaction with OH at high temperature range	113

Figure 7-2- DIPK ignition delay time; comparison between the experimental data for stoichiometric mixture of 2% DIPK in 20% O₂ and 78% Ar at 0.9 bar with the simulation using original mechanism (Allen et al) and the modified mechanism (current work) 124

Figure 7-3- CH₄ concentration shock tube experiment for DIPK pyrolysis compared to the high temperature reaction mechanism as well as original mechanism..... 124

LIST OF TABLES

Table 1-1- literature review on some ketones kinetics study	4
Table 2-1- HCCI engine properties for simulation and experiments	15
Table 2-2- RMG generated rate coefficients for added reactions in the modified mechanism	20
Table 2-3- Multi-zone model configuration	22
Table 3-1- Reactants, intermediates, products in α -R + O ₂ reaction; energies are at 0K relative to the reactants	51
Table 3-2- The structures of the reactions of α -R + O ₂	52
Table 3-3- Rate constants calculated for the reactions of α -R + O ₂	53
Table 3-4- Rate constants calculated for the reactions of β -R + O ₂	53
Table 4-1- DIPK oxidation Major products branching ratio relative to propene at 450 and 500 K	72
Table 5-1- The product yield relative to acetaldehyde as the major product in propanal Cl- initiated oxidation at 550 and 700 K.....	90
Table 6-1- DIPK ignition delay time	105
Table 7-1- DIPK estimated rates for H abstraction reactions by H, OH, HO ₂ , CH ₃ and C ₂ H ₅ radicals.....	113
Table 7-2- Addition of methyl or H atom to double bond (Curran et al 1998 [125])	114
Table 7-3- HP rate rules hydrogen atom shift for pressure-dependence calculations (Matheu et al 2003 [126]).....	116

LIST OF SCHEMES

Scheme 1-1- Ketones general structure	5
Scheme 2-1- Simplified oxidation scheme of DIPK at 20% fuel burn point, TBDC=422K, Pin=99kPa.....	19
Scheme 2-2- Added pathways to the oxidation scheme; C ₇ H ₁₂ O and IVK H-abstraction reactions and radical decompositions.	20
Scheme 3-1- Reaction pathways of α -RO ₂	48
Scheme 3-2- Reaction pathways of β -RO ₂	49
Scheme 4-1- DIPK low temperature oxidation pathway	57
Scheme 5-1- Aldehydes structures	74
Scheme 5-2- Acetaldehyde and acrolein production pathway in DIPK oxidation.....	75
Scheme 5-4- Acetaldehyde radicals.....	78
Scheme 5-5- Ketene formation from radical thermal decomposition	81
Scheme 5-6- Ketene formation from β -R radical of acetaldehyde	81
Scheme 5-7- Ketene formation from α -R radical of acetaldehyde	81
Scheme 5-8- Propanal radicals	87
Scheme 5-9- Acetaldehyde formation pathway from propanal oxidation.....	87
Scheme 5-10- Formaldehyde and ketene formation pathway from propanal oxidation	87
Scheme 5-11- Formation of C ₂ H ₄ from propanal oxidation.....	87
Scheme 5-12- Acrolein (2-propenal) radicals.....	91
Scheme 7-1- DIPK decomposition	108
Scheme 7-2- DIPK radicals- tertiary and primary radicals	109

Scheme 7-3- Isopropyl methyl ketone iPMK	110
Scheme 7-4- H atom migration in 1,2 H-Shift	115
Scheme 7-5- H abstraction from C ₇ H ₁₂ O	118
Scheme 7-6- DIPK high temperature oxidation pathway	121
Scheme 7-7- DIPK low temperature oxidation pathway	122

CHAPTER 1: INTRODUCTION

1.1 Motivation

The production of renewable fuels and energies are becoming a primary need as the energy costs increase and due to the environmental concerns. The biofuels considered have to be compatible with the next generation advanced engines and their production procedure must be efficient from cost and resource point of view. The new engines are often very sensitive to the fuel chemistry [1]. Therefore a co-development of engines and biofuels is the important optimized strategy [2].

The growth of renewable and alternative liquid fuel sources is compelled by the limited fossil fuel supplies and use of biofuels, especially in automotive applications, is a growing trend due to their potential to reduce the greenhouse gas concentrations in atmosphere [2]. Therefore the study of combustion kinetic of the advanced biofuels is important in order to determine the environmental effects as well as the biofuels performance in the next generation of advanced engines. The new internal combustion engines developed to have higher efficiency as well as lower emission which requires low temperature autoignition. The combination of theoretical calculations, simulation and experimental data can give a very good insight; however, all the methods are not always available. Therefore, developing a comprehensive model for combustion kinetic of the biofuel of interest would be very important (See Figure 1-1).

The liquid hydrocarbons are vastly used in transportation industries due to their high volumetric energy density and convenient methods of storage and transport. However, the environmental concerns as well as their limited source bring about the motivation to alternative

liquid fuels [3]. Furthermore, developing a combustion model for the biofuels will provide the capability of predicting the biofuels kinetic behavior.

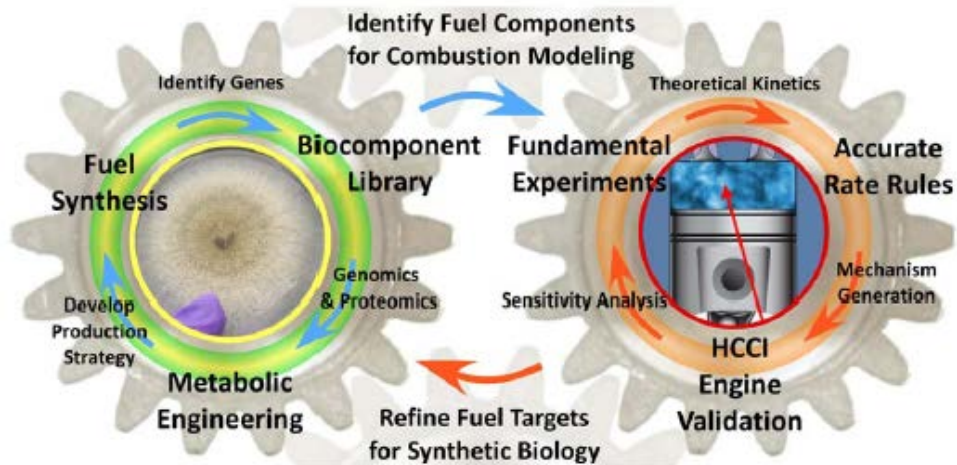


Figure 1-1- Biofuel-engine co-development [4]

Biofuels are in an unprocessed form such as fuelwood, wood chips and pellets, etc. or they are generated as a result of processing of biomass such as ethanol, biodiesel, DME, etc. Therefore they are categorized as primary (unprocessed) and secondary (processed) biofuels [5]. Today, the biomass-based fuels are those biofuels which are proper alternative from both environmental and economic standpoint [5]. Gasoline in spark-ignition engines can be replaced with alcohol fuels, while compression ignition (CI) engines consume biodiesel.

Current biofuels such as corn ethanol and biodiesel involve relatively small reduction of greenhouse gases relative to petroleum while next generation biofuels (cellulosic biofuels) will give much greater GHG reduction. Some microbial types for instance fungi, yeast, and microalgae can be utilized as potential bases for biofuel production. The biofuels of our interest in this study are produced based on metabolic processes of endophytic fungi which naturally live in symbiosis with woody plants. These organisms consume some of the biomass of the host plant and produce

volatile organic compounds, and useful fuels. Fungi can directly consume cellulose and other renewable sustainable carbon compounds and produce a spectrum of potentially useful volatile organic compounds. Several of fungi produce substantial amounts of ketones and other oxygenated fuels. The process of ketone production from cellulose by fungi is shown in Figure 1-2.

Ketones are potential biofuel candidates and are generated as intermediate products throughout the oxidation of oxygenated fuels like alcohols or esters or larger hydrocarbons. Ketones contains carbonyl group (C=O) shown in Scheme 1-1 where R and R' can be a variety of carbon-containing substituents.

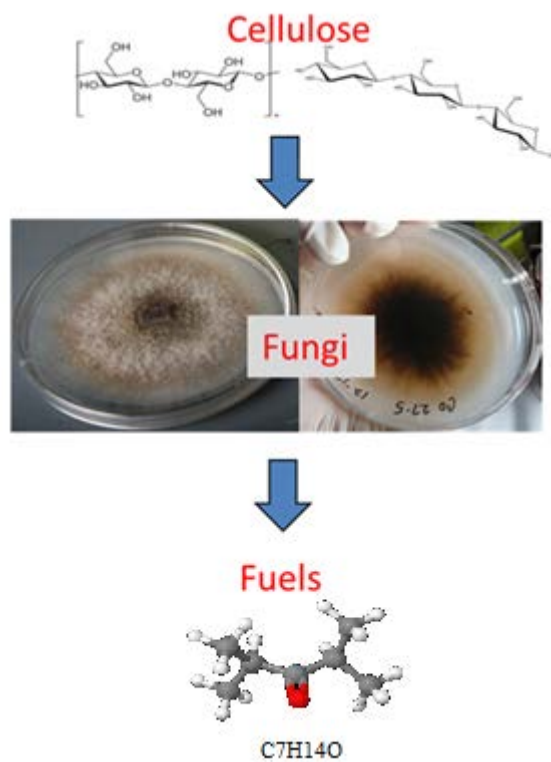


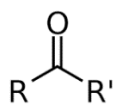
Figure 1-2- Ketone production from cellulose by endophytic fungi[4]

Few investigation and measurements are done on the larger straight-chained and branched ketones. Thus, the ignition characteristics and chemistry of oxidation are not well studied for larger ketones. A quick literature review on the kinetics studies on ketones is listed in Table 1-1.

The ketone which is studied in this work is a branched ketone, called diisopropyl ketone (DIPK) (Figure 1-3). A reaction mechanism has been developed for DIPK recently which represents a kinetic model to describe the pyrolysis and oxidation of DIPK [6]. The model was verified against experiment; however the ignition delay time measured by rapid compression machine for the temperature range of 590-720 K and at the pressure of 10 bar showed discrepancies comparing to the experimental results (see Figure 1-4). The significant shift in the NTC (temperature at which the negative temperature region starts) observed in this figure suggests that more investigation should be done to develop a model to be capable of predicting the combustion behavior of DIPK.

Table 1-1- literature review on some ketones kinetics study

Authors	year	ketone	study
Bott and Cohen [7]	1991	Acetone	rate constant of the reaction: acetone + OH
Black et al [8]	2007	Acetone	ignition delay times and laminar flame speed
Zhao et al [9]	2008	Acetone	reaction rate of acetone with atomic chlorine
Pichon et al [10]	2009	Acetone	ignition delay times at high temperatures
Davidson et al [11]	2010	Acetone	ignition delay times at high temperatures
Lam et al [12]	2013	Acetone	pyrolysis of acetone
Zhao et al [9]	2008	2-butanone	reaction rate of 2-butanone with atomic chlorine
Lam et al [13]	2012	2-butanone	reaction rate of 2-butanone with OH, Theoretical
Lam et al [12]	2013	2-butanone	reaction rate of 2-butanone with OH, experimental



Scheme 1-1- Ketones general structure

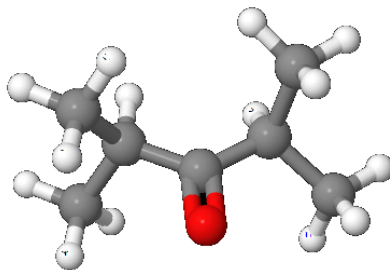


Figure 1-3- DIPK 3D structure

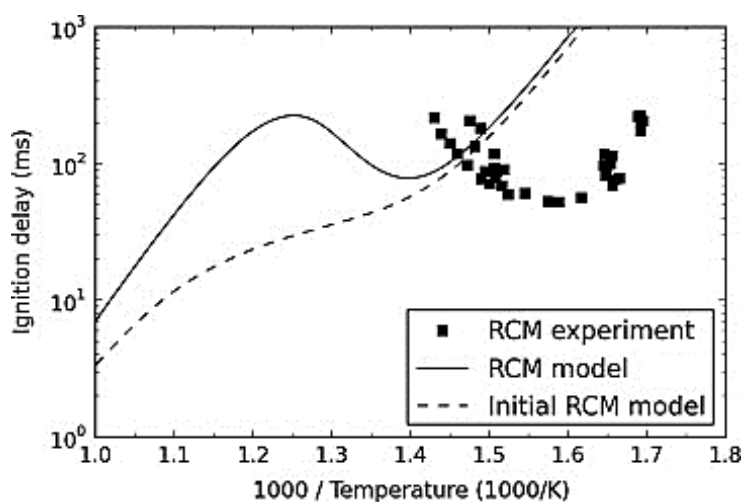


Figure 1-4- Experimental (markers) and modeled (solid line) ignition delay times for DIPK oxidation in a rapid compression machine (Allen et al. 2014 [6])

Pyrolysis is an advanced thermal process in the absence of oxygen. The pyrolysis results of DIPK compared to the experiment for some major species concentration versus maximum reactor temperature. Discrepancies between model and experiments can be observed in Figure 1-4.

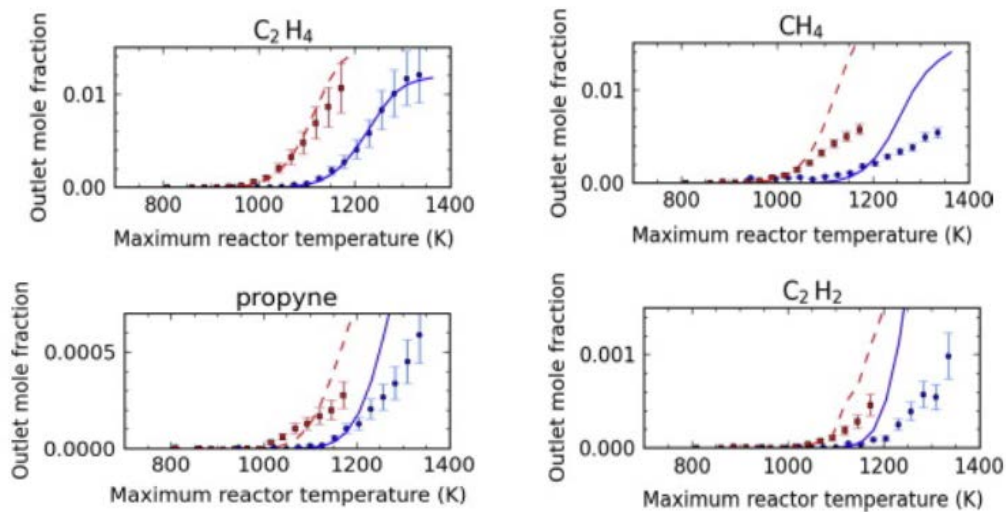


Figure 1-5- Experimental (markers) and modeled (lines) mole fractions for major products of DIPK pyrolysis at 760 Torr (red dashed line, square markers) and 30 Torr (blue solid line, circle markers) (Allen et al 2014 [6])

As the new biofuels are produced, the new combustion technologies are also emerging and the goal is to provide development for both fields. The homogenous compression ignition (HCCI) engines are one of the advanced combustion technologies based on low temperature combustion. A lean fuel-air mixture is compressed to the autoignition [4]. The temperature does not reach to the point at which NO_x forms. HCCI engine has high compression ratio similar to Diesel engines. As the control of combustion timing depends on the chemistry of the fuel's autoignition, it is used as the desired combustion strategy to understand the combustion behavior of the biofuel of interest [14].

Autoignition characteristics and HCCI engine combustion of DIPK has been investigated in the Sandia HCCI engine [15] and the results are compared with gasoline and ethanol. It was found that DIPK behaves similar to the low-reactivity ethanol in the sense that it shows strong temperature-sensitivity, even at boosted inlet pressure (See Figure 1-5). However, DIPK indicated much stronger pressure-sensitivity than ethanol. With such a pressure sensitivity, the required inlet

temperature decreases as the pressure increases which is similar to gasoline. With its temperature sensitivity, DIPK has lower heat release than gasoline which needs combustion timing retard to prevent knock. Therefore it was concluded that DIPK has higher thermal efficiency than gasoline at comparable loads (See Figure 1-5).

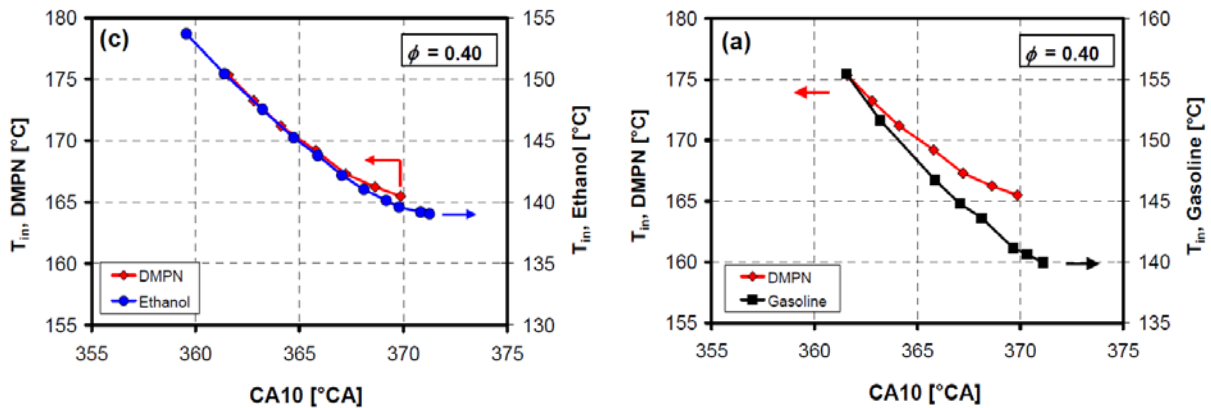


Figure 1-6- DIPK (denoted as DMPN) temperature sensitivity comparing to ethanol (left) and gasoline (right) (Yang and Dec 2013 [16])

1.2 Objective

This dissertation describes theoretical and experimental studies intended to investigate the advanced biofuels kinetics to employ in the new generation of combustion engines. The biofuels of interest are selected from different oxygenated fuel group including ketones (DIPK), alcohols (n-butanol) and aldehydes (acetaldehyde, propanal and acrolein). Among these biofuels, DIPK is investigated theoretically and experimentally. The theoretical investigation has been done using CHEMKIN-PRO [17] modeling software to simulate the fuel ignition and pyrolysis behavior. The quantum chemical calculation of the reactions has been done using Gaussian [18] to obtain the

energies and vibrational modes which are employed as an input for CanTherm [19] program to calculate the corresponding rate constants.

The general procedure adopted is as follows. In chapter two, a single zone HCCI engine model has been modeled and validated against recent experimental data from Sandia [15]. The calculated pressure trace and heat release rate showed discrepancies when compared to the experimental data. Therefore different HCCI modeling assumptions were tested and the DIPK reaction mechanism was modified with missing reactions and the required thermochemical data. The corresponding thermochemical properties for the fuel and radical species were calculated using the THERM [20] program and rates were either estimated in comparison with similar molecules or calculated using a rate estimation software such as RMG [21]. As a result, the HCCI pressure trace, heat release rate and reactivity have been improved. The ignition delay time predictions were improved, however, still showed deviations from the limited experimental data from the shock tube.

Chapter three covers the quantum chemical calculation for the most important reactions in DIPK oxidation. Gaussian 09 [18] software is used to obtain the bond dissociation energies and frequencies via the molecule electronic structure optimization up to the high level of theory. The kinetic rate constant for each reaction of interest is calculated using CanTherm [19].

In chapter four DIPK low temperature oxidation is studied through the experimental data obtained from the synchrotron photoionization experiments directed at the Advanced Light Source (ALS). The OH-initiated oxidation has been performed at 300-550 K. The primary products have been identified using their photoionization spectra. The H abstraction reaction branching ratios are obtained and the results are compared to the Cl-initiated oxidation.

In chapter five the Cl-initiated oxidation ALS measurement has been performed for aldehydes as important intermediate formed in low and intermediate temperature oxidation of many oxygenated fuels including ketones. Acetaldehyde, propanal and acrolein are studied and the primary products as well as the important product formation pathways are studied.

In chapter six, the experimental data for the product CH_4 concentration in DIPK pyrolysis as well as DIPK ignition delay time are obtained using UCF shock tube.

In chapter seven, the existing DIPK kinetic mechanism has been reviewed using classification into high and low temperature reactions for which the rate constants were assigned based on analogy to the similar reactions or literature recommendations. This procedure has been successfully applied in the case of butanol combustion mechanism by Sarathy et al.[22, 23]. The DIPK submechanism is then integrated into a recently published $\text{C}_0\text{-C}_4$ mechanism from the Galway group[24].

In chapter eight the work is summarized and the future needs are suggested.

CHAPTER 2: IMPROVED COMBUSTION KINETIC MODEL AND HCCI ENGINE SIMULATION OF DIPK

2.1 Introduction

DIPK fundamental combustion has been investigated using a variety of experimental techniques, and a kinetic model was developed to describe its pyrolysis and oxidation characteristics [25]. The fuel structure has strong effect on HCCI combustion. The saturated fuels and olefins usually show two-stage ignition whereas unsaturated compounds demonstrates single-stage ignition which associated with the more common low temperature heat release (LTHR) [26]. The high in-cylinder temperature is associated with the pre-ignition heat release which can be addressed by intermediate temperature heat release denoted as ITHR [27].

In order to investigate DIPK combustion behavior, homogeneous charge compression ignition (HCCI) engine was used. HCCI studies of two bio-ketones, DIPK and cyclopentanone, were performed by Sandia researchers Yang and Dec[15]. It was found that DIPK has considerably sensitive autoignition nature and showed distinctive low temperature heat release (LTHR) at higher intake pressures. LTHR in DIPK occurred earlier compared to gasoline fuels. Temperature effect on autoignition is a very important parameter in the study of HCCI combustion. The combustion timing of DIPK in HCCI engine was studied for different intake temperature and the results were compared to gasoline [15]. The results showed that in the same test condition (engine speed of 1200 rpm, intake pressure of 1 bar and fuel equivalence ratio 0.4) DIPK shows higher temperature sensitivity. In other words, for instance, DIPK intake temperature reduction results in more CA10 retard comparing to gasoline. For gasoline fuels and primary reference fuel (PRF) mixtures, it has been shown that increasing LTHR leads to increasing intermediate temperature

heat release ITHR [28]. However, in the case of DIPK, increasing LTHR did not result in increasing ITHR, which indicates that DIPK has unique chemical kinetic autoignition characteristics that warrant further investigation.

Homogeneous charge compression ignition is a type of engine process denoted as HCCI. In a HCCI engine, lean, well-mixed fuel and oxidizer mixtures are compressed to the point of autoignition, which has similar characteristics to both spark ignition (SI) and compression ignition (CI) engines. Many researches have been published in the past years on HCCI engines [29-32]. HCCI engine has a very fast combustion process due to the autoignition which results in the release of heat within 5-15 crank angle degrees (CAD). Fuel efficiency along with lower emissions are two important advantages of HCCI engines and their operations are affected by fuel autoignition kinetics. Creating a validated HCCI engine model and a kinetic mechanism that can describe the combustion process of a specific biofuel is important for the optimization of HCCI engine operating strategies for designers. An alternative to computational fluid dynamic (CFD) modeling is desired for quick computations and developing empirical correlations. The model can be multi-dimensional in which mass, momentum, species conservation, and energy equations are solved to find the thermodynamic state of the mixture at each CAD during the combustion process.

In the present study, DIPK combustion in an HCCI engine has been modelled and the results are analyzed in terms of pressure traces and compared to the Sandia engine data [15]. The DIPK literature mechanism [25] has been improved by adding some missing species and reactions. The ignition delay time has been calculated for high and low temperature ranges and compared with data [25] from shock tube and rapid compression machines. The modified DIPK chemical

kinetic mechanism is further verified by comparing with the results from pyrolysis experiments[25].

The single-zone model is conducted with heat transfer effects using the improved reaction mechanism which shows very good agreement with the experimental data. In order to account for heat loss effects in the single-zone model, the Woschni heat transfer correlation [33] has been used. The required bottom dead center temperature, TBDC, has been calculated versus engine speed in constant combustion phasing to estimate the HCCI reactivity for DIPK. The predicted HCCI reactivity is compared to the experimental data and auto-ignition characteristics of HCCI engine has been verified by studying the effects of intake pressure and temperature on the ignition timing within the single-zone model. The temperature and pressure sensitivity of DIPK is investigated to understand the most sensitive reactions in order to further improve the pressure trace predictions.

The effects of turbulent mixing on the combustion needs to be considered to accurately simulate the combustion and heat release rates; however, in the current simulation the contents of the model is presumed to be almost spatially uniform due to high diffusion rates which is the assumption of CHEMKIN. In other words, the formation rate of products from reactants is dominated by chemical reaction rates rather than mixing processes. The objective of this work was mainly to investigate the reaction mechanism and to adjust the kinetic constants. The single zone model can predict the ignition delay time but tends to over-predict the pressure trace. Therefore in the next section we used multi-zone model to address the temperature and composition inhomogeneity. The full investigation of turbulence effect on HCCI combustion can be addressed by CHEMKIN implementation in CFD analysis which can be the scope of another study.

The preliminary study of DIPK in HCCI engine has been done [34], however there are limitations of the single-zone model which results in under-predicting the unburned hydrocarbons and CO while over-predicting the pressure and heat release rate. Therefore, in this study, the multi-zone model has been performed to account for the inhomogeneity within the real engine and to avoid the long computational time of CFD studies. HCCI engine multi-zone modeling is based on the study by Aceves et al. [35]. In cylinder thermal stratification on reducing the pressure rise rate in HCCI engine has been investigated using this multi-zone model for other fuels by Sandia researchers successfully [36]. With considering this cold inactive zone, the pressure after the end of combustion is matched to the data. The multi-zone model has a cold inactive zone along with four active zones with thermal distribution such that for earlier combustion phasing, the cold zone thermal distribution requires to be wider to prevent from early ignition. In the current study, the 5-zone model with different mass fraction and BDC temperature has been simulated to compare the observed experimental pressure trace and heat release of the experimental data.

2.2 Computational Approach

2.2.1 Single-zone adiabatic engine model with the original mechanism

The simplified approach to model HCCI is to use zero-dimensional adiabatic modeling in which uniform properties are assumed throughout the gas mixture. In this section, the IC engine module available in CHEMKIN-PRO [37] is used to simulate DIPK experiments along with the published DIPK mechanism from Allen et al. [25]. The constant-volume, zero-dimensional, single-zone model coupled with chemical kinetics is based on a simulation of gas phase chemical reactions within a perfectly mixed reactor.

The real HCCI engine which is used for experimental investigation has a single cylinder design with a displacement of 981 cm³ and 102 mm bore. The piston with the compression ratio of 14:1 is used. The inlet valve is closed (IVC) at 205° and the exhaust valve is opened (EVO) at 480° CAD. Table 2-1 shows the properties of current HCCI experiments and simulations. As mentioned, the geometric compression ratio of the HCCI engine is 14.0 while the effective compression ratio used for HCCI engine simulations is 13.3, which showed good agreement with motored traces.

First the model is calibrated by comparing the motored pressure trace with the experimental motored data. The adiabatic single-zone model is used to simulate the DIPK combustion in HCCI engine with lower CR (the value used in this study was recommended based on the previous modeling in Sandia) than the geometric CR. THE BDC temperature is used as the intake temperature and the single-zone model is supposed to reproduce the temperature conditions in the hottest zone of cylinder. The compression ratio for the model is adjusted to match motored pressure traces. In order to account for the heat loss imposing a volume history that differs from the actual engine, assuming a shrinking of the boundary layer the reduced compression ratio is used instead of geometric CR. CR=13.3 was the value recommended by Sandia for the modeling which was used for their heat release rate/heat transfer analysis and for their CHEMKIN simulation.

Figure 2-1 shows the comparison of pressure traces for various TBDC between the experimental data (dashed lines) and the calculations (solid lines). Yang and Dec [15] experimentally studied DIPK in the Sandia HCCI engine for various operating parameter sweeps in which wide ranges of BDC temperature, intake pressure, engine speed, and equivalence ratio (ϕ , Φ) were taken into account. The equivalence ratio is 0.4 for both experiments and calculations

in Figure 2-1. The model starts to match with the experiment and reaches almost the same combustion timing as the experiment does; however, the peak pressure and the heat release were not following the experimental trace afterwards. This brings about the reaction-wise study of the fuel kinetic mechanism. The adiabatic single-zone model cannot properly predict the ignition behavior of DIPK in terms of peak pressure. The increase in pressure in an adiabatic constant-volume zone is directly related to the amount of heat generated by reactions. Therefore, it can be inferred that there should be some important reactions or intermediate species which are missing in the published reaction mechanism.

DIPK reaction mechanism has been developed by Allen et al was unable to predict ignition delay time. In this study, we are trying to examine the reaction mechanism for HCCI engine model and verify the result with the available experimental data from Sandia National lab. Figure 2-1 is shown to address that DIPK reaction mechanism demonstrates deficiencies in prediction of pressure trace and heat release rate which was the motivation for our study to review the mechanism.

Table 2-1- HCCI engine properties for simulation and experiments

HCCI Engine	Experiment	Simulation
Engine cylinder displacement volume	981 cm ³	981 cm ³
Geometric compression ratio	14:1	13.3:1
Engine speed	1200 rpm	1200 rpm
Fueling system	Fully premixed	Fully premixed
Intake temperature (TIN)	100-190 C	100-190 C
Intake pressure	100 kPa	100 kPa
Fuel	DIPK	DIPK

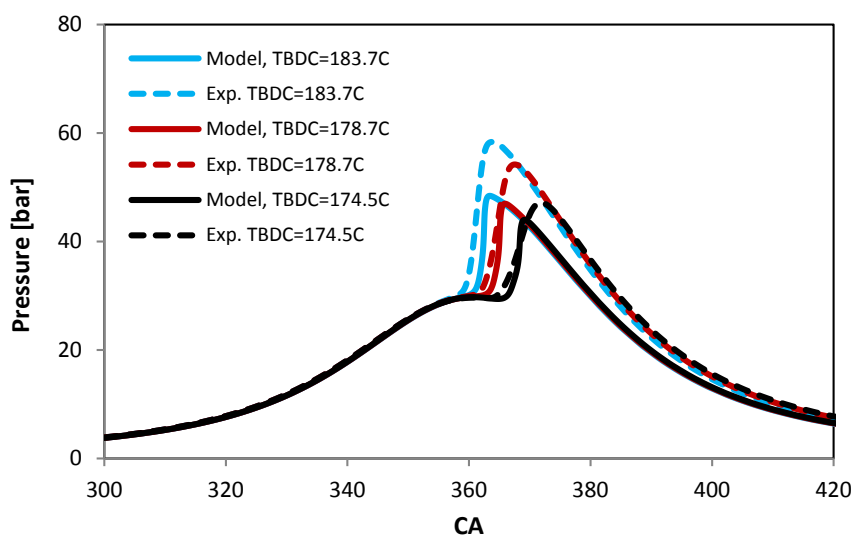


Figure 2-1- Comparison of simulated and measured pressure traces for TBDC sweep, $\Phi=0.4$, 1200 rpm using the original mechanism file for DIPK

2.2.2 Improved chemical kinetic mechanism

The detailed kinetic mechanism of the fuel includes most of the important reactions taking place during the combustion. The Reaction Mechanism Generator (RMG) is open-source software which constructs the kinetic mechanism consisting of thousands of elementary reactions between various species. RMG uses the group based approach to estimate the reactions rates [38]. A graph-matching method is used to identify the functional groups and the rates are estimated from a database of rules [39]. The details of obtaining the rates are described in RMG website and the relevant documents [38]. For DIPK, the published kinetic mechanism file was created using RMG (Allen et. al [25]) to predict the pyrolysis and oxidation of DIPK. As shown in Figure 2-1, the preliminary modeling by CHEMKIN-PRO [17] based on this mechanism shows discrepancies between simulations and the experiments. Therefore, the reaction mechanism is reviewed for possible improvements in terms of missing species and reactions, which were not considered in

the original mechanism. Scheme 2-1 shows the simplified oxidation scheme for DIPK for HCCI engine experiment with TBDC=442K, equivalence ratio of 0.4, inlet pressure, $P_{in}=99\text{kPa}$, and at 20% fuel burn point using CHEMKIN-PRO.

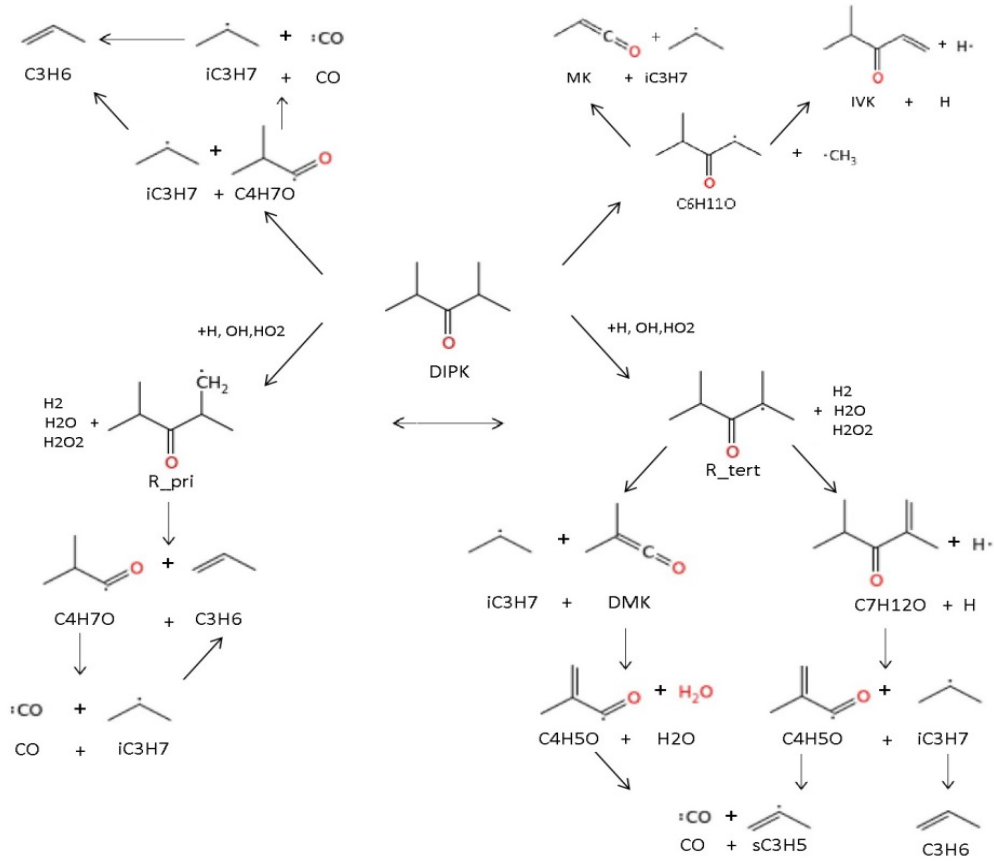
DIPK participates in H-abstraction reaction initially and this is the dominant channel for DIPK consumption in the studied temperature range. When the temperature increases, some of the fuel molecules decompose to iso- C_3H_7 and $\text{C}_4\text{H}_7\text{O}$ radicals after TDC. DIPK hydrogen abstraction reactions by H, OH, HO_2 radicals yield primary and tertiary radicals denoted as R-pri and R-tert, respectively. These radicals subsequently dissociate to produce the $\text{C}_7\text{H}_{12}\text{O}$, an unsaturated ketone. This species decomposes to $\text{C}_4\text{H}_7\text{O} + \text{sC}_3\text{H}_5$ and $\text{C}_4\text{H}_5\text{O} + \text{iC}_3\text{H}_7$ as shown in the oxidation scheme (Scheme 2-1). The H-abstraction reactions corresponding to this relatively stable intermediate species were not considered in the original reaction mechanism and only the recombination reactions of $\text{C}_7\text{H}_{12}\text{O}$ with radicals were included. The original mechanism was created automatically using RMG. The “Auto” option in RMG suggests that the user is no more required to specify conversions at which the edge reaction fluxes are estimated [21]. The user also does not need to decide whether to add a new species in the core reaction model. This option saves a lot of computational time and costs. However, it may end up with elimination of some reactions. $\text{C}_7\text{H}_{12}\text{O}$ is one of the important intermediates forming from DIPK primary and tertiary radicals. Therefore it is reasonable to include all the consumption reactions associated with this species and the relevant radicals. Thus the submechanism of $\text{C}_7\text{H}_{12}\text{O}$ removal has been modified by adding the H-abstraction reactions by H, OH and HO_2 radicals resulting in the formation of $\text{C}_7\text{H}_{11}\text{O}$ radical isomers that decompose to smaller species. The thermodynamic properties for the radicals and

added intermediate species have been computed using THERM [40] based on group additivity estimation and the reaction rates are estimated using RMG [38] which are given in Table 2-2.

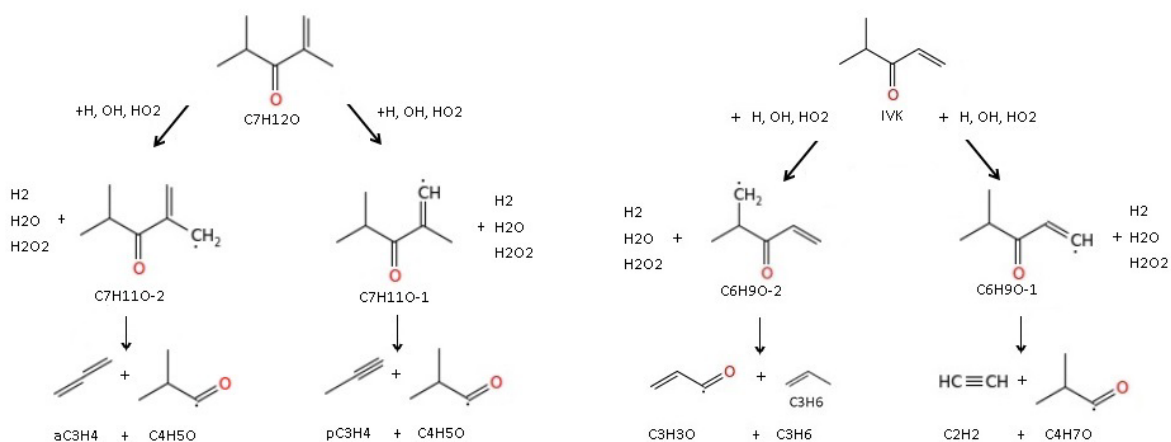
From the original oxidation path, it can be noticed that the unimolecular decomposition of DIPK yields iso-C₃H₇ (isopropyl radical) and C₄H₇O as well as methyl and C₆H₁₁O radicals. The H elimination reaction of C₆H₁₁O results in the formation of isopropyl vinyl ketone denoted as IVK which further decomposes through unimolecular decomposition. In this study, the H-abstraction reactions from IVK by H, OH and HO₂ radicals are also added to the oxidation pathway. These reactions result in the formation of C₆H₉O radical isomers, identified as C₆H₉O-1 and C₆H₉O-2. The β-scission of C₆H₉O-2 produces C₃H₃O-enone and C₃H₆ whereas the C₆H₉O-1 decomposes to C₂H₂ and C₄H₇O. Simplified scheme of added paths related to IVK and C₇H₁₂O H-abstraction reactions are illustrated in the Scheme 2-2 and the corresponding reactions and their rates are shown in Table 2-2.

The reaction of CO+OH=CO₂+H is not included in the original mechanism of DIPK. This has been visualized by showing the CO and CO₂ mole fraction for DIPK and was compared to 3-pentanone reaction mechanism. As a result CO mole fraction is remarkably higher than what is expected for a ketone (i.e. 3-pentanone). By inspecting the rate of production of CO and CO₂ in DIPK using the original mechanism, it is observed that the CO mole fraction is relatively high in DIPK comparing to other ketones (see the comparison between CO and CO₂ mole fractions for DIPK and 3-pentanone [41] in Figure 2-2). Therefore, the last reaction added to the mechanism is CO+OH→CO₂+H, which is a major heat release channel during combustion, and was not included in the original mechanism. The rate for this reaction is taken from the study by Yu et al. [42]. It is worth to mention that the aim of this work is not to focus on the accurate reaction rates

determination, therefore the rates based on RMG calculations are preliminary values and provide insights on how adding these reactions affects the HCCI engine modeling predictions.



Scheme 2-1- Simplified oxidation scheme of DIPK at 20% fuel burn point, TBDC=422K, Pin=99kPa.



Scheme 2-2- Added pathways to the oxidation scheme; C₇H₁₂O and IVK H-abstraction reactions and radical decompositions.

Table 2-2- RMG generated rate coefficients for added reactions in the modified mechanism

Reactions	<i>A</i>	<i>n</i>	<i>E_a</i>	Ref.
IVK+H=C ₆ H ₉ O-1+H ₂	5.06E+07	1.98	11.791	RMG[21]
IVK+H=C ₆ H ₉ O-2+H ₂	3.76E+08	1.75	7.510	RMG[21]
IVK+OH=C ₆ H ₉ O-1+H ₂ O	1.02E+13	0.00	5.945	RMG[21]
IVK+OH=C ₆ H ₉ O-2+H ₂ O	7.20E+06	2.00	0.860	RMG[21]
IVK+HO ₂ =C ₆ H ₉ O-1+H ₂ O ₂	2.80E+04	2.69	25.88	RMG[21]
IVK+HO ₂ =C ₆ H ₉ O-2+H ₂ O ₂	1.68E+13	0.00	20.450	RMG[21]
C ₂ H ₂ +C ₄ H ₇ O=C ₆ H ₉ O-1	2.00E+13	0.00	0.500	RMG[21]
C ₃ H ₆ +C ₃ H ₃ O=C ₆ H ₉ O-2	1.00E+13	0.00	0.500	RMG[21]
C ₆ H ₉ O-1= C ₆ H ₉ O-2	6.00E+16	0.00	25.02	RMG[21]
C ₇ H ₁₂ O+H=C ₇ H ₁₁ O-1+H ₂	5.06E+07	1.98	11.79	RMG[21]
C ₇ H ₁₂ O+H=C ₇ H ₁₁ O-2+H ₂	1.29E+06	2.38	2.800	RMG[21]
C ₇ H ₁₂ O+OH=C ₇ H ₁₁ O-1+H ₂ O	1.02E+13	0.00	5.940	RMG[21]
C ₇ H ₁₂ O+OH=C ₇ H ₁₁ O-2+H ₂ O	3.60E+06	2.00	0.000	RMG[21]
C ₇ H ₁₂ O+HO ₂ =C ₇ H ₁₁ O-1+H ₂ O ₂	2.80E+04	2.69	25.88	RMG[21]
C ₇ H ₁₂ O+HO ₂ =C ₇ H ₁₁ O-2+H ₂ O ₂	1.73E-03	4.65	9.780	RMG[21]
pC ₃ H ₄ +C ₄ H ₅ O=C ₇ H ₁₁ O-1	1.00E+13	0.00	0.500	RMG[21]
aC ₃ H ₄ +C ₄ H ₅ O=C ₇ H ₁₁ O-2	2.00E+13	0.00	0.500	RMG[21]
C ₇ H ₁₁ O-1=C ₇ H ₁₁ O-2	1.530E+16	0.97	37.73	RMG[21]
CO+OH=CO ₂ +H	7.05E+04	2.10	-0.356	[42]

The rate coefficient is $K(T) = A T^n \exp(-E_a/RT)$ cm³ mol⁻¹ s⁻¹, with *E_a* in kcal mol⁻¹

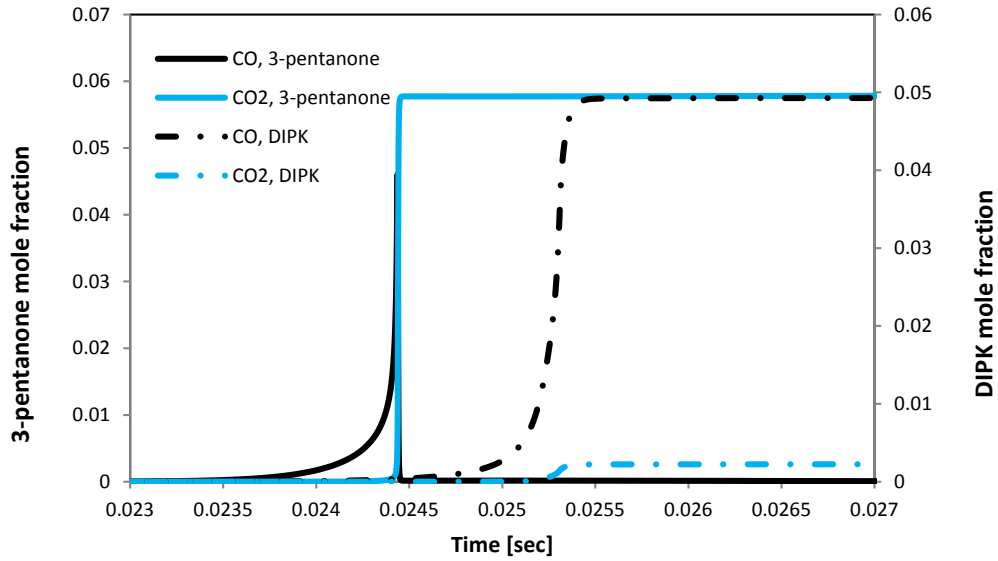


Figure 2-2- CO and CO₂ rate of production for 3-pentanone [41] and DIPK [25]

2.2.3 Multi-zone engine modeling

The limitations of single-zone modeling in precisely predicting of heat release rate result in considering additional computational zones corresponding to different physical regions in the HCCI engine. Although ignition timing can be investigated using the single-zone model, heat release rates in HCCI engines is largely controlled by charge non-uniformities. Since the charge in the Sandia HCCI engine was well premixed for these experiments, the heat-release rate is mainly affected by temperature non-uniformities resulting from heat transfer and turbulent convection. The multi-zone model can include all the important geometric effects while the computational time is kept short (compared to CFD). It is assumed that the cylinder volume is divided into multiple zones so that the summation of individual zone volume is equal to the cylinder volume. Each zone is treated as a closed homogenous reactor with the pressure which is the same for all the zones; however each zone has specified temperature and mass distribution. For the simulation,

CHEMKIN-PRO multi-zone HCCI engine model is used and a 5 zone model is employed for the validation which was used previously by Sjöberg et al [36] for modeling the iso-octane HCCI experiments from Sandia. According to this model, the 5 zone model consists of an inactive zone which is sufficiently cold and never ignites as well as four active zones with the same mass fraction and thermal width. The inactive zone and the four active zones make the pressure of the end of combustion and the pressure rise during the combustion to be matched with the experiment, respectively.

The multi zone model is used to account for the thermal non-uniformities of in-cylinder charge and to avoid the over-prediction of pressure peak in single zone model. The initial conditions for both single and multi-zone simulations are the same. The experimental data of pressure and heat release for DIPK combustion in HCCI engine were used performed in Sandia national lab and compared to the simulation to reproduce the temperature of the hot zones.

Table 2-3- Multi-zone model configuration

Zone #	1	2	3	4	5
Region	Inactive zone	Active zone			
Mass distribution [%]	10	22.5	22.5	22.5	22.5

The properties and configuration of the zones are summarized in Table 2-3. The engine properties such as compression ratio of 13.3, intake pressure of 98 kPa, equivalence ratio of 0.4 and 1200 RPM engine speed are used as in the single-zone modeling. The thermal width of each active zone is 5K which adds to a total of 20 K thermal width. The model has been performed to match the experimental data at TBDC=456 K. Since each zone in the model has particular BDC temperature, the model is identified by the maximum BDC temperature.

Thermal stratification has an important effect on increasing the HCCI engine load limit. Since the experimental data of DIPK combustion was obtained from Sandia HCCI engine, the multi zone model with the optimum thermal width of 20K at BDC (which is mainly the result of heat transfer) is used for simulation. This multi-zone model was introduced by Sjöberg et al [36], explored the HCCI combustion with thermal stratification and verified the model with the experimental data. It was observed that increasing the thermal width, decreases the pressure rise. Furthermore for a specific thermal width, the pressure increase rate drops with combustion retard.

2.3 Results and discussions

In this section, the improved kinetic model performance is studied against the data from shock tube and rapid compression machine experiment by comparing the ignition delay time as well as pyrolysis of DIPK, simulated in CHEMKIN. The improved kinetic model will also be used to conduct the single zone and multi zone models which are compared to the experimental pressure trace and heat release rate accordingly.

2.4 Ignition delay times

The ignition delay time is an important characteristic in a mixture combustion behavior. If the fuel has a short ignition delay time, it could autoignite before entering the combustor, which could cause structural damage to the engine components. There are strict emission standards which require proper engine design for sufficient mixing to provide lower pollutant levels. The ignition delay time calculations for DIPK have been performed with CHEMKIN-PRO using the Closed Homogenous Batch Reactor module at a pressure of 10 bar within the high and low temperature

range of 900-1050 K and 650-750 K respectively. Both the original and modified reaction mechanisms have been used to calculate the ignition delay time and compared to the DIPK experimental data from Allen et al. [25] and shown in Figure 2-3. For the high temperature range, the simulation is compared with the limited shock tube data, while for the low temperature region with the rapid compression machine (RCM) experiments. Note that the RCM is simulated using the experimentally derived volume history which accounts for heat losses after the compression ending [25]. The details of the experimental setup and operating conditions can be found in Allen et.al [25].

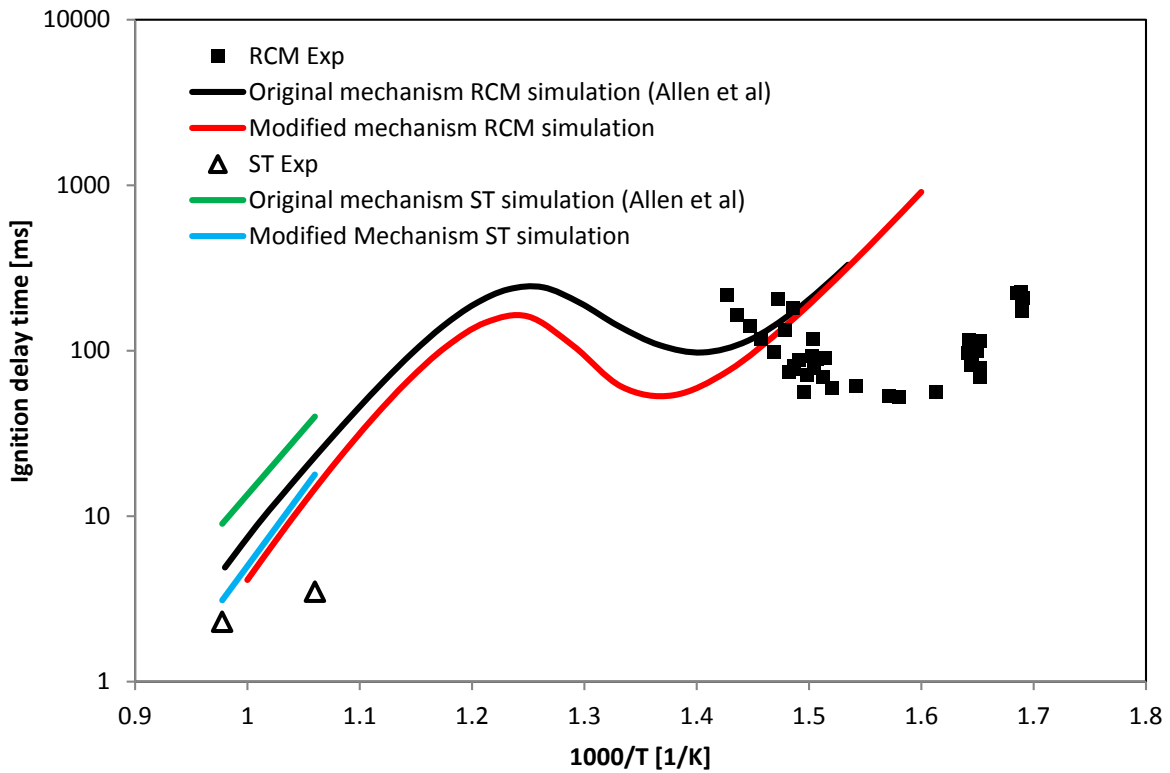


Figure 2-3- Modelled and measured [25] DIPK ignition delay times in shock tube and rapid compression machine at 10 bar

The model exhibits a reasonable prediction of ignition times at lower temperature ranges (RCM) while at higher temperatures, specifically at 943K (shock tube), some discrepancies can be observed between the simulation and the experiment. This may be caused by the uncertainties in the DIPK kinetic mechanism. However, the modified mechanism predictions for the shock tube data are better when compared to those of the original mechanism. The data from shock tube were limited to only two measurements and additional data within the high temperature region is needed to validate the DIPK kinetic model.

2.4.1 Pyrolysis experiments

The modified DIPK reaction mechanism has been further verified by comparison with the measured pyrolysis data from Allen et al. [25]. The pyrolysis modeling has been performed using the CHEMKIN-PRO plug flow reactor module. The reactor physical properties for simulation are the same as the experiment [25]. The tube is 230 mm long with 7.0 mm inner diameter. The inlet stream (2% DIPK in Argon) has been considered at the rate of 1 SLM at two different pressures of 30 and 760 Torr in the temperature ranges of 950-1350 K and 800-1200 K, respectively. The results are provided in Figure 2-4 for some of the major products. In general, the model is in reasonable agreement with the experiments for DIPK, H₂, CO, propene, ethylene, acetylene and propyne for both pressures and the performance is similar when compared to the original mechanism. However, significant improvements in the predictions for CH₄ and propyne concentrations are obtained with the modified model as compared to the original one.

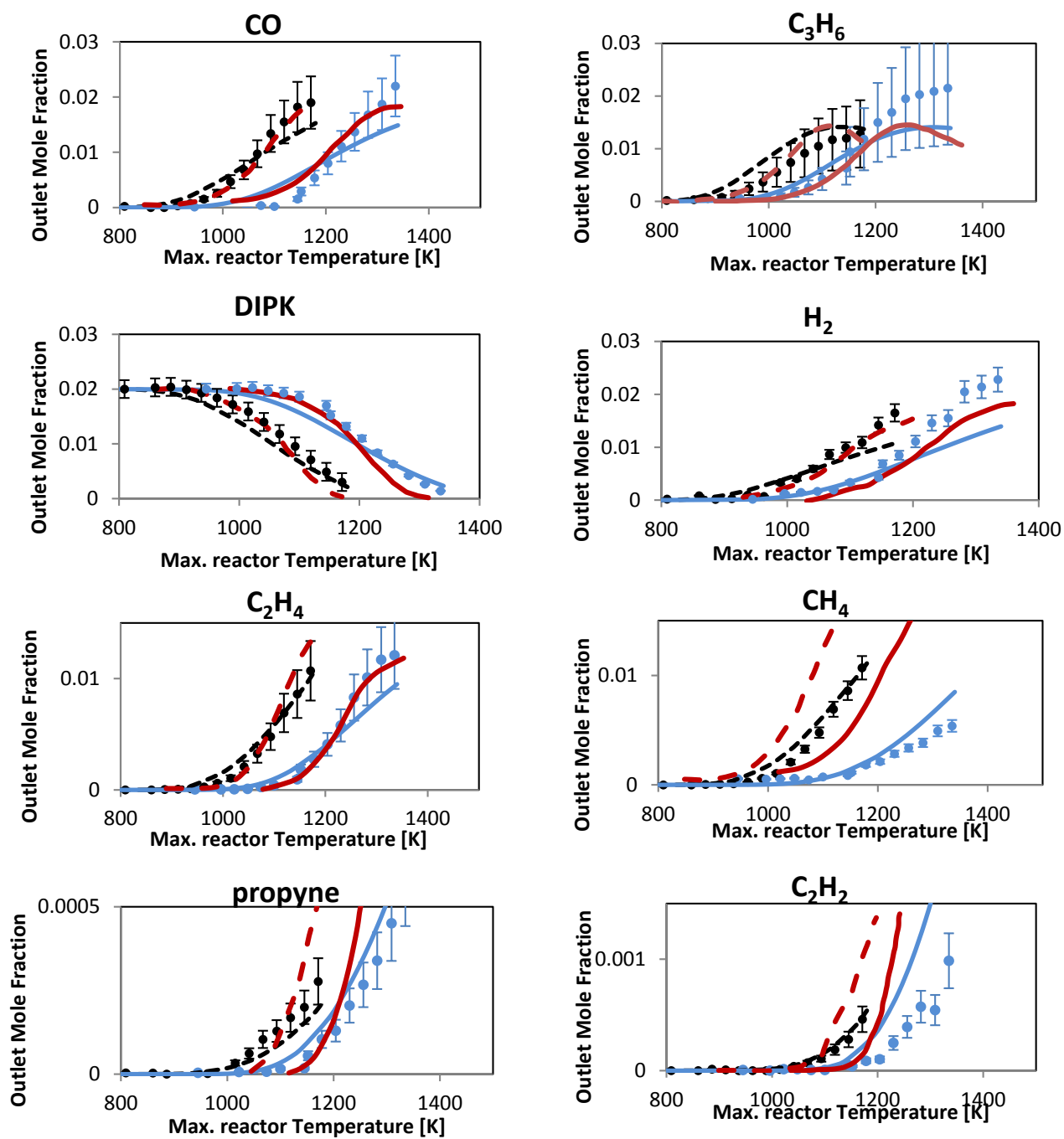


Figure 2-4- Measured (symbols) and predictions by the modified mechanism (lines) for the mole fractions during DIPK pyrolysis at 950-1350K at 30 Torr(blue) and 800-1200K at 760 Torr(black). The original mechanism predictions are also shown (red) at 30 Torr(solid) 760 Torr(dashed).

2.4.2 Single-zone model with heat transfer effects using improved reaction mechanism

The assumption of adiabatic condition for HCCI engine is not valid as heat is transferred during combustion in HCCI engines. Auto ignition in HCCI engines is usually coupled with heat transfer effects [8]. The radiation heat transfer is small due to the low amount of soot as well as low temperature from lean combustion. Therefore, the dominant form of heat transfer is forced convection from bulk gas to the walls of combustion cylinder. In order to account for the heat loss effects, the Woschni correlation [33] is typically used for calculating the heat transfer coefficient. Woschni presented a correlation that relates the gas velocity to the mean piston speed as well as the pressure rise ($P - P_{\text{motored}}$) due to the combustion. The correlations in equations (2-1) and (2-2) are based on the average velocity of the gas and instantaneous values of pressure and temperature in the combustion cylinder [33]. In the Woschni correlation, the average cylinder gas speed is estimated for calculation of Reynold's number from which the convective heat transfer coefficient between the gas mixture and chamber wall is obtained from Nusselt number. As a substitute for the mean piston speed, the average cylinder gas velocity, w , defined in (2-2), is used for Re calculation. c_{11} , c_{12} and c_2 are the modeling parameters and swirl ratio (Ratio of swirl velocity to mean piston speed which depends on swirl number) is taken to be 1.26 (considered to be constant for the simulation). All the coefficients in the Woschni correlation are set as default values except for heat transfer main coefficient, a , and average cylinder gas velocity coefficient, c_2 , which are adjusted based on the heat release rate (HRR) analysis from experiments.

$$Nu = a Re^b Pr^c \quad (2-1)$$

$$w = c_1 s_p + c_2 \frac{v_d T_r}{P_r v_r} (P - P_m) \quad (2-2)$$

$$c_1 = c_{11} + c_{12} \cdot \text{swirl ratio} \quad (2-3)$$

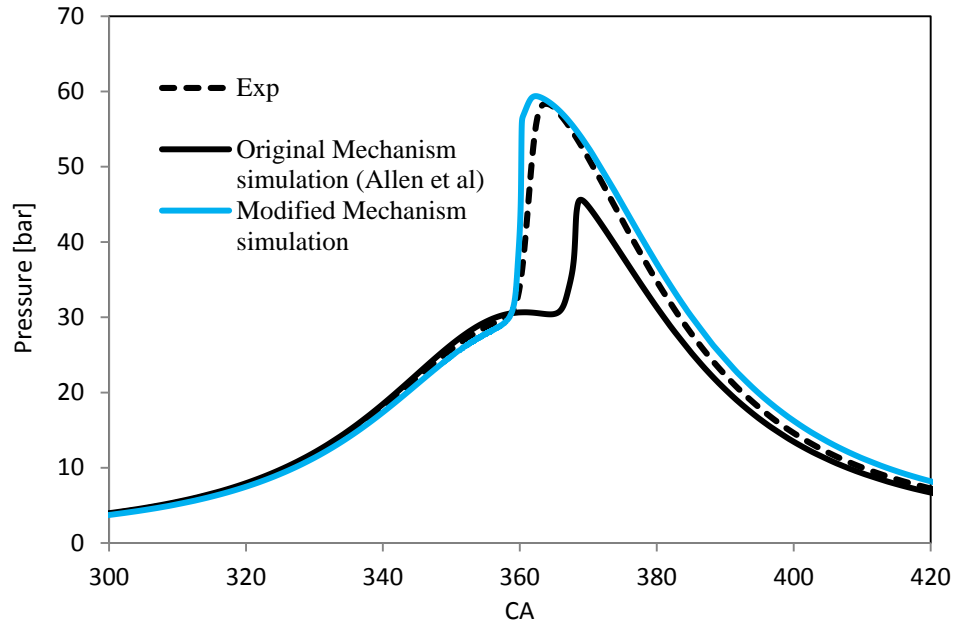


Figure 2-5- Single-zone model improved pressure trace for TBDC=456K.

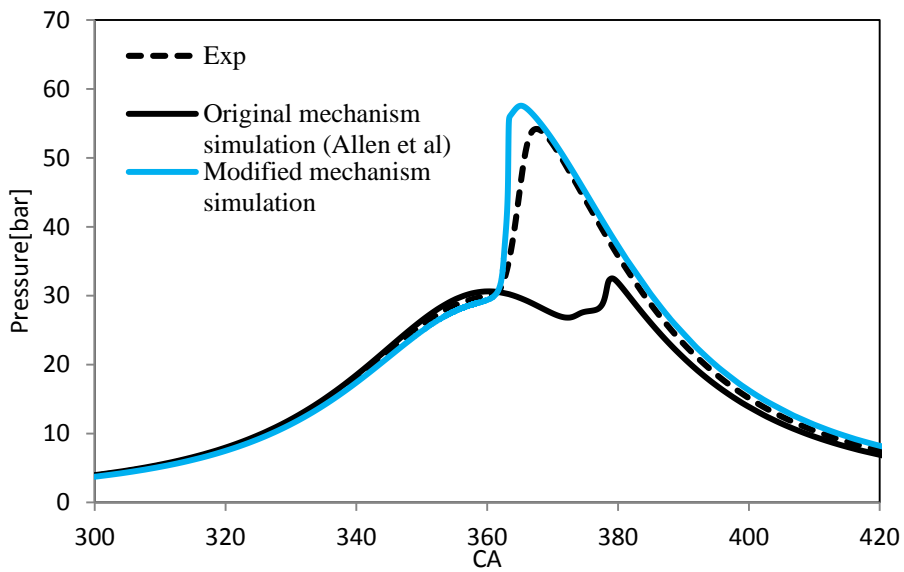


Figure 2-6- Single-zone model improved pressure trace for TBDC=452K

In Figure 2-5 and Figure 2-6, the non-adiabatic, single-zone HCCI engine pressure traces corresponding to two different BDC temperatures are calculated based on the modified chemical kinetic mechanism and compared to the experimental data. Also, the original model predictions are shown to indicate the improvements obtained. Note that the BDC temperature changed from 456K to 452K while the inlet pressure is adjusted to 98 kPa compared to the experimental value of 100 kPa. The crank angle corresponding to the inlet valve closed (IVC=205° CA) is taken to be the same as that of the engine used for experimental investigation. IVC in the original model was set at 180° CA to compensate the delay in the original model. As it can be noted from the pressure traces comparison, the modified model has very good agreement with the experimental pressure data. Still it could be argued that there are some small discrepancies from the onset of combustion up to the peak pressure which may be due to the uncertainties within DIPK mechanism reaction rates. Thus sensitivity analysis is conducted in the next section to understand the remaining discrepancies.

Also, not shown here are the predictions for the normalized heat release rates for various TBDC, corresponding to the pressure traces in Figure 2-5 and Figure 2-6. As with the pressure traces, the combustion phasing is kept the same between experiments and model (the intake pressure adjustment is used to maintain that value). The experimental heat release rate curves are broader with lower peaks than those of the computations. This discrepancy can be explained by the temperature inhomogeneity within the charge for the experiment, which are the result of heat transfer and turbulent convection, an effect that cannot not be considered in single-zone models.

2.4.3 Sensitivity analysis

Ignition delay time sensitivity analysis has been implemented. Figure 2-7 shows the sensitivity coefficient (defined in eqn.(2-4)) for the 10 most sensitive reactions of DIPK mechanism at 1023 K and 30 bar (TDC conditions). Where $\tau_{ign,ki}$ is the ignition delay time when the reaction rate (ki) is unmodified, and $\tau_{ign,2ki}$ and $\tau_{ign,0.5ki}$ are the ignition delay times when the reaction rate coefficient (ki) is multiplied and divided by a factor of 2, respectively. As can be seen from Figure 2-7, the most sensitive reaction is the H₂O₂ decomposition to two OH radicals.

Due to its chain-branching characteristic, the dissociation of H₂O₂ is considered as the dominant kinetic characteristic in engine knock for HCCI engines operation [43]. According to a recent study of this reaction (Hong et al. [43]) using laser absorption diagnostics and shock tube, the uncertainty associated with the reaction rates is $\pm 27\%$ for temperatures higher than 1200 K and $\pm 23\%$ between 1000 and 1200 K. However, the reactions that warrant further attention or detailed investigations are those related to DIPK production and consumption. The most sensitive reaction in which DIPK is involved is the H-abstraction reaction from the fuel by HO₂ radical. The large uncertainties associated with reactions involving H-abstractions by HO₂ are due to the difficulty in experimentally studying such reactions and thus only calculations and estimations exist in the literature. A detailed sensitivity analysis for DIPK in different temperature regime can be found in the recent publication [25].

$$s_i = \frac{\partial \ln \tau_{ign}}{\partial \ln k_i} \quad (2-4)$$

$$= \left(\frac{\Delta \tau_{ign}}{\Delta k_i} \right) \left(\frac{k_i}{\tau_{ign}} \right) = \left(\frac{\tau_{ign,2k_i} - \tau_{ign,0.5k_i}}{2k_i - 0.5k_i} \right) \left(\frac{k_i}{\tau_{ign,k_i}} \right) = \frac{\tau_{ign,2k_i} - \tau_{ign,0.5k_i}}{1.5 \tau_{ign,k_i}}$$

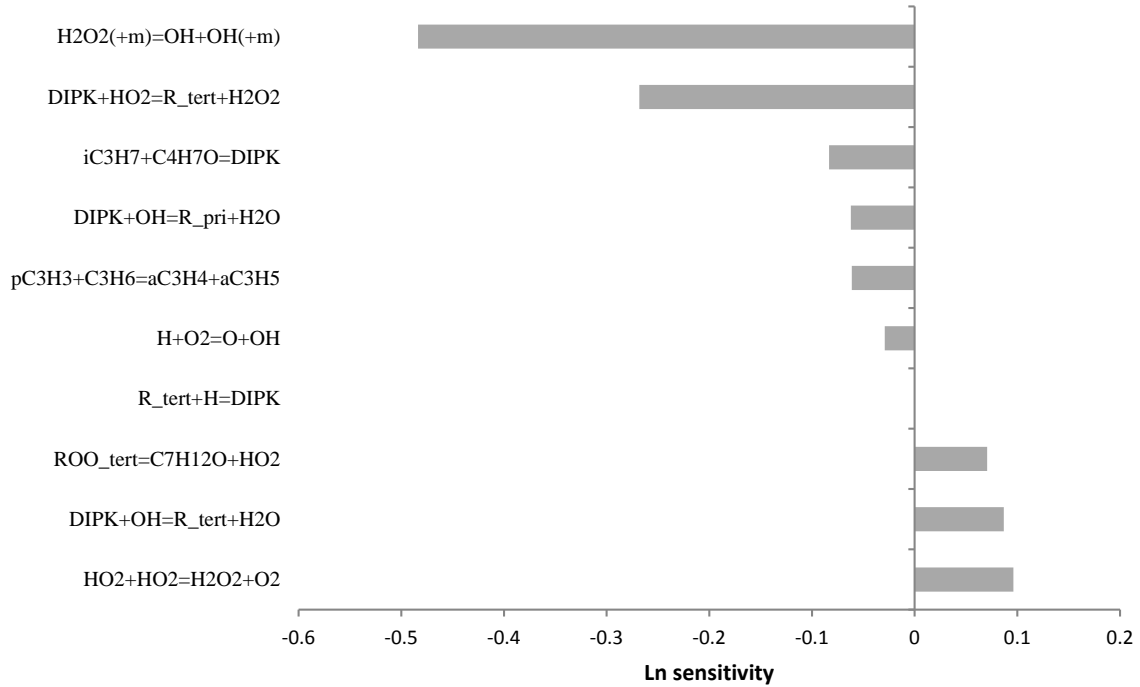


Figure 2-7- Ignition delay time sensitivity analysis at 1023 K, 30 bar

2.4.4 HCCI reactivity by engine speed sweep

The main heat release in HCCI engines occurs after early autoignition reactions at low and intermediate temperatures. Therefore, a high reactivity fuel (i.e. a fuel with strong low- and intermediate-temperature reactions) reaches hot ignition earlier than a fuel with low reactivity and the time of combustion can be used to compare the autoignition reactivity of different fuels. Also, the initial conditions for the HCCI engine such as, BDC temperature, intake pressure, engine speed, etc., can be varied in order to adjust the combustion timing to achieve a desired combustion

phasing. The reactivity of DIPK is calculated for various engine speeds versus BDC temperature sweep based on the modified reaction mechanism and compared to the Sandia experimental data [15] and are shown in Figure 2-8. As engine speed is varied, the combustion phasing is kept constant for the calculation by adjusting the initial temperature (the same as in the experiment). Here the 50% burn point (CA50) was at 372 deg. CA (12 deg. after top dead center) with constant equivalence ratio of $\Phi=0.38$ and 98 kPa constant intake pressure. Figure 2-8 shows that both the calculations and experiments indicate increasing trend of initial temperature required for higher engine speeds. Furthermore, the heat loss induces additional time to reach the desired CA50, which must be compensated for by higher BDC temperature. However, the rate of increasing trend at lower speeds (<1200 rpm) is greater than those at higher speeds (>1200 rpm) as there is less time for heat transfer to occur and the work increases nonlinearly with speed, increasing the charge temperature. The calculations have similar trend and very good agreement with the experiments. Note that the intake temperature in the experimental data has been compared to the BDC temperature of model since the model is the simulation of two phases of HCCI engine cycle, compression and combustion. Therefore, the BDC temperature is used as the initial temperature for the modeling.

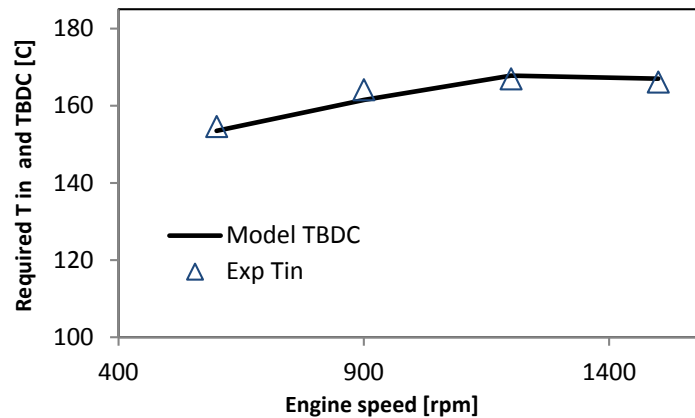


Figure 2-8- Comparison of HCCI reactivity, speed sweep vs. TBDC(model) and Tin (experiment[2]) at constant CA 372 deg. CA, P=100kPa, $\Phi=0.38$

2.4.5 Intake temperature effects on HCCI autoignition

The BDC temperature and intake pressure are two important parameters in HCCI engine and are used for controlling the combustion phasing, which is required for an efficient, stable combustion in the engine. Therefore, the effects of intake pressure and temperature have been studied on autoignition characteristics of HCCI engine. The model was performed at constant intake pressure of 98 kPa with constant equivalence ratio of $\Phi=0.4$ at 1200 RPM engine speed, for various intake temperatures and the results of intake temperature versus 10% burn points (CA10) are compared to the experimental data (see Figure 2-9). As the temperature increases, the ignition occurs at earlier crank angle and the model and data show reasonable agreement. However, some discrepancies can be observed at lower temperature where the model predicts shorter ignition time than the experiment by about 1 degree CA.

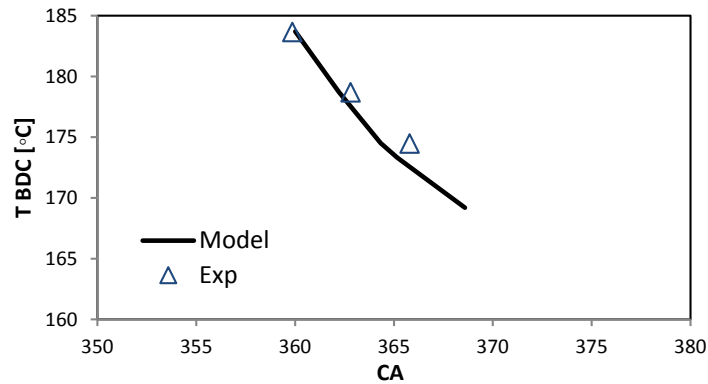


Figure 2-9- Comparison of experimental [2] BDC temperature with the simulation, the effects of BDC temperature on HCCI autoignition

2.4.6 Multi-zone engine

Figure 2-10 shows pressure, average accumulated heat release, heat release rate per crank angle, and average temperature resulting from the multi-zone simulation compared with the experimental data. The average temperature in the model stands for the average of 5 zones which is compared to the mass-averaged in-cylinder temperature from the experiments. The maximum required BDC temperature ($T_{BDC,max}$) for the model is 450K which is slightly lower than that of the experiment. As a result, the simulation performed with improved chemical kinetic modeling is able to reproduce the experimentally observed pressure and heat release behavior reasonably. The model tends to slightly underestimate the heat release and overestimate the temperature particularly at the end of combustion. This could be due to the deficiencies in the DIPK chemical kinetics, the inability of the simple multi-zone approach to capture the complex engine environment, or the uncertainties in the experimental techniques. However, the excellent agreement obtained for pressure (Figure 2-10) indicate that the performance of the multi-zone model is satisfactory from a design perspective.

Figure 2-11 (right) shows the pressure sweep effects on low and intermediate heat release rate of DIPK HCCI engine modeling using the improved reaction mechanism. The 5 zone model has been used for simulation with $\Phi=0.38$ for the pressure range of 1-2.4 bar. The zones temperatures are selected such that the combustion timing is fixed to 358.3 CA. Figure 2-11 shows a pre-ignition heat release rate which becomes stronger as the inlet pressure increases. Comparing the simulated heat release rate with the normalized experimental HRR by Yang and Dec [15], we notice early heat release within the simulation, while in the experiment (not shown here), the ITHR remains constant as the pressure goes up from 1 to 1.6 bar. For the pressures greater than 1.6 bar (Figure 2-11- left), the experiment shows low temperature heat release. Considering a wider range for the CA degree in the simulation, the LTHR would be negligible at the pressures lower than 1.6 bar, yet remarkable at the pressures greater than 2 bar which agrees with the experiments.

The heat release rate comparison between the simulation and experiment shows similar behavior for DIPK. The trend of heat release rate versus pressure sweep tends to remain constant for the pressures of less than 1.6 bar. As the pressure goes up, the heat release rate shows an early heat release which gets stronger as the pressure increases. As the reaction mechanism is developed mainly based on calculations, there are some reactions contributing to LTHR or ITHR producing for which the reaction rate may not be precisely calculated. These reactions can be studied further in order to develop a comprehensive kinetic reaction mechanism.

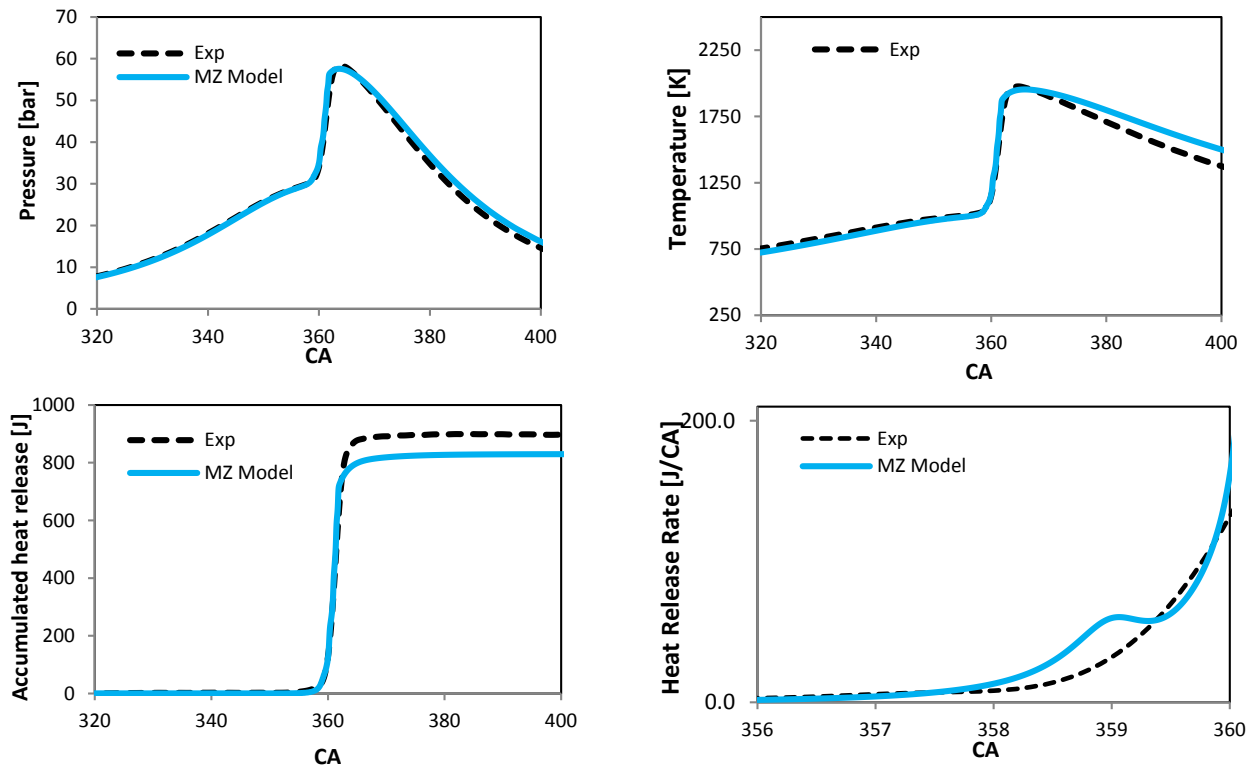


Figure 2-10- DIPK HCCI multi-zone model (TBDC,max = 450K); pressure (top left), average temperature (top right) average accumulated heat release (bottom left), and heat release rate (bottom right) vs. degree crank angle compared with the experimental data (TBDC=456K)

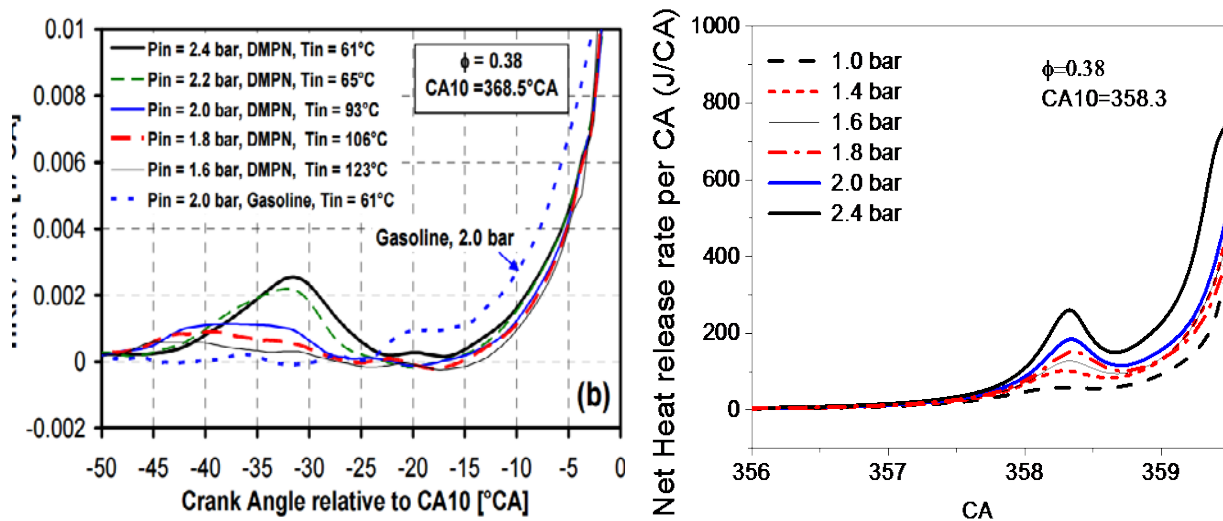


Figure 2-11- Pressure effects on ITHR of DIPK, Experimental ITHR (left) [15] and simulated ITHR (right). DMPN in the left graph stands for 2,4-dimethyl-3-pentanone (DIPK)

2.5 Conclusion

Ignition of a new biofuel- DIPK- in the Sandia HCCI engine was modeled. DIPK combustion in HCCI engine in combined simulation and experiment has been done and the simulation results of the pressure trace and heat release rate were verified against experimental data. The DIPK kinetic mechanism was modified to include intermediate reactions and species. The single-zone HCCI engine was simulated using CHEMKIN PRO for different BDC temperature and the modified mechanism displayed decent agreement with the experimental data for the pressure trace (when compared to the original mechanism predictions). Woschni correlation was used to account for heat transfer effects from the engine. DIPK HCCI reactivity was explored by calculation of the required BDC temperature for various engine speeds. The overall trends

showed that the required BDC temperature is increased by increasing the engine speed, however for the lower speed (<1200 rpm) the increase in the required temperature is higher than that of higher speed (>1200 rpm) in which there was not enough time for heat transfer. The DIPK mechanism was explored to determine the sensitive reactions that controlled ignition and heat release phenomena under current HCCI adiabatic single-zone model conditions (i.e. the reactions that had the biggest effect on the ignition timing and pressure rise). It was found that the predictions of the model were affected mainly by the rates of H-abstraction reactions of HO₂ and OH with the fuel, and that these reactions recommended for experimental investigation. The modified model was further validated based on data from shock tube, RCM, and pyrolysis experiments and indicated better agreement than the original mechanism. Since the single-zone model was not able to predict the experimental heat release rates, a multi-zone modeling study was conducted to investigate the heat release during the combustion and account for temperature variations within the bulk gas and low temperature regions in the thermal boundary layers and crevice. The pressure, heat release, and temperature profile for DIPK HCCI engine 5-zone model achieved very good agreement with the experiments. The present study provides engine designers a simple modeling approach (instead of the computationally expensive CFD techniques) for optimizing future HCCI engine operations while running exotic biofuels such as, ketones. (For more information refer to [44])

CHAPTER 3: QUANTUM CHEMICAL CALCULATIONS OF MAJOR REACTIONS OF DIPK

3.1 Introduction

The reaction mechanism of a fuel is expressed by all the elementary steps from initiation of the reactions to product formation. The structures of the species and the sequences of the steps as well as the transformation of the initial step to the final products via transition state and their corresponding energies should be considered [45]. The theoretical organic chemistry deals with determination of these parameters which are generally hard to be identified by experiments. In this regard, quantum chemistry introduces the ways to investigate the chemical reactions in order to find out the effective ways of developing a comprehensive model to control the chemical process i.e. the combustion behavior of a fuel in a newly designed engine.

Intrinsic mechanism of a reaction is basically referred to the structural changes occurring in a system of reactions. Intrinsic mechanism can be described by solving the time dependent Schrödinger equation which is very complicated. Therefore, another approach is used in order to get an insight to the dynamics of reaction, the calculation of potential energy surface (PES).

All the models explaining the kinetic and thermodynamic properties of organic molecules and their combinations based on the geometrical characteristics can be described by PES. In a simple representation, Figure 3-1 shows the Potential energy curve for a two atom molecule where R is the equilibrium bond length and $D_0 - D_e$ is the zero vibration energy.

The PES for a simple reaction can be very complicated depending on the total number of geometrical configurations, however in order to study the reaction mechanism it is sufficient to

have the information of certain part of PES, specifically the minima regions and to the saddle points which are also denoted as critical or stationary points [45].

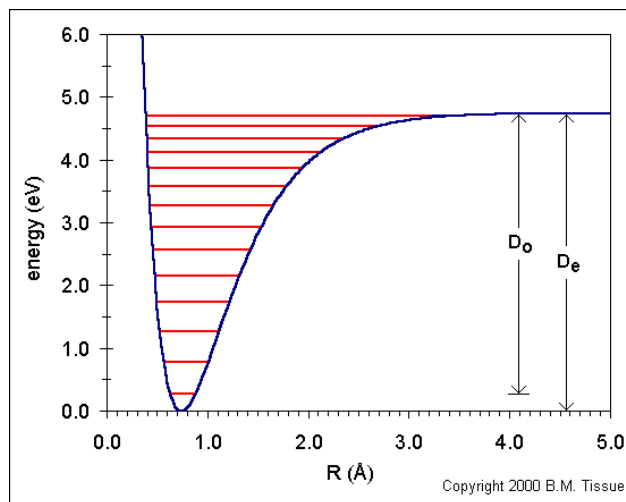


Figure 3-1- Potential energy curve for a two atom molecule; R is the equilibrium bond length; D_0 - D_e is the zero vibration energy

The joint experimental and theoretical work brings about a new aspect in the study of organic molecules at the excited state. The approach to find the transition state structures is to find the saddle point of PES. The characterization of the stationary point location on PES and calculation of its geometry and energy is called geometry optimization. The stationary point can be a minimum, a transition state or a higher order saddle point. Geometry optimization are performed by a guessed structure as the starting point going through an optimization procedure by computer program/algorithm to find the stationary point [46]. The program used in this work is Gaussian 09 [18] which provides the capabilities for electronic structure modeling.

Transition state theory (TST) which is referring to formation of an activated complex at the hypothetical state between reactant and product is used to determine the standard Gibbs free

energy, enthalpy and entropy of the reactions of our interest in DIPK kinetic mechanism. TST is used to study the rate of the important reactions of DIPK in high and low temperature region.

The goal of this chapter is to identify the important consumption pathways for the reactions of DIPK primary and tertiary radicals with O₂. The computational method of quantum chemical calculations is employed to obtain the energies and vibrational modes of various reaction pathways in the low temperature combustion of DIPK and estimate the corresponding rate constants for the reactions. The rate constant for each of the reactions of DIPK radicals with O₂ as well as the subsequent RO₂ radicals isomerization and decomposition reactions are estimated using CanTherm [19]. The transitional TST is used to compute the reaction rates with the option of tunneling correction. The geometry and frequency information from Gaussian output are used in CanTherm.

3.2 Theoretical method

3.2.1 Potential energy surfaces calculations

All calculations of Potential Energy Surfaces (PES) were achieved using the Gaussian 09 package of programs [47] at the DOE National Energy Research Supercomputer Center (NERSC). Molecular structures were generated and visualized with MolDen [48]. The transition state structures were located with STQN method using quadratic synchronous transit method to approach the quadratic area of the transition state followed by a quasi-Newton or eigenvector-following algorithm was used to accomplish the optimization [49]. The model chemistry CBS-QB3 was used to refine the enthalpies for the products, reactants, and transition states [50, 51]. This composite approach affords the best accuracy to computational effort ratio among the family

of the complete basis set (CBS) methods of Petersson et al [52]. It uses geometry optimized with B3LYP[53] hybrid density functional theory, and combines extrapolation to the CBS limit by using asymptotic convergence of Møller-Plesset second order (MP2) energies with correlation correction beyond second-order, up to the coupled cluster theory with single, double and perturbative triple electronic excitations (CCSD(T) level). In addition, this approach includes spin-orbit empirical correction. Specifically, CBS-QB3 method involves five steps: (1) geometry optimization at the B3LYP/6-311G(d,p) theory level; (2) B3LYP/6-311G(d,p) frequency calculation with a 0.99 scale factor for zero-point vibrational energies (ZPE); (3) UCCSD(T)/6-31+G(d') energy calculation; (4) MP4(SDQ)/6-31+G(df,p) energy calculation; (5) UMP2/6-311+G(2df,2p) energy calculation and CBS extrapolation. The CBS-QB3 approach is known to yield mean absolute deviation of 1.1 kcal/mol for the heats of formation on the G2/97 test set [54] and mean absolute deviation of 0.6 kcal/mol for the heats of formations for a set of 58 hydrocarbons [55].

3.3 Rate constant calculations

The high pressure rate constants for all the reactions are calculated using CanTherm [19]. The transition state theory (TST) with correction for tunneling is performed. The asymmetric Eckart tunneling [56] is used for tunneling correction. The temperature range of 298 – 1500 K was considered along with the scaling factor of 0.99 for all frequencies. The geometry, force constants and frequencies for each molecule in the reaction of interest were specified from the Gaussian outputs. The 0K energy computed at CBS-QB3 level of theory was also given from Gaussian. The rate constants were fitted to the modified Arrhenius equation.

3.4 Computational procedure

The computational procedure which was used can be summarized as the following steps:

- 1) Defined the reaction network and explored the pathways

This network gives us all the possible intermediates and products as well as the relevant pathways.

- 2) Conducted quantum chemistry calculations using Gaussian at CBS-QB3 theory level

The job script is prepared to conduct the quantum chemistry calculation in which the geometry is given as a so-called z-matrix. The z-matrix for each structure includes all the atoms, bond lengths, angles and their relative connections. A sample job script is shown in Figure 3-2.

- 3) Confirmed that the geometries have been optimized properly

The confirmation is obtained by checking each structure and transition state energy such that:

- a. Minimum energy of each structure
- b. Each saddle point (TS) have one and only one imaginary frequency

All the visual inspections are done via Molden program [48].

- 4) Prepared the CanTherm [19] input files to calculate the rate constants

CanTherm input file is prepared for each single reaction and includes the geometry file (GEOM), force constants (FORCEC) and CBS-QB3 energy file (ENERGY) which need to be provided for reactants, transition state and products. The molecular structure should also be specified whether the molecule is linear or not. Also the temperature range of interest is given in the input file. A sample CanTherm input file is shown in Figure 3-3.

- 5) Run CanTherm

CanTherm is run using Python. The CanTherm input files are prepared for unimolecular and bimolecular reactions to calculate the rate constants.

6) Inspected the output for the rates constants

The output from running the CanTherm includes the following parts:

- a. Thermodynamic Data
- b. Translational and vibrational contributions
- c. Reaction rates

The reaction rates are tabulated versus different temperature and the fitting parameters are calculated in terms of Arrhenius format or modified Arrhenius format. A sample output for CanTherm is given in the Appendix B.

```

#!/bin/bash
#PBS -S /bin/bash
#PBS -q ccm_queue
#PBS -l mppwidth=24,walltime=23:30:00
#PBS -j oe
export L=1;export S=12;export mem=50Gb;module load g09/d1; export CRAY_ROOTFS=DSL;export job=
#PBS_JOBNAME
# Carver Script: g091 and comment lines below; above: PBS -q debug; PBS -l nodes=3:ppn=8,wall
time=00:30:00
ulimit -Sv unlimited
# Hopper Script: ccmrun g091; above: PBS -q ccm_queue; PBS -l mppwidth=24,walltime=10:00:00
# rem. 3600MW=32Gb per node; MAX walltime=48; %mem=28100Mb %NprocS=24
module load ccm
mkdir -p $SCRATCH/g09/$PBS_JOBID
cd $SCRATCH/g09/$PBS_JOBID
mv $PBS_O_WORKDIR/$job.log1 $PBS_O_WORKDIR/$job.log2
mv $PBS_O_WORKDIR/$job.log $PBS_O_WORKDIR/$job.log1

export x=${job:0:6};export y=${job:0:9}
#cp $PBS_O_WORKDIR/${x}_bd_b3lyp.chk $PBS_O_WORKDIR/$job.chk
export GAUSS_DFTD3_SR6=1261000
export GAUSS_DFTD3_S8=1703000

ccmrun g09 << EOF > $PBS_O_WORKDIR/$job.log

%mem=$mem
%NprocS=$S
%NprocL=$L
%chk=$PBS_O_WORKDIR/$job.chk

#p CBS-QB3
Opt
! Opt(TS,CalcFC)
!Geom=AllCheck
EmpiricalDispersion=GD3

BD product

0 2
@ $PBS_O_WORKDIR/$y.z

EOF
mv fort.7 $PBS_O_WORKDIR/$job.mos
mv Test.FChk $PBS_O_WORKDIR/$job.FChk
cd $PBS_O_WORKDIR
chgrp m966 *
chmod g+r *

```

h			
c	1	ch2	
c	2	cc3	1 cch3
h	3	hc4	2 hcc4
h	3	hc5	2 hcc5
h	3	hc6	2 hcc6
c	2	cc7	3 ccc7
h	7	hc8	2 hcc8
h	7	hc9	2 hcc9
o	1	oh10	2 ohc10
o	2	oc11	3 occ11
h	7	hc12	2 hcc12
ch2		2.439601	
cc3		1.498670	
cch3		97.042	
hc4		1.088372	
hcc4		110.128	
dih4		121.116	
hc5		1.099059	
hcc5		108.687	
dih5		-119.627	
hc6		1.087812	
hcc6		111.639	
dih6		-0.453	
cc7		1.498111	
ccc7		118.800	
dih7		-53.243	
hc8		1.090613	
hcc8		111.819	
dih8		177.056	
hc9		1.091620	
hcc9		109.377	
dih9		56.089	
oh10		0.982819	
ohc10		71.594	
dih10		78.351	
oc11		1.365765	
occ11		117.982	
dih11		169.445	
hc12		1.099180	
hcc12		110.471	
dih12		-62.637	

Figure 3-2- A sample job script in Gaussian, with the z-matrix shown in the red box

```

Calculation: REAC
Reaction: Unimol
!Reaction: Bimol
Tunneling: ASymmEckart 1
!Tunneling: ASymmEckart 2
!Tunneling: SymmEckart
!Tunneling: Wigner
!Tunneling: None
TLIST: 8 298 300 400 500 600 800 1000 1500
Scale: 0.99

MOL 1
NONLINEAR
!LINEAR
!ATOM
:
GECM File ../rto21h_re_cbs.log
FORCEC File ../rto21h_re_freq.log
ENERGY File ../rto21h_re_cbs.log CBS-QB3
EXTSYM 1
NELEC 2
ROTORS 0
!ROTORS 4 ../ReactionRate/inertia_sBuOH.dat
!POTENTIAL separable files
!../ReactionRate/sBuOH-1.txt ../ReactionRate/sBuOH-2.txt ../ReactionRate/sBuOH-3.txt ../ReactionRate/sBuOH-4.txt
!BAC for C-H C-C C=C C.TB.C O-H C-O C=O
0 0 0 0 0 0

MOL 2
NONLINEAR
GECM File ../rto21h_ts_cbs.log
FORCEC File ../rto21h_ts_freq.log
ENERGY File ../rto21h_ts_cbs.log CBS-QB3
EXTSYM 1
NELEC 2
ROTORS 0
!ROTORS 2 ../ReactionRate/inertia_ts.dat
!POTENTIAL separable files
!../ReactionRate/TS1-1.txt ../ReactionRate/TS1-2.txt
!BAC for C-H C-C C=C C.TB.C O-H C-O C=O
0 0 0 0 0 0

MOL 3
NONLINEAR
GECM File ../rto21h_pr_cbs.log
FORCEC File ../rto21h_pr_freq.log
ENERGY File ../rto21h_pr_cbs.log CBS-QB3
EXTSYM 1
NELEC 2
ROTORS 0
!ROTORS 2 ../ReactionRate/inertia_1butene.dat
!POTENTIAL separable files
!../ReactionRate/Butene_1-1.txt ../ReactionRate/Butene_1-2.txt
!BAC for C-H C-C C=C C.TB.C O-H C-O C=O
0 0 0 0 0 0

```

→ Taken from Gaussian output

Figure 3-3- CanTherm input file sample

3.5 Results and discussion

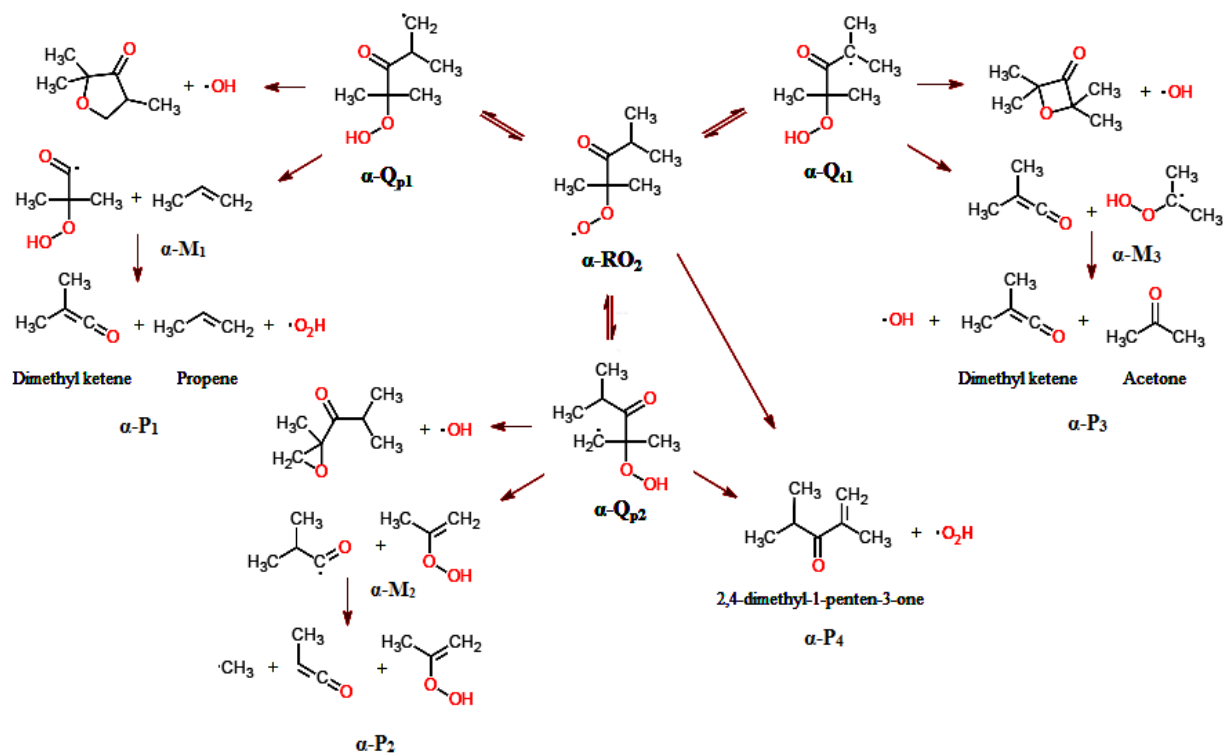
DIPK tertiary and primary radicals in lower temperature react with O₂ which form α -RO₂ and β -RO₂ respectively. RO₂ can either go through termination reaction by losing HO₂ and forming olefins, namely C₇H₁₂O or can lead to branching reaction channel which forms QOOH radical adding to O₂ due to the high oxygen concentrations at low temperature. QOOH decomposes to cyclic ether and OH radical or decompose through other pathways. All the possible reactions pathways for α -RO₂ and β -RO₂ are shown in Scheme 3-1 and 3-2.

3.5.1 α -R + O₂ reaction

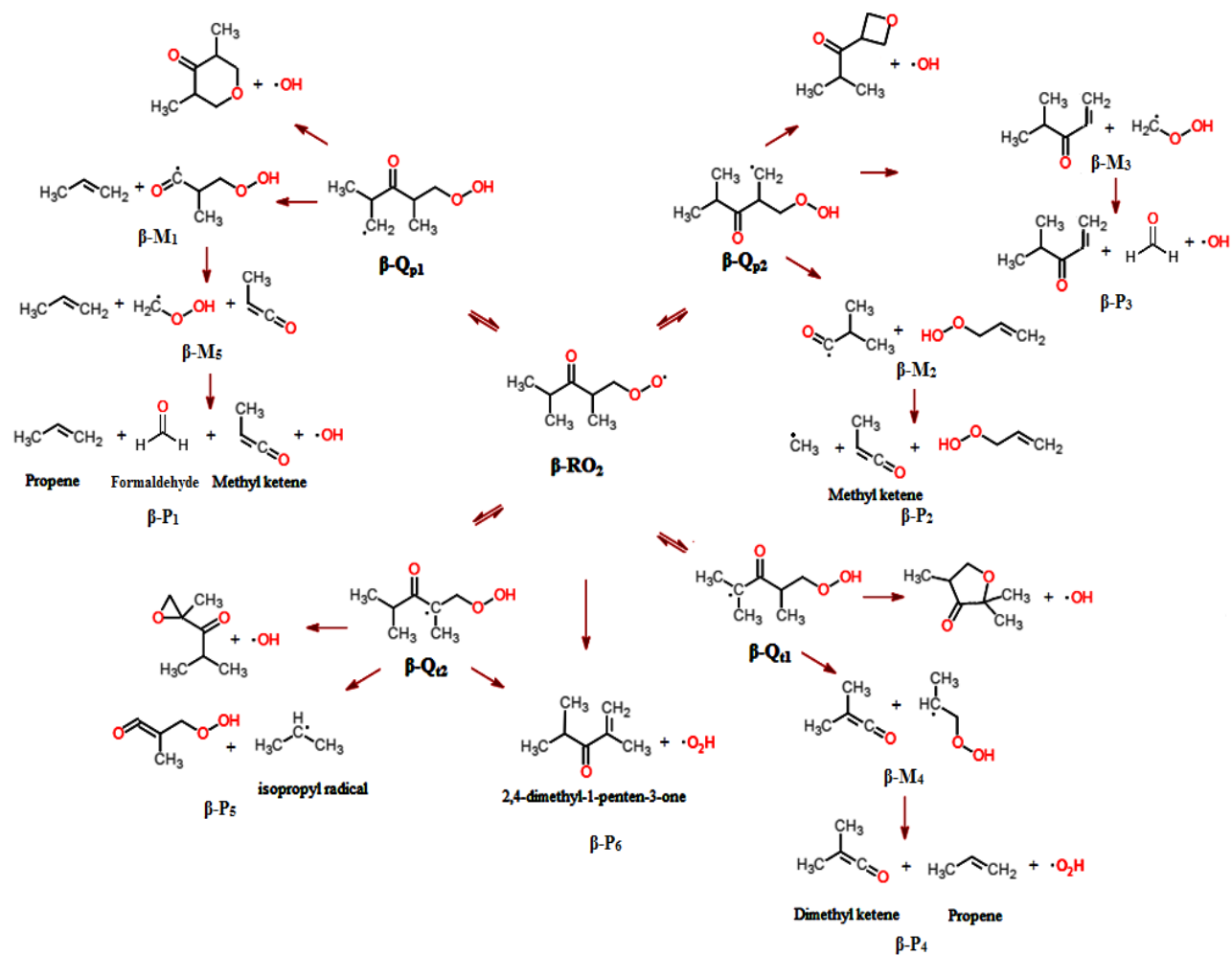
The reaction pathways of α -RO₂ are illustrated in Scheme 3-1. In order to build a simplified nomenclature, the α -QOOH isomers are shown by combination of p or t subscript with numbers. For example, α -Q_{p1} stands for a α -QOOH isomer which is formed by H migration from primary site to the unpaired radical in O atom. If there is more than one primary site for H atom, then the difference between the isomers are recognized by numbers (i.e. α -Q_{p1}, α -Q_{p2}, etc.). The decomposition of α -Q radicals result in α -M complex which is a radical and a stable intermediate. Furthermore, α -Q radicals decompose to cyclic ethers and OH radicals. Although these reaction pathways are shown, they are not considered as the scope of current work. The calculation regarding the energy barriers of cyclic ethers can be found in the previous literature [6]. Finally, the radicals in α -M complex decompose to the products set which are shown by α -P.

The stationary points on potential energy surface for α -R+O₂ reaction are shown in Figure 3-4. Energies are computed at CBS-QB3 level of theory and given at 0K relative to the reactants. The HO₂ elimination from α -Q_pO₂H is the most favorable pathway (in red).

DIPK tertiary and primary radicals react with O₂ and forms α-RO₂ and β- RO₂ which can either decompose or isomerize to QOOH. The reaction pathways of α-RO₂ and β- RO₂ are shown in Scheme 3-1 and Scheme 3-2. The products and intermediates are observed within the schemes.



Scheme 3-1- Reaction pathways of α-RO₂



Scheme 3-2- Reaction pathways of β -RO₂

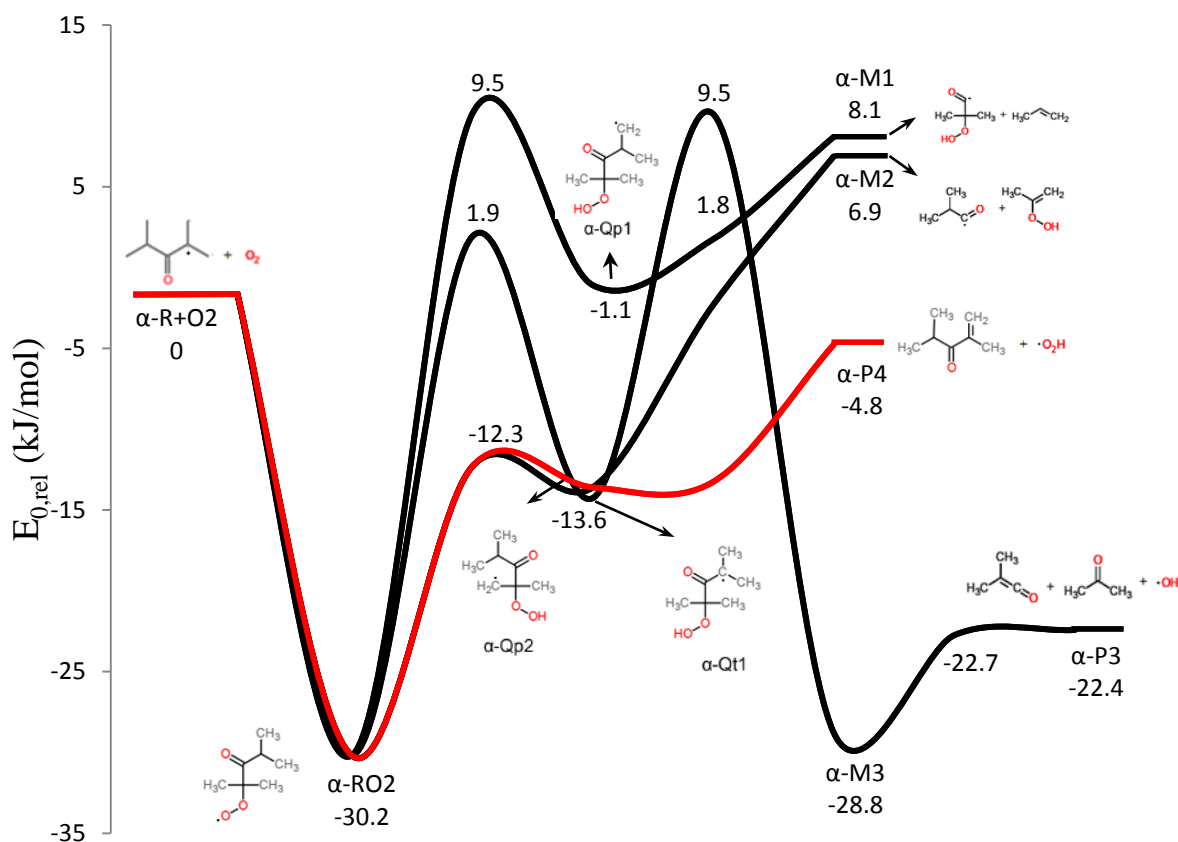


Figure 3-4- Stationary points on PES for $\alpha\text{-R} + \text{O}_2$ reaction. Energies are computed at CBS-QB3 level of theory and presented at 0K relative to the reactants. The HO_2 elimination from $\alpha\text{-QpOOH}$ (shown as $\alpha\text{-Qp2}$ in this figure) is the most favorable pathway, illustrated in red.

Table 3-1 shows the reactants, intermediates and products for $\alpha\text{-R} + \text{O}_2$ reaction with the corresponding structures. The corresponding reactions are given in Table 3-2. The rate constants calculated for $\alpha\text{-R} + \text{O}_2$ reactions using CanTherm are given in Table 3-3. Similarly the rate constant for $\beta\text{-R} + \text{O}_2$ reactions are tabulated in Table 3-4.

Table 3-1- Reactants, intermediates, products in α -R + O₂ reaction; energies are at 0K relative to the reactants

Label	Structure	E _{0,rel} (kJ/mol)
α -R + O ₂		0
α -RO ₂		-30.2
α -Q _{p1}		-1.1
α -Q _{p2}		-13.6
α -Q _{t1}		-14.3
α -M ₁		8.1
α -P ₁		30
α -M ₂		6.9
α -P ₂		41.8
α -M ₃		-28.8
α -P ₃		-22.4
α -P ₄		-8.0

Table 3-2- The structures of the reactions of $\alpha\text{-R} + \text{O}_2$

No.	Reaction	Structure
a0	$\alpha\text{-R} + \text{O}_2 \rightarrow \alpha\text{-RO}_2$	
a1	$\alpha\text{-RO}_2 \leftrightarrow \alpha\text{-Q}_{p1}$	
a2	$\alpha\text{-RO}_2 \leftrightarrow \alpha\text{-Q}_{p2}$	
a3	$\alpha\text{-RO}_2 \leftrightarrow \alpha\text{-Q}_{t1}$	
a4	$\alpha\text{-Q}_{p1} \rightarrow \alpha\text{-M}_1$	
a5	$\alpha\text{-Q}_{p2} \rightarrow \alpha\text{-M}_2$	
a6	$\alpha\text{-Q}_{t1} \rightarrow \alpha\text{-M}_3$	
a7	$\alpha\text{-M}_1 \rightarrow \alpha\text{-P}_1$	
a8	$\alpha\text{-M}_2 \rightarrow \alpha\text{-P}_2$	
a9	$\alpha\text{-M}_3 \rightarrow \alpha\text{-P}_3$	
a10	$\alpha\text{-R} + \text{O}_2 \rightarrow \alpha\text{-P}_4$	

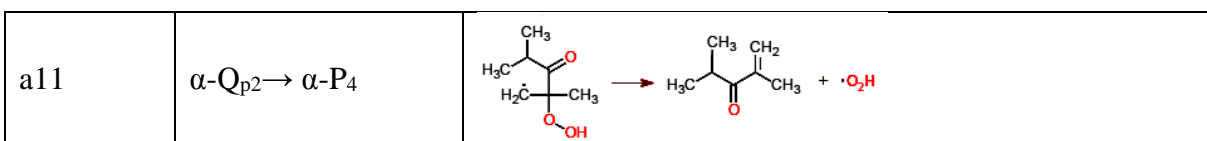


Table 3-3- Rate constants calculated for the reactions of $\alpha\text{-R} + \text{O}_2$

No.		A	n	Ea[kcal/mol]
a1	$\alpha\text{-RO}_2 \leftrightarrow \alpha\text{-Q}_{p1}$	3.35E+01	3.28	19.2
a2	$\alpha\text{-RO}_2 \leftrightarrow \alpha\text{-Q}_{p2}$	5.22E+10	0.87	18.11
a3	$\alpha\text{-RO}_2 \leftrightarrow \alpha\text{-Q}_{t1}$	1.45E-06	5.54	22.47
a4	$\alpha\text{-Q}_{p1} \rightarrow \alpha\text{-M}_1$	2.48E+15	0.2	4.12
a5	$\alpha\text{-Q}_{p2} \rightarrow \alpha\text{-M}_2$	2.94E+15	0.04	12.53
a6	$\alpha\text{-Q}_{t1} \rightarrow \alpha\text{-M}_3$	3.73E+12	0.24	24.36
a7	$\alpha\text{-M}_1 \rightarrow \alpha\text{-P}_1$	6.65E+12	0.32	58.59
a8	$\alpha\text{-M}_2 \rightarrow \alpha\text{-P}_2$	7.03E+32	1.6	36.61
a9	$\alpha\text{-M}_3 \rightarrow \alpha\text{-P}_3$	2.49E+06	0.05	6.06
a10	$\alpha\text{-R} + \text{O}_2 \rightarrow \alpha\text{-P}_4$	1.94E-24	10.80	12.10
a11	$\alpha\text{-Q}_{p2} \rightarrow \alpha\text{-P}_4$	7.57E+15	-0.38	1.38

Table 3-4- Rate constants calculated for the reactions of $\beta\text{-R} + \text{O}_2$

No.		A	n	Ea[kcal/mol]
b1	$\beta\text{-RO}_2 \leftrightarrow \beta\text{-Q}_{p1}$	1.22E+03	2.59	18.42
b2	$\beta\text{-RO}_2 \leftrightarrow \beta\text{-Q}_{p2}$	2.23E+10	0.9	21.93
b3	$\beta\text{-RO}_2 \leftrightarrow \beta\text{-Q}_{t1}$	3.91E+01	3.28	19.24
b4	$\beta\text{-RO}_2 \leftrightarrow \beta\text{-Q}_{t2}$	9.76E-08	5.62	5.78
b5	$\beta\text{-Q}_{p1} \rightarrow \beta\text{-M}_1$	9.93E+13	0.07	0.04
b6	$\beta\text{-Q}_{p2} \rightarrow \beta\text{-M}_2$	8.69E+36	0.17	11.49
b8	$\beta\text{-Q}_{t1} \rightarrow \beta\text{-M}_4$	1.76E+15	0.02	15.62
b9	$\beta\text{-Q}_{t2} \rightarrow \beta\text{-P}_5$	1.83E+11	0.76	8.63
b12	$\beta\text{-M}_2 \rightarrow \beta\text{-P}_2$	3.94E+12	0.28	78.15
b14	$\beta\text{-R} + \text{O}_2 \rightarrow \beta\text{-P}_6$	6.01E-06	5.22	16.15
b15	$\beta\text{-Q}_{t2} \rightarrow \beta\text{-P}_6$	7.43E+11	0.6	-1.39

3.6 Conclusion

The low temperature region kinetics is dominated by DIPK radicals reactions with O₂ for which the quantum chemical calculations are used to estimate the rate constants. The calculations were performed using Gaussian and the rate constants were calculated using CanTherm program.

The reaction network pathways for α -RO₂ and β -RO₂ were illustrated in which all the possible reactions were considered for calculation. The geometry structures were built using Molden and the optimizations and energy calculations were estimated at CBS-QB3 level of theory. The outputs from Gaussian were used to prepare the input file of CanTherm which calculated the corresponding reaction rates accordingly.

The reactions will be studied in the next chapter in terms of product identification and branching ratios at low temperature region. The reason is the quantum chemical calculations were performed for all the possible reactions, therefore the abundance of the products and the relevant quantifications are required to be investigated which is the scope of next chapter.

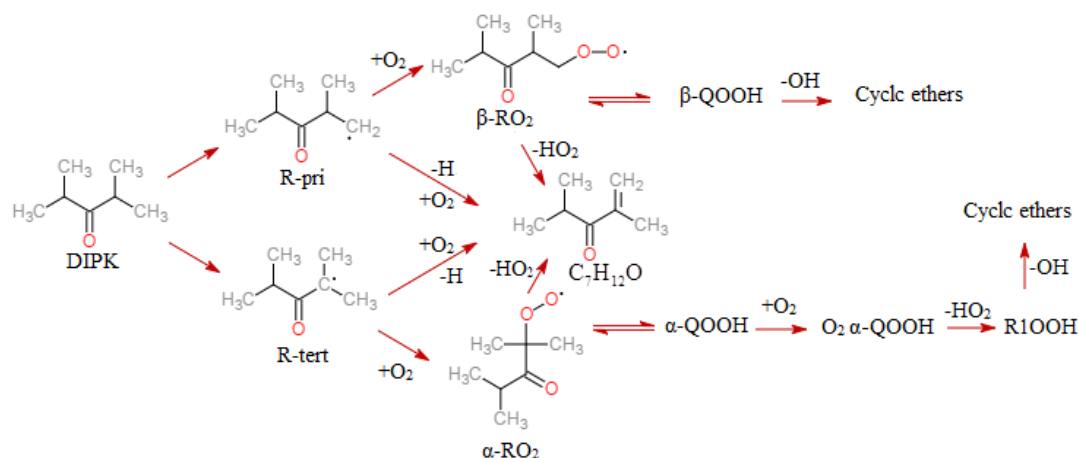
CHAPTER 4:OH-INITIATED OXIDATION OF DIPK AT LOW TEMPERATURE

4.1 Introduction

As the energy security requires new sources of energy, biofuels are getting increasing attention nowadays as a proper alternative fuel especially in transportation/engine industry. Microorganisms produce some advanced biofuels which show comparable characteristics to the fuels with petroleum basis [57]. Among the biofuels, the cellulosic types are more important due to the greater reduction of green-house gases [58-60]. The combustion properties of DIPK as a prototypical biofuel in a HCCI engine are studied for different operating parameter sweeps in which extensive ranges of BDC temperature, intake pressure, engine speed, and equivalence ratio have been taken into account [61]. It was found that DIPK shows strong temperature sensitivity which results in lower heat release rate. Therefore a HCCI engine working with DIPK can reach to a higher thermal efficiency comparing to an engine with the same load of gasoline[61]. DIPK kinetic model for oxidation and pyrolysis has been developed [6] using reaction mechanism generator software [21] and the model is evaluated using experiments. A CI-initiated oxidation of DIPK was investigated. However, the model is not able to predict the ignition behavior of DIPK in low and high temperature range. The low temperature oxidation kinetic is not very well-known for the larger ketones such as DIPK. The current work studies the primary phases in DIPK oxidation experimentally, concentrating on the low temperature region where peroxy radical (ROO) chemistry plays important part in the fuel combustion behavior [62, 63]. The oxidation of DIPK is initiated using pulsed- laser photolysis of hydrogen peroxide to produce OH radical.

Hydroxyl radical is an important part of the oxidation process in combustion [42, 64, 65] and contributes to major reaction channels [66, 67]. In the Cl-initiated oxidation, the chlorinated products are present and in addition, the secondary reactions of chlorine atom (Cl atom+other products) should be taken into account; while the OH-initiated oxidation gives the spectra of desirable products within the oxidation process.

The initiation reaction in low temperature oxidation is the H abstraction reaction from the fuel molecule. DIPK goes through H atom abstraction reactions at tertiary and primary sites (α and β carbon) resulting in the formation of two different fuel radicals, denoted as R_{pri} and R_{tert} . In the presence of excess O_2 , DIPK radicals in lower temperature react with O_2 which form R_pOO and R_tOO , generally denoted as α - RO_2 and β - RO_2 respectively. RO_2 can either go through termination reaction by losing HO_2 and forming unsaturated coproducts, olefins, such as $C_7H_{12}O$ or can lead to branching reaction channel which forms QOOH radical adding to O_2 due to the high oxygen concentrations and low temperature [68]. This branching channel results in the formation of cyclic ethers (CE) and OH radicals which increase the reactivity of the mixture. The low temperature oxidation pathways of DIPK is shown in Scheme 4-1. As the temperature increases from low region to the intermediate region, RO_2 formation is substituted by HO_2 which causes the reactivity to be decreased. The decrease of reactivity by increasing the temperature is known as negative temperature coefficient (NTC) behavior. The experimental data from RCM conducted by Allen et al [6] shows DIPK NTC behavior however the model based on their mechanism was unable to predict this region. The aim of the current work is to determine the dominant consumption pathways during oxidation of DIPK at low temperature based on the analysis of the products identified experimentally.



Scheme 4-1- DIPK low temperature oxidation pathway

4.2 ALS Experimental method

The present experiment uses tunable, high brightness radiation in the vacuum ultraviolet (VUV), as provided by beam line 9.0.2, at the Advanced Light Source (ALS) at Lawrence Berkeley National Lab (LBNL), which allows isomer-specific photoionization detection of reactants and products from photolytically initiated gas-phase reactions. Sandia's highly multiplexed photoionization mass spectroscopy (MPIMS) experiment which can monitor all products simultaneously with superior sensitivity [69] is used to isomer-resolved study of reactions and molecules. It is not possible to study the branching ratios or product spectrum using the shock tube/OH/H/O absorption or Laser Induced Fluorescence techniques [7, 70] (where the overall reaction is obtained by monitoring the decay of radicals). Hence the isomer specific detection provided by ALS MPIMS is critically needed to distinguish between products to derive branching ratios. By detecting the product spectrum branching ratios are estimated.

The Sandia apparatus is designed to study the kinetics of primary gas phase reactions by monitoring the time resolved concentrations of chemical species followed by the initiation reaction using laser photolysis [71]. The apparatus schematic is illustrated in Figure 4-1. The Sandia apparatus consists of a heated 1.05 cm inner diameter quartz flow tube with a ~ 650 μm aperture through which gas escapes. A collimated molecular beam is formed by passing the effluent through a skimmer. Continuous, tunable ionizing radiation provided by the synchrotron intersects the molecular beam orthogonally and ions are accelerated into a linear time-of-flight mass spectrometer. Because the apparatus collects time- and photon-energy-resolved mass spectra, the products are detected as a function of mass, time, and energy, yielding a 3-dimensional dataset [6, 69, 72-74] that can be sliced and integrated accordingly to obtain photoionization spectra and temporal profiles for individual species (see Figure 4-2). Photolysis by a pulsed excimer laser operating between 193-351 nm at 10 Hz is used to initiate experiments in some cases. Mass flow controllers (MKS) are used to introduce reactants and carrier gas into the flight tube (for details, refer to [6, 69, 72-74]). The position and time of arrival with respect to the photo-dissociation laser is recorded for each ion [71]. The experiment is repeated, and the signal averaged, for up to 20000 laser pulses. The schematic of the entire setup is shown in Figure 4-3.

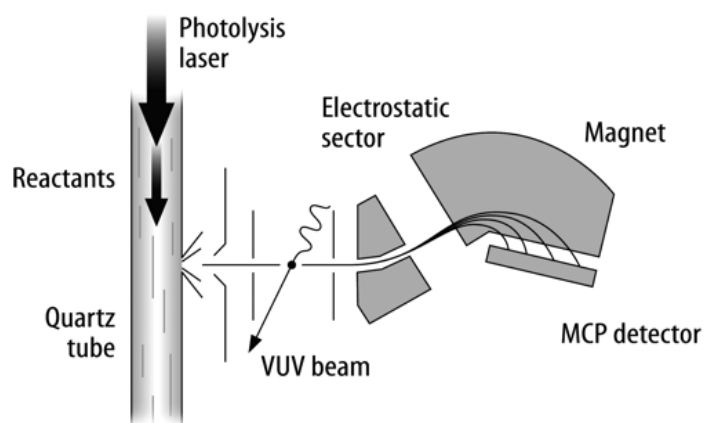


Figure 4-1- Schematic of experimental apparatus [69]

The oxidation of DIPK is initiated by flash photolysis laser towards hydrogen peroxide (H_2O_2). Photolysis of H_2O_2 -producing OH [73] - by a pulsed excimer laser operating at 248nm at 10 Hz is used to initiate experiments in the reactant mixture (urea-hydrogen peroxide adduct, biofuel, helium diluent): $\text{H}_2\text{O}_2 + h\nu (248 \text{ nm}) \rightarrow 2 \text{ OH}$.

Note that the absorption cross section of ketones in this wavelength region is very negligible – at least 1000 times weaker than the radical precursors (see ref. [75]). The H-abstraction reactions by OH radicals from the fuel result in the formation of primary and tertiary radicals which can react with O_2 accordingly to produce several possible products [42, 67, 71]:



Similarly for n-butanol, we come up with four different radicals which are reacting with excess O_2 .

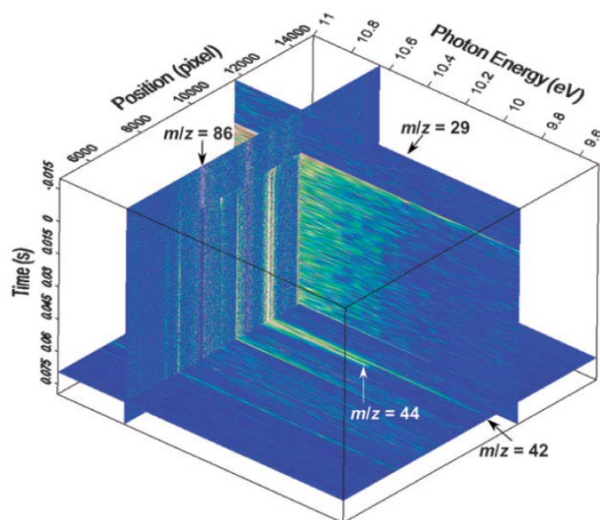
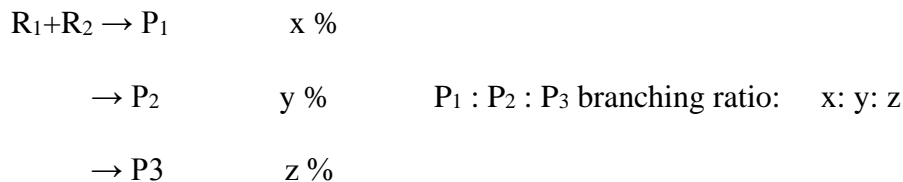


Figure 4-2- A sample three dimensional dataset measured in [76]

The relative contribution of biofuel bound oxygen to the OH initiated products is probed by replacing the fuel ^{16}O with ^{18}O . The OH-initiated oxidation in ALS experiments are performed for some fuels [42, 67] which are similar to the procedure recently used by our Sandia collaborators to probe Chlorine initiated reaction systems. The details regarding the Cl-initiated oxidation of DIPK can be found in the relevant literatures [6, 76, 77]. Along with the product identification, estimating the branching ratio is an important step to determine the relative concentrations of the products and is performed in this chapter as another goal of this experiment. The branching ratio for the reaction of R_1+R_2 in three different pathways resulting in three different product set is shown in . The percentage of generated products are also displayed in front of each product. The branching ratio of $\text{P}_1 : \text{P}_2 : \text{P}_3$ is simply defined as $x : y : z$.



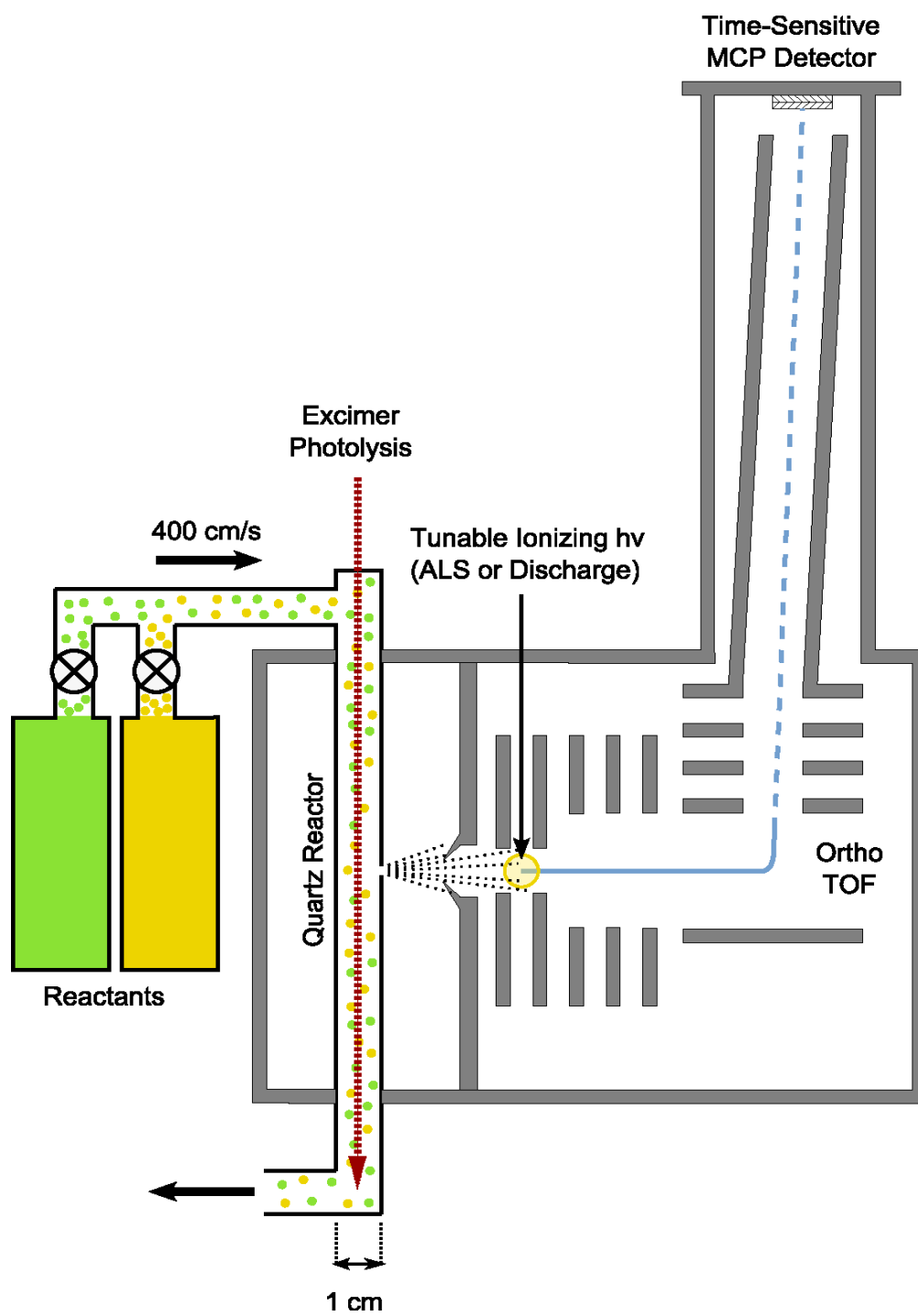


Figure 4-3- Experimental setup schematic [76]

4.3 Results and discussion

4.3.1 Diisopropyl ketone (DIPK) OH-initiated oxidation

DIPK oxidation experiments are performed at 450, 500 and 550 K; however, the oxidation is investigated at 450 and 500 K due to substantial decomposition of H₂O₂ at the wall of the reactor tube at higher temperatures. Species and products identification is based on a comparison of photoionization spectra at a particular mass-to-charge ratio with absolute photoionization cross sections [74, 76, 78]. The three dimensional dataset I(E, t, m/z) which is the signal I as a function of photon energy, time and mass to charge ratio, is integrated over a range of kinetic times to obtain the two dimensional dataset of I(E,m/z), the photoionization spectra corresponding to a specific mass to charge ratio.

The full spectra are recorded in every 20 μs over 150 ms kinetic time. The masses can be identified based on the exact locations of the peaks [79]. For the isomers, the identification is done by comparing the ionization efficiency and photoionization spectra which should be different from each other. The photoionization spectra is the intensity of the ion signal versus the photon energy. There are many known photoionization spectra corresponding to the known species that can be compared to the ion signal to assign a product to a peak.

The ions signal as a function of photon energy at a specific m/z is a sum over the isomeric contributions [79]:

$$S_{m/z}^{(t,t+\Delta t)}(E) = \varphi \alpha_{m/z} \sum_i c_i^{(t,t+\Delta t)} \sigma_i(E) \quad (4-1)$$

where $S_{m/z}^{(t,t+\Delta t)}(E)$ is the ion signal integrated over the kinetic time range of $(t, t + \Delta t)$ at a given m/z.

The signal is normalized to ALS photon energy. φ is the instrument factor, a collection of species-independent factor [80] and α is defined as :

$$\alpha_{m/z} = m_i^\beta \quad \begin{cases} \beta = 0.64 & 300 \text{ K}, 4 \text{ Torr} \\ \beta = 0.6 & 550 - 700 \text{ K}; 4 - 5.1 \text{ Torr} \end{cases} \quad (4-2)$$

$c_i^{(t,t+\Delta t)}$ is the concentration of isomer i averaged over the kinetic time range of $(t, t + \Delta t)$.

The ions signal is scaled such that they could be matched with the absolute photoionization cross section $\sigma_i(E)$. The expression for ion signal equation (4-1) can be written in terms of relative concentration or branching ratio:

$$S_{m/z}^{(t,t+\Delta t)}(E) = \sum_i x_i^{(t,t+\Delta t)} \sigma_i(E) \quad (4-3)$$

where x_i is the branching ratio for the species with the same mass.

Time-resolved photoionization mass spectrum of DIPK+H₂O₂+O₂ carried by Helium as the bath gas is obtained using the background-subtracted signal integrated over photon energies from 8.0–11.0 eV. The presence of numerous product peaks after the laser photolysis demonstrates the formation of product and co-products through various channels. By integrating the time-resolved photoionization mass spectrum over a period of time after laser photolysis, a time- and photon energy-integrated difference mass spectrum is achieved. Figure 4-4 displays the mass spectra obtained at 500K and 6 Torr for the mixture of DIPK+H₂O₂+O₂. The spectra show the changes in the products concentration and result from integrating the relative signal from 20ms to 40ms which is the duration immediately after the laser photolysis and from photon energies of 8.0-11.0 eV. The negative signal at m/z=114 shows the consumption of DIPK. The dissociative

ionization of DIPK is also observed at the negative signals of $m/z=70$ and 71 . The most significant peaks intensity are corresponding to m/z values of $42, 43, 44, 58, 59, 69, 70, 71, 85, 100, 112$ and 128 . The peaks at DIPK OH-initiated oxidation at 300 K show relatively weaker ion signals than 450 and 500 K . The presence of the strongest peaks at the masses smaller than DIPK ($m/z=114$) shows that the bond fission pathway is more dominant than the initial oxidation kinetic steps [78]. Some of the peaks are the products and some are the dissociative ionization of higher masses.

The identification of the products and stable intermediates is performed by comparing the photoionization spectrum at a mass over charge ratio of interest with the standard photoionization efficiency (PIE) corresponding to the same mass. Figure 4-5 shows the major peaks photoionization spectra of $m/z=42, 44,$ and 58 at the temperatures 450 K and 500 K . The peaks at $m/z=42$ and 44 are compared with propene and acetaldehyde PIE respectively which are found to be the most dominant contribution for those masses at all temperatures.

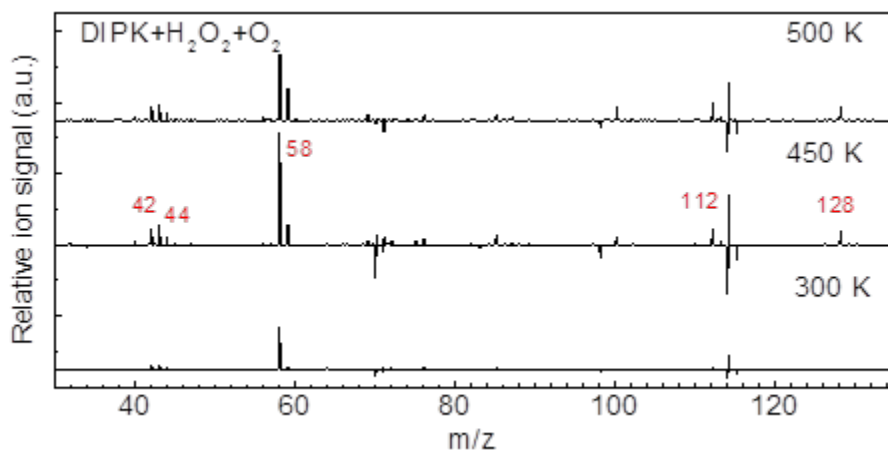


Figure 4-4- Integrated difference mass spectra for OH initiated oxidation of DIPK at $300, 450$ and 500 K , obtained by integration over the photon energy $8.4-11.0\text{ eV}$ and the kinetic times until 20 ms after the laser photolysis

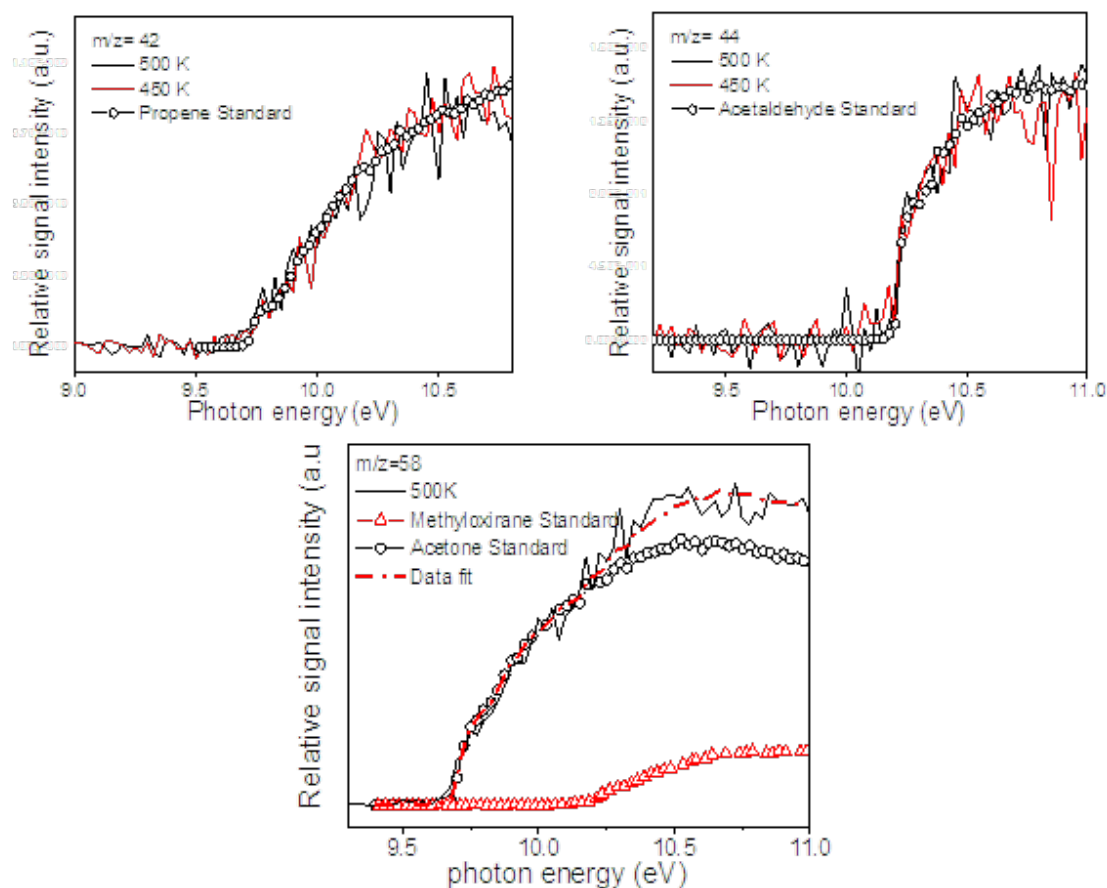


Figure 4-5- Photoionization spectra of $m/z=42$, 44 and 58 at different temperatures simulated by the standard PIE spectra of Propene [78], Acetaldehyde [78] and Acetone+Methyloxirane respectively

The peak of $m/z=58$ is the strongest ion signal in the mass spectra of OH-initiated oxidation of DIPK for the temperatures of 300, 450 and 500 K. The corresponding photoionization spectra at $m/z=58$ (Figure 4-5) is assigned to Acetone as the major contribution for energy range of lower than 10.2 eV; however, above 10.2 there is another contribution due to the presence of Methyloxirane. The branching ratio for Acetone: Methyloxirane is found: 10:3 at 500 K. The curve fitted to Acetone+Methyloxirane with the branching ratio of 10:3 is matched with the experimental data. At 300 and 450 K, Acetone was found to be in excess over Methyloxirane. The peaks associated with $m/z=59$ and 100 are the daughter ions of $m/z=128$.

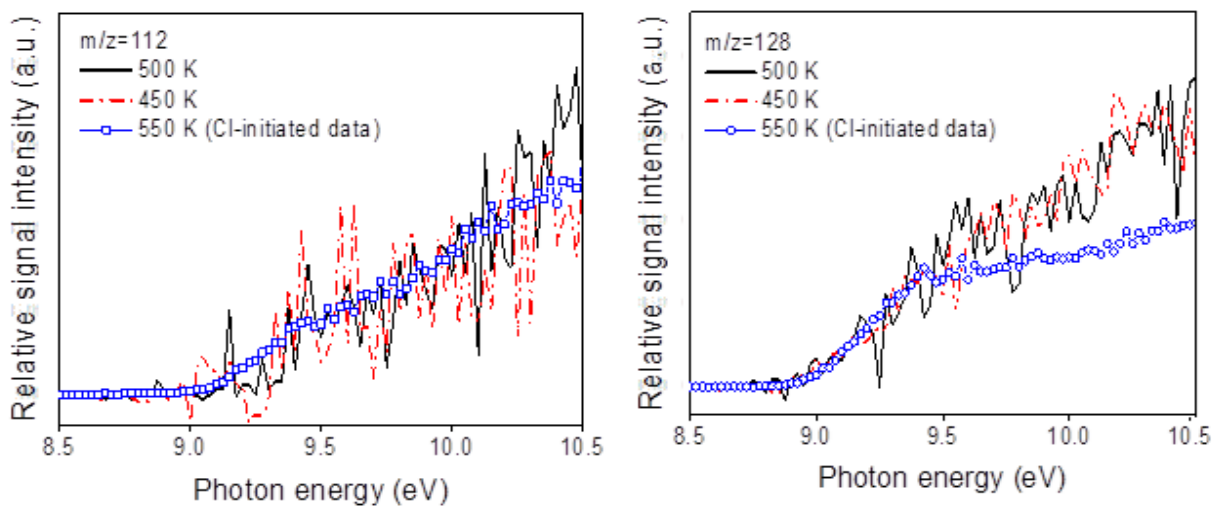


Figure 4-6- Photoionization spectra of $m/z=112$ corresponding to $C_7H_{12}O$, (left) and $m/z=128$ corresponding to cyclic ether, $C_7H_{12}O_2$ (right) at different temperatures along with a comparison to the PIE spectra from Cl-initiated experiment (Allen et al. [6])

As it is mentioned before, there are two important consumption pathways for the fuel. One is RO_2 isomerization to QOOH through H atom migration, which accordingly decomposes to OH radicals and different cyclic ethers ($m/z=128$), recognized by their structures (See Figure 4-7).

The adiabatic ionization energies corresponding to the possible cyclic ethers forming from this pathway are calculated at CBC-QB3 level of theory[6] using Gaussian [18]. Another main consumption pathway is through HO_2 elimination from the radicals which results in the formation of $C_7H_{12}O$ ($m/z=112$). The competition between these two pathways is a function of pressure and temperature and determines the kinetics of low temperature oxidation [78].

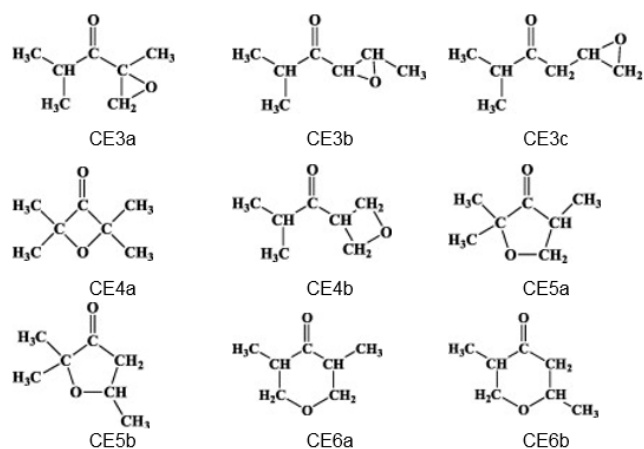


Figure 4-7- Possible cyclic ethers formed in DIPK oxidation

The photoionization spectra for $m/z=112$ and 128 are shown in Figure 4-6 at 450 and 500 K, compared to the Cl-initiated oxidation of DIPK. The scaled photoionization spectrum of $m/z=112$ at 450 and 500 K are in good agreement with the spectrum from DIPK Cl-initiated oxidation experiment. The OH-initiated photoionization spectra of $m/z=128$ as well as the Cl-initiated spectrum demonstrate similar onset at 8.8 eV. However, the photoionization spectrum of $m/z=128$ corresponding to OH-initiated oxidation of DIPK shows discrepancy comparing to the results from Cl-initiated experiment at the photon energies higher than 9.4 eV. While the former shows a smooth rise up to 10.5 eV, the latter seems to have a break point at 9.4 eV and tends to become a plateau after the rise. By looking into the AIE table for possible cyclic ethers calculated by Allen et al [6], we can find a three-membered ring cyclic ether (CE3) formed from R_2OO , the addition of O_2 to the secondary radical (which is formed from primary radical through radicals rearrangement). The three membered ring cyclic ethers which have relatively higher energy than their isomers with five or six membered ring, are usually expected to be formed in relatively much smaller amount; nevertheless, the photoionization spectrum from OH-initiated experiment shows

that CE3 has noticeable contribution to the peak $m/z=128$. CE3 can be produced through two different reaction pathways of $\beta\text{-RO}_2 \rightarrow \beta\text{-Q}_{12} \rightarrow \text{CE3} + \text{OH}$ or $\alpha\text{-RO}_2 \rightarrow \beta\text{-Q}_{12} \rightarrow \text{CE3} + \text{OH}$ (See Figure 4-7)

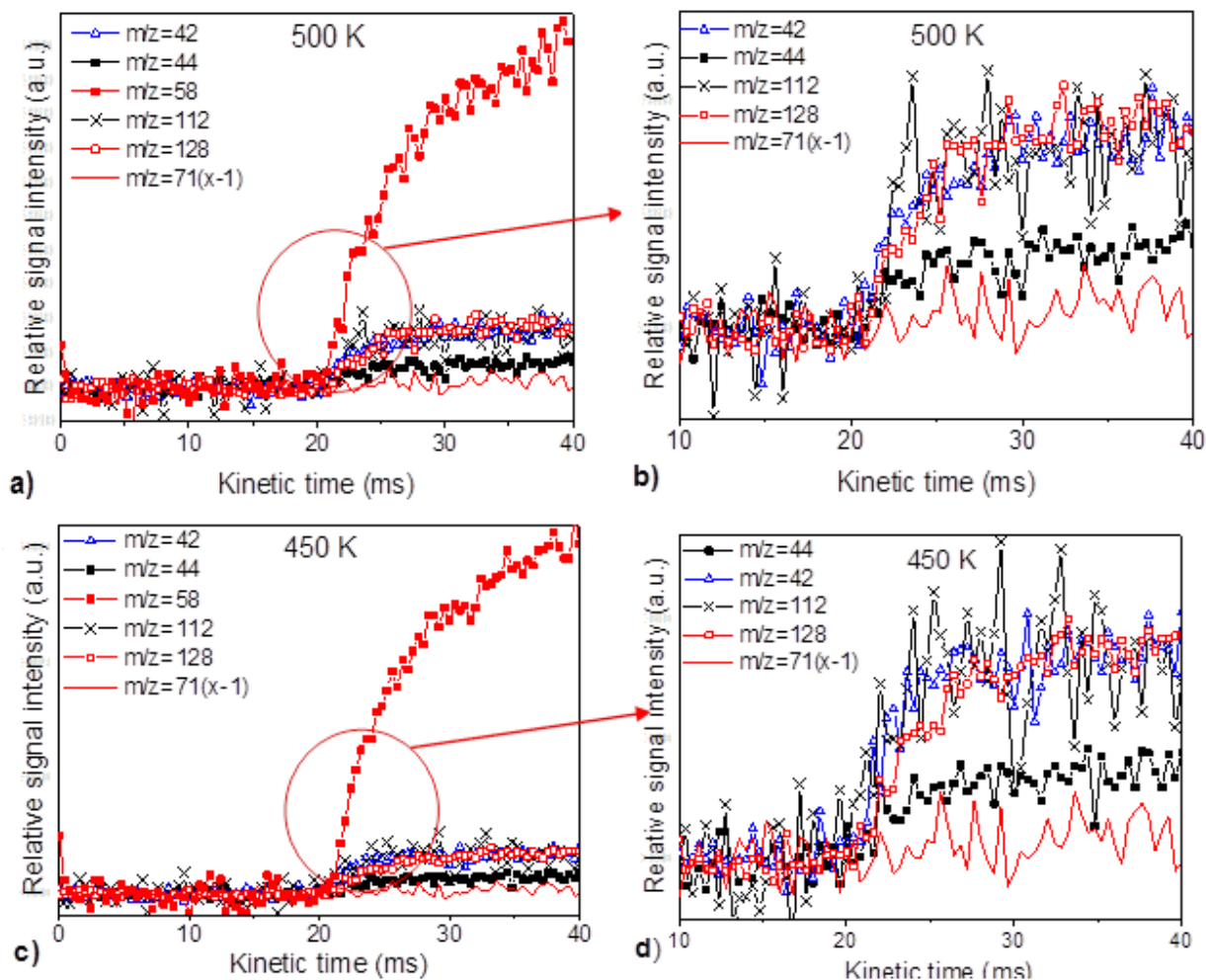


Figure 4-8- a) Time profiles of $m/z = 42, 44, 58, 112, 128,$ and 71 at 500 K , obtained by integration over photon energies from $8.4 - 11.0\text{ eV}$. The consumption of DIPK is shown by the profile of its daughter ion at $m/z = 71$, shown multiplied by (-1) ; b) time profiles of larger view ($m/z=58$ excluded); c) Time profiles at 450 K ; d) time profiles of larger view

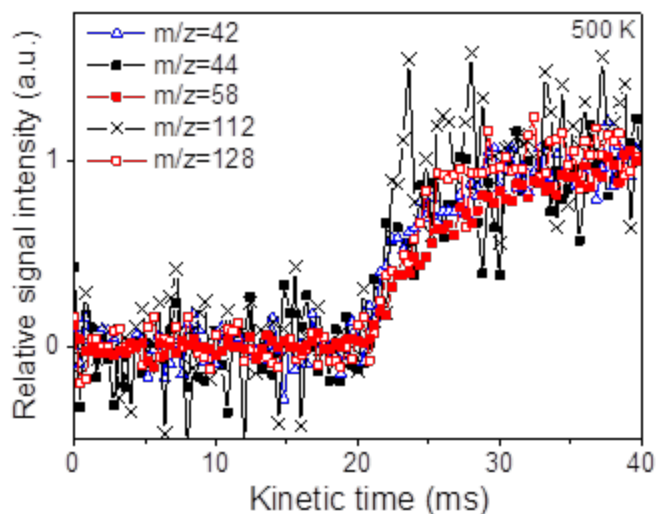


Figure 4-9- Time profiles of $m/z = 42, 44, 58, 112,$ and 128 at 500 K , obtained by integration over photon energies from $8.4 - 11.0\text{ eV}$, scaled such that all the profiles intensities (in arbitrary unit) are equal to unity at a kinetic time of 40 ms (20 ms after the laser photolysis).

One important feature of multiplexed photoionization mass spectroscopy (MPIMS) is combination of photoionization with time-resolved mass spectroscopy. The time profiles of the mass peaks matching to the major products formed at 500 K are given in Figure 4-8. The plots represent the background-subtracted data sliced at different m/z and obtained by integration over photon energies from $8.4 - 11.0\text{ eV}$ until 20 ms after photolysis, during which the temperature within the reactor tube remains constant. The consumption of DIPK is shown by the profile of its daughter ion at $m/z = 71$, shown multiplied by (-1) . The peak of $m/z=58$ which corresponds to Acetone and Methyloxirane, shows substantial rise after the photolysis. The time profiles of the mass peaks corresponding to the major products formed at 450 K are also shown in Figure 4-8. Figure 4-9 represents the time profiles of $m/z = 42, 44, 58, 112,$ and 128 at 500 K , obtained by integration over photon energies from $8.4 - 11.0\text{ eV}$, scaled such that all the profiles intensities (in arbitrary unit) are equal to unity at the kinetic time of 40 ms (20 ms after the laser photolysis). The

shape of the scaled time profiles for the major products are very similar to each other, suggesting that the branching ratios are the same at every kinetic time [79, 80].

The time profiles of major products at different temperatures display the competition between the fuel radicals thermal decomposition pathway and the radicals reaction with O₂. The time profile of Propene (m/z=42), acetaldehyde (m/z=44), C₇H₁₂O and cyclic ether are shown in Figure 4-10 at temperatures of 300, 450 and 500K. Cyclic ether and C₇H₁₂O are also found to be more produced as the temperature increases, yet their signals intensities are almost the same at 450 and 500 K. While propene is produced monotonically as temperature increases, acetaldehyde reaches a maximum at 450K and starts to decrease at 500 K. The intensities shown in Figure 4-10 are denoted as relative product yield [79]. The products branching ratio or “relative product yield”

$\frac{c_i(t)}{c_j(t)}$ which is defined as:

$$\frac{c_i(t)}{c_j(t)} = \left(\frac{I_i(t) / I_{mean,i}^{(t,t+\Delta t)}}{I_j(t) / I_{mean,j}^{(t,t+\Delta t)}} \right) \left(\frac{c_i^{(t,t+\Delta t)}}{c_j^{(t,t+\Delta t)}} \right) \quad (4-4)$$

Where $I_i(t)$ is the relative ion signal time profile of product i and $c_i^{(t,t+\Delta t)}$ is the concentration of isomer i averaged over $(t, t + \Delta t)$ time range which is calculated by comparing the photoionization spectra with the standard PIE. $I_{mean,i}^{(t,t+\Delta t)}$ is the mean value of species i ion signal over $(t, t + \Delta t)$ time range.

Based on the relative product yields profiles, the experimentally determined branching ratios at 450 and 500 K for Acetaldehyde, cyclic ether and 2,4-dimethyl-1-penten-3-one are

obtained relative to propene (Table 4-1). The branching ratio relative to other species can be calculated following the same approach.

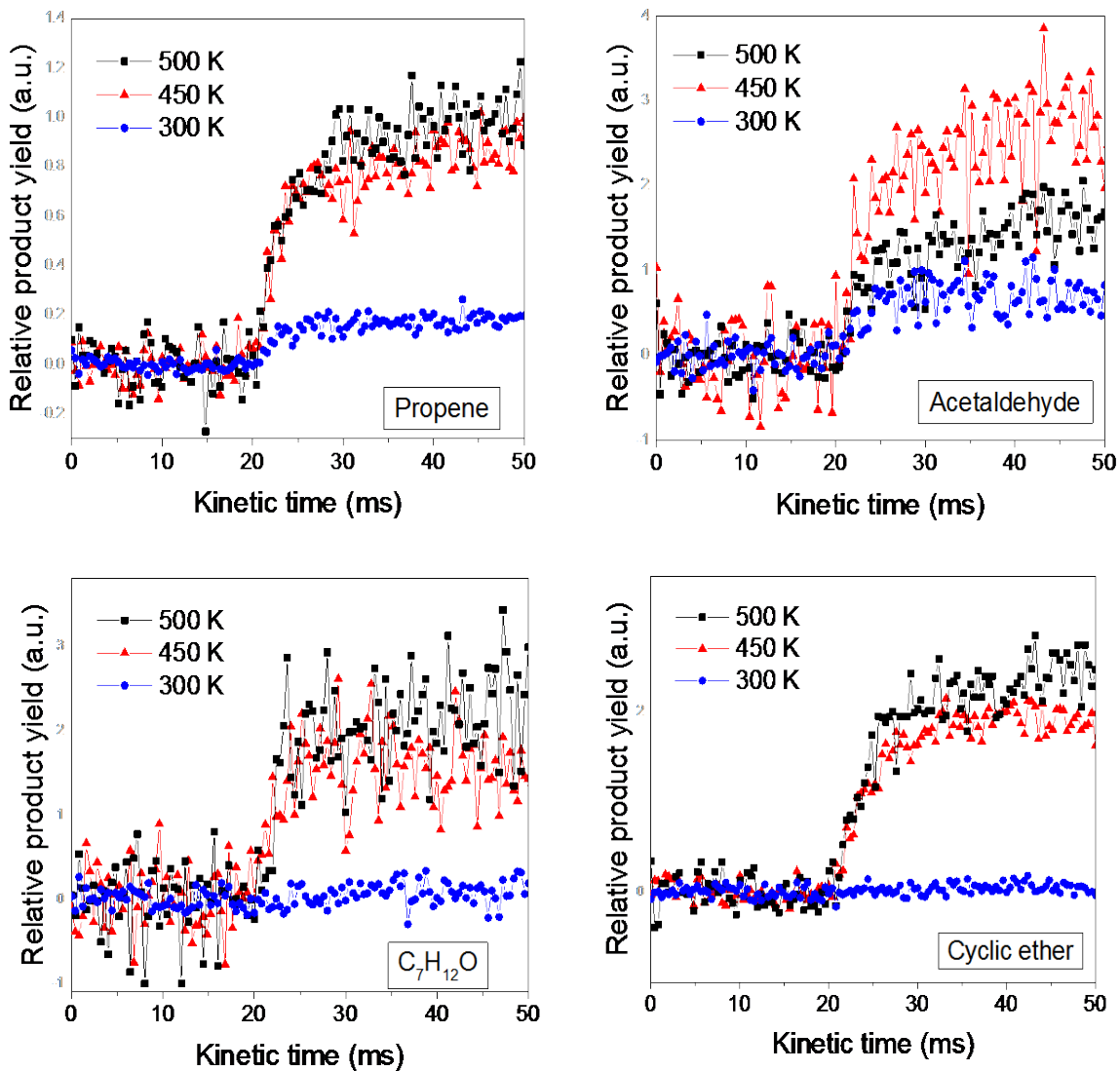


Figure 4-10- Time profiles of Propene, Acetaldehyde, C₇H₁₂O and cyclic ether at 300, 450 and 500 K up to 30 ms after laser photolysis

Table 4-1- DIPK oxidation Major products branching ratio relative to propene at 450 and 500 K

m/z (formula)	Products	Branching ratio relative to Propene	
		450 K	500 K
42 (C3H6)	Propene	1	1
44 (C2H4O)	Acetaldehyde	3	1.4
112 (C7H12O)	2,4-dimethyl-1-penten-3-one	2.6	2.6
128 (C7H12O2)	Cyclic ether	2.1	2.5

4.4 Conclusions

Products from low pressure OH-initiated oxidation of DIPK at 300, 450 and 500 K were identified using multiplexed synchrotron photoionization mass spectroscopy (MPIMS) and compared to the recently performed Cl-initiated oxidation experiments. In DIPK oxidation, the comparison of photoionization spectra of the major peaks with the standard PIE with the same mass to charge ratio identifies the major products which are found to be propene, acetaldehyde, acetone, Methyloxirane, cyclic ethers and 2,4-dimethyl-1-penten-3-one.

The major products time resolved spectra from DIPK oxidation have been compared at different temperatures. The time profiles of major products at different temperatures display the competition between the fuel radicals thermal decomposition pathway and the radicals reaction with O₂. While propene is produced monotonically as temperature increases, acetaldehyde reaches a maximum at 450K and starts to decrease at 500 K.

The results from the OH-initiated oxidation of DIPK are consistent with Cl-initiated oxidation.

CHAPTER 5: CI-INITIATED OXIDATION OF MAJOR ALDEHYDES INTERMEDIATES FROM DIPK COMBUSTION

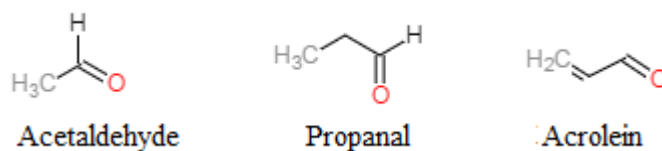
5.1 Introduction

Aldehydes are formed as a result of incomplete or partial combustion and are the major stable intermediate products in pyrolysis and oxidation of biofuel, which affect the reaction pathways and important combustion properties [81]. Aldehydes can be released to the atmosphere from gasoline and diesel engines, and also from biomass gasification or aerobic treatments [82]. Therefore, understanding of aldehydes combustion and pyrolysis behavior with chemical kinetics perspective is very important in order to predict pollutant release and be able to design environmentally friendly combustion systems [81, 83]. Studies of alcohols oxidation showed that aldehydes are the intermediates forming from radicals or molecular dehydrogenations [23, 84-86].

A comprehensive chemical kinetic reaction mechanism for the oxidation of aldehydes can help to understand and predict the emission from the combustion systems. At low temperature, the kinetics of reactions of OH radical with acetaldehyde and its alkyl is investigated [87],[88]. The high temperature measurements of the rate constants for some aldehydes with OH radical was studied using shock tube [89]. Along with the measurements, the reactions of C₁–C₄ aldehydes with NO₂ has been modeled theoretically using a direct dynamic approach [90].

In a recent study, a sub-mechanism for the high temperature kinetics of three aldehydes, (propanal,*n*-butanal and *n*-pentanal) pyrolysis and oxidation was developed and validated with the shock tube data [83]. However, a kinetic mechanism which can address the aldehydes kinetics at low temperature is not developed.

In this chapter, the Advanced Light Source methodology, explained in previous chapters, is used to identify the products and main oxidation pathways through the designed experiment of Cl-initiated oxidation of three important aldehyde: acetaldehyde (C_2H_4O), propanal (C_3H_6O) and acrolein (C_3H_4O). The structures are shown in Scheme 5-1. As it was mentioned before, in OH-initiated experiment, the OH radicals are produced through H_2O_2 laser photolysis whereas in Cl-initiated experiment the Cl radicals are formed through the molecular chlorine, Cl_2 , laser photolysis.



Scheme 5-1- Aldehydes structures

Aldehydes are generated as intermediates in DIPK oxidation. The pathways of acetaldehyde and acrolein production are shown in Scheme 5-2. DIPK oxidation in Ar is simulated in CHEMKIN and the mole fraction of the generated aldehydes i.e. acetaldehyde, acrolein and formaldehyde are illustrated in Figure 5-1.

The goal of this chapter is to study the oxidation pathways of the aforementioned aldehydes as well as the corresponding primary products. This experimental study is important in the sense that acetaldehyde and propanal are the intermediates forming in DIPK oxidation which gives us deeper insight to DIPK kinetic reaction mechanism and the rates for those corresponding reactions. Furthermore, the aldehydes oxidation have been studied in two different temperature within 500-700 K which belongs to low-intermediate temperature region [63]. This temperature regime ($T < 800$ K) is very important in the sense of fuel chemistry effects on autoignition behavior which

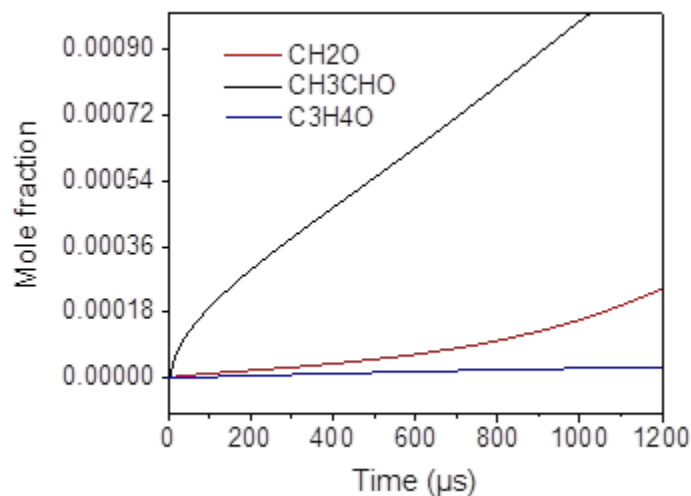


Figure 5-1- Aldehyde mole fraction in 2% DIPK oxidation in Ar in 1300 K and 0.9 atm

5.2 Experimental method

The reaction of photolytically generated Cl atoms with the aforementioned aldehydes is a convenient method to produce the different possible radicals through H atom abstraction reactions. The chemistry of these radicals' reactions in excess O₂ at low temperature (500-700 K) and low pressure (8 Torr) is studied using time and isomer resolved product detection from multiplexed photoionization mass spectroscopy (MPIMS). MPIMS experiments are performed using tunable vacuum-ultraviolet (VUV) radiation from Advanced Light Source (ALS) synchrotron at Lawrence Berkeley National Laboratory. The experimental setup has been explained previously. The identification of the species and isomers is based on a comparison of PIE spectra of a given m/z with absolute photoionization cross sections [78].

5.3 Results and discussion

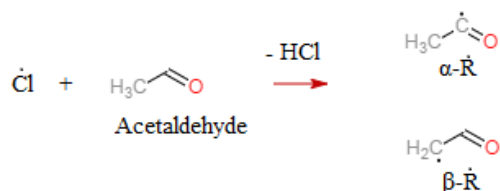
The low temperature oxidation of the aldehydes of our interest is initiated by hydrogen atom abstraction which results in the formation of the fuel radicals. The different radical isomers for each aldehyde are shown in Scheme 5-4, 5-8 and 5-12. Subsequently, the radicals react with O₂ to form RO₂. In low temperature, the chain terminating channel which produces HO₂ is competing with the chain propagation channel generating OH radicals [92]. Therefore, the chemistry of RO₂ radicals should be taken into account to address the autoignition behavior [93]. In the presence of excess O₂ at low temperature, the radicals react with O₂ but as the temperature goes up, the thermal unimolecular decomposition channel will be remarkably competes with O₂ reaction [80].

5.3.1 Products and pathways in acetaldehyde low temperature Cl-initiated oxidation

The photon energy integrated difference mass spectra for Cl-initiated oxidation of acetaldehyde (550 and 700 K) is illustrated in Figure 5-2. The average pre-photolysis signal is subtracted, therefore the difference mass spectra shows the difference between the signal after and before laser fires. The peaks with positive intensity are associated with the products while the negative peaks (are cut to highlight the product formation) are associated with the removal channel of acetaldehyde. The photoionization spectra is obtained by integration over kinetic time of up to 45 ms (which is 25 ms after the laser photolysis). The main peaks are indicated by their m/z values above them.

The two most dominant peaks in the oxidation of acetaldehyde in 500 and 700 K are at m/z=30 and m/z=42 for which the photoionization spectra are matched to that of formaldehyde

(ionization energy: 10.88 eV) and ketene (IE: 9.61) respectively (see Figure 5-3). The ion signal peaks at $m/z=47$ and 60 are also remarkable.



Scheme 5-3- Acetaldehyde radicals

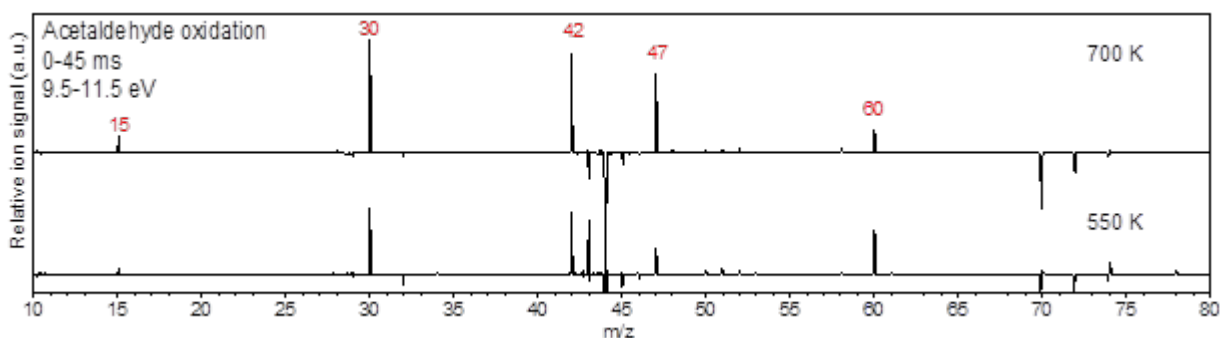


Figure 5-2- Integrated difference mass spectra for Cl-initiated oxidation of Acetaldehyde at 550 K and 700 K, obtained by integration over the photon energy 9.5-11.5 eV and the kinetic times until 25 ms after the laser photolysis

The signal for $m/z=42$ in the mass spectra is found to be ketene which is produced either through radicals thermal decomposition (Scheme 5-5) or the channel of $\text{R}+\text{O}_2 \rightarrow \text{RO}_2$ (Scheme 5-6/Scheme 5-7). The strong signal for $m/z=42$ demonstrates that the HO_2 elimination from the peroxy radicals is also a major channel in low temperature oxidation of acetaldehyde similar to the alkanes [63]. The reaction pathway in Scheme 5-6 explains the formation of ketene. $\beta\text{-R}$ reaction with excess O_2 forms $\beta\text{-RO}_2$ peroxy radical followed by isomerization to alkoxy-QOOH species which subsequently undergoes $\beta\text{-C}-\text{O}$ bond fission to form ketene and HO_2 radical. Ketene also

is formed through α -R (CH_3CO) forming α - RO_2 peroxy radical with the corresponding alkoxy- QOOH isomer which decomposes to ketene and HO_2 radical (see Scheme 5-7).

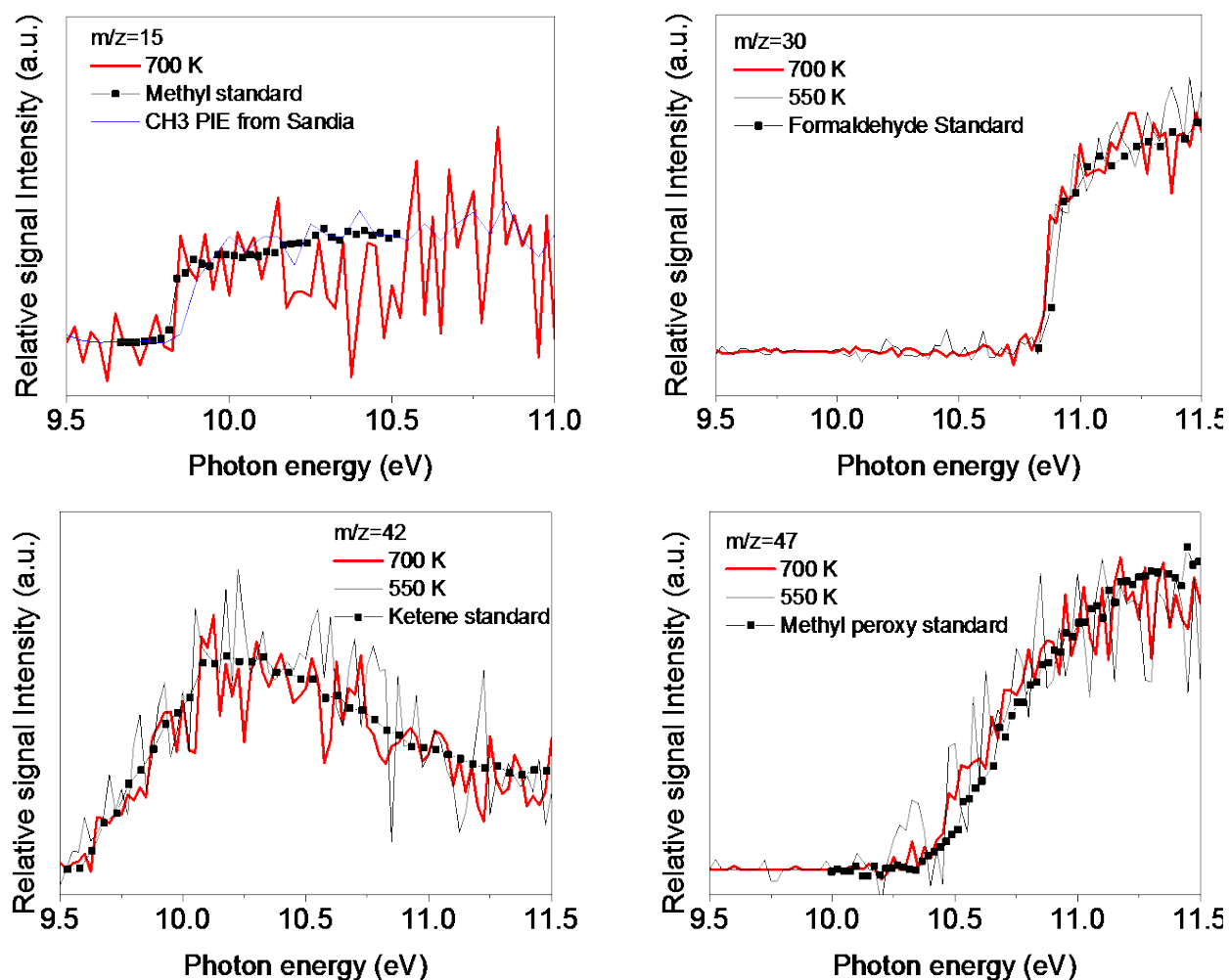


Figure 5-3- Primary products photoionization spectra of Acetaldehyde Cl-initiated oxidation at 550 and 700 K obtained by integration over kinetic time 25 ms after laser photolysis, compared to the corresponding standard photoionization cross section

Along with the reactions of CH_3CO radical with O_2 , the radical decomposition reactions should be taken into account which results in formation of methyl (CH_3) radical. The signal at $m/z=15$ which is matched with methyl photoionization spectra (Figure 5-3) verifies this assignment. For all the products, the photoionization cross sections are taken from Sandia National Lab photoionization

database. Those species for which there is no measured PIE available in Sandia's database [94], the calculated values or measured ionization energy from NIST webbook [95] are used.

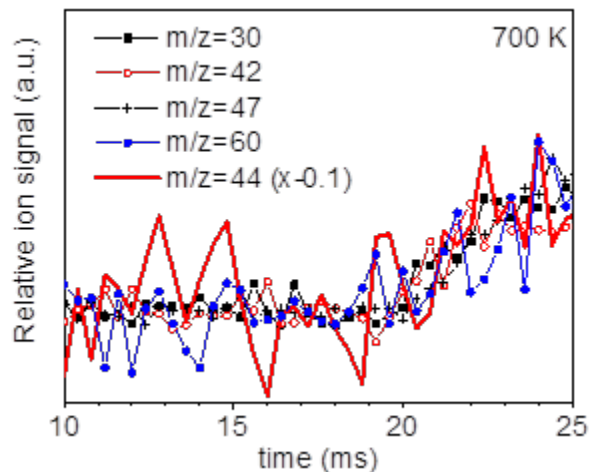


Figure 5-4- The scaled time profiles of $m/z=30$ (formaldehyde), 42 (ketene), 47 (methyl peroxy) and 60 compared to the inverted depletion rate of parent fuel, $m/z=44$ (acetaldehyde) in Cl-initiated oxidation of acetaldehyde at 700 K

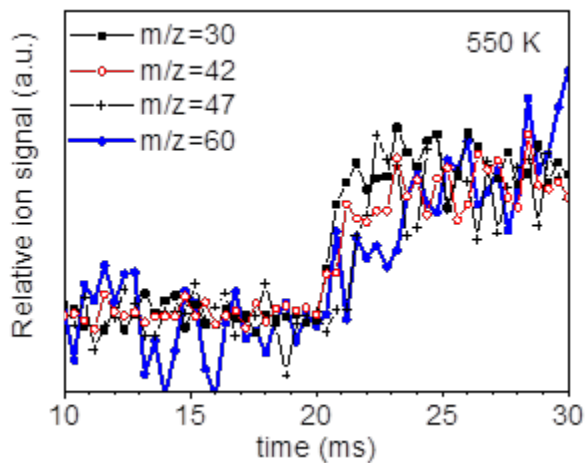
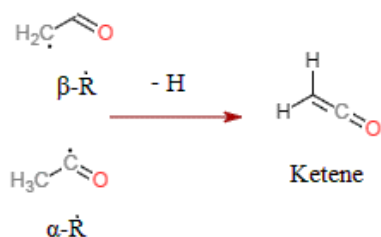
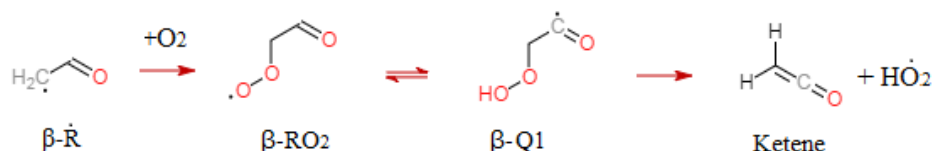


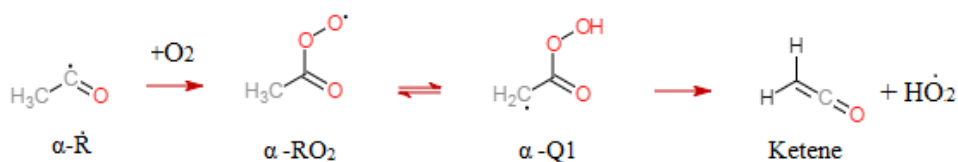
Figure 5-5- The scaled time profiles of $m/z=30$ (formaldehyde), 42 (ketene), 47 (methyl peroxy) and 60 in Cl-initiated oxidation of acetaldehyde at 550 K



Scheme 5-4- Ketene formation from radical thermal decomposition



Scheme 5-5- Ketene formation from β -R radical of acetaldehyde



Scheme 5-6- Ketene formation from α -R radical of acetaldehyde

In the low temperature region and in the presence of additional O_2 , the addition of molecular O_2 to methyl radicals generates methyl peroxy, CH_3O_2 ($m/z=47$). The competition between this reaction and radical decomposition reaction is found to be very important to obtain the overall rate and the properties of NTC region [96]. As the temperature goes up, the more methyl radical is expected to form and therefore the signal at $m/z=47$ associated with CH_3O_2 increases. The photoionization efficiency of $m/z=47$ is compared to photoionization cross section of CH_3O_2 obtained from a study on alkylperoxy radicals photoionization by Sandia National Lab [71].

A comparison of the time profiles for $m/z=30$, 42, 47, and 60 with the inverted and scaled time profile of the parent fuel ($m/z=44$) shows that the depletion of the ion signal of the

acetaldehyde is correlated with the generation of the products of $m/z=30$, 42, 47, and 60 supporting that these masses are the primary products. Figure 5-4 shows the scaled time profiles of $m/z=30$ (formaldehyde), 42 (ketene), 47 (methyl peroxy) and 60 in Cl-initiated oxidation of acetaldehyde at 700 K. The shapes of the time profiles are very similar to each other. Still it can be observed that $m/z=60$ is formed slightly delayed compared to the other masses. This delayed formation can be seen more noticeably in the time profiles comparison at 550 K which is illustrated in Figure 5-5. The signal associated with the depletion of acetaldehyde is hidden for better visibility.

Since the photoionization profiles of the primary products represent the averaged values of the signal over a specified range of time, comparing the contribution of two products of i and j with different m/z reflects the averaged values of branching ratios ($c_i^{(t,t+\Delta t)} / c_j^{(t,t+\Delta t)}$). The averaged values of branching ratio can be used instead of the one at each kinetic time provided that the shapes of the time profiles for the products of our interest are identical (which is the case for this study):

$$\frac{c_i^{(t,t+\Delta t)}}{c_j^{(t,t+\Delta t)}} = \frac{c_i(t)}{c_j(t)} \quad (5-1)$$

The quantification of the products yields is performed relative to formaldehyde as the major product. Ketene yield relative to formaldehyde is found to be 0.12 at 700K and 550K. Methyl peroxy yield relative to formaldehyde is found to be 0.02 (700 K) and 0.01 (550 K). The temperature dependent product yield at specific m/z is calculated by the following equation:

$$\frac{c_{700K}(t)}{c_{550K}(t)} = \frac{I_{700K}(t)}{I_{550K}(t)} \times \frac{I_{mean,550K}^{(t,t+\Delta t)}}{I_{mean,700K}^{(t,t+\Delta t)}} \times \frac{C_{700K}^{(t,t+\Delta t)}}{C_{550K}^{(t,t+\Delta t)}} \quad (5-2)$$

Where the temperature dependent averaged concentration ratio, $\frac{C_{700K}^{(t,t+\Delta t)}}{C_{550K}^{(t,t+\Delta t)}}$ is found from the comparison of photoionization spectrum for the mass of our interest with the corresponding standard PIE according to the equation:

$$S_{m/z}^{(t,t+\Delta t)}(E) = \varphi \alpha_{m/z} \sum_i c_i^{(t,t+\Delta t)} \sigma_i(E) \quad (5-3)$$

The mass discrimination factor α is cancelled out as the calculation is at a specific m/z. Also the standard photoionization cross section $\sigma(E)$ is cancelled out and therefore we will use the following expression:

$$\frac{C_{700K}^{(t,t+\Delta t)}}{C_{550K}^{(t,t+\Delta t)}} = \frac{S_{700K}^{(t,t+\Delta t)}}{S_{550K}^{(t,t+\Delta t)}} \quad (5-4)$$

Thus the temperature dependent product yield is rewritten as:

$$\frac{c_{700K}(t)}{c_{550K}(t)} = \frac{I_{700K}(t)}{I_{550K}(t)} \times \frac{I_{mean,550K}^{(t,t+\Delta t)}}{I_{mean,700K}^{(t,t+\Delta t)}} \times \frac{S_{700K}^{(t,t+\Delta t)}}{S_{550K}^{(t,t+\Delta t)}} \quad (5-5)$$

The temperature dependent time profiles of each product is shown in Figure 5-6. Formaldehyde (m/z=30), ketene (m/z=42) and methyl peroxy (m/z=47) are the products which increase monotonically with temperature while m/z=60 reaches to maximum at lower temperature (550 K).

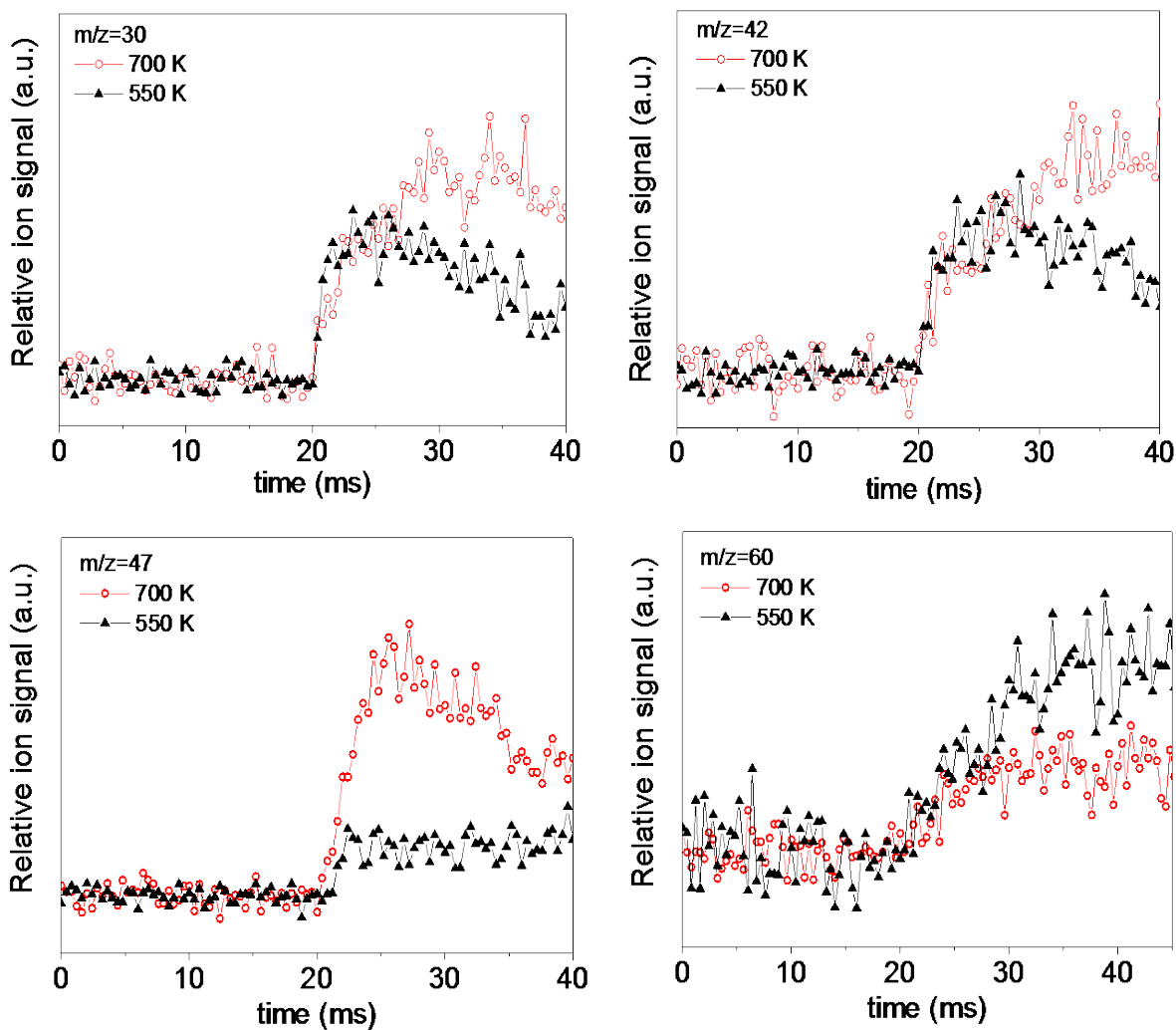


Figure 5-6- Temperature dependent time profiles of the products in Cl-initiated oxidation of acetaldehyde

5.3.2 Products and pathways in propanal low temperature Cl-initiated oxidation

The reaction of Cl atoms with propanal can result in formation of three different radicals (α -R, α' -R and β -R seen in Scheme 5-8) and therefore lead to a more complicated oxidation chemistry in comparison to acetaldehyde. As mentioned earlier, each of the radicals can either decompose or react with O₂ which is the typical pathways in low temperature oxidation. The formation of α' -R

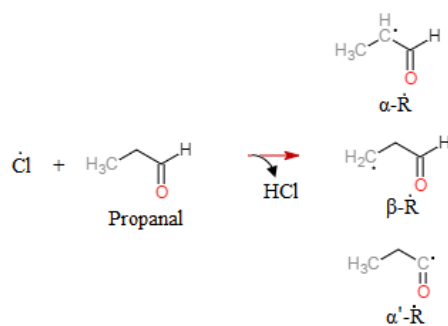
is the most possible as the reactivity of the carbonyl side of the molecule is higher than the other possible sites for H atom abstraction. The difference mass spectra for Cl-initiated oxidation of propanal is obtained by integration for a time period up to 45 ms, shown in Figure 5-7 for 550 and 700K. The negative signal (cut short) at $m/z=58$ is associated with propanal removal. The major ion signals are observed at $m/z=28, 30, 44$ and 74 as well as smaller signals at $m/z=42$ and 56 .

The most intense peak is at $m/z=44$ which corresponds to acetaldehyde due to the matched photoionization spectra with acetaldehyde standard PIE shown in Figure 5-8. α' -R can either go through decomposition and form ethyl radical (C_2H_5) and CO or it can react with O_2 and form α' - RO_2 . The ethyl radical from α' -R can also participate in reaction with O_2 and form acetaldehyde. The pathway of formation of acetaldehyde is shown in Scheme 5-9. The intermediate $C_2H_5O_2$ is also generated from the reaction of C_2H_5 with O_2 . A very small portion of that may decompose to acetaldehyde and OH radical. Through HO_2 elimination, the major portion of $C_2H_5O_2$ generates substantial amount of ethylene (C_2H_4) which is assigned to the major signal at $m/z=28$ according to its perfectly matched PIE with the standard photoionization spectrum (Figure 5-8). Alternatively, ethylene is formed as a result of thermal decomposition of β -R to formyl radical and ethylene. Along with CO_2 and OH radical, ethylene is also the co-product of decomposition of QOOH which is isomerized to α' - RO_2 . The formation of C_2H_4 from propanal oxidation is shown in Scheme 5-11. According to the scheme, ethylene is generated through the competition between the two propanal radicals; namely β -R thermal decomposition channel as well as C_2H_5 reaction with O_2 from α' -R decomposition reactions along with minor contribution of α' - RO_2+O_2 channel. The time-resolved profiles of the products will give an insight on which channel is more dominant.

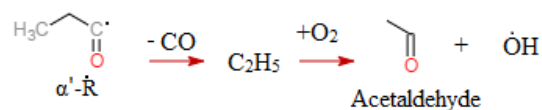
Furthermore, β -scission of α' -R results in the formation of methyl radical and ketene. This pathway has minor contribution comparing to the aforementioned pathways for α' -R, but still can be verified by the weak signal at $m/z=42$. Alternatively, ketene is formed along with formaldehyde and OH radical via β -RO₂ channel. Formaldehyde ion signal appears at $m/z=30$. The corresponding pathway is illustrated in Scheme 5-10.

Due to their kinetic, aldehydes provide source of alkyl radicals which hence react with O₂ in low temperature region and form the primary products and intermediates [96]. The ion signal at $m/z=74$ appears in the mass spectra is assigned to a data fit from ethyl formate and methyl acetate (C₃H₆O₂). However, another possible product is propanoic acid (C₃H₆O₂) which has ionization energy of 10.44 eV (the same as the PIE for $m/z=74$ in Figure 5-8). The fuel radical α' -R reaction with OH radical forms propanoic acid. Considering ethyl formate and methyl acetate as the only two contributions for $m/z=74$, the ratio of ethyl formate : methyl acetate is obtained to be 3.2:1.

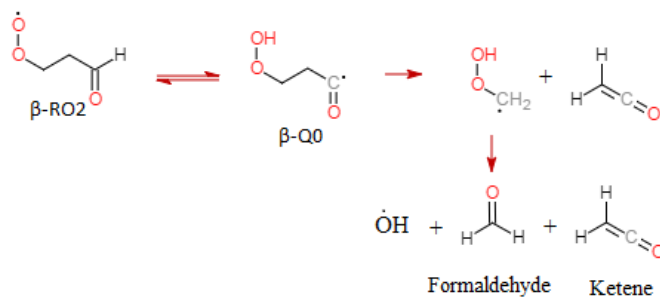
By looking at the latest kinetic mechanism for propanal, allylhydroperoxide (C₃H₅OOH) is one of the considered species which is generated through the reaction of n-propyl radical (n-C₃H₇) with O₂ [83]. The produced n-C₃H₇O₂ isomerizes with C₃H₆OOH and reacts with O₂ again. HO₂ elimination from resulting species forms allylhydroperoxide, a-C₃H₅OOH ($m/z=74$), which decomposes to C₃H₅O and OH radical accordingly. The ionization energy for allylhydroperoxide is calculated to be 9.52 eV [97] which is different from the onset of the $m/z=74$ signal (~10.45 eV).



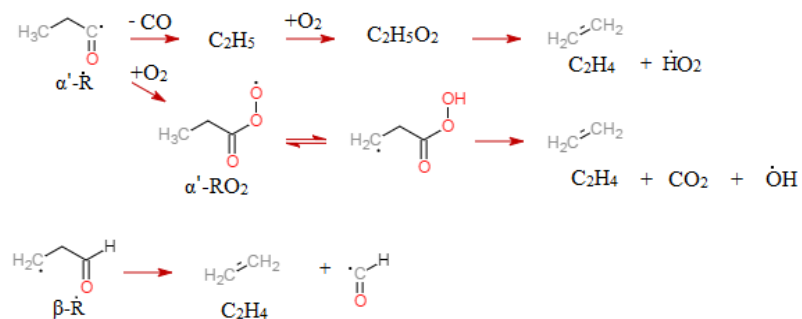
Scheme 5-7- Propanal radicals



Scheme 5-8- Acetaldehyde formation pathway from propanal oxidation



Scheme 5-9- Formaldehyde and ketene formation pathway from propanal oxidation



Scheme 5-10- Formation of C₂H₄ from propanal oxidation

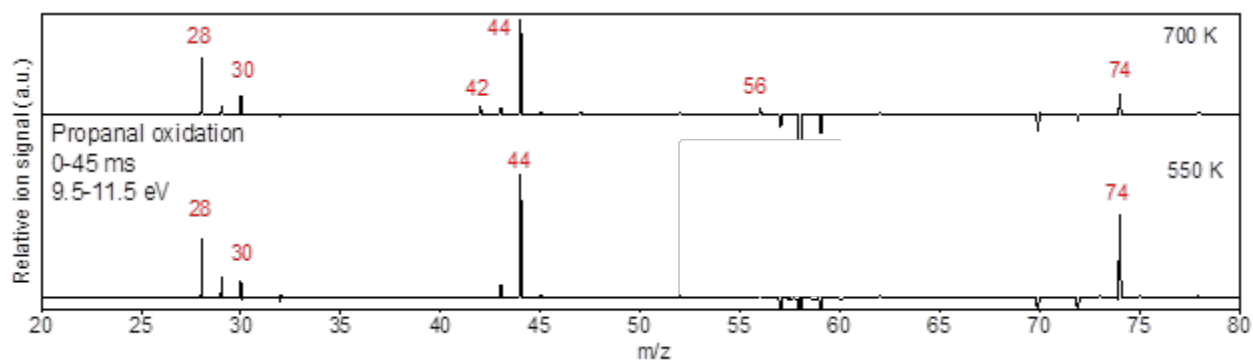


Figure 5-7- Cl-initiated oxidation of Propanal mass spectra at 550 K and 700 K, obtained by integration over the photon energy 9.5-11.5 eV and the kinetic times until 25 ms after the laser photolysis

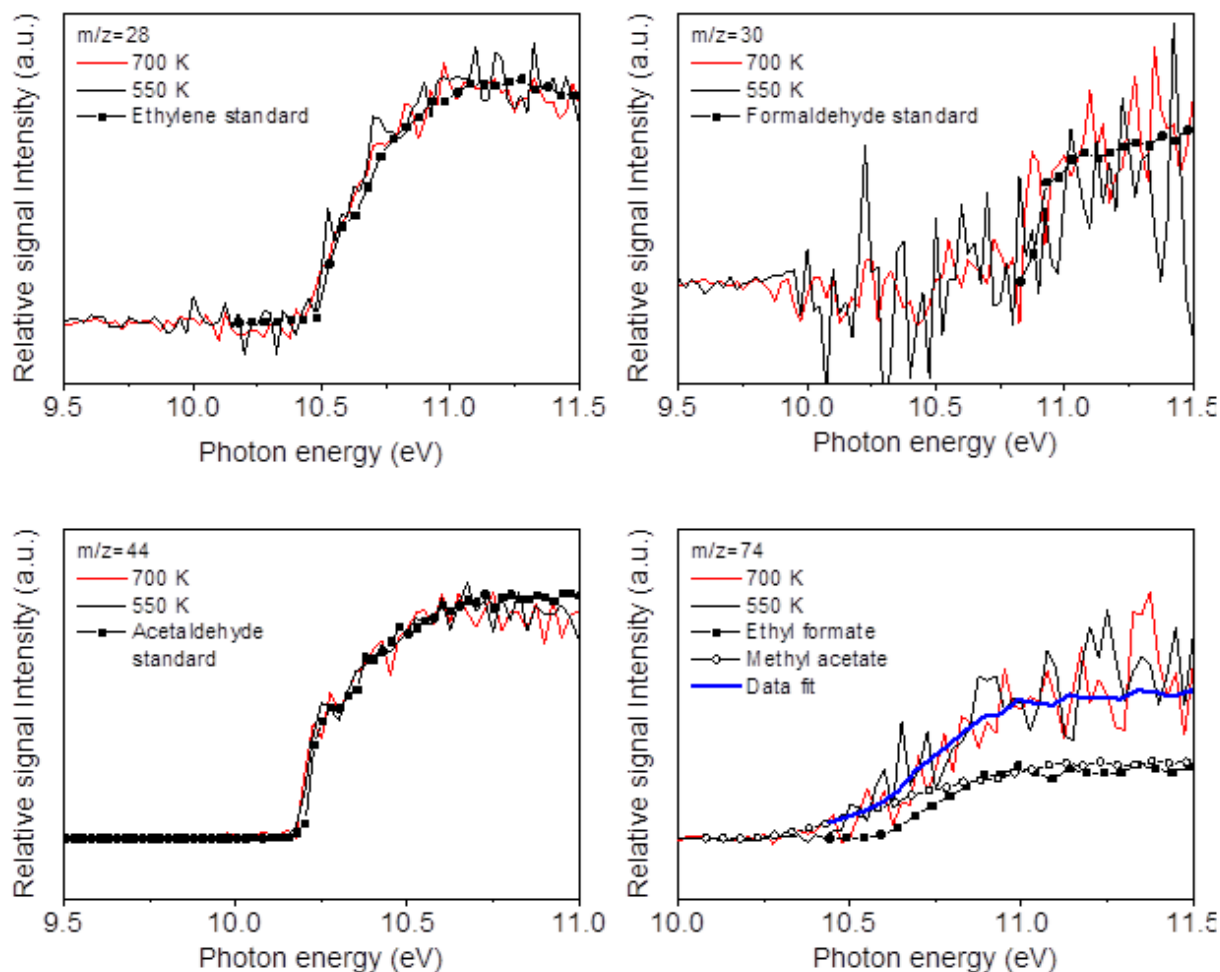


Figure 5-8- Primary products photoionization spectra of propanal Cl-initiated oxidation at 550 and 700 K compared to the corresponding standard PIE

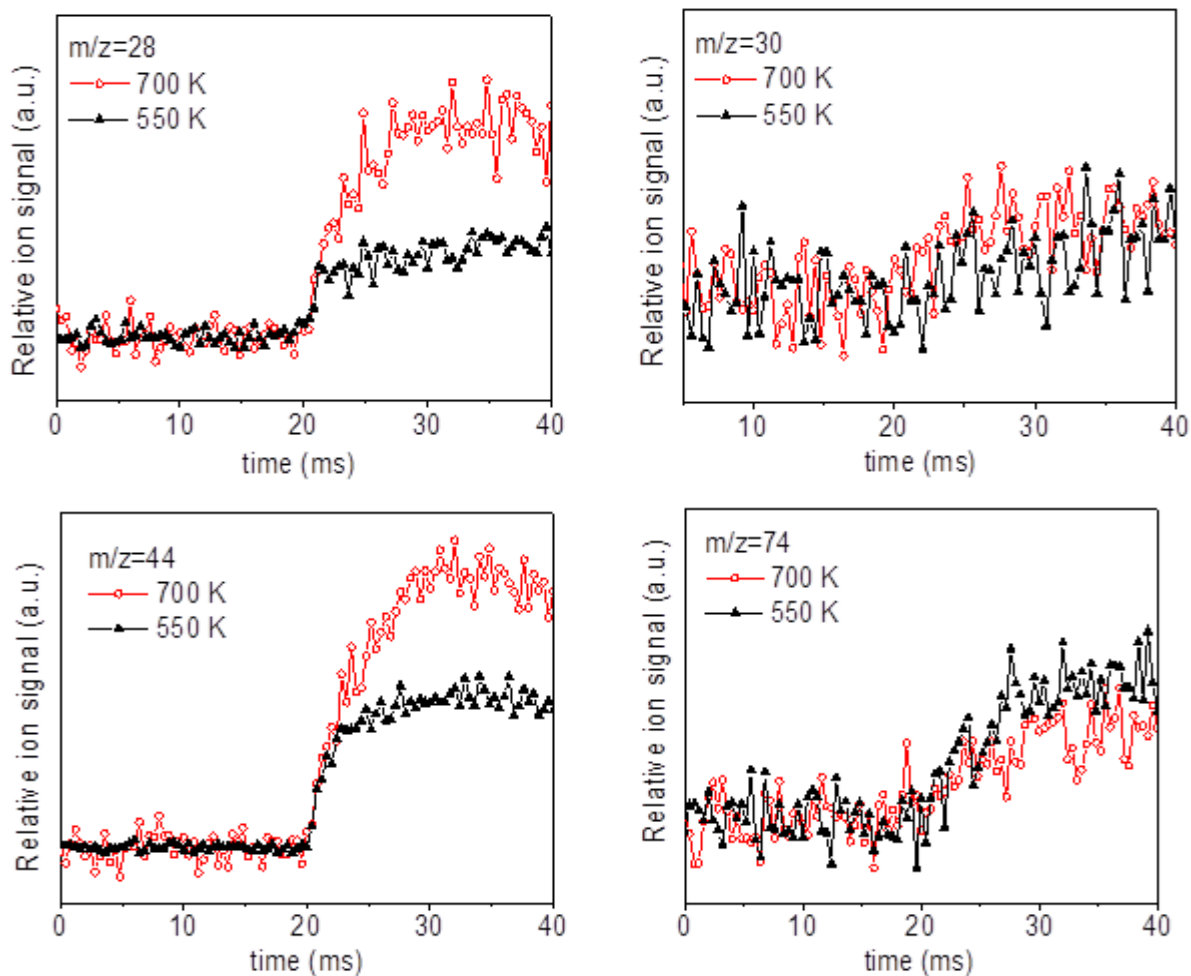


Figure 5-9- Temperature dependent time profiles of the products in Cl-initiated oxidation of propanal

Figure 5-9 shows the temperature dependent time profiles of the products from propanal Cl-initiated oxidation. The temperature dependent product yield is calculated for each temperature at the m/z of our interest based on the discussion in the previous section.

As the temperature goes up, ethylene is expected to form more from the thermal decomposition which can be observed in Figure 5-9. The ion signal intensity of ethylene, acetaldehyde and formaldehyde increase monotonically with temperature, whereas the intensity in time-resolved profile of $m/z=74$ decreases as the temperature increases from 550 K to 700 K.

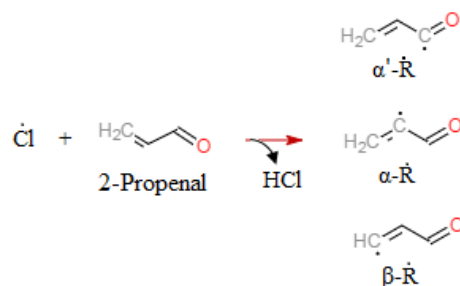
Table 5-1- The product yield relative to acetaldehyde as the major product in propanal Cl-initiated oxidation at 550 and 700 K

m/z	Chemical Formula	Product	Product yield relative to acetaldehyde	
			550 K	700 K
28	C ₂ H ₄	Ethylene	0.68	0.92
30	CH ₂ O	Formaldehyde	0.29	0.35
44	CH ₃ CHO	Acetaldehyde	1.0	1.0
74	C ₃ H ₆ O ₂	Ethyl formate	N/A	N/A
		Methyl acetate		
		Propanoic acid		

The product yield for the Ethylene and formaldehyde are calculated relative to acetaldehyde as the major product in propanal Cl-initiated oxidation. The calculations are based on the discussion in the previous section and the products yields are given at 550 and 700 K in Table 5-1.

5.3.3 Products and pathways in 2-propenal low temperature Cl-initiated oxidation

Acrolein or 2-propenal reaction with Cl results in formation of three different radicals based on the abstracted H atom site, shown in Scheme 5-12. The difference mass spectra as illustrated in Figure 5-10 shows the products ion signal peaks at m/z=30, 42, 44 and 78 with negative intensity signals at m/z=56 (2-propenal, the parent fuel) and 28 (a dissociative fraction of the parent fuel).



Scheme 5-11- Acrolein (2-propenal) radicals

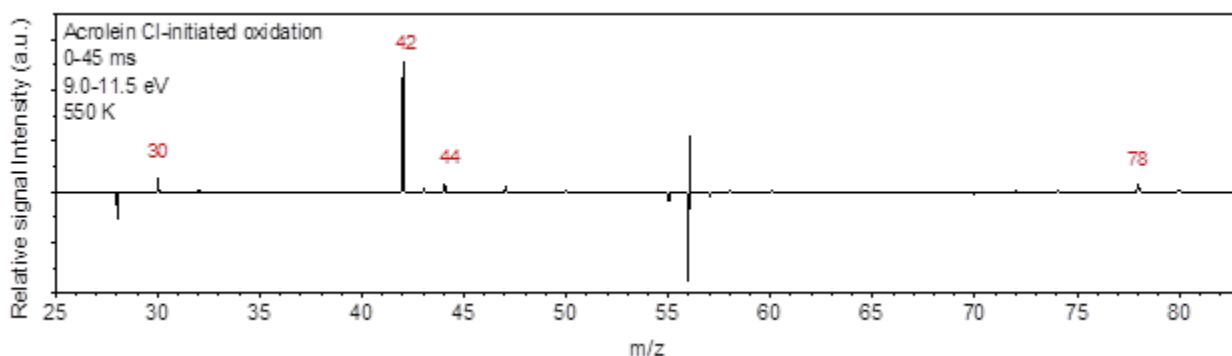


Figure 5-10- Cl-initiated oxidation mass spectra of 2-propenal at 550 K obtained by integration over the photon energy 9.5-11.5 eV and the kinetic times until 25 ms after the laser photolysis

The most intense signal is at $m/z=42$ which is found to be ketene according to the comparison to the corresponding standard photoionization spectrum. The H abstraction reaction from 2-propenal by H, OH, O, CH₃ and HO₂ generates α' -R (C₂H₃CO). The C₂H₃CO radical decomposition leads to formation of CO and C₂H₃. The latter is the source of ketene and formaldehyde formation in 2-propenal oxidation. The reaction of C₂H₃ with O₂ generates formaldehyde with HCO. In another channel for this reaction, CH₂CHO is formed with atomic oxygen. CH₂CHO generates ketene (CH₂CO) through decomposition. The photoionization spectra of $m/z=42$ and 30 for 2-propenal Cl-initiated oxidation at 550 K are compared to the photoionization cross section of ketene and formaldehyde respectively and illustrated in Figure 5-11. The product yield for formaldehyde relative to ketene is calculated to be 0.82 at 550 K.

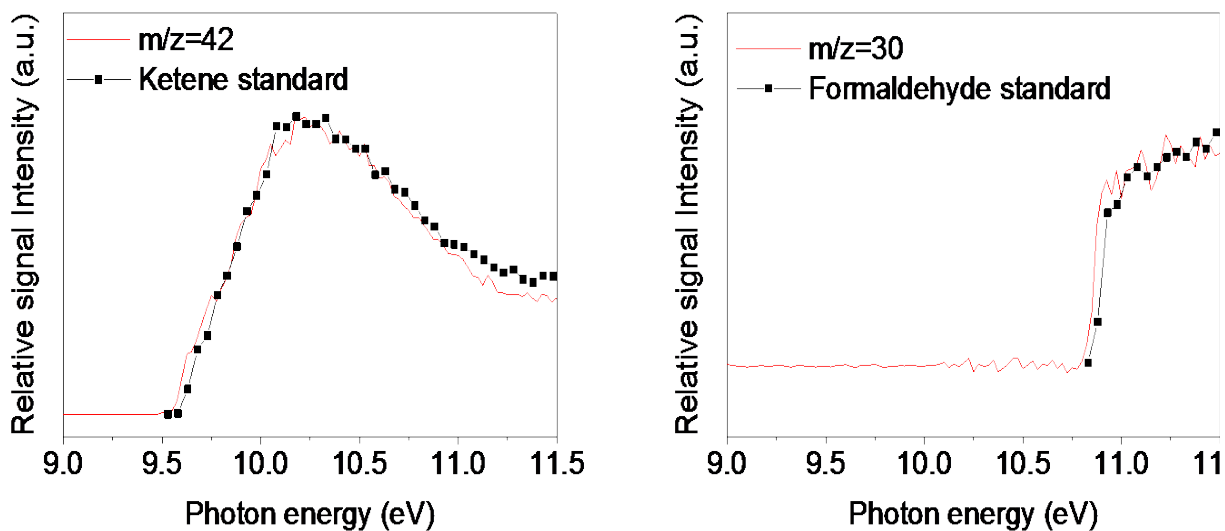


Figure 5-11- Primary products photoionization spectra of 2-propenal Cl-initiated oxidation at 550 compared to the corresponding standard PIE

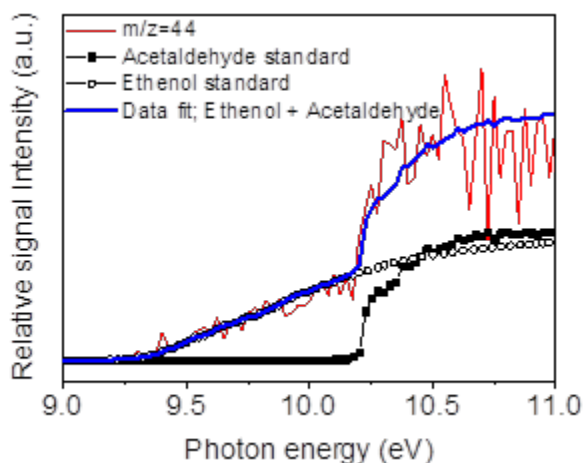


Figure 5-12- Comparison of the photoionization spectra of the peak at $m/z=44$ with the corresponding standard PIE of ethenol and acetaldehyde, along with the data fit, in 2-propenal Cl-initiated oxidation at 550

The signal peak at $m/z=44$ is assigned to ethenol (IE=9.3 eV) and acetaldehyde (IE=10.22 eV). As it can be seen in Figure 5-12, the photoionization spectra which has an onset at ~9.3 eV is matched to the photoionization cross sections of ethenol following by another rise at ~10.2 eV

which is due to the acetaldehyde contribution. A data fit to the trend based on both contributions returns the ratio of acetaldehyde to ethenol of 1.2:1.

The signal peak at $m/z=78$ is a chlorinated species which has a corresponding isotope peak at $m/z=80$ which has the isotope ratio of 3.12 in agreement with $^{35}\text{Cl}/^{37}\text{Cl}$ [98]. According to the ionization energy of ~ 10.5 eV, the likely species are acetyl chloride (IE=10.82 eV) or chloroacetaldehyde (IE=10.61 eV).

5.4 Conclusion

Products from the Cl-initiated oxidation of three aldehydes namely acetaldehyde, propanal and 2-propanal at low temperature (550-700 K) at low pressure (~ 8 Torr) were identified and computed using multiplexed synchrotron photoionization mass spectroscopy and the dominant pathways were detected.

In acetaldehyde Cl-initiated oxidation, the primary products are found to be formaldehyde ($m/z=30$), ketene ($m/z=42$) and methyl peroxy ($m/z=47$). The products are identified by comparison between their photoionization spectra with the standard photoionization cross sections. Ketene is generated within both α -R and β -R decomposition channels. Also it is formed through α -R+O₂ and β -R+O₂ via HO₂ elimination from the peroxy radicals. The temperature dependent time resolved profiles for the primary products have been presented at 550 and 700 K.

In propanal Cl-initiated oxidation, ethylene ($m/z=28$), formaldehyde ($m/z=30$) and acetaldehyde ($m/z=44$) are the primary products. α' -R is the radical which is most possible to form due to the higher reactivity of the carbonyl side of the molecule. The decomposition of α' -R to ethyl radical followed by the reaction with O₂ produces acetaldehyde. α' -R is also involved in the

formation of ethylene through decomposition as well as its reaction with O₂. Ketene is formed along with formaldehyde and OH radical via β-RO₂ channel isomerized to QOOH. The product yields relative to acetaldehyde as the major product in propanal Cl-initiated oxidation at 550 and 700 K are calculated.

Acrolein (2-propenal) Cl-initiated oxidation at 550 K reveals the primary products as formaldehyde (m/z=30), ketene (m/z=42) and acetaldehyde and ethenol (m/z=44). α'-R decomposition leads to formation of C₂H₃ which is the source of ketene and formaldehyde formation via its reaction with O₂.

The first step for developing a comprehensive low temperature submechanism for aldehydes oxidation is detection and quantification of the primary products which has been performed in this study. The detailed analysis of the experimental data can be verified by the quantum chemical calculations at high level of theory to find out the potential energy surfaces for the important reactions.

CHAPTER 6: SHOCK TUBE IGNITION AND PYROLYSIS OF DIPK

6.1 Introduction

A shock tube is an ideal tool to study a test gas of known initial temperature and pressure which has a chemical process specifically at high temperatures. A typical shock tube setup consists of driver and driven sections which are referring to high and low pressure sides, respectively. These two regions are separated by a diaphragm which creates a shock wave as a result of its rupture. For a shock tube experiment, helium, hydrogen and generally low density gases are used for the driver side. The gas mixture of interest is in driven side. A shock wave is produced by increasing the pressure in the driver section until the diaphragm bursts. As the diaphragm ruptures, a normal shock wave moves through the driven side such that the gas temperature and pressure increase. At the same time an expansion wave moves toward the driver section. For more details refer to [99].

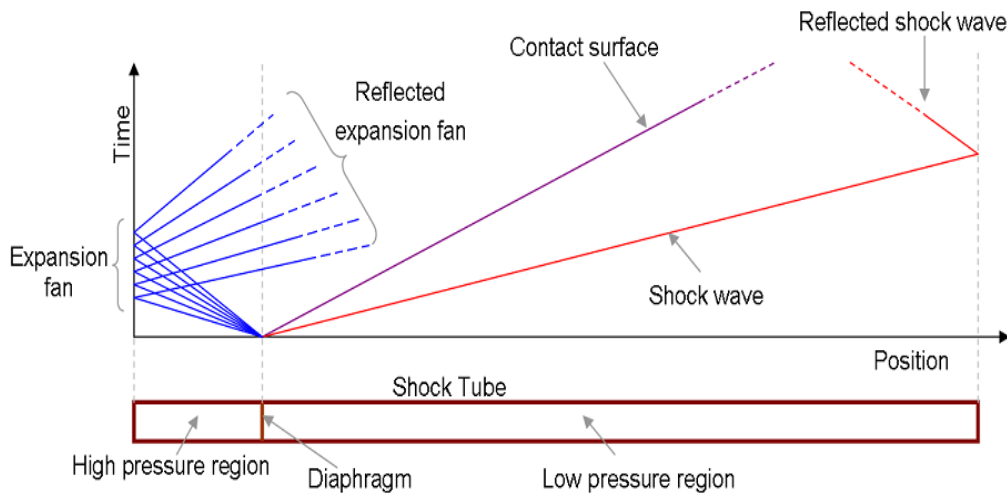


Figure 6-1- An ideal shock tube with different waves formed after diaphragm ruptures [100]

The autoignition characteristics of the mixture of fuel and oxidizer are determined by ignition delay time. It provides the understanding of the ignition mechanism, the chemical reaction pathway analysis, and verifying the kinetic models [101]. One important application of shock tube is the ignition delay time measurement for a mixture of interest. The ignition delay time is described as the interval between the arrival of the reflected shock wave and the initiation of the ignition which is determined either from the pressure trace or from the time history of an intermediate combustion species such as CH or OH [102-104].

The equation of radiative heat transfer across a slab of gas of width L is given by the Beer-Lambert law:

$$\alpha_i(\lambda, T, P) = -\ln\left(\frac{I}{I_o}\right)_\lambda = \beta_\lambda PL = \sigma_i(\lambda, T, P)n_iL \quad (6-1)$$

Where I_o and I are the intensities of the incident and transmitted radiant energy respectively. α_i is absorbance of gas species i ; σ_i is the absorption cross section; n_i is the number density of the absorbing species i , L is the path length and β_λ is the absorption coefficient. The number density of the species can be related to the pressure and temperature through the ideal gas law as follows:

$$\alpha_i(\lambda, T, P) = \sigma_i(\lambda, T, P) \frac{P}{RT} \chi_i L \quad (6-2)$$

where X_i is the mole fraction [99].

The Beer-Lambert law can be directly used for measurements of a single species, but there is often interference in the form of absorption from other species which is described as follows:

$$-\ln\left(\frac{I}{I_o}\right)_\lambda = \alpha_i + \alpha_{\text{interference}} \quad (6-3)$$

In order to eliminate the interference, a peak-valley wavelength absorption scheme is used which refers to subtraction of the two transmission measurements obtained at two different wavelengths.

$$\left[-\ln\left(\frac{I}{I_o}\right)_\lambda\right]_{\text{peak}} - \left[-\ln\left(\frac{I}{I_o}\right)_\lambda\right]_{\text{valley}} = (\alpha_i + \alpha_{\text{interference}})_{\text{peak}} - (\alpha_i + \alpha_{\text{interference}})_{\text{valley}} \quad (6-4)$$

Therefore, the effects of the interfering species are canceled out and only the absorbing species remains:

$$\left[-\ln\left(\frac{I}{I_o}\right)_\lambda\right]_{\text{peak}} - \left[-\ln\left(\frac{I}{I_o}\right)_\lambda\right]_{\text{valley}} \approx \alpha_{i,\text{peak}} - \alpha_{i,\text{valley}} \quad (6-5)$$

Substituting for α_i and solving for X_i , the mole fraction of the absorbing species will be related to the measured differential absorbance:

$$\chi_i = \frac{\alpha_{i,\text{peak}} - \alpha_{i,\text{valley}}}{(\sigma_{i,\text{peak}} - \sigma_{i,\text{valley}})P_{\text{tot}}L} \quad (6-6)$$

The cross section $\sigma(\lambda, T, P)$ can be typically obtained from databases (HITRAN [105], PNNL [99], NIST [95], etc.)

In the detailed kinetic mechanism study of DIPK developed by Allen et. al [6], the combustion of DIPK was investigated in a rapid compression machine. The observed experimental data showed a discrepancy comparing to the model. The model tends to predict shorter ignition delay time with the NTC region shifted about 80 K. The ignition delay times at higher temperatures were determined using a shock tube at Aachen's facilities for stoichiometric DIPK-air mixtures. However, due to the limited operation time of 1-5 ms, only two experimental data points are

measured within the measurable residence times. The shock tube and RCM experimental data are compared to the simulation in Figure 6-2.

In this chapter, the experimental results from a series of shock tube experiments on DIPK pyrolysis and oxidation are described, including ignition delay times and species concentration time histories. The kinetic model of DIPK reactions is compared to the experimental data.

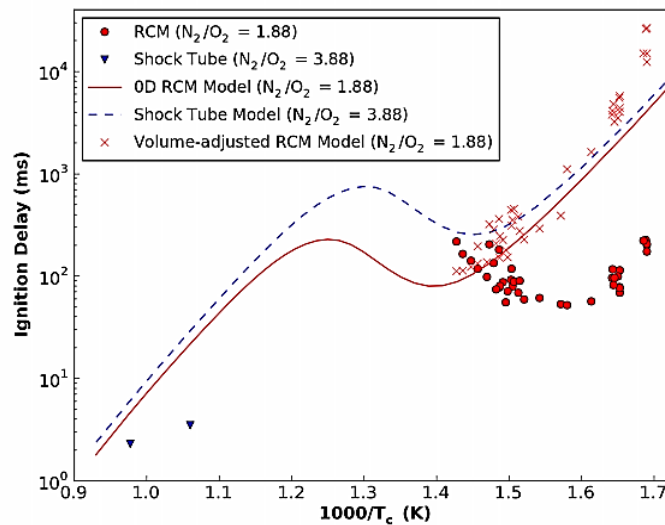


Figure 6-2- Rapid compression machine and shock tube experimental and modeled ignition delays (Allen et. al [6])

6.2 Experimental setup

6.2.1 UCF shock tube facility

The experiments were carried out in UCF shock tube facility including driver and driven section, tee section and test section. The shock tube cross section inside and outside diameter are 14cm and 16.8 cm, respectively. The driver (4.88 m long) and driven (8.54 m long) sections are separated by a diaphragm by a proper thickness which determines the driver and driven sections

pressure ratios $[P_4 / P_1]$. As a result, shock waves at different Mach numbers can be obtained. For this work, polycarbonate diaphragms of 0.001 and 0.003 inch are used. The tee section of the shock tube is used for vacuuming the driven section [99].

The test section of the shock tube is located at the end wall of the driven section of the shock tube providing 8 ports for optical access or for other sensors such as the pressure transducers. A piezoelectric pressure transducer (Kisler 603B1) located at 2cm from the end section of the shock tube is used to obtain the pressure trace during the experiment. The ignition delay time is determined by the pressure profile. It is also important to consider sufficient amount of test time to determine the ignition delay time. The shock tube simulation program KASIMIR [106, 107] is used to estimate the test time based on the initial conditions and the gas composition in the driver and driven sections. The temperature and pressure behind the reflected shock wave were calculated based on the derivation in [108]. The shock tube was evacuated to a pressure of $<2 \times 10^{-5}$ Torr before each experiment. Gas mixtures were prepared in a mixing tank, a stainless steel storage cylinder, resting over 12 hours prior to the shock test [99].

6.3 Results and discussion

6.3.1 Shock tube experiments

Experiments were performed to measure the methane time history during the pyrolysis of DIPK. One of the main issues was that DIPK is in a liquid state at STP (standard temperature and pressure) and has a low vapor pressure. In order to perform experiments in the UCF shocktube, the partial pressure of the liquid fuel must never be greater than the vapor pressure as this ensures homogeneity of the mixture and prevents any condensation on the walls. A quick experiment was

performed with DIPK to determine the vapor pressure by measuring the pressure of a system containing DIPK while vacuuming. As a result it was determined that the vapor pressure for DIPK was 26 torr, a sufficiently high pressure for the shock tube but not the mixing tank. As a result, the mixing tank was heated to 150 °C using a custom built heating jacket (more details in the papers) to prevent condensation.

Before doing the experiments, simulations were performed in the shock tube simulation program KASIMIR3 [109]. This program uses custom gas files and the ideal shock relations to simulate a shock tube without any non-idealities. This can be used to determine the theoretical temperature and guide the experiments.

Both sections of the shock tube are evacuated before the experiments are performed. The driver side is evacuated with a mechanical pump to as low as possible. The driven side was evacuated using a combination of a mechanical pump with a turbo-molecular vacuum pump. The pressure inside the driven side must reach at least 50 μ torr before any experiment can begin (can be as low as 7 μ torr overnight). The mixture is added using a manifold that connects the mixing tank and shock tube. The manifold is connected to two baratrons (100 torr and 1000 torr ranges) to measure the internal pressure while filling. Typical filling pressures are between 5 and 40 torr. After the mixture has been added to the desired pressure based on KASIMIR and previous experiments, the driver side is slowly filled until the diaphragm ruptures. This causes a shockwave to form from the pressure discontinuity and propels down the shock tube.

The speed of the shockwave is measured using 5 PCB pressure transducers spaced along the end section. The time between pressure peaks is recorded using 4 timer-counters. These times are then inputted into the FROSH computer code. FROSH (chemically frozen shock code)

determines the end wall conditions based on the gases, end wall velocity, and initial pressure. The end wall velocity is measured from the timer-counters to determine the attenuation of the shockwave. An uncertainty analysis has been performed starting from the measured times. Using a linear-regression analysis (Bevington and Robinson) described in Herbon's dissertation from Stanford, the average uncertainty for the temperature and pressure are 2.5% and 1.5%, respectively.

The raw data (kistler voltage, CH* emission, and laser intensity) was taken the pressure and absorption from the raw data and the FROSH results were calculated. The CH* emissions are normalized based on the peak value from the run. For the absorption value, it is then combined with its counterpart in the peak-valley pair and the methane concentration in ppm is determined.

6.3.2 Laser-absorption measurement

A continuous wave distributed feedback inter-band cascade laser (Nanoplus DFB ICL) was set up and used for measuring methane (CH₄) concentration time-histories. The wavelength was chosen as 3403.4 nm and the peak-minus-valley absorption scheme is used to obtain the time

history of methane. Pyun et al. [12, 110, 111] showed that many hydrocarbons have constant absorption cross section in the close vicinity of 3403.4 nm [99].

In order to obtain the concentration time-histories of Methane absorption cross section is required for obtaining the concentration time-histories. Figure 6-3 shows the CH₄ absorption cross section values measured for the temperature range of 1200-2000 K at three different wavelengths.

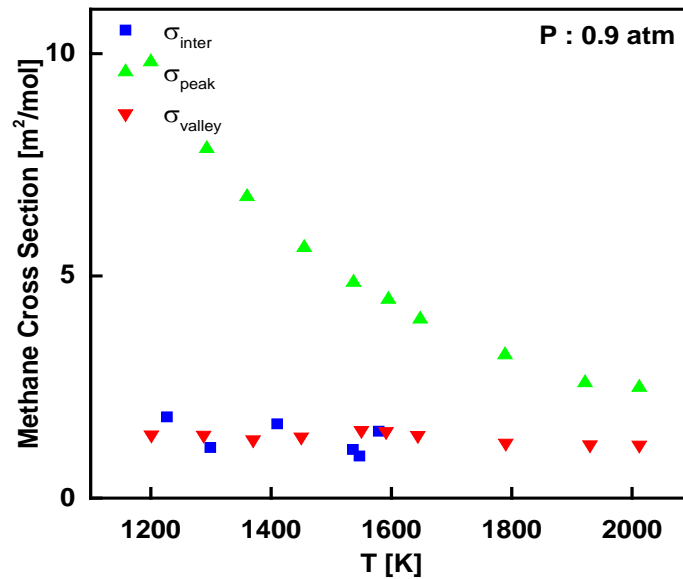


Figure 6-3- Methane Absorption Cross-section at each wavelength [99]

6.3.3 DIPK pyrolysis

The mixture for pyrolysis was prepared with 2% DIPK in argon in the temperature range of 1000-1500 K and atmospheric pressure. Methane concentration time histories for 2% DIPK pyrolysis in Argon at 1300 K and 1400 K are illustrated in and respectively. The results are

compared to the simulation using the original DIPK reaction mechanism by Allen et al. The discrepancy between the model and experiment is more significant at 1300 K.

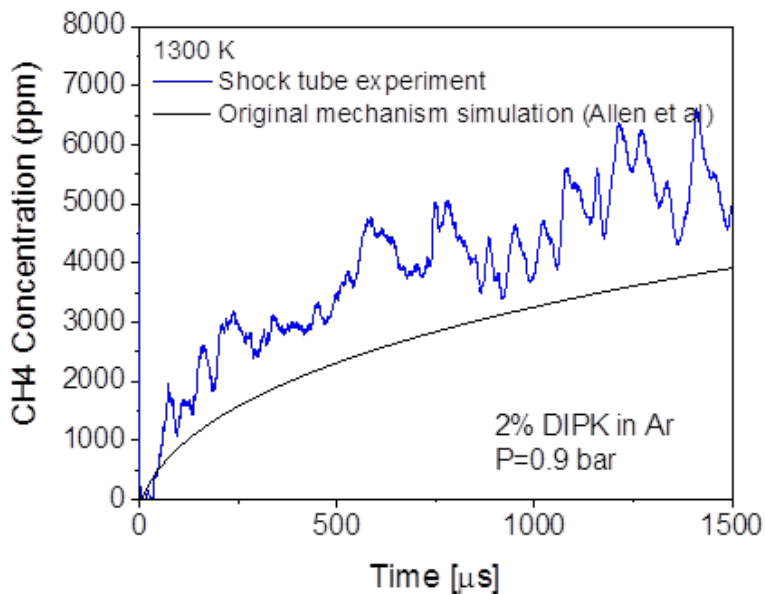


Figure 6-4- Methane Time history for 2% DIPK pyrolysis in Ar at 1300 K

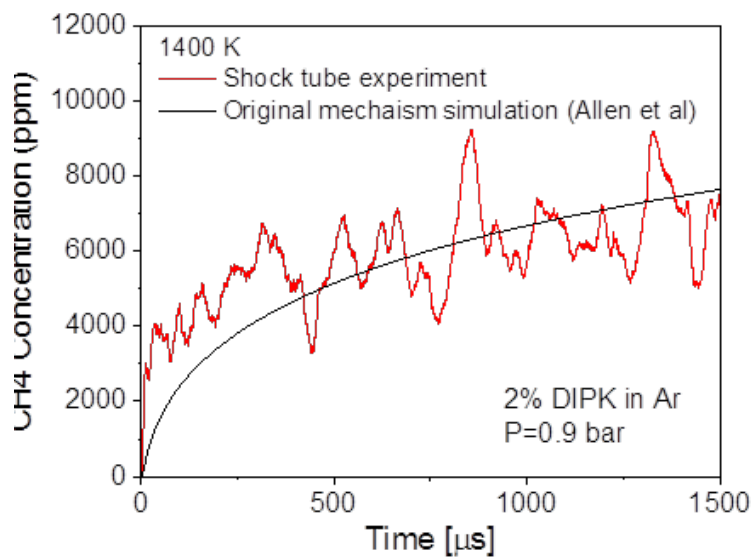


Figure 6-5- Methane Time history for 2% DIPK pyrolysis in Ar at 1400 K

6.3.4 DIPK oxidation

The stoichiometric mixture for DIPK oxidation was prepared with 2% DIPK in Oxygen and Argon. The temperature range is considered to be 1000-1500 K with the atmospheric pressure. There are several methods to measure the ignition delay time. One method is to determine the location of the peak and use that value. Another way is to use the halfway point to the peak. The best method (although it has its disadvantages) is to determine the tangent line at the 50% mark and to determine when the tangent line crosses the baseline. This method produces the smallest ignition delay time but also the hardest to measure the uncertainty. The zero time value is determined by determining the midpoint in the pressure trace for the reflected shockwave. The ignition delay time is the difference between the two values. DIPK experimental ignition delay time data for stoichiometric mixture of 2% DIPK in 20% O₂ and 78% Ar at 0.9 bar is shown in Figure 6-6.

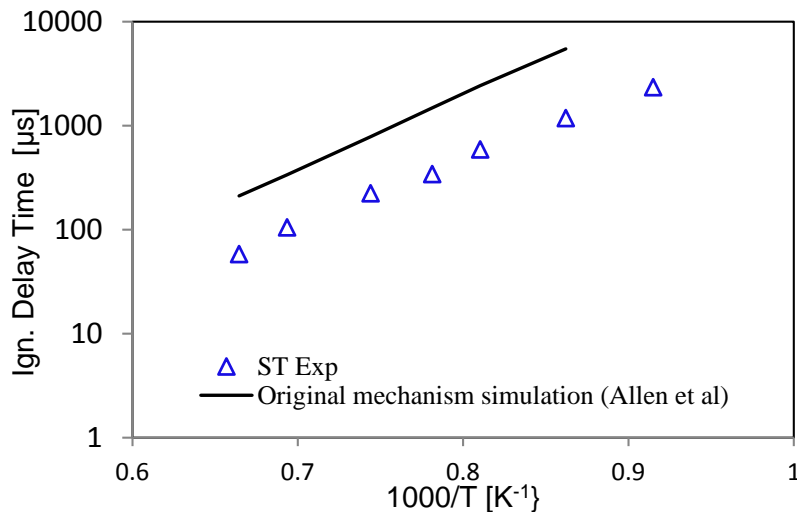


Figure 6-6- DIPK experimental ignition delay time data for stoichiometric mixture of 2% DIPK in 20% O₂ and 78% Ar at 0.9 bar compared to the original model for DIPK (Allen et al)

Table 6-1- DIPK ignition delay time

Temperature	1000/T	Ign. Delay Time (100%) μs	Ign. Delay Time (50%) μs
1093	0.91491	2340	2330
1160	0.86207	1179	1170
1234	0.81037	588	581
1280	0.78125	341	333
1344	0.74405	223	216
1442	0.69348	105	92
1505	0.66445	58	48

6.4 Conclusion

DIPK pyrolysis and ignition delay time measurements experiments were performed using UCF shock tube facilities. The ignition delay times were measured for the first time for 1000-1500 K temperature range. Methane concentration time histories were also measured during DIPK pyrolysis in Ar. The experimental results were compared to the original kinetic mechanism of DIPK developed by Allen et. al which shows some discrepancy, particularly at 1300 K.

In the next chapter, we will present a new kinetic mechanism for DIPK based on the calculations and modifications performed in this dissertation. The results are validated using the experimental data from shock tube.

CHAPTER 7: NEW DIPK REACTION KINETICS MECHANISM DEVELOPMENT USING THE REACTION CLASS APPROACH

7.1 Introduction

Use of biofuels, especially in automotive applications, is a growing trend due to their potential to reduce the greenhouse gas concentrations in atmosphere. Researchers have been exploring various methods - including endophytic fungal conversion of cellulose - to efficiently produce biofuels in order to decrease our dependence on fossil fuels. Di-isopropyl ketone (DIPK), 2,4-dimethyl-3-pentanone ($C_7H_{14}O$), is a prototype for biofuels produced by endophytic fungi. DIPK is a branched ketone and is a promising candidate as a biofuel to be used in new generation of combustion engine.

The sequence of steps that take place as reactant molecules are converted into products is called reaction mechanism. A reaction mechanism consists of multiple elementary processes with the species of known structure. As the experimental approach to study the kinetics of biofuels are costly and limited, developing a comprehensive reaction mechanism can help to investigate the different combustion behavior and find out how a reaction proceeds. A mechanism must display the order of bonds formation or dissociation and the rate of each elementary step [112].

The modeling of combustion phenomena is based on a comprehensive mechanism which includes details of the chemistry. In this regard, the smaller ketones such as acetone and 2-butanone have been investigated theoretically and experimentally in terms of pyrolysis, reaction rates and ignition delay time at different ranges of temperature [8, 12, 13, 113]. For the larger straight-chained and branched ketones, there are some measurements at combustion temperatures for ketone +OH reactions by Badra et al [114] using shock tube.

In order to study DIPK kinetics, the reaction class approach has been used. A detailed high temperature reaction pathway is created and reactions are classified into the important reaction classes for which the rate constants are assigned based on analogy to the similar reactions or literature recommendations. This procedure has been successfully applied in the case of butanol combustion mechanism by Sarathy et al.[22, 23]. The DIPK submechanism is then integrated into a recently published C₀-C₄ mechanism from the Galway group [24]. The corresponding thermodynamic properties for the fuel and primary fuel radical species were calculated using the THERM [20] program and rates were either estimated in comparison with similar molecules or calculated using a rate estimation software such as RMG [21].

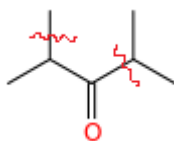
7.2 High temperature DIPK kinetic model development using reaction class approach

The kinetic model developed and discussed here is DIPK submechanism which is to be integrated to the C₄ mechanism established by NUI Galway combustion center [24]. The proposed detailed chemical kinetic submechanism includes the high temperature kinetic scheme. The oxidation mechanism is formulated and will be discussed separately for the fuel unimolecular decomposition, H-abstraction reactions by H, OH, HO₂, CH₃ and C₂H₅ radicals, decomposition and isomerization of the resulting fuel radicals. Since the aim of this study is to develop DIPK high temperature kinetic mechanism, the reactions with oxygen are not considered.

7.2.1 Unimolecular fuel decomposition reactions

The fuel unimolecular decomposition reactions are the fuel consumption reactions in high temperature region which are also denoted as initiation reactions. There are two possible classes

of unimolecular decomposition for DIPK, including bond scission and H atom elimination which result in the formation of alkyl radicals or one hydrogen atom respectively (Scheme 7-1). The rate constants are considered for recombination reactions which are listed below (R 5) to (R 8). The modified Arrhenius form rate constants of $1.93 \times 10^{14} \times T^{-0.32} s^{-1}$ for (R 5) and $9.03 \times 10^{12} \times T^{-0.35} s^{-1}$ for (R 6) are assumed as radical-radical recombination reaction rate based on Tsang recommendation for the recombination of n-propyl radical with methyl [115] and acetyl with isopropyl [116]. The rate constants for H-atom recombination with the fuel primary and tertiary radicals, namely (R 7) and (R 8) are assigned to be $1 \times 10^{14} s^{-1}$ based on the radical recombination recommended by Allara and Shaw [117].

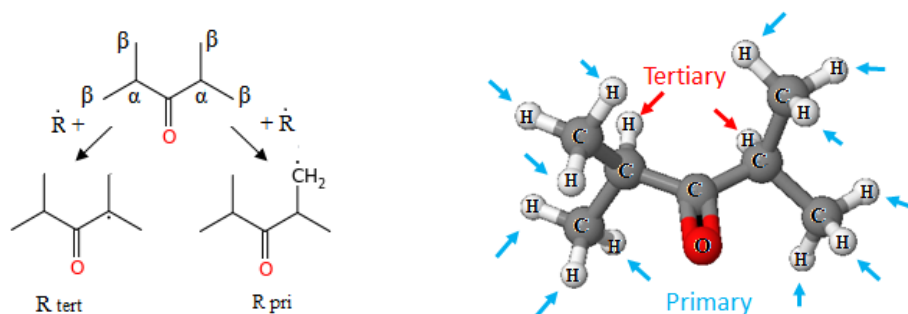


Scheme 7-1- DIPK decomposition



7.2.2 Fuel H-atom abstraction reactions

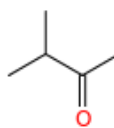
H atom abstraction takes place at primary (β) and tertiary sites (α) of DIPK which results in the formation of two different fuel radicals, denoted as R_{Pri} and R_{Tert} , (Scheme 7-2). The hydrogen atom is abstracted from DIPK by different radicals ($\dot{\text{R}}$) including H, OH, HO_2 , CH_3 and C_2H_5 .



Scheme 7-2- DIPK radicals- tertiary and primary radicals

Due to the variation of the activation energy required to dissociate the abstracted H bond, the abstraction reaction is very selective; therefore, the corresponding reaction rate depends on the site from which the H atom is abstracted as well as the radical which abstracts the H atom. The literatures [117] and [118] show that there is numerical agreement between the reactivity of primary β hydrogen of alkanes and that of ketones which is far from the carbonyl group. Therefore the rates of abstraction from β site by H, CH_3 and C_2H_5 , (namely (R 9), (R 15) and (R 17)

respectively), are considered to be analogous to twice of the corresponding rates of abstraction from previously studied ketone, 3-pentanone for which the rates are assigned based on the comparable values in alkanes [119]. The reaction rate for abstraction by HO_2 from DIPK primary β hydrogen, (R 11), is obtained twice of isopropyl methyl ketone (iPMK) based on ab-initio and chemical kinetic study of abstraction reactions by Mendes et. al [120]. The schematic structure of iPMK is shown in Scheme 7-3.



Scheme 7-3- Isopropyl methyl ketone iPMK

Assigning a rate to the H-abstraction reaction from the tertiary α site, however, is more complicated. The α position is next to the carbonyl group which is polar due to the greater electronegativity of oxygen and therefore has larger molecular dipole moments than do alkenes. The α -hydrogen atom is acidic and can be removed by common bases. The α -substitution reaction in a ketone stands for the substitution of a α -hydrogen atom by an electrophile, E, through either an enol or enolate ion. Since the rates in this study are related to high temperature limit, the details about the abstraction rate at low and intermediate temperature region are not discussed here.

Having obtained the rates of abstraction from β site, the rates of abstraction from α site by H and CH_3 are calculated based on the tertiary to primary branching ratio predicted for DIPK H-abstraction by Allen et al [6]. In the absence of branching ratio for C_2H_5 , the abstraction rate from the α site by this radical is updated based on the tertiary to primary branching ratio for a branched alkane, namely isobutene [117]. The reaction rate for abstraction by HO_2 from DIPK tertiary site

is similarly obtained to be twice of iPMK abstraction rate with HO₂ from the tertiary site, based on Mendes et. al [120].

One of the most important oxidation path of ketones are those reactions with OH radical [121]; however, there are few studies on the oxidation behavior of ketones, specifically larger ones. In a recently published work, the rate constants of OH reaction with large branched and straight chained ketones at combustion temperatures are measured. The OH reaction rate constants for four hexanone isomers were compared. In this study Badra et al [122] showed that the carbonyl group position in the hexanone isomers has negligible effect on the rate constants. In the current study, it is tried to use this concept to estimate the rate constants for DIPK + OH → products, along with Cohen's [79, 123] method of next-nearest-neighbor (NNN) to specify the site specific rate for primary and tertiary abstracted H. For this purpose, as our first approach, according to Badra et al [122] conclusion for hexanone isomers, it is assumed that the overall reaction rate of OH with isopropyl methyl ketone (iPMK) is approximately the same as its isomer, 3-pentanone. Now DIPK, iPMK and 3-pentanone are defined using NNN method.

$$k_{\text{DIPK+OH}} = 12P_{2,CO} + 2T_{100,CO} \quad (7-1)$$

$$k_{\text{iPMK+OH}} = P_{1,CO} + 6P_{2,CO} + T_{100,CO} \quad (7-2)$$

$$k_{\text{3-pentanone+OH}} = 6P_1 + 4S_{10,CO} \quad (7-3)$$

Where $P_{1,CO}$ is the rate constant for the primary site H abstraction by OH next to the carbonyl C=O, the same as in acetone; $P_{2,CO}$ and $T_{100,CO}$ refers to are the rates for primary and tertiary H abstraction by OH from CH and methyl next to the carbonyl group, correspondingly;

$S_{10,CO}$ is the rate constant for secondary H-abstraction by OH from CH₂ nearby the carbonyl group and P_1 is the rate constant for primary H-abstraction by OH from the methyl group at the site neighboring the CH₂ group based on Badra et al [122] definitions. Therefore, DIPK rate will be calculated as follows;

$$\begin{aligned}
 k_{\text{DIPK+OH}} &= 2(6P_{2,CO} + T_{100,CO}) = 2(k_{\text{iPMK+OH}} - P_{1,CO}) \approx 2(k_{\text{3-pentanone+OH}} - P_{1,CO}) \\
 k_{\text{DIPK+OH}} &= 6P_1 + 4S_{10,CO} - P_{1,CO}
 \end{aligned}
 \tag{7-4}$$

Badra et al. [122] estimated 3-pentanone+OH rate based on their calculation of $S_{10,CO}$ and $P_{1,CO}$ and verified their result by Lam et al [124] experimental data. DIPK rate constant with OH can be estimated by analogy approach, (2nd approach) which is based on using the *ab initio* calculation of $\text{iPMK} + \text{OH} \rightarrow \text{products}$ calculated in terms of overall and site specific rates by Zhou et al [118]. The total rate constants estimated for DIPK reaction with OH at high temperature range (700-2000 K) are illustrated in Figure 7-1 for two approaches which are based on Badra et al rate estimation for 3-pentanone versus Zhou et al [118] rate estimation for iPMK. As it is shown, the rate for the temperatures of over 1000 K are very close for both approaches, however, the rate based on the first approach tends to predict lower reactivity than the second one for 700-1000K. The rate constants for H abstraction reaction by different radicals are summarized in Table 7-1.

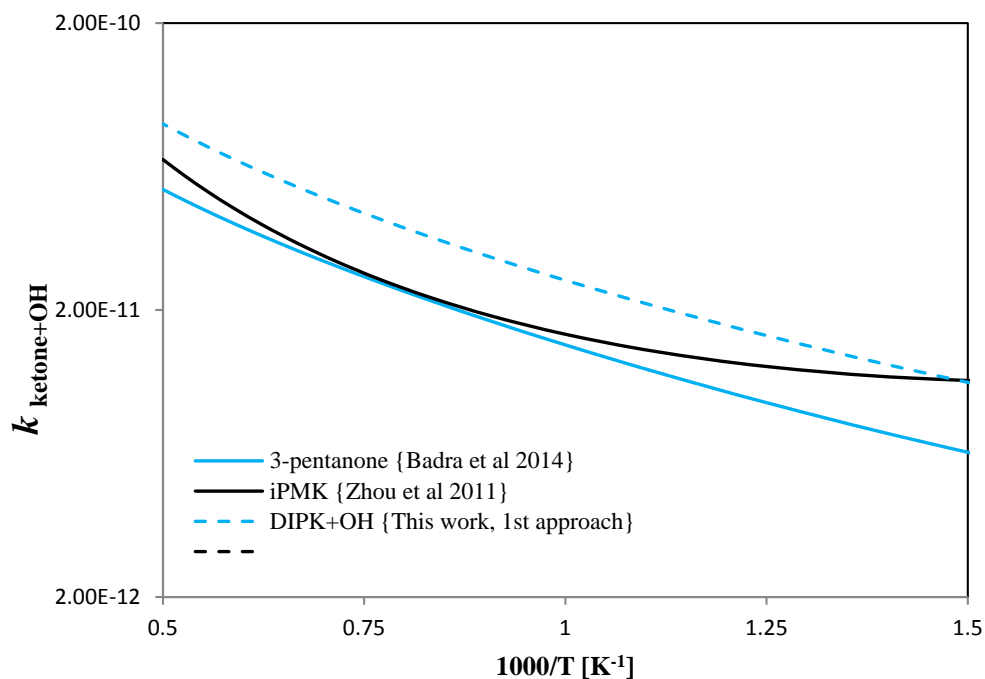


Figure 7-1- The total rate constants estimated for DIPK reaction with OH at high temperature range

Table 7-1- DIPK estimated rates for H abstraction reactions by H, OH, HO₂, CH₃ and C₂H₅ radicals

Reaction	A [†]	n	Ea ^{††}	No.
DIPK + H ⇌ H ₂ + R _{pri}	2.660 × 10 ⁶	2.450	6756	(R 9)
DIPK + H ⇌ H ₂ + R _{tert}	1.505 × 10 ⁶	2.41	2556	(R 10)
DIPK + OH ⇌ H ₂ O + R _{pri}	3.108 × 10 ¹	3.540	-2909	(R 11)
DIPK + OH ⇌ H ₂ O + R _{tert}	9.840 × 10 ³	2.700	-4036	(R 12)
DIPK + HO ₂ ⇌ H ₂ O ₂ + R _{pri}	4.760 × 10 ⁻³	4.560	15184	(R 13)
DIPK + HO ₂ ⇌ H ₂ O ₂ + R _{tert}	1.696 × 10 ⁰	3.53	11375	(R 14)
DIPK + CH ₃ ⇌ CH ₄ + R _{pri}	6.120 × 10 ⁰	3.650	7150	(R 15)
DIPK + CH ₃ ⇌ CH ₄ + R _{tert}	2.343 × 10 ³	2.71	3710	(R 16)
DIPK + C ₂ H ₅ ⇌ C ₂ H ₆ + R _{pri}	2.000 × 10 ¹¹	0.0	13400	(R 17)
DIPK + C ₂ H ₅ ⇌ C ₂ H ₆ + R _{tert}	2.646 × 10 ¹⁰	-0.19	10216	(R 18)

7.2.3 Ketonyl radical decomposition

The radicals produced from the H abstraction reactions are primary and tertiary radicals which decompose through an endothermic β -scission process. The rate constants are obtained in the reverse direction, namely the exothermic addition of H-atom or a radical across a double bond of an olefin [125]. Therefore, the rate constants for H atom addition to $C_7H_{12}O$ producing R_{pri} and R_{tert} (R 19 and (R 20) are assigned to have the same A-factor of $1.0 \times 10^{13} \text{ cm}^3 \text{ mol}^{-1} \text{ s}^{-1}$ with the activation energy of 2.9 kcal/mol and 1.2 kcal/mol respectively based on Curran et al recommendation [125]. Similarly the rate for alkyl radical addition across a double bond is considered to be the same as the rate of addition to the internal carbon atom, by Curran et.al [125]. Therefore the rate constants corresponding to the addition of methyl to $C_6H_{10}O$ to form R_{pri} (R 21) as well as the addition of isopropyl radical to dimethyl ketene (DMK) to produce R_{tert} (R 22) are estimated to be $8.5 \times 10^{10} \exp(-5334/T) \text{ s}^{-1}$. $C_6H_{11}O$ is also a radical formed by a methyl group removal from the fuel. The reaction rate constants for (R 23) and (R 24) are estimated based on similar approach to be $1.0 \times 10^{13} \exp(-1459/T) \text{ s}^{-1}$ and $8.5 \times 10^{10} \exp(-5334/T) \text{ s}^{-1}$ respectively.

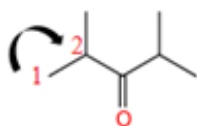
Table 7-2- Addition of methyl or H atom to double bond (Curran et al 1998 [125])

Additions	Modified Arrhenius Parameters		
	$A \text{ (cm}^3/(\text{mol s}^{-1} \text{ K}^{-n}))$	n	$E_a \text{ (kcal/mol)}$
H addition to terminal C atom of double bond	1.0E+13	0.00	1.2
H addition to internal C atom of double bond	1.0E+13	0.00	2.9
Alkyl addition to terminal C atom of double bond	8.5E+10	0.00	7.8
Alkyl addition to internal C atom of double bond	8.5E+10	0.00	10.6



7.2.4 Fuel radical isomerization reaction

The isomerization reaction of fuel radicals involves the transfer of primary H-atom to tertiary position at high pressure limits based on 1,2 H-Shift (Scheme 7-4) rate rule used in the pressure-dependence calculations by Matheu et al [126]. The expression of rate constant for (R 25) is assigned to be $3.56 \times 10^{10} \times T^{0.88} \exp(-14897/T) \text{ s}^{-1}$.



Scheme 7-4- H atom migration in 1,2 H-Shift

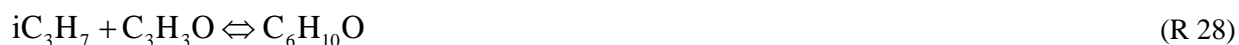
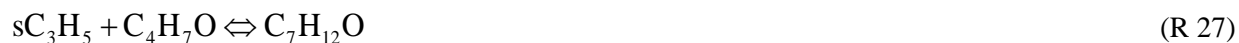
Table 7-3- HP rate rules hydrogen atom shift for pressure-dependence calculations (Matheu et al 2003 [126])

	Modified Arrhenius Parameters			Basis Reactant for E_a
	A ($\text{cm}^3/(\text{mol s}^{-1} \text{K}^{-n})$)	n	E_a (kcal/mol)	
1,2 H-shifts				
p → p	3.56E+10	0.88	40.0	C ₂ H ₅
p → s	3.56E+10	0.88	37.3	CCC.
p → t	3.56E+10	0.88	34.6	CC(C.)C
p → a	3.56E+10	0.88	29.6	C*CCC.
s → s	3.56E+10	0.88	39.1	CC.CC
s → t	3.56E+10	0.88	37.7	CC(C)C.C
s → a	3.56E+10	0.88	31.5	C*CCC.C
t → t	3.56E+10	0.88	40.0	CC(C)C.(C)C
1,3 H-shifts				
v → a	3.80E+10	0.67	38.7	C*CC.
p → p	3.80E+10	0.67	38.8	CCC.
p → s	3.80E+10	0.67	36.6	CCCC.
p → t	3.80E+10	0.67	34.3	CC(C)CC.
s → s	3.80E+10	0.67	38.2	CCCC.C
s → t	3.80E+10	0.67	36.1	CC(C)CC.C
t → t	3.80E+10	0.67	36.6	CC(C)CC.(C)C

7.2.5 Olefin unimolecular decomposition reactions

The radical decomposition through β -scission rule produces unsaturated species with carbon atoms double bond for which the decomposition and abstraction rate constants are to be determined. DIPK radicals β -scission results in the formation of C₇H₁₂O. The unimolecular decomposition reaction of DIPK by removing a methyl group also yields C₆H₁₁O radical which undergoes β -scission to produce C₆H₁₀O and H radical. The rates of decomposition for C₇H₁₂O are considered in reverse direction as recombination reaction of isopropyl radical with C₄H₅O as well as sC₃H₅ and C₄H₇O. The rate for the former is estimated to be $9.033 \times 10^{12} \times T^{-0.35} \text{ s}^{-1}$ based on Tsang recommendation [115] found in NIST web book [95] for recombination of

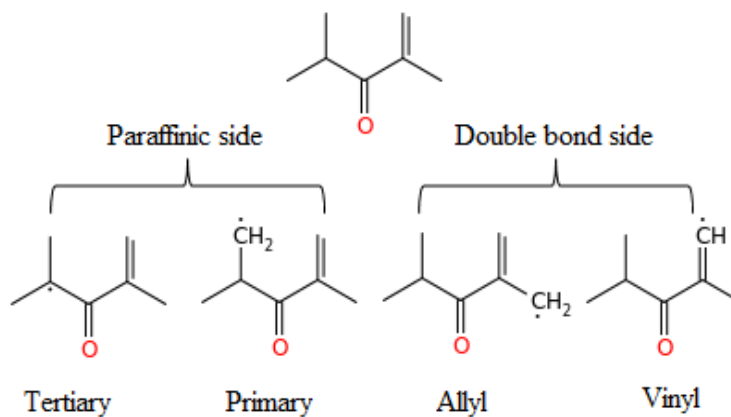
isopropyl to acetyl group. Similarly the rate for C_3H_5 and acetyl radical recombination is used to estimate the (R 27) rate constant [116]. (R 28) rate constant is estimated the same as (R 26).



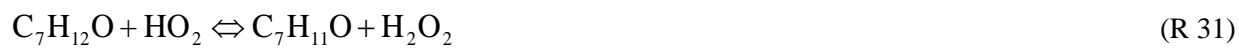
7.2.6 Olefin H-abstraction reaction

The H abstraction from large olefins ($>C_4$) formed during DIPK oxidation are assumed to occur either in paraffinic side or double bond carbon side, although the latter has smaller effects on the large molecule [127]. Therefore, in $C_7H_{12}O$, the H abstraction reactions are from allylic and vinyl sites as well as primary and tertiary positions (see Scheme 7-5). The rate constants for the H abstraction reactions from $C_7H_{12}O$ paraffinic side by all the radicals considered here (R 29 to (R 32) are half of that of DIPK in order to form primary and tertiary radicals. The rate constant for the H abstraction by H atom from vinyl site is assigned to be $5.06 \times 10^7 \times T^{1.98} \exp(-5910/T) s^{-1}$ based on group additivity rate calculation by Sumathi et al [128] for $R_2C = CH_2 + H \rightarrow R_2C = \dot{C}H + H_2$. Similarly from the same reference, the rate of abstraction from allylic site is assumed to be $1.299 \times 10^6 \times T^{2.38} \exp(-1410/T) s^{-1}$ predicted for $R_2C = CRCH_3 + H \rightarrow R_2C = CRCH_2 + H_2$. The H abstraction reaction rate of $C_7H_{12}O$ by OH from vinyl site is estimated by similarity to that of 2-butene-2-one reaction measured by Badra et al [114] to be $8.513 \times 10^{12} \times \exp(-4666/T) s^{-1}$. The rest of the rates including the abstraction

reactions by CH_3 and HO_2 are assumed to be similar to isobutene [129] H abstraction resulting in vinyl and allylic radicals, found in the latest version of isooctane reaction mechanism [130]. In the reactions (R 29) to (R 32), $\text{C}_7\text{H}_{11}\text{O}$ stands for the general representation of all radicals.



Scheme 7-5- H abstraction from $\text{C}_7\text{H}_{12}\text{O}$



7.2.7 Olefin radical isomerization reaction

As mentioned in the previous section, there are four different radicals formed from $C_7H_{12}O$ H abstraction reactions. The isomerization rate constants are estimated for 1,3 H-shift from vinyl to form allylic radical (v→a) as well as 1,2 H-shift from primary to form tertiary radical (p→t) to be $3.80 \times 10^{10} \times T^{0.67} \exp(-19476/T) s^{-1}$ and $3.56 \times 10^{10} \times T^{0.88} \exp(-14897/T) s^{-1}$ respectively based on Matheu et al [126] calculations.

The thermochemistry properties for these radicals are estimated by THERM program [20].



7.2.8 Olefin radical decomposition reaction

The decomposition rate constants for radicals are estimated in reverse direction. It is assumed that all the radicals decompose to smaller species for which the rate constants are all $2.5 \times 10^{13} \times \exp(-22647/T) s^{-1}$ based on Curran et al [127].



7.2.9 Keto-enol tautomerization

Ketones are often in rapid equilibrium with a tautomeric form known as an enol the isomerization called keto-enol tautomerization in which the hydrogen in α position (next to the carbonyl group) moves to form the hydroxyl group by shifting the double bond from the carbonyl group to the carbon atoms bond next to OH. As the concerted keto-enol tautomerization is constrained by the transition state geometry requirements, an acid or a base catalysis is required for tautomerization to take place. This kind of reaction usually occurs in favor of ketone formation which is more stable species. Sarathy et al [23] estimated the rate for butanol isomers enol-keto tautomerization catalyzed by H, HO_2 and formic acid. In order to estimate the rate for this type of reaction, supplementary information is required which is not available at the moment.

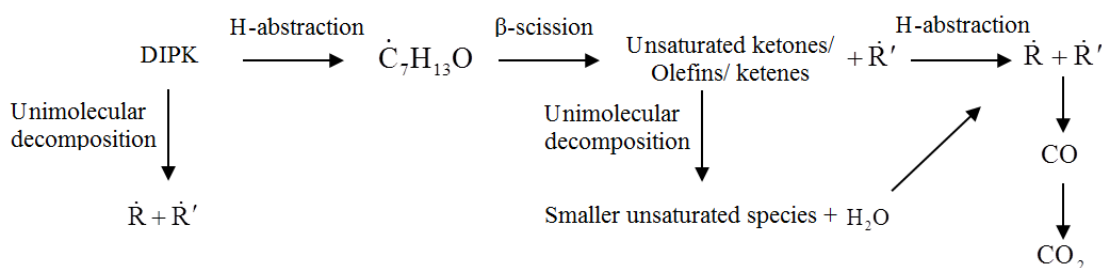
7.3 Low temperature DIPK kinetic model development

DIPK radicals in lower temperature react with O_2 which form a R_pOO or R_tOO , generally denoted as $\beta\text{-RO}_2$ and $\alpha\text{-RO}_2$ respectively. RO_2 can either go through termination reaction by losing HO_2 and forming olefins, namely $\text{C}_7\text{H}_{12}\text{O}$ or can lead to branching reaction channel which forms QOOH radical adding to O_2 due to the high oxygen concentrations and low temperature. This branching channel results in the formation of OH radicals which increase the reactivity of the mixture. As the temperature increases from low region to the intermediate region, RO_2 formation is substituted by HO_2 which causes the reactivity to be decreased [63]. The decrease of reactivity by increasing the temperature is known as negative temperature coefficient (NTC) behavior. The experimental data from RCM conducted by Allen et al [6] shows DIPK NTC behavior however

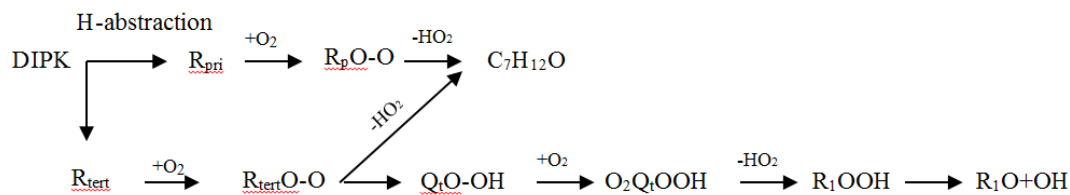
the model based on their mechanism was unable to predict this region. Therefore in addition to the high temperature region, the zero dimensional model based on our expected reaction mechanism should also predict the NTC and low temperature region very well.

7.4 Mechanism validation

The reaction class approach has been used to develop a basic reaction mechanism for DIPK. The overall high temperature reaction mechanism simplified scheme included in this study for DIPK is shown in Scheme 7-6. The naming of \dot{R} and \dot{R}' stand for ketonyl and unsaturated radicals as well as the known radicals such as H, OH, etc. The high temperature submechanism has been added to Galway NUI C4 mechanism [24]. The thermochemical data for the rest of species were adopted from Burcat [131] database. The low temperature reaction mechanism is also shown in Scheme 7-7. The comprehensive mechanism for DIPK must address all the important pathways as well as the intermediates and products to be able to predict the combustion behavior of this biofuel properly. This basic mechanism will be improved in the following chapters.



Scheme 7-6- DIPK high temperature oxidation pathway



Scheme 7-7- DIPK low temperature oxidation pathway

7.4.1 Kinetic model analysis

The ignition delay behind the reflected shock waves was simulated using a zero-dimensional model with adiabatic boundaries and constant volume, solving energy equation in CHEMKIN-PRO [17]. This modeling method has been used to estimate ignition delay time in many studies [84, 85, 101, 132, 133]. DIPK improved reaction mechanism is used to simulate the ignition delay time as well as CH₄ concentration time history.

The reactions for improvement were selected based on the results of sensitivity analysis and reaction path analysis. The A-factor sensitivity reveals that DIPK decomposition reaction to CH₃ + C₆H₁₁O was one of the most sensitive reactions. Also C₆H₁₁O decomposition to C₃H₄O+iC₃H₇ was also an important reaction. As it was mentioned, Curran's recommendation [125] for (CH₃+alkyl)= fuel) to estimate the rate for CH₃+C₆H₁₁O = DIPK which was apparently low. That higher reaction rate can be explained by the carbonyl group which is polar comparing to alkanes. The rate for C₆H₁₁O =C₃H₄O+iC₃H₇ was taken from Curran et al., for Alkyl radical decomposition. The alkyl through double bond with internal C atom was used for the rate. For the modified HT mechanism the reaction rate A-factor was increased.

The results for ignition delay time simulation using the modified high temperature mechanism is shown in Figure 7-2. The ignition delay time simulated using the modified high temperature mechanism is perfectly matched at higher temperature ($T > 1200$ K) with the experimental data from UCF's shock tube. The results for pyrolysis at 1300 K are also shown in Figure 7-3 which shows a decent agreement between the experiment and HT mechanism simulation.

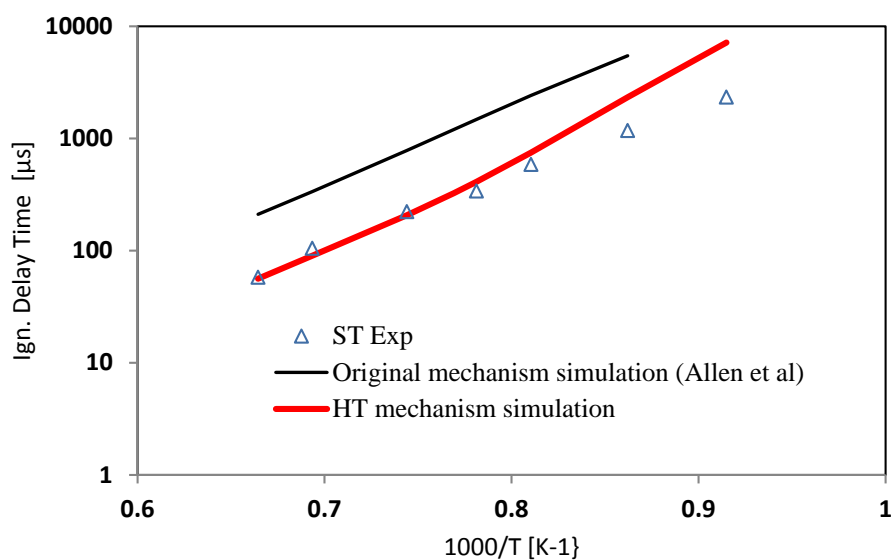


Figure 7-2- DIPK ignition delay time; comparison between the experimental data for stoichiometric mixture of 2% DIPK in 20% O₂ and 78% Ar at 0.9 bar with the simulation using original mechanism (Allen et al) and the modified mechanism (current work)

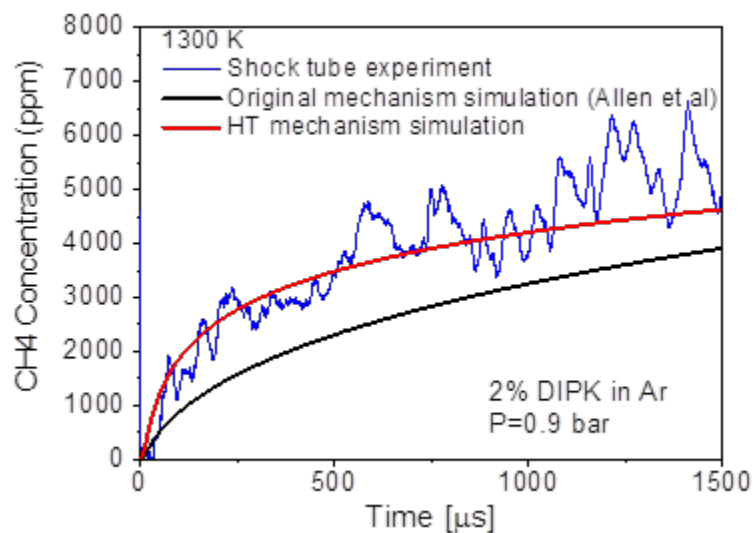


Figure 7-3- CH₄ concentration shock tube experiment for DIPK pyrolysis compared to the high temperature reaction mechanism as well as original mechanism

7.5 Conclusion

The high temperature reaction mechanism of DIPK has been developed and the reactions rates have been estimated using reaction class approach. The high and low temperature reaction rates were added to the GUI C1-C4 mechanism to develop the final reaction mechanism for DIPK. The experimental results of ignition delay time for DIPK oxidation have been used to evaluate the simulated ignition time. The prediction of ignition time at higher temperature ($T > 1200$ K) is perfectly matched with the experimental data from UCF's shock tube.

CHAPTER 8: SUMMARY

The combustion kinetics of advanced biofuels were investigated in this dissertation. Diisopropyl ketone, as a prototypical biofuel is produced from endophytic fungi. This fuel along with other oxygenated fuels such as alcohols is promising fuels for the next generation of engines. DIPK kinetic mechanism was reviewed using high and low temperature reactions classes and the reaction rate constants were assigned based on analogy to the similar reactions or literature recommendations.

A single zone HCCI engine model was developed and validated against recent experimental data from Sandia to find out the deficiencies associated with DIPK reaction mechanism. Different HCCI simulation assumptions were tested and the DIPK reaction mechanism was modified with missing reactions and the required thermochemical data. As a result, the HCCI pressure trace, heat release rate and reactivity have been improved comparing to the original mechanism.

The kinetic investigation was followed by quantum chemical calculation of DIPK radicals reactions with O₂. The barrier energies and vibrational modes were calculated in Gaussian and the reactions rate constants were calculated. The data was used to modify the reaction rates within the mechanism.

DIPK low temperature oxidation was studied through the experimental data obtained from the synchrotron photoionization experiments directed at the Advanced Light Source (ALS). The important reaction pathways as well as the primary product were identified. The oxidation of many oxygenated fuels including ketones (i.e. DIPK) generates aldehydes as intermediates. Hence, the Cl-initiated oxidation ALS measurements were performed to identify the reaction pathways and

products. The results were used to investigate the DIPK kinetic behavior within negative temperature coefficient region.

The experimental data for the product CH₄ concentration in DIPK pyrolysis as well as DIPK ignition delay time were obtained using UCF shock tube to verify the model. The developed reaction mechanism was validated against the experimental ignition delay time which showed very good agreement.

The most obvious future work would include experimental studies of the DIPK oxidation at high pressure to investigate the kinetic mechanism for range of pressure and temperature. The oxidation experimental data can be extended to obtain more products time histories so that the model can be verified against various products formations. The oxidation experiment with shock tube can be done with different fuel equivalence ratio to investigate the fuel lean and rich flow effects on ignition delay time as well as the products mole fraction.

APPENDIX A

DIPK HIGH TEMPERATURE MECHANISM

!=====
 !DIPK UNI-MOLECULAR DECOMPOSITION/RECOMBINATION REACTIONS:
 !=====

IC3H7+IC4H7O(+m)=DIPK(+m) 1.0e+00 0.0 0.0
 !NetReaction from PDepNetwork #1 (C7H14O) High-P Limit:
 R_Recombination exact: [C_rad/H/NonDeC , CO_rad/NonDe]
 TCHEB / 300.0 2000.0 /
 PCHEB / 0.009869232667160128 98.69232667160128 /
 CHEB / 6 4 /
 CHEB / 1.2707000e+01 1.6666000e-01 -3.9327000e-02 8.4603000e-04 /
 CHEB / -3.9341000e-01 3.1328000e-01 -7.2054000e-02 8.6253000e-04 /
 CHEB / -2.4853000e-01 2.5892000e-01 -5.4499000e-02 -1.1907000e-03 /
 CHEB / -1.7237000e-01 1.8538000e-01 -3.1726000e-02 -3.4359000e-03 /
 CHEB / -1.0942000e-01 1.1126000e-01 -1.0504000e-02 -4.8596000e-03 /
 CHEB / -5.9763000e-02 5.2146000e-02 3.9331000e-03 -4.9745000e-03 /
 ! For the above reaction, deltaHrxn(T=298K) = -82.3 kcal/mol

! From Chemical Kinetic Data Base for Combustion Chemistry. Part 3: Propane.
 Journal of Physical and Chemical Reference Data, 1988. 17(2): p. 887-951. And
 Tsang, W., J. Phys. Chem. Ref. Data, 1991. 20(2): p. 235.
 Sensitivity analysis was done for CH4 and A factor was increased for
 CH3+C6H11OJ<=>DIPK.

CH3+C6H11OJ<=>DIPK 6.00e+15 -0.32 0.0
 IC3H7+IC4H7O<=>DIPK 9.03e+12 -0.35 0.0

! Allara, D. L., and Shaw, R., J. Phys. Chem. Ref. Data 9: 523-559 (1980).
 R_pri+H<=>DIPK 1.00e+14 0.0 0.0
 R_tert+H<=>DIPK 1.00e+14 0.0 0.0

!DIPK H ABSTRACTION REACTIONS:
 !=====

! C.-W. Zhou; J. M. Simmie; H. J. Curran, Phys. Chem. Chem. Phys. 13 (2011)
 11175-11192.
 DIPK+OH<=>R_tert+H2O 9.840e+03 2.700 -4036

! C.-W. Zhou; J. M. Simmie; H. J. Curran, Phys. Chem. Chem. Phys. 13 (2011)
 11175-11192.
 DIPK+OH<=>R_pri+H2O 3.108e+01 3.540 -2909

! J. Mendes; C.-W. Zhou; H. J. Curran
 DIPK+H2=R_tert+H2O2 1.696e+00 3.530 11375

! J. Mendes; C.-W. Zhou; H. J. Curran
 DIPK+H2=R_pri+H2O2 4.760e-03 4.560 15184

! Computed by using the branching ratio from Allen et. al., Combustion and
 flame 161 (2014) 711-724 and the 3-pentanone H abstraction reactions rates by
 Serinyel et. al. (2010).
 DIPK+H=R_tert+H2 1.505e+06 2.410 2556

! Computed by using the 3-pentanone H abstraction reactions rates by Serinyel
 et. al. (2010).
 DIPK+H=R_pri+H2 2.664e+06 2.450 6756

! Computed by using the branching ratio from Allen et. al , Combustion and flame 161 (2014) 711-724 and the 3-pentanone H abstraction reactions rates by Serinyel et. al. (2010) (A factor x2).
 DIPK+CH3=R_tert+CH4 4.686e+03 2.710 3710

! Computed by using the 3-pentanone H abstraction reactions rates by Serinyel et. al. (2010) (A factor x2).
 DIPK+CH3=R_pri+CH4 12.24e+00 3.650 7150

! Computed by using the iso-butanol reaction rate for H abstraction by C2H5 by Sarathy et. al. Combustion and flame(2012).
 DIPK+C2H5=R_tert+C2H6 2.646e+10 -0.19 10216

! Computed by using the 3-pentanone H abstraction reactions rates by Serinyel et. al. (2010).
 DIPK+C2H5=R_pri+C2H6 2.000e+11 0.0 13400

! DIPK RADICALS DECOMPOSITION:
 !=====

! Curran et al., Combustion and flame 129:253-280 (2002) Alkyl radical decomposition.

C7H120+H<=>R_pri 1.000e+13 0.0 2900
 C7H120+H<=>R_tert 1.000e+13 0.0 1200
 C3H6+IC4H70<=>R_pri 1.506e+00 3.380 3640
 !DIPK mech
 CH3+C6H100-1<=>R_pri 8.500e+10 0.0 10600
 DMK+IC3H7<=>R_tert 8.500e+10 0.0 10600
 C3H40+IC3H7=C6H110J 8.500e+11 0.0 10600
 H+C6H100-1=C6H110J 1.000e+13 0.0 2900

! DIPK RADICALS ISOMERIZATION:
 !=====

! Matheu et al.
 R_pri=R_tert 3.564E+10 0.88 29600

! C7H120 UNI-MOLECULAR DECOMPOSITION/RECOMBINATION REACTIONS:
 !=====

! Computed based on Tsang, Chemical kinetic data for propane-page 943 (1988)
 IC3H7+C4H50=C7H120 9.033e+12 -0.35 0.0

! Computed based on Tsang, Chemical kinetic database for combustion chemistry, part V. vol 20 (1991)
 C3H5-S+IC4H70=C7H120 1.812e+13 0.0 0.0
 IC3H7+C3H30=C6H100-1 9.033e+12 -0.35 0.0

! C7H120 H ABSTRACTION REACTIONS:
 !=====

!The radicals of C7H110-p, C7H110-t C7H110-v and C7H110-a are considered as primary, tertiary, vinyl and allylic radicals.
 ! Abstraction rate constants by H atom from primary and tertiary are half of DIPK rates.
 ! Abstraction rate constants by H atom from vinyl and allylic sites are Computed by using the reaction rate estimation based on group additivity, Sumathi et. al, MIT (2001).


```

! estimated based on half of DIPK rates
C7H120+H=H2+C7H110- p      1. 332e+06      2. 450      6756
C7H120+OH=H2O+C7H110- p    1. 558e+01      3. 540     -2909
C7H120+H02=H2O2+C7H110- p  2. 380e- 03     4. 560     15184
C7H120+CH3=CH4+C7H110- p   3. 060e+00     3. 650      7150

! estimated based on half of DIPK rates
C7H120+H=H2+C7H110- t      0. 752e+06     2. 410      2556
C7H120+OH=H2O+C7H110- t    4. 920e+03     2. 700     -4036
C7H120+H02=H2O2+C7H110- t  0. 848e+00     3. 530     11375
C7H120+CH3=CH4+C7H110- t   1. 171e+03     2. 710      3710

C7H120+H=H2+C7H110- v      5. 060e+07     1. 98      11743
C7H120+OH=H2O+C7H110- v    8. 513e+12     0. 0       4666
! Badra et al
! C7H120+H02=H2O2+C7H110- v
! could not find a rate
C7H120+CH3=CH4+C7H110- v   2. 00e+12      0. 00      15000

C7H120+H=H2+C7H110- a      1. 299e+06     2. 38      2801
C7H120+OH=H2O+C7H110- a    2. 70e+13      0. 00      3000
!2009 Yasunaga et al. for isobutene! Butene mechanism file, Zhao et. al
(2014), using the isomerization rate of IC4H7-1 and IC4H7 from Yasunaga et.
al (2009)
C7H120+H02=H2O2+C7H110- a   4. 00e+13      0. 00      21000
!2009 Yasunaga et al. for isobutene
C7H120+CH3=CH4+C7H110- a   3. 20e+12      0. 00      10000
!2009 Yasunaga et al. for isobutene

```

! C7H120 RADICALS DECOMPOSITION:

```

! =====
! Curran et al -isooctane- (2002)
C7H110- t=DMK+C3H5- S      2. 500e+13      0. 0       45000
C7H110- p=C3H6+C4H50      2. 500e+13      0. 0       45000
C7H110- a=C3H4- A+IC4H70   2. 500e+13      0. 0       45000
C7H110- v=C3H4- P+IC4H70   2. 500e+13      0. 0       45000

```

! C7H120 RADICALS ISOMERIZATION:

```

! =====
! Matheu et al.
C7H110- v=C7H110- a      3. 80e+10      0. 67      38700
C7H110- p=C7H110- t     3. 56e+10      0. 88      29600

```

! Reactions to complete the pathway

```

! =====
! Using DIPK mechanism , Allen. et. al (2014)

```

! C4H50 reactions:

```

! -----
CO+C3H5- S(+M)=C4H50(+M)   1. 000e+00  0. 000    0. 000
  TCHEB/ 300. 000  4000. 000 /
  PCHEB/  0. 010   98. 692  /
  CHEB/  6 4/
  CHEB/  8. 327e+00  1. 045e+00  -1. 693e- 01  1. 401e- 02  /
  CHEB/  3. 491e- 01  8. 739e- 01  7. 308e- 02  -4. 427e- 02  /

```

CHEB/	-4.610e-01	1.706e-01	8.270e-02	3.850e-03	/
CHEB/	-1.040e-01	-6.360e-02	2.008e-02	1.444e-02	/
CHEB/	5.753e-02	-4.048e-02	-1.766e-02	6.050e-03	/
CHEB/	1.012e-02	-1.791e-02	-6.172e-03	-2.737e-03	/

!C3H40 reactions:

```

!-----
!C3H40+I C3H7=C6H110J
C3H40+OH=C3H30+H2O
C3H40+H=C3H30+H2
HCCO+CH3(+M)=C3H40(+M)
  TCHEB/ 300.000 4000.000 /
  PCHEB/ 0.010 98.692 /
  CHEB/ 6 4/
  CHEB/ 1.155e+01 1.830e+00 -1.030e-01 -4.369e-02 /
  CHEB/ -1.172e+00 1.493e-01 8.769e-02 3.464e-02 /
  CHEB/ -6.424e-01 3.943e-02 2.498e-02 1.169e-02 /
  CHEB/ -2.490e-01 -1.324e-02 -6.134e-03 -8.001e-04 /
  CHEB/ -7.211e-02 -8.132e-03 -5.121e-03 -2.345e-03 /
  CHEB/ 7.658e-03 -1.544e-03 -1.651e-03 -1.384e-03 /
C3H30+H(+M)=C3H40(+M)
  TCHEB/ 300.000 4000.000 /
  PCHEB/ 0.010 98.692 /
  CHEB/ 6 4/
  CHEB/ 1.143e+01 1.781e+00 -1.253e-01 -4.680e-02 /
  CHEB/ -1.359e+00 2.034e-01 1.121e-01 3.762e-02 /
  CHEB/ -7.290e-01 4.515e-02 2.844e-02 1.314e-02 /
  CHEB/ -2.823e-01 -2.015e-02 -8.535e-03 -2.917e-04 /
  CHEB/ -8.307e-02 -9.528e-03 -6.195e-03 -2.955e-03 /
  CHEB/ 9.711e-03 -2.488e-03 -2.426e-03 -1.870e-03 /
C3H30+H2O2=C3H40+H2O
C3H40+CH3=C3H30+CH4
C3H40+C2H5=C3H30+C2H6
C2H4+CO(+M)=C3H40(+M)
  TCHEB/ 300.000 4000.000 /
  PCHEB/ 0.010 98.692 /
  CHEB/ 6 4/
  CHEB/ -1.268e+01 5.221e-01 -8.463e-02 5.228e-03 /
  CHEB/ 2.110e+01 8.232e-01 -6.911e-02 -1.338e-02 /
  CHEB/ -7.231e-01 4.407e-01 2.956e-02 -2.060e-02 /
  CHEB/ -4.609e-01 1.526e-01 5.396e-02 -3.380e-03 /
  CHEB/ -1.508e-01 7.555e-03 3.076e-02 8.809e-03 /
  CHEB/ -8.067e-02 -3.699e-02 3.766e-03 8.207e-03 /
CH2CO+CH2(+M)=C3H40(+M)
  TCHEB/ 300.000 4000.000 /
  PCHEB/ 0.010 98.692 /
  CHEB/ 6 4/
  CHEB/ 8.628e+00 1.656e+00 -1.779e-01 -5.025e-02 /
  CHEB/ 3.120e-01 3.165e-01 1.517e-01 3.141e-02 /
  CHEB/ -5.259e-01 7.403e-02 4.702e-02 2.115e-02 /
  CHEB/ -2.868e-01 -2.028e-02 -4.023e-03 5.351e-03 /
  CHEB/ -1.275e-01 -2.122e-02 -1.162e-02 -3.479e-03 /
  CHEB/ -1.664e-02 -8.779e-03 -6.978e-03 -4.346e-03 /
HCO+C2H3(+M)=C3H40(+M)
  TCHEB/ 300.000 4000.000 /
  PCHEB/ 0.010 98.692 /
  CHEB/ 6 4/
  CHEB/ 1.142e+01 1.550e+00 -2.170e-01 -4.976e-02 /
  CHEB/ -1.253e+00 3.864e-01 1.689e-01 2.281e-02 /
  CHEB/ -7.400e-01 1.141e-01 6.476e-02 2.251e-02 /
  CHEB/ -3.488e-01 -1.490e-02 3.163e-03 1.040e-02 /

```

CHEB/ -1.332e-01 -2.738e-02 -1.219e-02 -8.790e-04 /
 CHEB/ -2.835e-02 -1.555e-02 -1.067e-02 -5.139e-03 /

!C3H30 reactions:

!-----
 !
 CO+C2H3(+M)=C3H30(+M) 1.000e+00 0.000 0.000
 TCHEB/ 300.000 4000.000 /
 PCHEB/ 0.010 98.692 /
 CHEB/ 6 4/
 CHEB/ 7.989e+00 1.437e+00 -2.160e-01 -2.457e-02 /
 CHEB/ 4.693e-01 5.146e-01 1.627e-01 -6.262e-03 /
 CHEB/ -4.124e-01 9.260e-02 6.516e-02 1.987e-02 /
 CHEB/ -9.013e-02 -3.487e-02 -8.185e-03 1.025e-02 /
 CHEB/ 9.066e-02 -2.862e-02 -1.364e-02 -3.187e-03 /
 CHEB/ 3.766e-02 1.160e-02 -1.132e-02 -6.599e-03 /

!C6H100 reaction:

!-----
 !
 IC4H70+C2H3=C6H100-1 1.000e+13 0.000 0.000

END

!-----
 ---!

APPENDIX B

QUANTUM CHEMICAL CALCULATIONS OF DIPK RADICALS REACTIONS WITH O₂

α -RO2 \leftrightarrow α -Qp1

Molecule 1:

Geometry:

Mass(amu)	X(ang)	Y(ang)	Z(ang)
12.000	0.3884	0.6793	0.1307
15.995	0.5833	1.8571	0.3262
12.000	1.5240	-0.3330	0.0264
1.008	1.2374	-1.2115	0.6120
12.000	-1.0956	0.2415	-0.0498
12.000	1.6884	-0.7860	-1.4420
1.008	2.4996	-1.5148	-1.5085
1.008	0.7847	-1.2585	-1.8293
1.008	1.9449	0.0624	-2.0831
12.000	2.8232	0.2508	0.5869
1.008	2.7095	0.5422	1.6331
1.008	3.6238	-0.4904	0.5222
1.008	3.1258	1.1393	0.0293
12.000	-1.9109	0.6451	1.1757
1.008	-1.8050	1.7189	1.3288
1.008	-2.9641	0.4025	1.0182
1.008	-1.5576	0.1221	2.0638
12.000	-1.6510	0.8304	-1.3458
1.008	-1.5533	1.9158	-1.3124
1.008	-2.7050	0.5675	-1.4549
15.995	-0.9722	-1.9361	0.8235
15.995	-1.2032	-1.2221	-0.2596
1.008	-1.1075	0.4582	-2.2164

Frequencies (cm⁻¹):

42.073	79.138	137.288
192.893	197.512	212.084
214.352	250.151	254.590
270.098	299.189	321.086
336.634	369.797	393.363
451.065	552.293	604.364
694.215	758.419	793.316
860.816	903.017	948.208
951.432	975.306	1024.899
1043.693	1105.899	1125.884
1145.433	1188.247	1200.032
1217.261	1237.550	1310.489
1380.547	1391.083	1402.968
1410.684	1421.948	1474.547
1482.422	1484.651	1487.429
1491.967	1500.492	1510.714
1513.669	1771.539	3017.284
3025.087	3032.843	3037.483
3039.203	3082.214	3090.819
3099.266	3101.519	3104.297
3112.392	3121.007	3131.051

External Symmetry = 1.0

Principal Moments of Inertia = 291.365023939 473.81092957 546.431407586

Electronic Degeneracy = 2

Thermodynamic Data

Translational Contributions						
Temperature	298.00	300.00	400.00	500.00	600.00	
800.00	1000.00	1500.00				
Entropy	40.83	40.86	42.29	43.40	44.30	
45.73	46.84	48.85				
Cp	4.97	4.97	4.97	4.97	4.97	
4.97	4.97	4.97				
dH	1.48	1.49	1.99	2.48	2.98	
3.97	4.97	7.45				
q _{trans}	6.86e+07	6.98e+07	1.43e+08	2.50e+08	3.95e+08	
8.10e+08	1.42e+09	3.90e+09				

Translational Contributions

Temperature	298.15
Entropy	40.83
Cp	4.97
dH	1.48
q _{trans}	6.87e+07

Vibrational Contributions

Entropy:						
Temperature	298.00	300.00	400.00	500.00	600.00	
800.00	1000.00	1500.00				
Entropy	35.59	35.85	48.50	60.71	72.39	
93.92	113.16	153.12				
Cp	38.31	38.54	49.77	59.77	68.22	
81.33	90.87	105.39				
dH	5.83	5.91	10.34	15.83	22.25	
37.30	54.58	104.14				
q _{vib}	3.17e+03	3.38e+03	8.94e+04	2.23e+06	5.18e+07	
2.18e+10	6.33e+12	1.95e+18				

Vibrational Contributions

Entropy:	
Temperature	298.15
Entropy	35.61
Cp	38.32
dH	5.84
q _{vib}	3.18e+03

External Rotational Contributions

Temperature	298.00	300.00	400.00	500.00	600.00	
800.00	1000.00	1500.00				
Entropy	29.62	29.64	30.50	31.16	31.70	
32.56	33.23	34.44				
Cp	2.98	2.98	2.98	2.98	2.98	
2.98	2.98	2.98				
dH	0.89	0.89	1.19	1.49	1.79	
2.38	2.98	4.47				
q _{rot}	662983.05	669668.56	1031022.20	1440897.32	1894108.72	
2916171.15	4075473.08	7487122.13				

External Rotational Contributions

Temperature	298.15
Entropy	29.62
Cp	2.98
dH	0.89

q_rot 663483.69

Hf298 S298 Cps:

-65.0594250885 107.434154134 46.2552838012 46.4856476637 57.7198625114
67.7198876299 76.1732803406 89.2816010199 98.8202900972 113.342514168Molecule
2:

Geometry:

Mass(amu)	X(ang)	Y(ang)	Z(ang)
12.000	0.3393	0.7720	-0.0320
15.995	0.5373	1.9134	-0.3791
12.000	1.5259	-0.1393	0.3439
1.008	1.3307	-0.5023	1.3608
12.000	-1.1269	0.2513	0.0882
12.000	1.6319	-1.3546	-0.5592
1.008	2.3839	-2.0872	-0.2712
1.008	0.4029	-1.9858	-0.3322
1.008	1.5758	-1.1759	-1.6324
12.000	2.8453	0.6539	0.3557
1.008	2.7796	1.5018	1.0402
1.008	3.6673	0.0091	0.6752
1.008	3.0730	1.0479	-0.6360
12.000	-1.5155	0.0671	1.5575
1.008	-1.3861	1.0065	2.1010
1.008	-2.5652	-0.2285	1.6183
1.008	-0.9174	-0.7071	2.0354
12.000	-2.0790	1.1984	-0.6364
1.008	-2.0176	2.1963	-0.2038
1.008	-3.0996	0.8229	-0.5476
15.995	-0.6789	-2.0858	-0.0193
15.995	-1.2893	-0.9883	-0.6616
1.008	-1.8187	1.2714	-1.6931

Frequencies (cm-1):

Imaginary Frequency: -1649.42137239

47.586	88.650	185.395
196.793	218.959	225.905
252.165	275.719	291.208
316.566	360.889	370.470
378.640	415.286	516.784
572.209	586.069	620.109
679.993	758.005	825.413
883.034	906.392	912.746
943.736	961.344	974.547
992.875	1031.075	1096.946
1120.859	1130.484	1178.659
1198.882	1217.438	1260.651
1308.647	1342.089	1395.293
1403.217	1415.224	1451.974
1469.048	1481.682	1482.815
1485.820	1488.667	1491.214
1509.776	1772.718	3005.955
3026.403	3029.037	3042.207
3064.779	3094.113	3094.901
3104.954	3113.848	3124.047
3127.820	3155.207	

External Symmetry = 1.0

Principal Moments of Inertia = 288.887033494 431.284132075 577.844518429
 Electronic Degeneracy = 2

Thermodynamic Data

Translational Contributions

Temperature	298.00	300.00	400.00	500.00	600.00
800.00	1000.00	1500.00			
Entropy	40.83	40.86	42.29	43.40	44.30
45.73	46.84	48.85			
Cp	4.97	4.97	4.97	4.97	4.97
4.97	4.97	4.97			
dH	1.48	1.49	1.99	2.48	2.98
3.97	4.97	7.45			
qtrans	6.86e+07	6.98e+07	1.43e+08	2.50e+08	3.95e+08
8.10e+08	1.42e+09	3.90e+09			

Translational Contributions

Temperature	298.15
Entropy	40.83
Cp	4.97
dH	1.48
qtrans	6.87e+07

Vibrational Contributions

Entropy:

Temperature	298.00	300.00	400.00	500.00	600.00
800.00	1000.00	1500.00			
Entropy	31.73	31.98	44.45	56.65	68.33
89.89	109.09	148.80			
Cp	37.32	37.57	49.49	59.80	68.34
81.31	90.57	104.47			
dH	5.36	5.43	9.80	15.28	21.71
36.77	54.03	103.26			
q_vib	1.01e+03	1.08e+03	2.30e+04	5.00e+05	1.06e+07
3.98e+09	1.08e+12	2.99e+17			

Vibrational Contributions

Entropy:

Temperature	298.15
Entropy	31.75
Cp	37.34
dH	5.36
q_vib	1.02e+03

External Rotational Contributions

Temperature	298.00	300.00	400.00	500.00	600.00
800.00	1000.00	1500.00			
Entropy	29.57	29.59	30.45	31.11	31.66
32.52	33.18	34.39			
Cp	2.98	2.98	2.98	2.98	2.98
2.98	2.98	2.98			
dH	0.89	0.89	1.19	1.49	1.79
2.38	2.98	4.47			
q_rot	647686.16	654217.42	1007233.60	1407651.75	1850406.29
2848886.85	3981440.40	7314373.07			

External Rotational Contributions

Temperature	298.15
Entropy	29.57
Cp	2.98
dH	0.89
q_rot	648175.24

Hf298 S298 Cps:

-32.4863634848 210.957877442 45.2705197825 45.5191432808 57.4370196169
 67.7485636326 76.2876569712 89.2541907834 98.5154632494 112.418327784Molecule
 3:

 Geometry:

Mass(amu)	X(ang)	Y(ang)	Z(ang)
12.000	0.3683	0.6872	0.0921
15.995	0.5412	1.8593	0.3326
12.000	1.5505	-0.2792	-0.1710
1.008	1.3378	-1.1965	0.3825
12.000	-1.0867	0.1568	-0.0262
12.000	1.5695	-0.5923	-1.6314
1.008	2.0520	0.0910	-2.3211
1.008	-1.5312	-2.2381	1.4714
1.008	1.0121	-1.4294	-2.0289
12.000	2.8631	0.3455	0.3168
1.008	2.8153	0.5730	1.3842
1.008	3.6909	-0.3457	0.1443
1.008	3.0705	1.2788	-0.2101
12.000	-1.9363	0.6865	1.1306
1.008	-1.8891	1.7748	1.1483
1.008	-2.9755	0.3731	1.0009
1.008	-1.5672	0.3137	2.0863
12.000	-1.6597	0.5894	-1.3831
1.008	-1.6223	1.6773	-1.4548
1.008	-2.6968	0.2583	-1.4698
15.995	-0.6998	-1.8554	1.1597
15.995	-1.1319	-1.2812	-0.1073
1.008	-1.0832	0.1631	-2.2054

Frequencies (cm-1):

48.291	61.944	154.846
184.812	201.235	209.292
215.041	237.740	246.744
251.420	284.531	292.965
299.681	338.426	373.217
402.149	458.017	531.597
560.901	588.242	686.036
760.866	829.622	883.528
906.784	921.732	934.624
946.632	1019.271	1031.099
1053.973	1135.652	1157.472
1189.237	1210.170	1245.168
1285.632	1347.581	1365.477
1386.789	1405.851	1407.777
1444.894	1473.634	1485.093
1487.885	1491.101	1491.650
1514.254	1768.272	3025.088
3028.265	3031.894	3062.291
3091.928	3100.980	3102.195
3105.199	3115.633	3121.837

3125.771 3236.625 3759.652

External Symmetry = 1.0

Principal Moments of Inertia = 292.499866812 478.825708902 531.931877469

Electronic Degeneracy = 2

Thermodynamic Data

Translational Contributions

Temperature	298.00	300.00	400.00	500.00	600.00
800.00	1000.00	1500.00			
Entropy	40.83	40.86	42.29	43.40	44.30
45.73	46.84	48.85			
Cp	4.97	4.97	4.97	4.97	4.97
4.97	4.97	4.97			
dH	1.48	1.49	1.99	2.48	2.98
3.97	4.97	7.45			
qtrans	6.86e+07	6.98e+07	1.43e+08	2.50e+08	3.95e+08
8.10e+08	1.42e+09	3.90e+09			

Translational Contributions

Temperature	298.15
Entropy	40.83
Cp	4.97
dH	1.48
qtrans	6.87e+07

Vibrational Contributions

Entropy:

Temperature	298.00	300.00	400.00	500.00	600.00
800.00	1000.00	1500.00			
Entropy	38.08	38.35	51.82	64.62	76.70
98.72	118.18	158.31			
Cp	41.12	41.35	52.54	62.21	70.26
82.62	91.64	105.57			
dH	6.28	6.36	11.07	16.83	23.47
38.85	56.34	106.09			
q_vib	5.22e+03	5.61e+03	1.89e+05	5.84e+06	1.64e+08
9.17e+10	3.28e+13	1.38e+19			

Vibrational Contributions

Entropy:

Temperature	298.15
Entropy	38.10
Cp	41.13
dH	6.28
q_vib	5.25e+03

External Rotational Contributions

Temperature	298.00	300.00	400.00	500.00	600.00
800.00	1000.00	1500.00			
Entropy	29.61	29.63	30.48	31.15	31.69
32.55	33.21	34.42			
Cp	2.98	2.98	2.98	2.98	2.98
2.98	2.98	2.98			
dH	0.89	0.89	1.19	1.49	1.79
2.38	2.98	4.47			
q_rot	658859.67	665503.61	1024609.83	1431935.77	1882328.45
2898034.24	4050125.97	7440556.52			

External Rotational Contributions

Temperature 298.15
 Entropy 29.61
 Cp 2.98
 dH 0.89
 q_rot 659357.20

Hf298 S298 Cps:

-34.4224594548 320.868241801 49.0659234687 49.3005705213 60.4925197974
 70.1633680309 78.2071832506 90.5710189833 99.58780681 113.520920626

Rate Data: Modified Arrhenius format

$r = A \cdot (T/1000)^n \cdot \exp(-E_a/R/T)$ 2.35e+11 3.28 19.20
 $r = A \cdot T^n \cdot \exp(-E_a/R/T)$ 3.35e+01 3.28 19.20

Temperature	Rate	Fit Rate
298.00	3.90e-05	3.65e-05
300.00	4.87e-05	4.63e-05
400.00	3.11e-01	3.74e-01
500.00	8.96e+01	9.75e+01
600.00	4.54e+03	4.44e+03
800.00	7.25e+05	6.40e+05
1000.00	1.68e+07	1.49e+07
1500.00	1.26e+09	1.41e+09

Rate Data: Arrhenius format

$r = A \cdot \exp(-E_a/R/T)$ 1.39e+12 22.80

Temperature	Rate	Fit Rate
298.00	3.90e-05	2.66e-05
300.00	4.87e-05	3.43e-05
400.00	3.11e-01	4.87e-01
500.00	8.96e+01	1.51e+02
600.00	4.54e+03	6.92e+03
800.00	7.25e+05	8.24e+05
1000.00	1.68e+07	1.45e+07
1500.00	1.26e+09	6.65e+08

α -RO2 \leftrightarrow α -Qp2

Molecule 1:

Geometry:

Mass(amu)	X(ang)	Y(ang)	Z(ang)
12.000	1.0716	-0.0424	-2.0618
12.000	1.3587	-0.4612	-0.6030
12.000	2.8529	-0.4049	-0.2810
12.000	0.5706	0.4284	0.3482
12.000	-0.9809	0.3513	0.4029
15.995	-1.4984	-0.7425	-0.4518
15.995	-1.2382	-1.9475	0.0134
15.995	1.0973	1.2517	1.0608
12.000	-1.4449	0.1376	1.8396
12.000	-1.5712	1.6102	-0.2279
1.008	0.9935	-1.4843	-0.4735
1.008	1.6408	-0.6803	-2.7418
1.008	0.0155	-0.1419	-2.3152
1.008	1.3801	0.9931	-2.2328
1.008	3.0484	-0.7183	0.7464
1.008	3.4063	-1.0626	-0.9558
1.008	3.2352	0.6119	-0.3921
1.008	-1.0899	-0.8216	2.2151
1.008	-1.0402	0.9369	2.4598
1.008	-2.5359	0.1549	1.8832
1.008	-1.2013	2.4811	0.3137
1.008	-2.6607	1.5817	-0.1667
1.008	-1.2814	1.6999	-1.2763

Frequencies (cm⁻¹):

47.116	79.506	140.941
198.995	203.110	214.058
217.528	252.072	256.776
273.716	302.936	321.048
337.878	370.311	392.684
453.781	554.511	602.545
693.846	759.419	796.359
863.549	905.254	947.034
953.535	976.107	1026.275
1047.995	1105.671	1128.806
1146.968	1189.802	1201.234
1220.122	1241.699	1309.328
1379.082	1391.048	1402.231
1410.357	1420.128	1474.578
1482.752	1484.591	1486.254
1492.047	1500.420	1510.695
1514.783	1773.265	3017.105
3024.734	3034.048	3038.237
3038.767	3082.405	3092.946
3097.963	3104.140	3107.879
3114.230	3121.854	3132.344

External Symmetry = 1.0

Principal Moments of Inertia = 290.4326892 470.404960158 541.613904255

Electronic Degeneracy = 2

Thermodynamic Data

Translational Contributions						
Temperature	298.00	300.00	400.00	500.00	600.00	
800.00	1000.00	1500.00				
Entropy	40.83	40.86	42.29	43.40	44.30	
45.73	46.84	48.85				
Cp	4.97	4.97	4.97	4.97	4.97	
4.97	4.97	4.97				
dH	1.48	1.49	1.99	2.48	2.98	
3.97	4.97	7.45				
q _{trans}	6.86e+07	6.98e+07	1.43e+08	2.50e+08	3.95e+08	
8.10e+08	1.42e+09	3.90e+09				

Translational Contributions

Temperature	298.15
Entropy	40.83
Cp	4.97
dH	1.48
q _{trans}	6.87e+07

Vibrational Contributions

Entropy:						
Temperature	298.00	300.00	400.00	500.00	600.00	
800.00	1000.00	1500.00				
Entropy	35.06	35.31	47.94	60.14	71.81	
93.33	112.56	152.51				
Cp	38.22	38.45	49.70	59.72	68.18	
81.30	90.85	105.38				
dH	5.79	5.87	10.29	15.78	22.19	
37.23	54.51	104.05				
q _{vib}	2.60e+03	2.77e+03	7.19e+04	1.77e+06	4.08e+07	
1.69e+10	4.86e+12	1.48e+18				

Vibrational Contributions

Entropy:	
Temperature	298.15
Entropy	35.07
Cp	38.24
dH	5.80
q _{vib}	2.61e+03

External Rotational Contributions

Temperature	298.00	300.00	400.00	500.00	600.00	
800.00	1000.00	1500.00				
Entropy	29.60	29.62	30.48	31.14	31.69	
32.54	33.21	34.42				
Cp	2.98	2.98	2.98	2.98	2.98	
2.98	2.98	2.98				
dH	0.89	0.89	1.19	1.49	1.79	
2.38	2.98	4.47				
q _{rot}	656624.30	663245.69	1021133.54	1427077.50	1875942.09	
2888201.79	4036384.71	7415312.22				

External Rotational Contributions

Temperature	298.15
Entropy	29.60
Cp	2.98
dH	0.89

q_rot 657120.13

Hf298 S298 Cps:

-79.9458742149 106.880353207 46.1684389183 46.3992361566 57.6510235177
67.6641872064 76.127522983 89.248697947 98.794953507 113.327424805

Molecule 2:

Geometry:

Mass(amu)	X(ang)	Y(ang)	Z(ang)
12.000	0.3014	-0.3569	0.6441
15.995	0.3832	-1.0221	1.6520
12.000	1.5038	0.3469	0.0258
1.008	1.4861	0.1328	-1.0457
12.000	-1.1136	-0.1862	0.0105
12.000	1.3692	1.8762	0.1964
1.008	2.2530	2.3678	-0.2179
1.008	0.4933	2.2592	-0.3265
1.008	1.3025	2.1451	1.2550
12.000	2.8049	-0.1752	0.6394
1.008	2.9008	-1.2548	0.5064
1.008	3.6630	0.3105	0.1676
1.008	2.8360	0.0257	1.7123
12.000	-1.7786	-1.5167	-0.1291
1.008	-1.2746	-2.3192	-0.6494
1.008	-2.7216	-1.7164	0.3618
1.008	-1.1729	-0.6654	-2.7343
12.000	-1.9264	0.7661	0.8954
1.008	-1.9690	0.3523	1.9036
1.008	-2.9379	0.8655	0.4971
15.995	-0.4070	-0.3263	-2.2502
15.995	-1.0608	0.5144	-1.2635
1.008	-1.4660	1.7536	0.9365

Frequencies (cm-1):

Imaginary Frequency: -151.505125928

56.381	75.548	157.934
192.267	212.577	222.693
231.368	248.914	269.351
295.339	301.609	322.446
335.165	364.853	394.508
453.493	513.622	560.202
626.656	695.872	760.334
839.058	874.952	896.343
920.566	946.524	960.044
975.085	1035.966	1097.721
1125.377	1134.826	1195.362
1222.993	1227.636	1313.586
1355.453	1378.985	1394.888
1399.281	1417.922	1441.838
1482.137	1484.558	1487.841
1496.300	1501.103	1518.611
1766.717	3014.709	3022.405
3035.375	3055.634	3077.387
3089.311	3097.081	3110.069
3115.024	3123.465	3136.224
3249.628	3746.324	

External Symmetry = 1.0

Principal Moments of Inertia = 294.766674423 474.770772249 535.915144647

Electronic Degeneracy = 2

Thermodynamic Data

Translational Contributions

Temperature	298.00	300.00	400.00	500.00	600.00
800.00	1000.00	1500.00			
Entropy	40.83	40.86	42.29	43.40	44.30
45.73	46.84	48.85			
Cp	4.97	4.97	4.97	4.97	4.97
4.97	4.97	4.97			
dH	1.48	1.49	1.99	2.48	2.98
3.97	4.97	7.45			
qtrans	6.86e+07	6.98e+07	1.43e+08	2.50e+08	3.95e+08
8.10e+08	1.42e+09	3.90e+09			

Translational Contributions

Temperature	298.15
Entropy	40.83
Cp	4.97
dH	1.48
qtrans	6.87e+07

Vibrational Contributions

Temperature	298.00	300.00	400.00	500.00	600.00
800.00	1000.00	1500.00			
Entropy	34.77	35.03	47.91	60.25	71.96
93.38	112.39	151.71			
Cp	39.10	39.34	50.49	60.15	68.19
80.58	89.61	103.57			
dH	5.84	5.92	10.42	15.97	22.41
37.37	54.46	103.21			
q_vib	2.08e+03	2.22e+03	5.97e+04	1.53e+06	3.66e+07
1.58e+10	4.59e+12	1.31e+18			

Vibrational Contributions

Temperature	298.15
Entropy	34.79
Cp	39.12
dH	5.84
q_vib	2.09e+03

External Rotational Contributions

Temperature	298.00	300.00	400.00	500.00	600.00
800.00	1000.00	1500.00			
Entropy	29.61	29.63	30.49	31.16	31.70
32.56	33.22	34.43			
Cp	2.98	2.98	2.98	2.98	2.98
2.98	2.98	2.98			
dH	0.89	0.89	1.19	1.49	1.79
2.38	2.98	4.47			
q_rot	661062.54	667728.68	1028035.56	1436723.37	1888621.92
2907723.66	4063667.35	7465433.62			

External Rotational Contributions

Temperature	298.15
-------------	--------

Entropy	29.61
Cp	2.98
dH	0.89
q_rot	661561.72

Hf298 S298 Cps:

-53.8591459214 213.489634776 47.0512606318 47.2846954318 58.4367327368
 68.0950783782 76.1411346525 88.5242533579 97.560146664 111.518929105Molecule
 3:

 Geometry:

Mass(amu)	X(ang)	Y(ang)	Z(ang)
12.000	1.0052	-0.0262	-2.0957
12.000	1.3246	-0.4657	-0.6503
12.000	2.8293	-0.4401	-0.3736
12.000	0.5832	0.4061	0.3557
12.000	-0.9722	0.3806	0.4074
15.995	-1.5477	-0.6880	-0.3776
15.995	-1.1848	-1.9654	0.2106
15.995	1.1532	1.1612	1.1100
12.000	-1.4473	0.3271	1.8174
12.000	-1.4931	1.6468	-0.3103
1.008	0.9407	-1.4814	-0.5234
1.008	1.5756	-0.6413	-2.7960
1.008	-0.0532	-0.1479	-2.3238
1.008	1.2913	1.0174	-2.2585
1.008	3.0507	-0.7609	0.6462
1.008	3.3490	-1.1049	-1.0683
1.008	3.2290	0.5695	-0.4924
1.008	-2.4973	0.1331	2.0019
1.008	-0.7957	0.6204	2.6266
1.008	-1.9589	-2.1471	0.7616
1.008	-1.0769	2.5240	0.1852
1.008	-2.5822	1.6777	-0.2519
1.008	-1.1943	1.6512	-1.3600

Frequencies (cm-1):

61.902	72.552	161.793
194.022	205.333	215.944
218.270	227.709	246.408
261.698	273.602	302.741
312.174	329.975	364.883
401.120	462.205	520.182
566.356	601.978	687.730
759.655	844.425	876.733
913.391	936.583	945.991
973.244	995.022	1027.227
1055.010	1117.664	1133.278
1192.825	1211.601	1237.460
1315.281	1358.460	1376.075
1388.401	1398.112	1417.171
1425.133	1477.691	1483.288
1486.267	1491.836	1500.654
1518.453	1773.901	3015.352
3022.649	3032.782	3052.944
3077.487	3090.799	3095.834
3107.128	3117.240	3123.731
3131.600	3259.319	3746.965

External Symmetry = 1.0
 Principal Moments of Inertia = 293.207035407 475.362187451 535.059192039
 Electronic Degeneracy = 2

Thermodynamic Data

Translational Contributions

Temperature	298.00	300.00	400.00	500.00	600.00
800.00	1000.00	1500.00			
Entropy	40.83	40.86	42.29	43.40	44.30
45.73	46.84	48.85			
Cp	4.97	4.97	4.97	4.97	4.97
4.97	4.97	4.97			
dH	1.48	1.49	1.99	2.48	2.98
3.97	4.97	7.45			
q _{trans}	6.86e+07	6.98e+07	1.43e+08	2.50e+08	3.95e+08
8.10e+08	1.42e+09	3.90e+09			

Translational Contributions

Temperature	298.15
Entropy	40.83
Cp	4.97
dH	1.48
q _{trans}	6.87e+07

Vibrational Contributions

Entropy:

Temperature	298.00	300.00	400.00	500.00	600.00
800.00	1000.00	1500.00			
Entropy	36.97	37.25	50.68	63.46	75.53
97.53	116.99	157.11			
Cp	41.01	41.24	52.45	62.14	70.19
82.58	91.62	105.57			
dH	6.21	6.29	10.99	16.74	23.38
38.74	56.23	105.98			
q _{vib}	3.34e+03	3.59e+03	1.17e+05	3.56e+06	9.80e+07
5.39e+10	1.90e+13	7.87e+18			

Vibrational Contributions

Entropy:

Temperature	298.15
Entropy	36.99
Cp	41.02
dH	6.22
q _{vib}	3.36e+03

External Rotational Contributions

Temperature	298.00	300.00	400.00	500.00	600.00
800.00	1000.00	1500.00			
Entropy	29.61	29.63	30.48	31.15	31.69
32.55	33.22	34.42			
Cp	2.98	2.98	2.98	2.98	2.98
2.98	2.98	2.98			
dH	0.89	0.89	1.19	1.49	1.79
2.38	2.98	4.47			
q _{rot}	659194.81	665842.12	1025131.00	1432664.13	1883285.91
2899508.33	4052186.08	7444341.18			

External Rotational Contributions

Temperature 298.15
 Entropy 29.61
 Cp 2.98
 dH 0.89
 q_rot 659692.58

Hf298 S298 Cps:

-46.5574661179 322.293926605 48.9543302547 49.1893351467 60.3978173105
 70.0839492159 78.142220668 90.5304596092 99.5639975706 113.515686605

Rate Data: Modified Arrhenius format

$r = A \cdot (T/1000)^n \cdot \exp(-E_a/R/T)$ 2.17e+13 0.87 18.11
 $r = A \cdot T^n \cdot \exp(-E_a/R/T)$ 5.22e+10 0.87 18.11

Temperature	Rate	Fit Rate
298.00	3.99e-01	3.94e-01
300.00	4.91e-01	4.86e-01
400.00	1.21e+03	1.24e+03
500.00	1.41e+05	1.44e+05
600.00	3.51e+06	3.52e+06
800.00	2.06e+08	2.02e+08
1000.00	2.46e+09	2.39e+09
1500.00	6.94e+10	7.10e+10

Rate Data: Arrhenius format

$r = A \cdot \exp(-E_a/R/T)$ 3.49e+13 19.07

Temperature	Rate	Fit Rate
298.00	3.99e-01	3.62e-01
300.00	4.91e-01	4.49e-01
400.00	1.21e+03	1.33e+03
500.00	1.41e+05	1.62e+05
600.00	3.51e+06	3.96e+06
800.00	2.06e+08	2.16e+08
1000.00	2.46e+09	2.37e+09
1500.00	6.94e+10	5.81e+10

α -RO2 \leftrightarrow α -Qt1

Molecule 1:

Geometry:

Mass(amu)	X(ang)	Y(ang)	Z(ang)
12.000	-1.4163	-0.4623	-0.4502
1.008	-1.6360	-0.6021	0.6123
12.000	0.0970	-0.4969	-0.6117
15.995	0.6481	-1.1467	-1.4702
12.000	1.0114	0.3632	0.3050
12.000	-1.9493	0.9283	-0.8599
1.008	-3.0356	0.9492	-0.7461
1.008	-1.5329	1.7241	-0.2413
1.008	-1.7157	1.1366	-1.9081
12.000	-2.0711	-1.5816	-1.2613
1.008	-1.8532	-1.4676	-2.3253
1.008	-1.7008	-2.5617	-0.9541
1.008	-3.1547	-1.5606	-1.1216
12.000	2.0790	-0.5132	0.9512
1.008	2.6329	-1.0256	0.1651
1.008	2.7611	0.1056	1.5380
1.008	1.6189	-1.2528	1.6055
12.000	1.6024	1.5129	-0.5075
1.008	0.8187	2.1652	-0.8967
1.008	2.1624	1.0987	-1.3463
15.995	-0.2429	0.2347	2.2830
15.995	0.2288	1.0481	1.3601
1.008	2.2727	2.1051	0.1182

Frequencies (cm⁻¹):

47.235	81.745	140.353
198.192	204.347	212.757
225.879	253.472	258.311
272.242	302.130	322.483
337.290	370.021	392.625
453.814	553.579	603.218
694.052	758.944	797.795
863.711	905.573	948.582
954.346	976.361	1025.817
1047.862	1105.059	1129.243
1147.531	1190.461	1201.644
1221.272	1242.384	1307.203
1379.673	1390.740	1402.664
1411.040	1420.703	1474.449
1483.158	1485.046	1486.733
1492.327	1500.913	1510.355
1514.455	1773.586	3016.611
3025.165	3034.004	3037.859
3038.162	3082.231	3093.306
3098.559	3104.035	3107.674
3114.059	3122.001	3132.496

External Symmetry = 1.0

Principal Moments of Inertia = 290.432672919 470.403807533 541.616804745

Electronic Degeneracy = 2

Thermodynamic Data

Translational Contributions

Temperature	298.00	300.00	400.00	500.00	600.00
800.00	1000.00	1500.00			
Entropy	40.83	40.86	42.29	43.40	44.30
45.73	46.84	48.85			
Cp	4.97	4.97	4.97	4.97	4.97
4.97	4.97	4.97			
dH	1.48	1.49	1.99	2.48	2.98
3.97	4.97	7.45			
q _{trans}	6.86e+07	6.98e+07	1.43e+08	2.50e+08	3.95e+08
8.10e+08	1.42e+09	3.90e+09			

Translational Contributions

Temperature	298.15
Entropy	40.83
Cp	4.97
dH	1.48
q _{trans}	6.87e+07

Vibrational Contributions

Entropy:

Temperature	298.00	300.00	400.00	500.00	600.00
800.00	1000.00	1500.00			
Entropy	34.93	35.19	47.81	60.01	71.67
93.19	112.42	152.37			
Cp	38.20	38.43	49.69	59.70	68.17
81.29	90.84	105.38			
dH	5.78	5.86	10.27	15.76	22.17
37.21	54.49	104.03			
q _{vib}	2.49e+03	2.65e+03	6.85e+04	1.68e+06	3.86e+07
1.59e+10	4.58e+12	1.39e+18			

Vibrational Contributions

Entropy:

Temperature	298.15
Entropy	34.95
Cp	38.22
dH	5.79
q _{vib}	2.50e+03

External Rotational Contributions

Temperature	298.00	300.00	400.00	500.00	600.00
800.00	1000.00	1500.00			
Entropy	29.60	29.62	30.48	31.14	31.69
32.54	33.21	34.42			
Cp	2.98	2.98	2.98	2.98	2.98
2.98	2.98	2.98			
dH	0.89	0.89	1.19	1.49	1.79
2.38	2.98	4.47			
q _{rot}	656625.23	663246.63	1021134.99	1427079.53	1875944.77
2888205.91	4036390.46	7415322.78			

External Rotational Contributions

Temperature	298.15
Entropy	29.60
Cp	2.98

dH 0.89
q_rot 657121.07

Hf298 S298 Cps:

-79.956146027 106.756361929 46.1477502705 46.3786440485 57.6340104506
67.6498613169 76.1155356634 89.2403478346 98.7890202392 113.324521705 Molecule
2:

Geometry:

Mass(amu)	X(ang)	Y(ang)	Z(ang)
12.000	-1.2534	0.6073	-0.3526
1.008	-1.2663	0.0832	0.8934
12.000	-0.0035	-0.1156	-0.7993
15.995	0.1467	-0.5132	-1.9350
12.000	1.0767	-0.4099	0.2762
12.000	-1.0693	2.0890	-0.0703
1.008	-1.9854	2.5165	0.3437
1.008	-0.2526	2.2691	0.6304
1.008	-0.8424	2.6228	-1.0028
12.000	-2.5007	0.2158	-1.1083
1.008	-2.4136	0.5337	-2.1545
1.008	-2.6481	-0.8661	-1.1141
1.008	-3.3846	0.6917	-0.6781
12.000	1.3103	-1.9196	0.3694
1.008	1.5677	-2.3169	-0.6131
1.008	2.1259	-2.1199	1.0675
1.008	0.4109	-2.4194	0.7302
12.000	2.3594	0.3602	-0.0326
1.008	2.1797	1.4368	-0.0606
1.008	2.7438	0.0432	-1.0030
15.995	-0.6655	-0.3931	1.8167
15.995	0.6206	0.1200	1.5471
1.008	3.1095	0.1535	0.7336

Frequencies (cm-1):

Imaginary Frequency: -1892.78097631

55.483	122.798	160.390
192.356	201.160	213.963
230.543	251.924	263.633
285.976	304.206	323.639
354.762	420.271	471.427
488.690	578.111	599.985
698.432	763.257	827.608
876.251	927.218	945.730
947.456	958.905	992.386
1025.001	1032.658	1062.997
1128.870	1182.656	1195.198
1222.893	1237.422	1264.967
1387.675	1390.472	1404.454
1407.985	1464.268	1472.002
1474.877	1482.640	1485.690
1490.094	1496.468	1510.858
1579.252	1752.841	2986.334
2999.437	3029.860	3034.254
3061.713	3065.415	3097.314
3099.623	3104.440	3107.557
3114.849	3121.329	

External Symmetry = 1.0
 Principal Moments of Inertia = 286.393415081 448.764000938 510.31755153
 Electronic Degeneracy = 2

Thermodynamic Data

Translational Contributions

Temperature	298.00	300.00	400.00	500.00	600.00
800.00	1000.00	1500.00			
Entropy	40.83	40.86	42.29	43.40	44.30
45.73	46.84	48.85			
Cp	4.97	4.97	4.97	4.97	4.97
4.97	4.97	4.97			
dH	1.48	1.49	1.99	2.48	2.98
3.97	4.97	7.45			
qtrans	6.86e+07	6.98e+07	1.43e+08	2.50e+08	3.95e+08
8.10e+08	1.42e+09	3.90e+09			

Translational Contributions

Temperature	298.15
Entropy	40.83
Cp	4.97
dH	1.48
qtrans	6.87e+07

Vibrational Contributions

Entropy:

Temperature	298.00	300.00	400.00	500.00	600.00
800.00	1000.00	1500.00			
Entropy	32.83	33.09	45.64	57.81	69.47
90.96	110.12	149.79			
Cp	37.81	38.04	49.54	59.64	68.11
81.10	90.42	104.42			
dH	5.58	5.65	10.05	15.53	21.93
36.95	54.17	103.35			
q_vib	1.22e+03	1.29e+03	3.05e+04	7.06e+05	1.56e+07
6.10e+09	1.69e+12	4.76e+17			

Vibrational Contributions

Entropy:

Temperature	298.15
Entropy	32.85
Cp	37.82
dH	5.58
q_vib	1.22e+03

External Rotational Contributions

Temperature	298.00	300.00	400.00	500.00	600.00
800.00	1000.00	1500.00			
Entropy	29.48	29.50	30.36	31.02	31.57
32.42	33.09	34.30			
Cp	2.98	2.98	2.98	2.98	2.98
2.98	2.98	2.98			
dH	0.89	0.89	1.19	1.49	1.79
2.38	2.98	4.47			
q_rot	618193.06	624426.91	961368.12	1343552.79	1766146.01
2719159.66	3800141.15	6981305.08			

External Rotational Contributions

Temperature 298.15
 Entropy 29.48
 Cp 2.98
 dH 0.89
 q_rot 618659.87

Hf298 S298 Cps:

-39.9057229989 211.295135125 45.755540153 45.993009228 57.4848609287
 67.59297463 76.0624752141 89.0470263578 98.3687062156 112.364995129Mol ecul e
 3:

Geometry:

Mass(amu)	X(ang)	Y(ang)	Z(ang)
12.000	-1.1971	-0.2753	-0.9954
1.008	-1.4197	0.2663	1.9561
12.000	0.1371	-0.5953	-0.5173
15.995	0.6688	-1.6579	-0.8566
12.000	0.9713	0.3724	0.3709
12.000	-1.9150	1.0259	-0.8127
1.008	-2.9088	0.8527	-0.3774
1.008	-1.3827	1.7387	-0.1903
1.008	-2.1053	1.4860	-1.7919
12.000	-1.9054	-1.3102	-1.8093
1.008	-2.0713	-0.9454	-2.8319
1.008	-1.3327	-2.2336	-1.8574
1.008	-2.8996	-1.5147	-1.3930
12.000	2.0690	-0.3917	1.1114
1.008	2.7175	-0.9091	0.4061
1.008	2.6566	0.3137	1.7030
1.008	1.6308	-1.1333	1.7784
12.000	1.5658	1.4917	-0.4958
1.008	0.7958	2.0470	-1.0337
1.008	2.2516	1.0550	-1.2242
15.995	-0.4936	0.1263	2.1967
15.995	0.1532	1.0910	1.3193
1.008	2.1210	2.1896	0.1346

Frequencies (cm-1):

41.602	66.719	81.148
110.014	144.889	173.492
194.886	220.164	239.110
251.509	280.944	334.116
350.216	354.219	380.988
407.677	494.394	534.103
572.626	651.295	709.364
835.589	889.519	921.798
942.664	946.785	953.329
960.725	1018.881	1039.582
1077.442	1178.800	1216.505
1237.360	1270.919	1351.121
1360.347	1388.547	1394.210
1404.630	1411.799	1458.149
1469.641	1473.448	1481.574
1490.945	1492.435	1504.758
1510.296	1566.720	2973.137
2983.528	3002.357	3019.745
3029.041	3041.025	3101.086

3107.157 3116.073 3132.668
 3132.886 3151.021 3752.616

External Symmetry = 1.0
 Principal Moments of Inertia = 294.388029391 472.098246464 542.169390049
 Electronic Degeneracy = 2

Thermodynamic Data

Translational Contributions

Temperature	298.00	300.00	400.00	500.00	600.00
800.00	1000.00	1500.00			
Entropy	40.83	40.86	42.29	43.40	44.30
45.73	46.84	48.85			
Cp	4.97	4.97	4.97	4.97	4.97
4.97	4.97	4.97			
dH	1.48	1.49	1.99	2.48	2.98
3.97	4.97	7.45			
qtrans	6.86e+07	6.98e+07	1.43e+08	2.50e+08	3.95e+08
8.10e+08	1.42e+09	3.90e+09			

Translational Contributions

Temperature	298.15
Entropy	40.83
Cp	4.97
dH	1.48
qtrans	6.87e+07

Vibrational Contributions

Entropy:					
Temperature	298.00	300.00	400.00	500.00	600.00
800.00	1000.00	1500.00			
Entropy	40.73	41.00	54.18	66.76	78.68
100.51	119.89	159.96			
Cp	40.25	40.48	51.52	61.26	69.46
82.13	91.36	105.52			
dH	6.39	6.47	11.08	16.74	23.30
38.54	55.96	105.65			
q_vib	1.64e+04	1.76e+04	6.10e+05	1.87e+07	5.13e+08
2.74e+11	9.38e+13	3.69e+19			

Vibrational Contributions

Entropy:	
Temperature	298.15
Entropy	40.75
Cp	40.27
dH	6.40
q_vib	1.65e+04

External Rotational Contributions

Temperature	298.00	300.00	400.00	500.00	600.00
800.00	1000.00	1500.00			
Entropy	29.62	29.64	30.49	31.16	31.70
32.56	33.23	34.43			
Cp	2.98	2.98	2.98	2.98	2.98
2.98	2.98	2.98			
dH	0.89	0.89	1.19	1.49	1.79
2.38	2.98	4.47			
q_rot	662608.67	669290.41	1030440.00	1440083.67	1893039.15
2914524.43	4073171.72	7482894.27			

External Rotational Contributions

Temperature 298.15
 Entropy 29.62
 Cp 2.98
 dH 0.89
 q_rot 663109.03

Hf298 S298 Cps:

-47.3143933986 323.866893729 48.2000375189 48.4278779019 59.4667540111
 69.2117288736 77.4098919342 90.0816057774 99.3101230528 113.465388756

Rate Data: Modified Arrhenius format

$r = A \cdot (T/1000)^n \cdot \exp(-E_a/R/T)$ 6.25e+10 5.54 22.47

$r = A \cdot T^n \cdot \exp(-E_a/R/T)$ 1.45e-06 5.54 22.47

Temperature	Rate	Fit Rate
298.00	2.95e-09	2.54e-09
300.00	3.81e-09	3.39e-09
400.00	1.36e-04	2.06e-04
500.00	1.69e-01	2.03e-01
600.00	2.57e+01	2.41e+01
800.00	1.74e+04	1.32e+04
1000.00	9.82e+05	7.69e+05
1500.00	2.47e+08	3.15e+08

Rate Data: Arrhenius format

$r = A \cdot \exp(-E_a/R/T)$ 1.27e+12 28.54

Temperature	Rate	Fit Rate
298.00	2.95e-09	1.48e-09
300.00	3.81e-09	2.05e-09
400.00	1.36e-04	3.23e-04
500.00	1.69e-01	4.25e-01
600.00	2.57e+01	5.10e+01
800.00	1.74e+04	2.03e+04
1000.00	9.82e+05	7.34e+05
1500.00	2.47e+08	8.82e+07

α -Qp1 \rightarrow α -M1

Molecule 1:

Geometry:

Mass(amu)	X(ang)	Y(ang)	Z(ang)
12.000	0.3683	0.6872	0.0921
15.995	0.5412	1.8593	0.3326
12.000	1.5505	-0.2792	-0.1710
1.008	1.3378	-1.1965	0.3825
12.000	-1.0867	0.1568	-0.0262
12.000	1.5695	-0.5923	-1.6314
1.008	2.0520	0.0910	-2.3211
1.008	-1.5312	-2.2381	1.4714
1.008	1.0121	-1.4294	-2.0289
12.000	2.8631	0.3455	0.3168
1.008	2.8153	0.5730	1.3842
1.008	3.6909	-0.3457	0.1443
1.008	3.0705	1.2788	-0.2101
12.000	-1.9363	0.6865	1.1306
1.008	-1.8891	1.7748	1.1483
1.008	-2.9755	0.3731	1.0009
1.008	-1.5672	0.3137	2.0863
12.000	-1.6597	0.5894	-1.3831
1.008	-1.6223	1.6773	-1.4548
1.008	-2.6968	0.2583	-1.4698
15.995	-0.6998	-1.8554	1.1597
15.995	-1.1319	-1.2812	-0.1073
1.008	-1.0832	0.1631	-2.2054

Frequencies (cm⁻¹):

48.291	61.944	154.846
184.812	201.235	209.292
215.041	237.740	246.744
251.420	284.531	292.965
299.681	338.426	373.217
402.149	458.017	531.597
560.901	588.242	686.036
760.866	829.622	883.528
906.784	921.732	934.624
946.632	1019.271	1031.099
1053.973	1135.652	1157.472
1189.237	1210.170	1245.168
1285.632	1347.581	1365.477
1386.789	1405.851	1407.777
1444.894	1473.634	1485.093
1487.885	1491.101	1491.650
1514.254	1768.272	3025.088
3028.265	3031.894	3062.291
3091.928	3100.980	3102.195
3105.199	3115.633	3121.837
3125.771	3236.625	3759.652

External Symmetry = 1.0

Principal Moments of Inertia = 292.499866812 478.825708902 531.931877469

Electronic Degeneracy = 2

Thermodynamic Data

Translational Contributions						
Temperature	298.00	300.00	400.00	500.00	600.00	
800.00	1000.00	1500.00				
Entropy	40.83	40.86	42.29	43.40	44.30	
45.73	46.84	48.85				
Cp	4.97	4.97	4.97	4.97	4.97	
4.97	4.97	4.97				
dH	1.48	1.49	1.99	2.48	2.98	
3.97	4.97	7.45				
q _{trans}	6.86e+07	6.98e+07	1.43e+08	2.50e+08	3.95e+08	
8.10e+08	1.42e+09	3.90e+09				

Translational Contributions

Temperature	298.15
Entropy	40.83
Cp	4.97
dH	1.48
q _{trans}	6.87e+07

Vibrational Contributions

Entropy:						
Temperature	298.00	300.00	400.00	500.00	600.00	
800.00	1000.00	1500.00				
Entropy	38.08	38.35	51.82	64.62	76.70	
98.72	118.18	158.31				
Cp	41.12	41.35	52.54	62.21	70.26	
82.62	91.64	105.57				
dH	6.28	6.36	11.07	16.83	23.47	
38.85	56.34	106.09				
q _{vib}	5.22e+03	5.61e+03	1.89e+05	5.84e+06	1.64e+08	
9.17e+10	3.28e+13	1.38e+19				

Vibrational Contributions

Entropy:	
Temperature	298.15
Entropy	38.10
Cp	41.13
dH	6.28
q _{vib}	5.25e+03

External Rotational Contributions

Temperature	298.00	300.00	400.00	500.00	600.00
800.00	1000.00	1500.00			
Entropy	29.61	29.63	30.48	31.15	31.69
32.55	33.21	34.42			
Cp	2.98	2.98	2.98	2.98	2.98
2.98	2.98	2.98			
dH	0.89	0.89	1.19	1.49	1.79
2.38	2.98	4.47			
q _{rot}	658859.67	665503.61	1024609.83	1431935.77	1882328.45
2898034.24	4050125.97	7440556.52			

External Rotational Contributions

Temperature	298.15
Entropy	29.61
Cp	2.98
dH	0.89

q_rot 659357.20

Hf298 S298 Cps:

-50.3624831204 109.910364359 49.0659234687 49.3005705213 60.4925197974
70.1633680309 78.2071832506 90.5710189833 99.58780681 113.520920626

Molecule
2:

Geometry:

Mass (amu)	X (ang)	Y (ang)	Z (ang)
12.000	-0.4652	-0.5141	1.1792
15.995	-0.5062	-0.6053	2.3536
12.000	2.2952	-0.5549	-1.0516
1.008	1.2598	-0.6978	-1.3513
12.000	-1.0997	0.6382	0.3467
12.000	2.9352	0.5401	-1.4553
1.008	3.9671	0.7354	-1.1765
1.008	-2.3975	-0.6164	-1.8711
1.008	2.4497	1.2779	-2.0851
12.000	2.8803	-1.6266	-0.1803
1.008	2.2871	-1.7456	0.7328
1.008	2.8631	-2.5960	-0.6910
1.008	3.9130	-1.4052	0.1013
12.000	-2.5480	0.8496	0.7892
1.008	-2.5851	1.0683	1.8572
1.008	-2.9755	1.6878	0.2332
1.008	-3.1390	-0.0461	0.5969
12.000	-0.2202	1.8773	0.5268
1.008	-0.2312	2.1827	1.5741
1.008	-0.6156	2.6888	-0.0881
15.995	-1.6760	-0.9165	-1.3011
15.995	-1.0047	0.3497	-1.0457
1.008	0.8048	1.6665	0.2191

Frequencies (cm⁻¹):

Imaginary Frequency: -6.63138173665

22.480	28.876	53.339
66.835	85.533	106.863
155.160	213.325	215.866
225.302	240.764	277.060
288.588	344.550	359.514
434.052	444.447	500.820
586.020	600.982	694.037
841.691	908.198	919.721
931.356	940.361	954.292
955.096	1013.199	1037.000
1074.338	1179.112	1188.379
1195.182	1210.527	1334.793
1358.033	1387.016	1401.558
1408.032	1442.105	1470.126
1471.621	1484.834	1490.085
1491.218	1512.203	1699.556
1915.828	2998.236	3026.917
3030.307	3045.828	3075.485
3101.727	3103.410	3105.838
3118.182	3119.863	3136.967
3188.386	3756.030	

External Symmetry = 1.0

Principal Moments of Inertia = 321.932894821 694.950739026 752.514280953
 Electronic Degeneracy = 2

Thermodynamic Data

Translational Contributions

Temperature	298.00	300.00	400.00	500.00	600.00
800.00	1000.00	1500.00			
Entropy	40.83	40.86	42.29	43.40	44.30
45.73	46.84	48.85			
Cp	4.97	4.97	4.97	4.97	4.97
4.97	4.97	4.97			
dH	1.48	1.49	1.99	2.48	2.98
3.97	4.97	7.45			
qtrans	6.86e+07	6.98e+07	1.43e+08	2.50e+08	3.95e+08
8.10e+08	1.42e+09	3.90e+09			

Translational Contributions

Temperature	298.15
Entropy	40.83
Cp	4.97
dH	1.48
qtrans	6.87e+07

Vibrational Contributions

Entropy:

Temperature	298.00	300.00	400.00	500.00	600.00
800.00	1000.00	1500.00			
Entropy	49.46	49.73	63.06	75.61	87.42
108.92	127.96	167.28			
Cp	41.06	41.28	51.68	60.87	68.63
80.74	89.68	103.58			
dH	6.97	7.05	11.71	17.36	23.85
38.87	55.97	104.74			
q_vib	4.96e+05	5.36e+05	2.40e+07	8.63e+08	2.61e+10
1.53e+13	5.38e+15	1.99e+21			

Vibrational Contributions

Entropy:

Temperature	298.15
Entropy	49.48
Cp	41.08
dH	6.98
q_vib	4.99e+05

External Rotational Contributions

Temperature	298.00	300.00	400.00	500.00	600.00
800.00	1000.00	1500.00			
Entropy	30.42	30.44	31.29	31.96	32.50
33.36	34.02	35.23			
Cp	2.98	2.98	2.98	2.98	2.98
2.98	2.98	2.98			
dH	0.89	0.89	1.19	1.49	1.79
2.38	2.98	4.47			
q_rot	990445.11	1000432.75	1540266.98	2152588.54	2829651.12
4356532.89	6088439.81	11185178.15			

External Rotational Contributions

Temperature 298.15
 Entropy 30.42
 Cp 2.98
 dH 0.89
 q_rot 991193.03

Hf298 S298 Cps:

-38.1724208964 232.008767244 49.0112492309 49.2261055809 59.6320521908
 68.8179756254 76.5758299573 88.6864422182 97.6261306672 111.53030681

Rate Data: Modified Arrhenius format

$r = A \cdot (T/1000)^n \cdot \exp(-E_a/R/T)$ 9.67e+15 0.20 4.12

$r = A \cdot T^n \cdot \exp(-E_a/R/T)$ 2.48e+15 0.20 4.12

Temperature	Rate	Fit Rate
298.00	7.30e+12	7.26e+12
300.00	7.65e+12	7.61e+12
400.00	4.46e+13	4.53e+13
500.00	1.32e+14	1.34e+14
600.00	2.77e+14	2.76e+14
800.00	7.02e+14	6.94e+14
1000.00	1.23e+15	1.22e+15
1500.00	2.60e+15	2.63e+15

Rate Data: Arrhenius format

$r = A \cdot \exp(-E_a/R/T)$ 1.08e+16 4.34

Temperature	Rate	Fit Rate
298.00	7.30e+12	7.12e+12
300.00	7.65e+12	7.48e+12
400.00	4.46e+13	4.61e+13
500.00	1.32e+14	1.37e+14
600.00	2.77e+14	2.84e+14
800.00	7.02e+14	7.04e+14
1000.00	1.23e+15	1.21e+15
1500.00	2.60e+15	2.51e+15

α -Qp2 \rightarrow α -M2

Molecule 1:

Geometry:

Mass(amu)	X(ang)	Y(ang)	Z(ang)
12.000	1.0052	-0.0262	-2.0957
12.000	1.3246	-0.4657	-0.6503
12.000	2.8293	-0.4401	-0.3736
12.000	0.5832	0.4061	0.3557
12.000	-0.9722	0.3806	0.4074
15.995	-1.5477	-0.6880	-0.3776
15.995	-1.1848	-1.9654	0.2106
15.995	1.1532	1.1612	1.1100
12.000	-1.4473	0.3271	1.8174
12.000	-1.4931	1.6468	-0.3103
1.008	0.9407	-1.4814	-0.5234
1.008	1.5756	-0.6413	-2.7960
1.008	-0.0532	-0.1479	-2.3238
1.008	1.2913	1.0174	-2.2585
1.008	3.0507	-0.7609	0.6462
1.008	3.3490	-1.1049	-1.0683
1.008	3.2290	0.5695	-0.4924
1.008	-2.4973	0.1331	2.0019
1.008	-0.7957	0.6204	2.6266
1.008	-1.9589	-2.1471	0.7616
1.008	-1.0769	2.5240	0.1852
1.008	-2.5822	1.6777	-0.2519
1.008	-1.1943	1.6512	-1.3600

Frequencies (cm⁻¹):

61.902	72.552	161.793
194.022	205.333	215.944
218.270	227.709	246.408
261.698	273.602	302.741
312.174	329.975	364.883
401.120	462.205	520.182
566.356	601.978	687.730
759.655	844.425	876.733
913.391	936.583	945.991
973.244	995.022	1027.227
1055.010	1117.664	1133.278
1192.825	1211.601	1237.460
1315.281	1358.460	1376.075
1388.401	1398.112	1417.171
1425.133	1477.691	1483.288
1486.267	1491.836	1500.654
1518.453	1773.901	3015.352
3022.649	3032.782	3052.944
3077.487	3090.799	3095.834
3107.128	3117.240	3123.731
3131.600	3259.319	3746.965

External Symmetry = 1.0

Principal Moments of Inertia = 293.207035407 475.362187451 535.059192039

Electronic Degeneracy = 2

Thermodynamic Data

Translational Contributions						
Temperature	298.00	300.00	400.00	500.00	600.00	
800.00	1000.00	1500.00				
Entropy	40.83	40.86	42.29	43.40	44.30	
45.73	46.84	48.85				
Cp	4.97	4.97	4.97	4.97	4.97	
4.97	4.97	4.97				
dH	1.48	1.49	1.99	2.48	2.98	
3.97	4.97	7.45				
q _{trans}	6.86e+07	6.98e+07	1.43e+08	2.50e+08	3.95e+08	
8.10e+08	1.42e+09	3.90e+09				

Translational Contributions

Temperature	298.15
Entropy	40.83
Cp	4.97
dH	1.48
q _{trans}	6.87e+07

Vibrational Contributions

Entropy:						
Temperature	298.00	300.00	400.00	500.00	600.00	
800.00	1000.00	1500.00				
Entropy	36.97	37.25	50.68	63.46	75.53	
97.53	116.99	157.11				
Cp	41.01	41.24	52.45	62.14	70.19	
82.58	91.62	105.57				
dH	6.21	6.29	10.99	16.74	23.38	
38.74	56.23	105.98				
q _{vib}	3.34e+03	3.59e+03	1.17e+05	3.56e+06	9.80e+07	
5.39e+10	1.90e+13	7.87e+18				

Vibrational Contributions

Entropy:	
Temperature	298.15
Entropy	36.99
Cp	41.02
dH	6.22
q _{vib}	3.36e+03

External Rotational Contributions

Temperature	298.00	300.00	400.00	500.00	600.00	
800.00	1000.00	1500.00				
Entropy	29.61	29.63	30.48	31.15	31.69	
32.55	33.22	34.42				
Cp	2.98	2.98	2.98	2.98	2.98	
2.98	2.98	2.98				
dH	0.89	0.89	1.19	1.49	1.79	
2.38	2.98	4.47				
q _{rot}	659194.81	665842.12	1025131.00	1432664.13	1883285.91	
2899508.33	4052186.08	7444341.18				

External Rotational Contributions

Temperature	298.15
Entropy	29.61
Cp	2.98
dH	0.89

q_rot 659692.58

Hf298 S298 Cps:

-62.9375650765 108.804291829 48.9543302547 49.1893351467 60.3978173105
70.0839492159 78.142220668 90.5304596092 99.5639975706 113.515686605 Molecule
2:

Geometry:

Mass(amu)	X(ang)	Y(ang)	Z(ang)
12.000	1.5960	0.5723	-1.6443
12.000	1.5963	0.4542	-0.1158
12.000	2.9993	0.5192	0.5018
12.000	0.6667	1.5005	0.5016
12.000	-1.8202	-0.7042	0.1922
15.995	-1.2818	-1.0799	-1.0276
15.995	-0.3444	-2.1695	-0.8994
15.995	0.8311	2.1415	1.4804
12.000	-1.5836	-1.3038	1.3555
12.000	-2.6820	0.4966	-0.0489
1.008	1.1171	-0.4953	0.1483
1.008	2.1961	-0.2313	-2.0772
1.008	0.5822	0.4901	-2.0375
1.008	2.0239	1.5274	-1.9633
1.008	2.9527	0.4456	1.5899
1.008	3.6165	-0.2989	0.1209
1.008	3.4900	1.4630	0.2492
1.008	-0.9175	-2.1490	1.4353
1.008	-2.0545	-0.9237	2.2505
1.008	-0.9049	-2.9249	-1.1313
1.008	-3.1854	0.7861	0.8730
1.008	-3.4319	0.2891	-0.8172
1.008	-2.0614	1.3298	-0.3889

Frequencies (cm-1):

Imaginary Frequency: -1.983914995e-05

33.204	48.634	63.620
77.695	86.781	107.310
161.387	167.001	178.258
212.721	245.850	266.142
326.569	360.927	409.287
448.129	502.780	553.069
588.825	741.190	748.315
848.890	861.531	884.041
923.651	944.332	959.952
969.447	1022.085	1060.886
1071.147	1139.587	1185.439
1259.395	1282.618	1325.337
1369.406	1395.382	1399.356
1415.683	1426.061	1466.620
1481.750	1484.466	1485.434
1497.966	1503.149	1717.260
1905.386	3015.008	3018.299
3020.235	3035.119	3078.434
3078.626	3085.070	3096.229
3110.602	3119.616	3164.808
3257.616	3732.578	

External Symmetry = 1.0

Principal Moments of Inertia = 325.491243242 624.670457712 756.559128497
 Electronic Degeneracy = 2

Thermodynamic Data

Translational Contributions

Temperature	298.00	300.00	400.00	500.00	600.00
800.00	1000.00	1500.00			
Entropy	40.83	40.86	42.29	43.40	44.30
45.73	46.84	48.85			
Cp	4.97	4.97	4.97	4.97	4.97
4.97	4.97	4.97			
dH	1.48	1.49	1.99	2.48	2.98
3.97	4.97	7.45			
qtrans	6.86e+07	6.98e+07	1.43e+08	2.50e+08	3.95e+08
8.10e+08	1.42e+09	3.90e+09			

Translational Contributions

Temperature	298.15
Entropy	40.83
Cp	4.97
dH	1.48
qtrans	6.87e+07

Vibrational Contributions

Entropy:

Temperature	298.00	300.00	400.00	500.00	600.00
800.00	1000.00	1500.00			
Entropy	46.79	47.06	60.19	72.62	84.35
105.76	124.74	164.01			
Cp	40.31	40.53	51.07	60.37	68.23
80.47	89.49	103.49			
dH	6.81	6.89	11.49	17.08	23.53
38.48	55.54	104.23			
q_vib	1.70e+05	1.84e+05	7.58e+06	2.56e+08	7.34e+09
4.00e+12	1.33e+15	4.55e+20			

Vibrational Contributions

Entropy:

Temperature	298.15
Entropy	46.81
Cp	40.33
dH	6.82
q_vib	1.71e+05

External Rotational Contributions

Temperature	298.00	300.00	400.00	500.00	600.00
800.00	1000.00	1500.00			
Entropy	30.33	30.35	31.20	31.87	32.41
33.27	33.93	35.14			
Cp	2.98	2.98	2.98	2.98	2.98
2.98	2.98	2.98			
dH	0.89	0.89	1.19	1.49	1.79
2.38	2.98	4.47			
q_rot	946738.26	956285.16	1472297.31	2057598.05	2704782.87
4164285.65	5819766.12	10691593.07			

External Rotational Contributions

Temperature 298.15
 Entropy 30.33
 Cp 2.98
 dH 0.89
 q_rot 947453.17

Hf298 S298 Cps:

-42.46155114 228.151929636 48.2636394727 48.4806700855 59.0149914753
 68.322122191 76.1772156277 88.4204870616 97.4394046049 111.438224292

Rate Data: Modified Arrhenius format

$r = A*(T/1000)^n*\exp(-Ea/R/T)$ 3.90e+15 0.04 12.53

$r = A*T^n*\exp(-Ea/R/T)$ 2.94e+15 0.04 12.53

Temperature	Rate	Fit Rate
298.00	2.39e+06	2.38e+06
300.00	2.75e+06	2.75e+06
400.00	5.27e+08	5.33e+08
500.00	1.25e+10	1.26e+10
600.00	1.04e+11	1.04e+11
800.00	1.47e+12	1.46e+12
1000.00	7.16e+12	7.11e+12
1500.00	5.88e+13	5.92e+13

Rate Data: Arrhenius format

$r = A*\exp(-Ea/R/T)$ 3.99e+15 12.58

Temperature	Rate	Fit Rate
298.00	2.39e+06	2.37e+06
300.00	2.75e+06	2.74e+06
400.00	5.27e+08	5.35e+08
500.00	1.25e+10	1.27e+10
600.00	1.04e+11	1.05e+11
800.00	1.47e+12	1.46e+12
1000.00	7.16e+12	7.11e+12
1500.00	5.88e+13	5.87e+13

α -Qt1 \rightarrow α -M3

Molecule 1:

Geometry:

Mass(amu)	X(ang)	Y(ang)	Z(ang)
12.000	-1.1971	-0.2753	-0.9954
1.008	-1.4197	0.2663	1.9561
12.000	0.1371	-0.5953	-0.5173
15.995	0.6688	-1.6579	-0.8566
12.000	0.9713	0.3724	0.3709
12.000	-1.9150	1.0259	-0.8127
1.008	-2.9088	0.8527	-0.3774
1.008	-1.3827	1.7387	-0.1903
1.008	-2.1053	1.4860	-1.7919
12.000	-1.9054	-1.3102	-1.8093
1.008	-2.0713	-0.9454	-2.8319
1.008	-1.3327	-2.2336	-1.8574
1.008	-2.8996	-1.5147	-1.3930
12.000	2.0690	-0.3917	1.1114
1.008	2.7175	-0.9091	0.4061
1.008	2.6566	0.3137	1.7030
1.008	1.6308	-1.1333	1.7784
12.000	1.5658	1.4917	-0.4958
1.008	0.7958	2.0470	-1.0337
1.008	2.2516	1.0550	-1.2242
15.995	-0.4936	0.1263	2.1967
15.995	0.1532	1.0910	1.3193
1.008	2.1210	2.1896	0.1346

Frequencies (cm-1):

41.602	66.719	81.148
110.014	144.889	173.492
194.886	220.164	239.110
251.509	280.944	334.116
350.216	354.219	380.988
407.677	494.394	534.103
572.626	651.295	709.364
835.589	889.519	921.798
942.664	946.785	953.329
960.725	1018.881	1039.582
1077.442	1178.800	1216.505
1237.360	1270.919	1351.121
1360.347	1388.547	1394.210
1404.630	1411.799	1458.149
1469.641	1473.448	1481.574
1490.945	1492.435	1504.758
1510.296	1566.720	2973.137
2983.528	3002.357	3019.745
3029.041	3041.025	3101.086
3107.157	3116.073	3132.668
3132.886	3151.021	3752.616

External Symmetry = 1.0

Principal Moments of Inertia = 294.388029391 472.098246464 542.169390049

Electronic Degeneracy = 2

Thermodynamic Data

Translational Contributions						
Temperature	298.00	300.00	400.00	500.00	600.00	
800.00	1000.00	1500.00				
Entropy	40.83	40.86	42.29	43.40	44.30	
45.73	46.84	48.85				
Cp	4.97	4.97	4.97	4.97	4.97	
4.97	4.97	4.97				
dH	1.48	1.49	1.99	2.48	2.98	
3.97	4.97	7.45				
q _{trans}	6.86e+07	6.98e+07	1.43e+08	2.50e+08	3.95e+08	
8.10e+08	1.42e+09	3.90e+09				

Translational Contributions

Temperature	298.15
Entropy	40.83
Cp	4.97
dH	1.48
q _{trans}	6.87e+07

Vibrational Contributions

Entropy:						
Temperature	298.00	300.00	400.00	500.00	600.00	
800.00	1000.00	1500.00				
Entropy	40.73	41.00	54.18	66.76	78.68	
100.51	119.89	159.96				
Cp	40.25	40.48	51.52	61.26	69.46	
82.13	91.36	105.52				
dH	6.39	6.47	11.08	16.74	23.30	
38.54	55.96	105.65				
q _{vib}	1.64e+04	1.76e+04	6.10e+05	1.87e+07	5.13e+08	
2.74e+11	9.38e+13	3.69e+19				

Vibrational Contributions

Entropy:	
Temperature	298.15
Entropy	40.75
Cp	40.27
dH	6.40
q _{vib}	1.65e+04

External Rotational Contributions

Temperature	298.00	300.00	400.00	500.00	600.00	
800.00	1000.00	1500.00				
Entropy	29.62	29.64	30.49	31.16	31.70	
32.56	33.23	34.43				
Cp	2.98	2.98	2.98	2.98	2.98	
2.98	2.98	2.98				
dH	0.89	0.89	1.19	1.49	1.79	
2.38	2.98	4.47				
q _{rot}	662608.67	669290.41	1030440.00	1440083.67	1893039.15	
2914524.43	4073171.72	7482894.27				

External Rotational Contributions

Temperature	298.15
Entropy	29.62
Cp	2.98
dH	0.89

q_rot 663109.03

Hf298 S298 Cps:

-63.4235299336 112.571758603 48.2000375189 48.4278779019 59.4667540111
69.2117288736 77.4098919342 90.0816057774 99.3101230528 113.465388756
Molecule
2:

Geometry:

Mass(amu)	X(ang)	Y(ang)	Z(ang)
12.000	-1.0615	-0.8063	-0.9359
1.008	-0.7886	-0.7567	1.2407
12.000	0.2562	-0.6073	-1.0658
15.995	1.3468	-0.8569	-1.4547
12.000	0.8542	0.9326	0.6091
12.000	-2.1204	0.2473	-0.7226
1.008	-2.8192	-0.0434	0.0698
1.008	-1.7132	1.2179	-0.4562
1.008	-2.7077	0.3629	-1.6417
12.000	-1.5553	-2.1886	-1.3483
1.008	-2.1161	-2.1293	-2.2895
1.008	-0.7358	-2.8955	-1.4864
1.008	-2.2319	-2.5965	-0.5893
12.000	2.0629	0.2190	1.1345
1.008	2.7760	0.0481	0.3302
1.008	2.5358	0.8464	1.9030
1.008	1.8001	-0.7334	1.5897
12.000	1.0440	2.2068	-0.1556
1.008	0.0977	2.6012	-0.5275
1.008	1.7124	2.0266	-0.9996
15.995	-0.5522	-0.2389	2.0419
15.995	-0.2352	1.0349	1.4264
1.008	1.5038	2.9739	0.4836

Frequencies (cm-1):

Imaginary Frequency: -180.523565868

49.902	70.336	125.517
130.868	147.190	152.849
176.759	191.003	209.969
243.039	269.855	292.497
323.666	366.358	382.091
393.954	496.898	531.034
561.514	594.105	731.020
799.622	890.847	950.652
980.873	984.752	990.337
1000.341	1011.142	1084.211
1099.647	1175.614	1260.417
1278.515	1363.224	1396.192
1397.664	1404.818	1427.007
1448.296	1461.424	1467.077
1471.566	1481.599	1485.593
1486.694	1490.821	1510.915
2006.149	2973.256	2981.267
2983.074	2990.951	3027.916
3031.705	3067.099	3094.658
3100.125	3112.001	3145.828
3154.719	3453.616	

External Symmetry = 1.0

Principal Moments of Inertia = 308.275666603 499.427743042 582.86208209
 Electronic Degeneracy = 2

Thermodynamic Data

Translational Contributions

Temperature	298.00	300.00	400.00	500.00	600.00
800.00	1000.00	1500.00			
Entropy	40.83	40.86	42.29	43.40	44.30
45.73	46.84	48.85			
Cp	4.97	4.97	4.97	4.97	4.97
4.97	4.97	4.97			
dH	1.48	1.49	1.99	2.48	2.98
3.97	4.97	7.45			
qtrans	6.86e+07	6.98e+07	1.43e+08	2.50e+08	3.95e+08
8.10e+08	1.42e+09	3.90e+09			

Translational Contributions

Temperature	298.15
Entropy	40.83
Cp	4.97
dH	1.48
qtrans	6.87e+07

Vibrational Contributions

Entropy:

Temperature	298.00	300.00	400.00	500.00	600.00
800.00	1000.00	1500.00			
Entropy	40.39	40.66	53.71	66.05	77.72
99.06	118.03	157.34			
Cp	40.07	40.29	50.71	60.00	67.91
80.33	89.50	103.64			
dH	6.44	6.52	11.09	16.64	23.05
37.96	55.01	103.75			
q_vib	1.27e+04	1.36e+04	4.79e+05	1.45e+07	3.87e+08
1.90e+11	5.93e+13	1.86e+19			

Vibrational Contributions

Entropy:

Temperature	298.15
Entropy	40.41
Cp	40.09
dH	6.45
q_vib	1.27e+04

External Rotational Contributions

Temperature	298.00	300.00	400.00	500.00	600.00
800.00	1000.00	1500.00			
Entropy	29.79	29.81	30.67	31.33	31.88
32.73	33.40	34.61			
Cp	2.98	2.98	2.98	2.98	2.98
2.98	2.98	2.98			
dH	0.89	0.89	1.19	1.49	1.79
2.38	2.98	4.47			
q_rot	723106.41	730398.20	1124521.59	1571566.70	2065878.08
3180627.38	4445061.89	8166100.13			

External Rotational Contributions

Temperature	298.15
Entropy	29.79
Cp	2.98
dH	0.89
q_rot	723652.44

Hf298 S298 Cps:

-30.8451913702 224.983603306 48.0218516307 48.2365329135 58.660389664
67.9487452894 75.8588058852 88.2806684627 97.4488582483 111.590869678

Rate Data: Modified Arrhenius format

$r = A*(T/1000)^n*\exp(-Ea/R/T)$ 1.93e+13 0.24 24.36

$r = A*T^n*\exp(-Ea/R/T)$ 3.73e+12 0.24 24.36

Temperature	Rate	Fit Rate
298.00	1.97e-05	1.96e-05
300.00	2.60e-05	2.59e-05
400.00	7.46e-01	7.58e-01
500.00	3.64e+02	3.67e+02
600.00	2.29e+04	2.28e+04
800.00	4.09e+06	4.04e+06
1000.00	9.23e+07	9.14e+07
1500.00	5.93e+09	5.99e+09

Rate Data: Arrhenius format

$r = A*\exp(-Ea/R/T)$ 2.19e+13 24.62

Temperature	Rate	Fit Rate
298.00	1.97e-05	1.92e-05
300.00	2.60e-05	2.53e-05
400.00	7.46e-01	7.72e-01
500.00	3.64e+02	3.79e+02
600.00	2.29e+04	2.36e+04
800.00	4.09e+06	4.12e+06
1000.00	9.23e+07	9.12e+07
1500.00	5.93e+09	5.67e+09

α -M1 \rightarrow α -P1

Molecule 1:

Geometry:

Mass(amu)	X(ang)	Y(ang)	Z(ang)
12.000	-0.9354	-0.2340	0.8572
15.995	-0.9320	-0.1779	2.0346
12.000	0.3370	-0.2211	-0.0429
1.008	-0.1348	1.6974	-2.0826
12.000	1.2948	0.8722	0.4317
1.008	1.5563	0.7131	1.4786
1.008	2.2026	0.8473	-0.1766
1.008	0.8276	1.8527	0.3374
12.000	0.9468	-1.6233	0.0098
1.008	1.2617	-1.8506	1.0293
1.008	1.8144	-1.6629	-0.6523
15.995	-0.7586	1.1915	-1.5437
15.995	-0.0305	-0.0599	-1.4088
1.008	0.2215	-2.3692	-0.3185

Frequencies (cm⁻¹):

74.283	149.042	205.747
223.822	239.285	280.282
289.247	340.623	359.097
441.074	504.702	584.675
692.709	840.801	908.460
940.965	952.825	1010.685
1178.214	1194.241	1211.489
1360.122	1386.176	1406.107
1469.260	1481.584	1487.777
1509.145	1916.394	3026.722
3031.796	3101.722	3106.146
3116.266	3119.032	3754.484

External Symmetry = 1.0

Principal Moments of Inertia = 149.767711643 224.284364073 264.127311378

Electronic Degeneracy = 2

Thermodynamic Data

Translational Contributions

Temperature	298.00	300.00	400.00	500.00	600.00
800.00	1000.00	1500.00			
Entropy	39.81	39.84	41.27	42.38	43.28
44.71	45.82	47.83			
Cp	4.97	4.97	4.97	4.97	4.97
4.97	4.97	4.97			
dH	1.48	1.49	1.99	2.48	2.98
3.97	4.97	7.45			
qtrans	4.11e+07	4.18e+07	8.57e+07	1.50e+08	2.36e+08
4.85e+08	8.47e+08	2.33e+09			

Translational Contributions

Temperature	298.15
Entropy	39.81
Cp	4.97
dH	1.48
qtrans	4.11e+07

Vibrational Contributions

Entropy:

Temperature	298.00	300.00	400.00	500.00	600.00
800.00	1000.00	1500.00			
Entropy	21.24	21.40	29.29	36.74	43.74
56.46	67.67	90.71			
Cp	24.16	24.29	30.67	36.13	40.67
47.64	52.71	60.53			
dH	3.63	3.68	6.44	9.79	13.64
22.52	32.59	61.15			
q_vib	9.57e+01	9.97e+01	7.67e+02	5.65e+03	3.92e+04
1.54e+06	4.64e+07	8.21e+10			

Vibrational Contributions

Entropy:

Temperature	298.15
Entropy	21.25
Cp	24.17
dH	3.63
q_vib	9.60e+01

External Rotational Contributions

Temperature	298.00	300.00	400.00	500.00	600.00
800.00	1000.00	1500.00			
Entropy	27.49	27.51	28.37	29.03	29.58
30.44	31.10	32.31			
Cp	2.98	2.98	2.98	2.98	2.98
2.98	2.98	2.98			
dH	0.89	0.89	1.19	1.49	1.79
2.38	2.98	4.47			
q_rot	227367.61	229660.39	353585.29	494150.47	649577.66
1000090.24	1397668.60	2567681.17			

External Rotational Contributions

Temperature	298.15
Entropy	27.49
Cp	2.98
dH	0.89
q_rot	227539.31

Hf298 S298 Cps:

-44.886125871 89.9316407641 32.1069820756 32.2420940795 38.615656658
 44.0763558802 48.6157251591 55.5895485368 60.6612841465 68.4738770423Molecule
 2:

Geometry:

Mass(amu)	X(ang)	Y(ang)	Z(ang)
12.000	-0.6953	-0.3190	1.3360
15.995	-1.0295	0.6917	1.8793
12.000	0.4631	-0.5415	0.4725
1.008	-1.4659	0.6994	-0.8821
12.000	1.4665	0.5183	0.3229
1.008	2.4837	0.1239	0.2644

1.008	1.2652	1.0055	-0.6716
1.008	1.3812	1.2919	1.0859
12.000	0.7011	-1.8922	-0.1062
1.008	-0.2094	-2.4912	-0.1178
1.008	1.4585	-2.4240	0.4848
15.995	-0.7980	0.1637	-1.3513
1.008	1.0880	-1.7998	-1.1247
15.995	-0.0025	1.0474	-1.9869

Frequencies (cm-1):

Imaginary Frequency: -81.2077535007

68.297	89.568	163.385
175.581	222.749	239.758
279.919	314.503	374.075
465.208	584.037	605.172
774.391	889.907	975.065
993.481	1011.340	1069.992
1256.997	1285.382	1374.811
1395.120	1399.557	1433.198
1458.875	1472.267	1479.393
1798.862	2598.543	2991.109
3047.004	3057.166	3112.383
3119.061	3596.249	

External Symmetry = 1.0

Principal Moments of Inertia = 172.71675395 243.428197359 296.003326876

Electronic Degeneracy = 2

Thermodynamic Data

Translational Contributions

Temperature	298.00	300.00	400.00	500.00	600.00
800.00	1000.00	1500.00			
Entropy	39.81	39.84	41.27	42.38	43.28
44.71	45.82	47.83			
Cp	4.97	4.97	4.97	4.97	4.97
4.97	4.97	4.97			
dH	1.48	1.49	1.99	2.48	2.98
3.97	4.97	7.45			
qtrans	4.11e+07	4.18e+07	8.57e+07	1.50e+08	2.36e+08
4.85e+08	8.47e+08	2.33e+09			

Translational Contributions

Temperature	298.15
Entropy	39.81
Cp	4.97
dH	1.48
qtrans	4.11e+07

Vibrational Contributions

Entropy:

Temperature	298.00	300.00	400.00	500.00	600.00
800.00	1000.00	1500.00			
Entropy	23.24	23.39	31.01	38.18	44.94
57.26	68.15	90.59			
Cp	23.43	23.55	29.55	34.83	39.29
46.23	51.28	58.97			
dH	3.74	3.79	6.45	9.68	13.40
22.00	31.79	59.61			
q_vib	2.15e+02	2.24e+02	1.78e+03	1.30e+04	8.75e+04
3.19e+06	8.86e+07	1.30e+11			

Vibrational Contributions

Entropy:
 Temperature 298.15
 Entropy 23.25
 Cp 23.44
 dH 3.75
 q_vib 2.16e+02

External Rotational Contributions

Temperature	298.00	300.00	400.00	500.00	600.00
800.00	1000.00	1500.00			
Entropy	27.83	27.85	28.71	29.37	29.91
30.77	31.44	32.65			
Cp	2.98	2.98	2.98	2.98	2.98
2.98	2.98	2.98			
dH	0.89	0.89	1.19	1.49	1.79
2.38	2.98	4.47			
q_rot	269286.34	272001.82	418774.20	585254.73	769337.32
1184472.30	1655350.36	3041072.79			

External Rotational Contributions

Temperature	298.15
Entropy	27.83
Cp	2.98
dH	0.89
q_rot	269489.69

Hf298 S298 Cps:

19.2708812371 182.192858134 31.3755832144 31.5001086084 37.495337107
 42.7783958415 47.2431631581 54.1777313331 59.2268422826 66.92261418

Rate Data: Modified Arrhenius format

$r = A \cdot (T/1000)^n \cdot \exp(-E_a/R/T)$ 6.20e+13 0.32 58.59

$r = A \cdot T^n \cdot \exp(-E_a/R/T)$ 6.65e+12 0.32 58.59

Temperature	Rate	Fit Rate
298.00	4.50e-30	4.49e-30
300.00	8.71e-30	8.70e-30
400.00	4.46e-19	4.48e-19
500.00	1.21e-12	1.22e-12
600.00	2.39e-08	2.39e-08
800.00	5.70e-03	5.68e-03
1000.00	9.74e+00	9.71e+00
1500.00	2.05e+05	2.05e+05

Rate Data: Arrhenius format

$r = A \cdot \exp(-E_a/R/T)$ 7.39e+13 58.95

Temperature	Rate	Fit Rate
298.00	4.50e-30	4.35e-30
300.00	8.71e-30	8.45e-30
400.00	4.46e-19	4.60e-19
500.00	1.21e-12	1.27e-12
600.00	2.39e-08	2.50e-08
800.00	5.70e-03	5.83e-03
1000.00	9.74e+00	9.69e+00
1500.00	2.05e+05	1.91e+05

α -M2 \rightarrow α -P2

Molecule 1:

Geometry:

Mass(amu)	X(ang)	Y(ang)	Z(ang)
12.000	-0.0289	-0.6034	-1.7372
12.000	-0.0283	-0.6214	-0.2024
12.000	1.3808	-0.6083	0.4029
12.000	-0.8837	0.5348	0.3315
15.995	-0.6181	1.2968	1.1931
1.008	-0.5690	-1.5172	0.1307
1.008	0.5008	-1.4778	-2.1228
1.008	-1.0464	-0.6108	-2.1334
1.008	0.4770	0.2901	-2.1136
1.008	1.3404	-0.6067	1.4936
1.008	1.9434	-1.4862	0.0740
1.008	1.9251	0.2853	0.0867

Frequencies (cm-1):

62.455	213.382	240.032
264.522	356.424	445.772
594.836	742.261	877.750
939.339	965.549	1063.061
1132.256	1182.354	1279.080
1313.904	1397.521	1416.308
1480.636	1486.109	1497.236
1503.458	1911.816	2998.194
3016.630	3019.840	3081.175
3086.343	3095.253	3098.704

External Symmetry = 1.0

Principal Moments of Inertia = 63.7204083278 125.182667208 170.561551506

Electronic Degeneracy = 2

Thermodynamic Data

Translational Contributions

Temperature	298.00	300.00	400.00	500.00	600.00
800.00	1000.00	1500.00			
Entropy	38.70	38.73	40.16	41.27	42.17
43.60	44.71	46.73			
Cp	4.97	4.97	4.97	4.97	4.97
4.97	4.97	4.97			
dH	1.48	1.49	1.99	2.48	2.98
3.97	4.97	7.45			
qtrans	2.35e+07	2.39e+07	4.91e+07	8.58e+07	1.35e+08
2.78e+08	4.85e+08	1.34e+09			

Translational Contributions

Temperature	298.15
Entropy	38.70
Cp	4.97
dH	1.48
qtrans	2.35e+07

Vibrational Contributions

Entropy:

Temperature	298.00	300.00	400.00	500.00	600.00
800.00	1000.00	1500.00			

Entropy	13.33	13.43	18.57	23.71	28.75
38.28	46.98	65.42			
Cp	15.19	15.30	20.63	25.52	29.74
36.45	41.43	49.10			
dH	2.20	2.23	4.03	6.35	9.12
15.78	23.60	46.48			
q_vib	1.99e+01	2.04e+01	7.17e+01	2.56e+02	9.16e+02
1.14e+04	1.29e+05	3.35e+07			

Vibrational Contributions

Entropy:

Temperature	298.15
Entropy	13.33
Cp	15.20
dH	2.20
q_vib	1.99e+01

External Rotational Contributions

Temperature	298.00	300.00	400.00	500.00	600.00
800.00	1000.00	1500.00			
Entropy	25.63	25.65	26.51	27.17	27.71
28.57	29.24	30.45			
Cp	2.98	2.98	2.98	2.98	2.98
2.98	2.98	2.98			
dH	0.89	0.89	1.19	1.49	1.79
2.38	2.98	4.47			
q_rot	89035.93	89933.77	138462.09	193506.66	254371.10
391629.94	547319.47	1005490.08			

External Rotational Contributions

Temperature	298.15
Entropy	25.63
Cp	2.98
dH	0.89
q_rot	89103.16

Hf298 S298 Cps:

-17.73536204 79.0408056876 23.1377507974 23.2450322083 28.5823877079
 33.4705074969 37.6933215821 44.3992194102 49.3774920774 57.0482866873Molecule
 2:

Geometry:

Mass(amu)	X(ang)	Y(ang)	Z(ang)
12.000	-0.4725	-0.6065	-1.8987
12.000	-0.9647	-0.6162	-0.4676
12.000	3.7281	-0.7006	1.2559
12.000	-1.1912	0.4697	0.2297
15.995	-1.3926	1.4355	0.8498
1.008	-1.1384	-1.5553	0.0448
1.008	0.5010	-1.0989	-1.9807
1.008	-1.1724	-1.1305	-2.5562
1.008	-0.3620	0.4118	-2.2760
1.008	3.3473	-0.6898	2.2671

1.008	3.9010	-1.6416	0.7534
1.008	3.9293	0.2301	0.7451

Frequencies (cm-1):

Imaginary Frequency: -34.5408539045

0.000	0.000	0.000
14.635	23.461	138.150
210.368	503.579	514.800
557.956	653.846	897.628
1049.609	1077.737	1149.037
1396.023	1397.007	1405.498
1412.549	1479.190	1504.955
2210.270	3006.952	3056.483
3088.211	3090.499	3164.881
3267.423	3268.408	

External Symmetry = 1.0

Principal Moments of Inertia = 124.048704451 320.620425237 419.025335052

Electronic Degeneracy = 2

Thermodynamic Data

Translational Contributions

Temperature	298.00	300.00	400.00	500.00	600.00
800.00	1000.00	1500.00			
Entropy	38.70	38.73	40.16	41.27	42.17
43.60	44.71	46.73			
Cp	4.97	4.97	4.97	4.97	4.97
4.97	4.97	4.97			
dH	1.48	1.49	1.99	2.48	2.98
3.97	4.97	7.45			
qtrans	2.35e+07	2.39e+07	4.91e+07	8.58e+07	1.35e+08
2.78e+08	4.85e+08	1.34e+09			

Translational Contributions

Temperature	298.15
Entropy	38.70
Cp	4.97
dH	1.48
qtrans	2.35e+07

Vibrational Contributions

Entropy:					
Temperature	298.00	300.00	400.00	500.00	600.00
800.00	1000.00	1500.00			
Entropy	120.76	120.90	127.30	133.15	138.56
148.32	156.95	174.92			
Cp	20.23	20.32	24.37	28.05	31.27
36.59	40.76	47.59	4.31	6.54	9.17
dH	4.27	4.31	6.54	9.17	12.15
18.96	26.72	49.02			
q_vib	1.84e+23	1.93e+23	1.76e+24	1.23e+25	7.19e+25
1.71e+27	2.89e+28	1.22e+31			

Vibrational Contributions

Entropy:	
Temperature	298.15
Entropy	120.77
Cp	20.24
dH	4.27
q_vib	1.84e+23

External Rotational Contributions						
Temperature	298.00	300.00	400.00	500.00	600.00	
800.00	1000.00	1500.00				
Entropy	28.12	28.14	29.00	29.66	30.20	
31.06	31.73	32.94				
Cp	2.98	2.98	2.98	2.98	2.98	
2.98	2.98	2.98				
dH	0.89	0.89	1.19	1.49	1.79	
2.38	2.98	4.47				
q_rot	311619.91	314762.28	484608.24	677260.60	890282.18	
1370679.09	1915582.26	3519149.32				

External Rotational Contributions

Temperature	298.15
Entropy	28.12
Cp	2.98
dH	0.89
q_rot	311855.23

Hf298 S298 Cps:

23.4534058958	268.009666095	28.1816598195	28.2643232541	32.3165520974
35.9976448317	39.2201124327	44.5390553216	48.7123620871	55.5411980942

Rate Data: Modified Arrhenius format

$r = A \cdot (T/1000)^n \cdot \exp(-E_a/R/T)$ 4.37e+37 1.60 36.61

$r = A \cdot T^n \cdot \exp(-E_a/R/T)$ 7.03e+32 1.60 36.61

Temperature	Rate	Fit Rate
298.00	9.21e+09	9.00e+09
300.00	1.40e+10	1.37e+10
400.00	9.53e+16	1.01e+17
500.00	1.39e+21	1.44e+21
600.00	8.95e+23	8.96e+23
800.00	3.21e+27	3.06e+27
1000.00	4.61e+29	4.37e+29
1500.00	3.70e+32	3.88e+32

Rate Data: Arrhenius format

$r = A \cdot \exp(-E_a/R/T)$ 1.04e+38 38.36

Temperature	Rate	Fit Rate
298.00	9.21e+09	7.71e+09
300.00	1.40e+10	1.19e+10
400.00	9.53e+16	1.15e+17
500.00	1.39e+21	1.79e+21
600.00	8.95e+23	1.11e+24
800.00	3.21e+27	3.46e+27
1000.00	4.61e+29	4.31e+29
1500.00	3.70e+32	2.68e+32

α -M3 \rightarrow α -P3

Molecule 1:

Geometry:

Mass(amu)	X(ang)	Y(ang)	Z(ang)
1.008	0.0545	-0.5617	-1.8902
12.000	-0.2440	0.1136	0.6767
12.000	1.1756	0.6159	0.5287
1.008	1.2191	1.6827	0.7700
1.008	1.8258	0.1032	1.2445
1.008	1.5330	0.4477	-0.4859
12.000	-0.8942	0.2834	2.0323
1.008	-0.9250	1.3435	2.3029
1.008	-0.3016	-0.2236	2.8001
15.995	0.7257	-0.5226	-2.6115
15.995	-0.8484	-0.4055	-0.2432
1.008	-1.9040	-0.1233	2.0140

Frequencies (cm-1):

0.000	49.103	82.772
126.023	185.296	398.730
488.051	548.206	562.229
566.851	792.051	885.497
897.831	1089.470	1117.295
1246.511	1384.554	1390.678
1456.498	1458.426	1468.810
1481.012	1766.082	3012.590
3019.556	3069.001	3076.585
3129.722	3131.487	3493.968

External Symmetry = 1.0

Principal Moments of Inertia = 54.6258845077 216.865232259 265.262297596

Electronic Degeneracy = 2

Thermodynamic Data

Translational Contributions

Temperature	298.00	300.00	400.00	500.00	600.00
800.00	1000.00	1500.00			
Entropy	38.86	38.89	40.32	41.43	42.34
43.77	44.87	46.89			
Cp	4.97	4.97	4.97	4.97	4.97
4.97	4.97	4.97			
dH	1.48	1.49	1.99	2.48	2.98
3.97	4.97	7.45			
qtrans	2.55e+07	2.60e+07	5.33e+07	9.31e+07	1.47e+08
3.01e+08	5.27e+08	1.45e+09			

Translational Contributions

Temperature	298.15
Entropy	38.86
Cp	4.97
dH	1.48
qtrans	2.56e+07

Vibrational Contributions

Entropy:					
Temperature	298.00	300.00	400.00	500.00	600.00
800.00	1000.00	1500.00			

Entropy	51.82	51.95	58.13	63.98	69.50
79.59	88.58	107.28			
Cp	18.96	19.07	24.05	28.41	32.12
38.01	42.44	49.49			
dH	3.29	3.33	5.49	8.12	11.16
18.21	26.28	49.49			
q_vib	8.14e+08	8.45e+08	5.05e+09	2.70e+10	1.33e+11
2.63e+12	4.11e+13	1.72e+16			

Vibrational Contributions

Entropy:

Temperature	298.15
Entropy	51.83
Cp	18.97
dH	3.30
q_vib	8.16e+08

External Rotational Contributions

Temperature	298.00	300.00	400.00	500.00	600.00
800.00	1000.00	1500.00			
Entropy	26.46	26.48	27.34	28.00	28.55
29.40	30.07	31.28			
Cp	2.98	2.98	2.98	2.98	2.98
2.98	2.98	2.98			
dH	0.89	0.89	1.19	1.49	1.79
2.38	2.98	4.47			
q_rot	135314.81	136679.32	210431.58	294087.07	386587.50
595190.39	831803.85	1528121.25			

External Rotational Contributions

Temperature	298.15
Entropy	26.46
Cp	2.98
dH	0.89
q_rot	135416.99

Hf298 S298 Cps:

-52.573507791 118.531811283 26.9134765946 27.0173362057 31.9942142531
 36.3601961889 40.069798234 45.9551988594 50.3931087461 57.4375440433Molecule
 2:

Geometry:

Mass(amu)	X(ang)	Y(ang)	Z(ang)
1.008	-0.6838	-0.0014	-5.2419
12.000	0.2124	0.0000	1.7005
12.000	1.6176	-0.0040	2.2765
1.008	1.7628	0.8574	2.9361
1.008	1.7729	-0.9008	2.8849
1.008	2.3467	0.0215	1.4680
12.000	-0.9253	0.0064	2.7064
1.008	-0.8706	0.9036	3.3315
1.008	-0.8465	-0.8546	3.3776
15.995	-0.7907	-0.0002	-6.2112

15.995	0.0110	-0.0021	0.5078
1.008	-1.8799	-0.0187	2.1828

Frequencies (cm⁻¹):

Imaginary Frequency: -39.2650439464

49.668	81.008	124.666
186.959	393.404	486.873
492.927	530.935	558.343
756.427	880.569	947.382
1094.342	1118.661	1239.410
1380.304	1391.020	1447.341
1451.416	1470.594	1483.427
1770.852	2943.357	3014.211
3034.895	3094.436	3124.615
3136.440	3583.348	

External Symmetry = 1.0

Principal Moments of Inertia = 59.4213157595 896.817943285 950.002436348

Electronic Degeneracy = 2

Thermodynamic Data

Translational Contributions

Temperature	298.00	300.00	400.00	500.00	600.00
800.00	1000.00	1500.00			
Entropy	38.86	38.89	40.32	41.43	42.34
43.77	44.87	46.89			
Cp	4.97	4.97	4.97	4.97	4.97
4.97	4.97	4.97			
dH	1.48	1.49	1.99	2.48	2.98
3.97	4.97	7.45			
qtrans	2.55e+07	2.60e+07	5.33e+07	9.31e+07	1.47e+08
3.01e+08	5.27e+08	1.45e+09			

Translational Contributions

Temperature	298.15
Entropy	38.86
Cp	4.97
dH	1.48
qtrans	2.56e+07

Vibrational Contributions

Entropy:					
Temperature	298.00	300.00	400.00	500.00	600.00
800.00	1000.00	1500.00			
Entropy	18.38	18.49	24.16	29.60	34.77
44.32	52.87	70.78			
Cp	17.21	17.31	22.22	26.54	30.23
36.08	40.50	47.52			
dH	2.75	2.78	4.76	7.21	10.06
16.72	24.41	46.64			
q_vib	1.00e+02	1.04e+02	4.75e+02	2.07e+03	8.63e+03
1.31e+05	1.66e+06	4.73e+08			

Vibrational Contributions

Entropy:	
Temperature	298.15
Entropy	18.39
Cp	17.21
dH	2.75
q_vib	1.01e+02

External Rotational Contributions

Temperature	298.00	300.00	400.00	500.00	600.00
800.00	1000.00	1500.00			
Entropy	29.22	29.24	30.10	30.76	31.31
32.17	32.83	34.04			
Cp	2.98	2.98	2.98	2.98	2.98
2.98	2.98	2.98			
dH	0.89	0.89	1.19	1.49	1.79
2.38	2.98	4.47			
q_rot	543123.99	548600.85	844626.26	1180401.08	1551677.52
2388963.82	3338678.44	6133543.94			

External Rotational Contributions

Temperature	298.15
Entropy	29.22
Cp	2.98
dH	0.89
q_rot	543534.12

Hf298 S298 Cps:

-41.4293305224 206.380741441 25.1547510188 25.2571599841 30.1689008926
 34.4924885403 38.1764070373 44.0329543853 48.452811372 55.4709797046

Rate Data: Modified Arrhenius format

$r = A \cdot (T/1000)^n \cdot \exp(-E_a/R/T)$ 3.42e+06 0.05 6.06
 $r = A \cdot T^n \cdot \exp(-E_a/R/T)$ 2.49e+06 0.05 6.06

Temperature	Rate	Fit Rate
298.00	1.17e+02	1.17e+02
300.00	1.26e+02	1.26e+02
400.00	1.61e+03	1.61e+03
500.00	7.46e+03	7.47e+03
600.00	2.08e+04	2.08e+04
800.00	7.51e+04	7.50e+04
1000.00	1.63e+05	1.62e+05
1500.00	4.56e+05	4.57e+05

Rate Data: Arrhenius format

$r = A \cdot \exp(-E_a/R/T)$ 3.51e+06 6.11

Temperature	Rate	Fit Rate
298.00	1.17e+02	1.17e+02
300.00	1.26e+02	1.25e+02
400.00	1.61e+03	1.62e+03
500.00	7.46e+03	7.52e+03
600.00	2.08e+04	2.09e+04
800.00	7.51e+04	7.53e+04
1000.00	1.63e+05	1.62e+05
1500.00	4.56e+05	4.52e+05

α -Qp2 \rightarrow α -P4

Molecule 1:

Geometry:

Mass(amu)	X(ang)	Y(ang)	Z(ang)
12.000	1.0052	-0.0262	-2.0957
12.000	1.3246	-0.4657	-0.6503
12.000	2.8293	-0.4401	-0.3736
12.000	0.5832	0.4061	0.3557
12.000	-0.9722	0.3806	0.4074
15.995	-1.5477	-0.6880	-0.3776
15.995	-1.1848	-1.9654	0.2106
15.995	1.1532	1.1612	1.1100
12.000	-1.4473	0.3271	1.8174
12.000	-1.4931	1.6468	-0.3103
1.008	0.9407	-1.4814	-0.5234
1.008	1.5756	-0.6413	-2.7960
1.008	-0.0532	-0.1479	-2.3238
1.008	1.2913	1.0174	-2.2585
1.008	3.0507	-0.7609	0.6462
1.008	3.3490	-1.1049	-1.0683
1.008	3.2290	0.5695	-0.4924
1.008	-2.4973	0.1331	2.0019
1.008	-0.7957	0.6204	2.6266
1.008	-1.9589	-2.1471	0.7616
1.008	-1.0769	2.5240	0.1852
1.008	-2.5822	1.6777	-0.2519
1.008	-1.1943	1.6512	-1.3600

Frequencies (cm⁻¹):

61.902	72.552	161.793
194.022	205.333	215.944
218.270	227.709	246.408
261.698	273.602	302.741
312.174	329.975	364.883
401.120	462.205	520.182
566.356	601.978	687.730
759.655	844.425	876.733
913.391	936.583	945.991
973.244	995.022	1027.227
1055.010	1117.664	1133.278
1192.825	1211.601	1237.460
1315.281	1358.460	1376.075
1388.401	1398.112	1417.171
1425.133	1477.691	1483.288
1486.267	1491.836	1500.654
1518.453	1773.901	3015.352
3022.649	3032.782	3052.944
3077.487	3090.799	3095.834
3107.128	3117.240	3123.731
3131.600	3259.319	3746.965

External Symmetry = 1.0

Principal Moments of Inertia = 293.207035407 475.362187451 535.059192039

Electronic Degeneracy = 2

Thermodynamic Data

Translational Contributions						
Temperature	298.00	300.00	400.00	500.00	600.00	
800.00	1000.00	1500.00				
Entropy	40.83	40.86	42.29	43.40	44.30	
45.73	46.84	48.85				
Cp	4.97	4.97	4.97	4.97	4.97	
4.97	4.97	4.97				
dH	1.48	1.49	1.99	2.48	2.98	
3.97	4.97	7.45				
q _{trans}	6.86e+07	6.98e+07	1.43e+08	2.50e+08	3.95e+08	
8.10e+08	1.42e+09	3.90e+09				

Translational Contributions

Temperature	298.15
Entropy	40.83
Cp	4.97
dH	1.48
q _{trans}	6.87e+07

Vibrational Contributions

Entropy:						
Temperature	298.00	300.00	400.00	500.00	600.00	
800.00	1000.00	1500.00				
Entropy	36.97	37.25	50.68	63.46	75.53	
97.53	116.99	157.11				
Cp	41.01	41.24	52.45	62.14	70.19	
82.58	91.62	105.57				
dH	6.21	6.29	10.99	16.74	23.38	
38.74	56.23	105.98				
q _{vib}	3.34e+03	3.59e+03	1.17e+05	3.56e+06	9.80e+07	
5.39e+10	1.90e+13	7.87e+18				

Vibrational Contributions

Entropy:	
Temperature	298.15
Entropy	36.99
Cp	41.02
dH	6.22
q _{vib}	3.36e+03

External Rotational Contributions

Temperature	298.00	300.00	400.00	500.00	600.00	
800.00	1000.00	1500.00				
Entropy	29.61	29.63	30.48	31.15	31.69	
32.55	33.22	34.42				
Cp	2.98	2.98	2.98	2.98	2.98	
2.98	2.98	2.98				
dH	0.89	0.89	1.19	1.49	1.79	
2.38	2.98	4.47				
q _{rot}	659194.81	665842.12	1025131.00	1432664.13	1883285.91	
2899508.33	4052186.08	7444341.18				

External Rotational Contributions

Temperature	298.15
Entropy	29.61
Cp	2.98
dH	0.89

q_rot 659692.58

Hf298 S298 Cps:

-62.9375650765 108.804291829 48.9543302547 49.1893351467 60.3978173105
70.0839492159 78.142220668 90.5304596092 99.5639975706 113.515686605 Molecule
2:

Geometry:

Mass(amu)	X(ang)	Y(ang)	Z(ang)
12.000	1.2308	-0.5666	-2.1880
12.000	1.2564	-0.5492	-0.6577
12.000	2.7000	-0.5180	-0.1129
12.000	0.5103	0.6733	-0.1246
12.000	-0.1353	0.6480	1.2454
15.995	-1.9360	-1.3152	-0.9865
15.995	-2.5544	-1.2461	0.1852
15.995	0.4594	1.7060	-0.7617
12.000	-0.0985	-0.4322	2.0405
12.000	-0.8162	1.9281	1.6442
1.008	0.7603	-1.4530	-0.2959
1.008	1.7969	-1.4226	-2.5644
1.008	0.2049	-0.6417	-2.5526
1.008	1.6682	0.3493	-2.5888
1.008	2.7273	-0.5085	0.9796
1.008	3.2507	-1.3961	-0.4593
1.008	3.2206	0.3733	-0.4735
1.008	0.4053	-1.3469	1.7551
1.008	-0.5488	-0.4155	3.0278
1.008	-1.8951	-0.8502	0.8007
1.008	-0.0979	2.7514	1.6433
1.008	-1.2719	1.8486	2.6322
1.008	-1.5816	2.1955	0.9113

Frequencies (cm-1):

Imaginary Frequency: -3.29973312645e-05

35.851	49.278	65.120
76.987	89.489	164.144
175.637	202.215	226.037
229.671	267.879	315.249
351.370	394.469	420.493
427.845	493.166	590.245
666.972	728.845	817.732
874.108	926.166	944.947
969.160	977.220	1000.620
1060.570	1064.663	1113.140
1126.089	1175.397	1198.784
1287.983	1315.849	1384.590
1398.916	1409.300	1415.899
1436.664	1462.960	1472.256
1484.002	1486.170	1488.980
1499.252	1512.670	1670.321
1747.382	3013.895	3024.769
3025.836	3048.054	3082.556
3083.319	3084.513	3093.485
3106.446	3107.613	3124.222
3212.238	3419.609	

External Symmetry = 1.0

Principal Moments of Inertia = 394.874001193 500.733362272 653.302449748
 Electronic Degeneracy = 2

Thermodynamic Data

Translational Contributions

Temperature	298.00	300.00	400.00	500.00	600.00
800.00	1000.00	1500.00			
Entropy	40.83	40.86	42.29	43.40	44.30
45.73	46.84	48.85			
Cp	4.97	4.97	4.97	4.97	4.97
4.97	4.97	4.97			
dH	1.48	1.49	1.99	2.48	2.98
3.97	4.97	7.45			
qtrans	6.86e+07	6.98e+07	1.43e+08	2.50e+08	3.95e+08
8.10e+08	1.42e+09	3.90e+09			

Translational Contributions

Temperature	298.15
Entropy	40.83
Cp	4.97
dH	1.48
qtrans	6.87e+07

Vibrational Contributions

Entropy:

Temperature	298.00	300.00	400.00	500.00	600.00
800.00	1000.00	1500.00			
Entropy	43.49	43.75	56.46	68.60	80.12
101.31	120.19	159.39			
Cp	38.85	39.07	49.66	59.17	67.25
79.88	89.15	103.42			
dH	6.43	6.51	10.96	16.42	22.75
37.55	54.52	103.13			
q_vib	6.13e+04	6.60e+04	2.26e+06	6.55e+07	1.67e+09
7.62e+11	2.25e+14	6.42e+19			

Vibrational Contributions

Entropy:

Temperature	298.15
Entropy	43.51
Cp	38.87
dH	6.44
q_vib	6.17e+04

External Rotational Contributions

Temperature	298.00	300.00	400.00	500.00	600.00
800.00	1000.00	1500.00			
Entropy	30.15	30.17	31.03	31.70	32.24
33.10	33.76	34.97			
Cp	2.98	2.98	2.98	2.98	2.98
2.98	2.98	2.98			
dH	0.89	0.89	1.19	1.49	1.79
2.38	2.98	4.47			
q_rot	867567.01	876315.54	1349176.04	1885530.84	2478594.66
3816046.11	5333086.57	9797505.64			

External Rotational Contributions

Temperature 298.15
 Entropy 30.15
 Cp 2.98
 dH 0.89
 q_rot 868222.14

Hf298 S298 Cps:

-53.7897948549 224.671356821 46.8007492273 47.0167658057 57.6120331981
 67.1183047275 75.2017612375 87.8283443892 97.0993533413 111.371576968

Rate Data: Modified Arrhenius format

$r = A \cdot (T/1000)^n \cdot \exp(-E_a/R/T)$ 5.52e+14 -0.38 1.38
 $r = A \cdot T^n \cdot \exp(-E_a/R/T)$ 7.57e+15 -0.38 1.38

Temperature	Rate	Fit Rate
298.00	8.44e+13	8.45e+13
300.00	8.55e+13	8.56e+13
400.00	1.37e+14	1.37e+14
500.00	1.79e+14	1.78e+14
600.00	2.11e+14	2.10e+14
800.00	2.51e+14	2.52e+14
1000.00	2.73e+14	2.75e+14
1500.00	2.99e+14	2.98e+14

Rate Data: Arrhenius format

$r = A \cdot \exp(-E_a/R/T)$ 4.49e+14 0.97

Temperature	Rate	Fit Rate
298.00	8.44e+13	8.77e+13
300.00	8.55e+13	8.86e+13
400.00	1.37e+14	1.33e+14
500.00	1.79e+14	1.70e+14
600.00	2.11e+14	2.00e+14
800.00	2.51e+14	2.44e+14
1000.00	2.73e+14	2.76e+14
1500.00	2.99e+14	3.25e+14

LIST OF REFERENCES

1. Manley, D.K., A. McIlroy, and C.A. Taatjes, *Research needs for future internal combustion engines*. Phys. Today, 2008. **61**: p. 47-52.
2. Gladden, J.M., et al., *Tailoring Next-Generation Biofuels and their Combustion in Next-Generation Engines*. 2013, Sandia National Laboratories: Livermore, California. p. 100.
3. EIA, U., *Energy Information Administration "International Energy Outlook"*. 2010, report DOE/EIA-0484.
4. Gladden, J.M., et al., *Tailoring Next-Generation Biofuels and their Combustion in Next-Generation Engines*. Sandia Report 2013-10094, 2013.
5. Nigam, P.S. and A. Singh, *Production of liquid biofuels from renewable resources*. Progress in Energy and Combustion Science, 2011. **37**(1): p. 52-68.
6. Allen, J.W., et al., *A Coordinated Investigation of the Combustion Chemistry of Diisopropyl Ketone, a Prototype for Biofuels Produced by Endophytic Fungi*. Combust. Flame, 2014. **161**: p. 711-724.
7. Bott, J.F. and N. Cohen, *A Shock Tube Study of the Reactions of the Hydroxyl Radical with Several Combustion Species*. Int. J. Chem. Kinet., 1991. **23**: p. 1075-1094.
8. Black, G., et al., *An Experimental and Modelling Study of the Combustion of Acetone*, in *Third European Combustion Meeting ECM*. 2007.
9. Zhao, Z., et al., *Kinetics Study of the Gas-Phase Reactions of Atomic Chlorine with Acetone, 2-Butanone, and 3-Pentanone*. International Journal of Chemical Kinetics, 2008. **40**: p. 259-267.
10. Pichon, S., et al., *The combustion chemistry of a fuel tracer: Measured flame speeds and ignition delays and a detailed chemical kinetic model for the oxidation of acetone*. Combustion and Flame, 2009. **156**(2): p. 494-504.

11. Davidson, D.F., et al., *Ignition Delay Time Measurements of Normal Alkanes and Simple Oxygenates*. Journal of Propulsion and Power, 2010. **26**(2): p. 280-287.
12. Lam, K.-Y., et al., *Multi-species time-history measurements during high-temperature acetone and 2-butanone pyrolysis*. Proceedings of the Combustion Institute, 2013. **34**(1): p. 607-615.
13. Lam, K.-Y., D.F. Davidson, and R.K. Hanson, *High-Temperature Measurements of the Reactions of OH with a Series of Ketones: Acetone, 2-Butanone, 3-Pentanone, and 2-Pentanone*. Journal of Physical Chemistry A, 2012. **116**: p. 5549-5559.
14. Mehl, M., et al., *detailed kinetic modeling of low-temperature heat release for PRF fuels in an HCCI Engine*. SAE Technical Paper No: 2009-01-1806, 2009.
15. Yang, Y.a.D., J., *Bio-Ketones: Autoignition Characteristics and Their Potential as Fuels for HCCI Engines*. SAE Int. J. Fuels Lubr., 2013. **6**(3): p. 713-728.
16. Yang, Y. and J.E. Dec, *Bio-Ketones: Autoignition Characteristics and Their Potential as Fuels for HCCI Engines*. SAE Technical Paper 2013-01-2627, 2013.
17. Reaction Design, *CHEMKIN-PRO 15112*. 2011: San Diego.
18. Frisch, M.J., et al., *Gaussian 09, Revision A.02*. 2009, Gaussian, Inc.: Wallingford CT.
19. Allen, J.W., et al. *CanTherm*. 2013; Available from: <http://github.com/GreenGroup/RMG-Py>.
20. Ritter, E.R. and J.W. Bozzelli, *THERM: Thermodynamic property estimation for gas phase radicals and molecules*. International Journal of Chemical Kinetics, 1991. **23**(9): p. 767-778.
21. W. H. Green et al. *RMG (Reaction Mechanism Generator) version 3.3*. 2011; Available from: <http://rmg.sourceforge.net>.
22. Sarathy, S.M., et al., *Alcohol combustion chemistry*. Prog. Energ. Combust. Sci., 2014. **44**: p. 40-102.
23. Sarathy, S.M., et al., *A comprehensive chemical kinetic combustion model for the four butanol isomers*. combustion and flame, 2012. **159**(6): p. 2028-2055.

24. Curran, H.J. and J.M. Simmie, <http://c3.nuigalway.ie/mechanisms.html>, 2012.
25. Allen, J.W., et al., *A coordinated investigation of the combustion chemistry of diisopropyl ketone, a prototype for biofuels produced by endophytic fungi*. Combustion and Flame, 2014. **161**(3): p. 711-724.
26. Tanaka, S., et al., Combust. Flame, 2003. **132**: p. 219.
27. Vuilleumier, D., et al., *Intermediate temperature heat release in an HCCI engine fueled by ethanol/n-heptane mixtures: An experimental and modeling study*. Combustion and Flame, 2014. **161**(3): p. 680-695.
28. Vuilleumier, D., Selim, H., Dibble, R., and Sarathy, M., "*Exploration of Heat Release in a Homogeneous Charge Compression Ignition Engine with Primary Reference Fuels*," SAE Technical Paper 2013.
29. Agarwal, A.K., et al., *Characterization of exhaust particulates from diesel fueled homogenous charge compression ignition combustion engine*. Journal of Aerosol Science, 2013. **58**(0): p. 71-85.
30. Maurya, R.K. and A.K. Agarwal, *Experimental investigations of performance, combustion and emission characteristics of ethanol and methanol fueled HCCI engine*. Fuel Processing Technology, 2014. **126**: p. 30-48.
31. Xie, H., et al., *Investigation on gasoline homogeneous charge compression ignition (HCCI) combustion implemented by residual gas trapping combined with intake preheating through waste heat recovery*. Energy Conversion and Management, 2014. **86**(0): p. 8-19.
32. Yasar, H., et al., *Double-Wiebe function: An approach for single-zone HCCI engine modeling*. Applied Thermal Engineering, 2008. **28**(11–12): p. 1284-1290.
33. *Woschni G A Universally Applicable Equation for the Instantaneous Heat Transfer Coefficient in the Internal Combustion Engine*. SAE 670931. 1967.

34. Barari, G., Koroglu, B. Vasu, S. S. ,Dec, J. E., Taatjes, C. A., *HCCI engine modeling of diisopropyl ketone, a prototypical biofuel*. ESS Fall Technical meeting, Clemson, SC, 2013(Paper No: 085IC-0049).
35. Aceves, S., Flowers, D., Westbrook, C., Smith, J. et al., *A Multi-Zone Model for Prediction of HCCI Combustion and Emissions*. SAE Technical Paper 2000-01-0327, 2000.
36. Sjöberg, M., Dec, J., and Cernansky, N., *Potential of Thermal Stratification and Combustion Retard for Reducing Pressure-Rise Rates in HCCI Engines, Based on Multi-Zone Modeling and Experiments*. SAE Technical Paper 2005-01-0113, 2005.
37. *CHEMKIN-PRO 15131*. 2013, Reactiondesign: San Diego, CA.
38. Vasu, S.S., D.F. Davidson, and R.K. Hanson, *Jet fuel ignition delay times: Shock tube experiments over wide conditions and surrogate model predictions*. Combustion and Flame, 2008. **152**: p. 125.
39. Richard H. West, J.W.A., and William H. Green, *Automatic Reaction Mechanism Generation with Group Additive Kinetics*. Massachusetts Institute of Technology, Department of Chemical Engineering.
40. Ritter, E.R., *THERM: a computer code for estimating thermodynamic properties for species important to combustion and reaction modeling*. J. Chem. Inf. Comput. Sci., 1991. **31 (3)**: p. 400-408.
41. Dames, E.E., et al., *An improved kinetic mechanism for 3-pentanone pyrolysis and oxidation developed using multispecies time histories in shock-tubes*. Combustion and Flame, 2014. **161(5)**: p. 1135-1145.
42. Ray, A.W., et al., *Synchrotron Photoionization Measurements of OH-Initiated Cyclohexene Oxidation: Ring-Preserving Products in OH + Cyclohexene and Hydroxycyclohexyl + O₂ Reactions*. The Journal of Physical Chemistry A, 2012. **116(25)**: p. 6720-6730.

43. Hong, Z., Davidson, D. F. Hanson, R. K., *An improved H₂/O₂ mechanism based on recent shock tube/laser absorption measurements*. Combustion and Flame, 2011. **158**(4): p. 633-644.
44. Barari, G., S.M. Sarathy, and S.S. Vasu, *Improved combustion kinetic model and HCCI engine simulations of di-isopropyl ketone ignition*. Fuel, 2016. **164**: p. 141-150.
45. Minkin, V.I., B.Y. Simkin, and R.M. Minyaev, *Quantum chemistry of organic compounds: mechanisms of reactions*. 2012: Springer Science & Business Media.
46. Lewars, E.G., *Computational chemistry: introduction to the theory and applications of molecular and quantum mechanics*. 2010: Springer Science & Business Media.
47. Frisch, M.J. and e. al., *Gaussian 09, Revision D.01*, <http://www.gaussian.com>.
48. Schaftenaar, G. and J.H. Noordik, *Molden: a pre- and post-processing program for molecular and electronic structures*. J. Comput.-Aided Mol. Design., 2000. **14**: p. 123-134.
49. Peng, C.Y., et al., *Using redundant internal coordinates to optimize equilibrium geometries and transition states*. Journal of Computational Chemistry, 1996. **17**(1): p. 49-56.
50. Montgomery, J.A., et al., *A complete basis set model chemistry. VI. Use of density functional geometries and frequencies*. Journal of Chemical Physics, 1999. **110**(6): p. 2822-2827.
51. Montgomery, J.A., et al., *A complete basis set model chemistry. VII. Use of the minimum population localization method*. Journal of Chemical Physics, 2000. **112**(15): p. 6532-6542.
52. Peterson, K.A., D. Feller, and D.A. Dixon, *Chemical accuracy in ab initio thermochemistry and spectroscopy: current strategies and future challenges*. Theoretical Chemistry Accounts, 2012. **131**(1).
53. Becke, A.D., *Density-Functional Thermochemistry .3. The Role of Exact Exchange*. Journal of Chemical Physics, 1993. **98**(7): p. 5648-5652.
54. Wood, G.P.F., et al., *A restricted-open-shell complete-basis-set model chemistry*. Journal of Chemical Physics, 2006. **125**(9).

55. Saeys, M., et al., *Ab initio calculations for hydrocarbons: Enthalpy of formation, transition state geometry, and activation energy for radical reactions*. Journal of Physical Chemistry A, 2003. **107**(43): p. 9147-9159.
56. Eckart, C., *The Penetration of a Potential Barrier by Electrons*. Physical Review, 1930. **35**(11): p. 1303-1309.
57. Peralta-Yahya, P.P., et al., *Microbial engineering for the production of advanced biofuels*. Nature, 2012. **488**: p. 320-328.
58. Griffin, M.A., et al., *Volatile organic compound production by organisms in the genus Ascocoryne and a re-evaluation of myco-diesel production by NRRL 0072*. Microbiology 2010. **156**: p. 3814–3829.
59. Strobel, G.A., *Methods of discovery and techniques to study endophytic fungi producing fuel-related hydrocarbons*. Natural Product Reports, 2014. **31**(2): p. 259-272.
60. Strobel, G.A., et al., *The production of myco-diesel hydrocarbons and their derivatives by the endophytic fungus Gliocladium roseum (NRRL 50072)*. Microbiology-Sgm, 2008. **154**: p. 3319-3328.
61. Dec, J. and Y. Yang, *Bio-Ketones: Autoignition Characteristics and Their Potential as Fuels for HCCI Engines*. SAE Int. J. Fuels Lubr., 2013. **6**(3).
62. Vranckx, S., et al., *Role of peroxy chemistry in the high-pressure ignition of n-butanol – Experiments and detailed kinetic modelling*. combustion and flame, 2011. **158**(8): p. 1444-1455.
63. Zádor, J., C.A. Taatjes, and R.X. Fernandes, *Kinetics of elementary reactions in low-temperature autoignition chemistry*. Prog. Energy Combust. Sci., 2011. **37**: p. 371-421.
64. Eskola, A.J., et al., *Synchrotron photoionization measurements of fundamental autoignition reactions: Product formation in low-temperature isobutane oxidation*. Proc. Combust. Inst., 2013. **34**(1): p. 385-392.

65. Taatjes, C.A., et al., *Synchrotron photoionization measurements of combustion intermediates: Photoionization efficiency and identification of C₃H₂ isomers*. *Physical Chemistry Chemical Physics*, 2005. **7**(5): p. 806-813.
66. Hippler, H. and B. Viskolcz, *Phys. Chem. Chem. Phys.*, 2002. **2**: p. 3591.
67. Greenwald, E.E., et al., *Isomer-Selective Study of the OH Initiated Oxidation of Isoprene in the Presence of O₂ and NO. I. The Minor Inner OH-Addition Channel*. *The Journal of Physical Chemistry A*, 2010. **114**(2): p. 904-912.
68. Battin-Leclerc, F., et al., *Experimental Confirmation of the Low-Temperature Oxidation Scheme of Alkanes*. *Angew. Chem. Int. Ed.*, 2010. **49**: p. 3169-3172.
69. Taatjes, C.A., et al., *"Imaging" combustion chemistry via multiplexed synchrotron-photoionization mass spectrometry*. *Phys. Chem. Chem. Phys.*, 2008. **10**: p. 20-34.
70. Bott, J.F. and N. Cohen, *A Shock Tube Study of the Reaction of Methyl Radicals with Hydroxyl Radicals*. *International Journal of Chemical Kinetics*, 1991. **23**: p. 1017-1033.
71. Meloni, G., et al., *Energy-Resolved Photoionization of Alkylperoxy Radicals and the Stability of Their Cations*. *Journal of the American Chemical Society*, 2006. **128**(41): p. 13559-13567.
72. Welz, O., et al., *Direct Kinetic Measurements of Criegee Intermediate (CH₂OO) Formed by Reaction of CH₂I with O₂*. *Science*, 2012. **335**: p. 204-207.
73. Taatjes, C.A., et al., *Products of the Benzene + O(³P) Reaction*. *J. Phys. Chem. A*, 2010. **114**: p. 3355-3370.
74. Osborn, D.L., et al., *The multiplexed chemical kinetic photoionization mass spectrometer: A new approach to isomer-resolved chemical kinetics*. *Rev. Sci. Instrum.*, 2008. **79**(10).
75. Keller-Rudek, H., et al., *The MPI-Mainz UV/VIS Spectral Atlas of Gaseous Molecules of Atmospheric Interest*. *Earth Syst. Sci. Data*, 2013. **5**(2): p. 365-373.

76. Taatjes, C.A., et al., *"Imaging" combustion chemistry via multiplexed synchrotron-photoionization mass spectrometry*. Physical Chemistry Chemical Physics, 2008. **10**(1): p. 20-34.
77. Allen, J.W., et al., *A detailed kinetics model for the combustion of diisopropyl ketone*. Poster at the 22nd International Symposium on Gas Kinetics, Boulder, CO, 2012.
78. Welz, O., et al., *Low-temperature combustion chemistry of biofuels: pathways in the initial low-temperature (550 K-750 K) oxidation chemistry of isopentanol*. Physical Chemistry Chemical Physics, 2012. **14**(9): p. 3112-3127.
79. Welz, O., et al., *Low-Temperature Combustion Chemistry of n-Butanol: Principal Oxidation Pathways of Hydroxybutyl Radicals*. The Journal of Physical Chemistry A, 2013. **117**(46): p. 11983-12001.
80. Welz, O., et al., *Low-temperature combustion chemistry of biofuels: Pathways in the low-temperature (550–700K) oxidation chemistry of isobutanol and tert-butanol*. Proceedings of the Combustion Institute, 2013. **34**(1): p. 493-500.
81. Ranzi, E., et al., *Kinetic modeling of the thermal degradation and combustion of biomass*. Chemical Engineering Science, 2014. **110**: p. 2-12.
82. He, P.-J., et al., *The emission patterns of volatile organic compounds during aerobic biotreatment of municipal solid waste using continuous and intermittent aeration*. Journal of the Air & Waste Management Association, 2012. **62**(4): p. 461-470.
83. Pelucchi, M., et al., *An experimental and kinetic modeling study of the pyrolysis and oxidation of n-C3C5 aldehydes in shock tubes*. Combustion and Flame, 2015. **162**(2): p. 265-286.
84. Mani Sarathy, S., et al., *A comprehensive experimental and modeling study of iso-pentanol combustion*. Combustion and Flame, 2013. **160**(12): p. 2712-2728.
85. Vasu, S.S. and S.M. Sarathy, *On the High-Temperature Combustion of n-Butanol: Shock Tube Data and an Improved Kinetic Model*. Energy & Fuels, 2013. **27**(11): p. 7072-7080.

86. Heufer, K.A., et al., *Detailed Kinetic Modeling Study of n-Pentanol Oxidation*. Energy & Fuels, 2012. **26**(11): p. 6678-6685.
87. Dóbé, S., L.A. Khachatryan, and T. Bérces, *Kinetics of Reactions of Hydroxyl Radicals with a Series of Aliphatic Aldehydes*. Berichte der Bunsengesellschaft für physikalische Chemie, 1989. **93**(8): p. 847-852.
88. Sivakumaran, V. and J.N. Crowley, *Reaction between OH and CH₃CHO Part 2. Temperature dependent rate coefficients (201-348 K)*. Physical Chemistry Chemical Physics, 2003. **5**(1): p. 106-111.
89. Wang, S., D.F. Davidson, and R.K. Hanson, *High temperature measurements for the rate constants of C1–C4 aldehydes with OH in a shock tube*. Proceedings of the Combustion Institute, 2015. **35**(1): p. 473-480.
90. Ji, Y., et al., *Theoretical study of the reaction mechanism and kinetics of low-molecular-weight atmospheric aldehydes (C1–C4) with NO₂*. Atmospheric Environment, 2012. **54**: p. 288-295.
91. Miller, J.A., M.J. Pilling, and J. Troe, Proc. Combust. Inst., 2005. **30**: p. 43.
92. Taatjes, C.A., et al., *Advanced Fuel Chemistry for Advanced Engines*. 2009, SAND2009-6051, Sandia National Laboratories, Livermore, California.
93. Fernandes, R.X., et al., *Formally direct pathways and low-temperature chain branching in hydrocarbon autoignition: the cyclohexyl+ O₂ reaction at high pressure*. Physical Chemistry Chemical Physics, 2009. **11**(9): p. 1320-1327.
94. "IGOR Photoionization Database." ALS Kinetics, A., 22:59 UTC. 27 Aug 2015, 22:39 <https://share.sandia.gov/alskinetics/index.php?title=IGOR_Photoionization_Database&oldid=1355>.
95. NIST kinetic database: <http://kinetics.nist.gov/kinetics/index.jsp>, 2011.

96. Kaiser, E., C. Westbrook, and W. Pitz, *Acetaldehyde oxidation in the negative temperature coefficient regime: Experimental and modeling results*. International journal of chemical kinetics, 1986. **18**(6): p. 655-688.
97. Cord, M., et al., *Study of the Low Temperature Oxidation of Propane*. The journal of physical chemistry. A, 2012. **116**(50): p. 12214-12228.
98. Rosman, K. and P. Taylor, *Isotopic compositions of the elements 1997*. Journal of Physical and Chemical Reference Data, 1998. **27**(6): p. 1275-1287.
99. Batikan Koroglu; Owen Pryor; Joseph Lopez; Leigh Nash; Subith S. Vasu; , "*Shock tube ignition delay times and methane time-histories measurements during excess CO₂ diluted oxy-methane combustion*". Combustion and Flame **accepted 11/2015**.
100. https://commons.wikimedia.org/wiki/File:Shock_tube.png#/media/File:Shock_tube.png, S.t.b.m.-O.w.L.u.P.D.v.C.-.
101. Zhang, Y., et al., *Experimental and kinetic study on ignition delay times of methane/hydrogen/oxygen/nitrogen mixtures by shock tube*. Chinese Science Bulletin, 2011. **56**(26): p. 2853-2861.
102. Badra, J., et al., *A shock tube and laser absorption study of ignition delay times and OH reaction rates of ketones: 2-Butanone and 3-buten-2-one*. Combustion and Flame, 2014. **161**(3): p. 725-734.
103. Stranic, I., et al., *Shock tube measurements of ignition delay times for the butanol isomers*. combustion and flame, 2012. **159**(2): p. 516-527.
104. Lam, K.Y., et al., *Shock tube ignition delay time measurements in propane/O₂/argon mixtures at near-constant-volume conditions*. Proceedings of the Combustion Institute, 2011. **33**(1): p. 251-258.
105. HITRAN, *High-resolution transmission molecular absorption database*. www.cfa.harvard.edu/hitran/.

106. Esser, B., *Die Zustandsgrößen im Stoßwellenkanal als Ergebnisse eines exakten Riemannlösers*. PhD thesis, RWTH Aachen, 1991.
107. Heufer, K.A. and H. Olivier, *Determination of ignition delay times of different hydrocarbons in a new high pressure shock tube*. Shock Waves, 2010. **20**(4): p. 307-316.
108. Gaydon, A.G. and I.R. Hurlle *The shock tube in high-temperature chemical physics*. 1963.
109. KASIMIR 3. <http://www.swl.rwth-aachen.de/en/industry-solutions/kasimir/>.
110. Pyun, S.H., et al., *Interference-free mid-IR laser absorption detection of methane*. Measurement Science and Technology, 2011. **22**(2).
111. Pyun, S.H., et al., *Methane and ethylene time-history measurements in n-butane and n-heptane pyrolysis behind reflected shock waves*. Fuel, 2013. **108**(0): p. 557-564.
112. Chevalier, C., et al., *Hydrocarbon ignition: Automatic generation of reaction mechanisms and applications to modeling of engine knock*. Symposium (International) on Combustion, 1992. **24**(1): p. 93-101.
113. Vasudevan, V., D.F. Davidson, and R.K. Hanson, *High-Temperature Measurements of the Reactions of OH with Toluene and Acetone*. Journal of Physical Chemistry A, 2005. **109**: p. 3352-3359.
114. Badra, J., et al., *A shock tube and laser absorption study of ignition delay times and OH reaction rates of ketones: 2-Butanone and 3-Buten-2-one*. Combust. Flame, 2014. **161**: p. 725-734.
115. Tsang, W., *Chemical Kinetic Data Base for Combustion Chemistry. Part 3: Propane*. Journal of Physical and Chemical Reference Data, 1988. **17**(2): p. 887-951.
116. Tsang, W., J. Phys. Chem. Ref. Data, 1991. **20**(2): p. 235.
117. Singh, A., S.I. Olsen, and P.S. Nigam, *A viable technology to generate third-generation biofuel*. Journal of Chemical Technology & Biotechnology, 2011. **86**(11): p. 1349-1353.

118. Zhou, C.-W., J.M. Simmie, and H.J. Curran, *Ab initio and kinetic study of the reaction of ketones with OH for $T = 500 - 2000$ K. Part I: hydrogen-abstraction from $H_3CC(O)CH_{3-x}(CH_3)_x$, $x = 0 \rightarrow 3$* . Phys. Chem. Chem. Phys., 2011. **13**: p. 11175-11192.
119. Serinyel, Z., et al., *Experimental and Chemical Kinetic Modeling Study of 3-Pentanone Oxidation*. Journal of Physical Chemistry A, 2010. **114**: p. 12176-12186.
120. Mendes, J., C.-W. Zhou, and H.J. Curran, *Theoretical and Kinetic Study of the Reactions of Ketones with HO₂ Radicals. Part I: Abstraction Reaction Channels*. The Journal of Physical Chemistry A, 2013. **117**(22): p. 4515-4525.
121. Vasu, S.S., D.F. Davidson, and R.K. Hanson, *OH time-histories during oxidation of n-heptane and methylcyclohexane at high pressures and temperatures*. Combust. Flame, 2009. **156**: p. 736.
122. Badra, J., A. Elwardany, and A. Farooq, *Reaction rate constants of H-abstraction by OH from large ketones: measurements and site-specific rate rules*. Phys. Chem. Chem. Phys., 2014. **161**: p. 725-734.
123. Cohen, N., *Are reaction rate coefficients additive? Revised transition state theory calculations for OH + alkane reactions*. International Journal of Chemical Kinetics, 1991. **23**(5): p. 397-417.
124. Lam, K.-Y., et al., *Shock tube measurements of 3-pentanone pyrolysis and oxidation*. Combustion and Flame, 2012. **159**(11): p. 3251-3263.
125. Curran, H.J., et al., Combust. Flame, 1998. **114**: p. 149.
126. Matheu, D.M., et al., *Mechanism Generation with Integrated Pressure Dependence: A New Model for Methane Pyrolysis*. The Journal of Physical Chemistry A, 2003. **107**(41): p. 8552-8565.
127. Curran, H.J., et al., *A comprehensive modeling study of iso-octane oxidation*. combustion and flame, 2002. **129**(3): p. 253-280.

128. Sumathi, R., H.H. Carstensen, and W.H. Green, *Reaction Rate Prediction via Group Additivity Part 1: H Abstraction from Alkanes by H and CH₃*. The Journal of Physical Chemistry A, 2001. **105**(28): p. 6910-6925.
129. Zhao, P., et al., *Laminar flame speeds, counterflow ignition, and kinetic modeling of the butene isomers*. Proceedings of the Combustion Institute, 2015. **35**(1): p. 309-316.
130. Mehl, M., et al. *Chemical kinetic modeling of component mixtures relevant to gasoline*. in *European Combustion Meeting*. 2009.
131. Goos, E., A. Burcat, and B. Ruscic. *EXTENDED THIRD MILLENNIUM IDEAL GAS AND CONDENSED PHASE THERMOCHEMICAL DATABASE FOR COMBUSTION WITH UPDATES FROM ACTIVE THERMOCHEMICAL TABLES*. 2011 July 23, 2014]; Available from: <http://garfield.chem.elte.hu/Burcat/THERM.DAT>.
132. Zhang, J., et al., *Shock Tube and Kinetic Modeling Study of Isobutanol Oxidation*. Energy & Fuels, 2013. **27**(5): p. 2804-2810.
133. Zhang, J., et al., *Experimental and modeling study of the auto-ignition of n-heptane/n-butanol mixtures*. combustion and flame, 2013. **160**(1): p. 31-39.